High Efficiency Multicrystalline Silicon Solar Cells

by

Matthew Justin Stocks

A thesis submitted for the degree of
Doctor of Philosophy
of The Australian National University

May, 1998

I certify that this thesis does not incorporate without acknowledgment any material previously submitted for a degree or diploma in any university, and that, to the best of my knowledge, it does not contain any material previously published or written by another person except where due reference is made in the text. The work in this thesis is my own, except for the contributions made by others as described in the Acknowledgements.

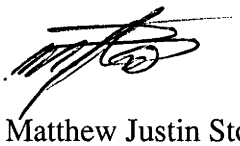

Matthew Justin Stocks

Acknowledgements

I wish to thank my supervisors, Andrew Blakers and Andres Cuevas for their encouragement, patience and support. They have been the source of much useful advice and discussions on many issues throughout this research.

Many members of the solar energy group at the ANU also provided valuable practical assistance and advice throughout the project. Stephane Armand processed many multicrystalline cells at various stages of the work, and Christopher Samundsett assisted with processing and lifetime measurements of the boron diffused cells and samples for determining surface recombination velocities of steam oxides. Anna Carr assisted with the reflectance measurements from the textured samples in chapter 2 and Susannah Hiron continued the work on TiO_2 deposition from liquid sources. I am grateful to Michael Stuckings for many useful discussions for overcoming practical problems in the laboratory. I would also like to thank Will Keogh for his computing advice, Josephine Farmer for her administrative support and Vaman Kuber for repair and maintenance of equipment.

Assistance was also received at the Australian National University from outside the solar group. The Electron Microscopy Unit at the Research School of Biological Science provided equipment and guidance for obtaining the images of the textured multicrystalline surfaces and elipsometry measurements were made with the equipment and assistance of the Plasma Research Laboratory at the Research School of Physical Science and Engineering. I also wish to thank Mark Ridgway, from Electronics Materials Engineering at the Research School of Physical Science and Engineering for forming part of my supervisory panel.

I would like to extend my appreciation to Francesca Ferrazza for supplying the multicrystalline silicon from Eurosolare which was used throughout this work.

Ron Sinton, Sinton Consulting, USA, was the source of useful discussions and suggestions on the use of quasi–steady state photoconductance measurements for which I am grateful.

Finally, I would like to thank my wife, Christine, and our families whose understanding and support have helped to ensure my continued enjoyment of research.

Abstract

In this work, high efficiency approaches to the design and manufacture of multicrystalline silicon solar cells were investigated. The following areas were addressed: reflection control and light trapping, recombination processes in multicrystalline silicon, both in the bulk and at the surface, process monitoring and optimisation, and device design, complemented with theoretical modelling. This work has lead to improvements in the efficiencies of multicrystalline silicon solar cells at the solar group from the ANU from less than 15% to greater than 18%.

A texture using isotropic etching suitable for multicrystalline silicon was developed. The resulting 'tubs' provided excellent reflection control after encapsulation, relying upon total internal reflection at the air/glass interface, and demonstrated light trapping properties superior to those of inverted pyramids and microgrooves. Low reflectance losses of 5%, including finger reflection, were achieved on completed cells.

Theoretical comparisons were made between multilayer and conventional thin film cells on low lifetime material. Unlike previously reported investigations, device thickness was optimised for maximum efficiency. This optimisation decreased the apparent gap between multilayer and conventional device performance.

Systematic use was made throughout this investigation of quasi–steady state photoconductance (QSSPC) technique for large area effective lifetime measurements. QSSPC provided superior measurements of effective lifetime on multicrystalline silicon to the photoconductance decay technique. Good correlation was found between measured lifetimes and final device performance.

The importance of process monitoring for improving device performance was established. Mobile impurities were found to strongly influence cell behaviour in Eurosil multicrystalline silicon. Record high effective lifetimes were achieved on 1.5Ωcm substrates using phosphorus gettering treatments. Phosphorus pre–gettering prevented lifetime degradation during oxidations after phosphorus diffusions, thereby increasing processing and design flexibility.

Modelling highlighted the increased importance of rear surface recombination when diffusion lengths are increased due to phosphorus gettering. Appropriate cell designs enabled the demonstration of record open circuit voltages greater than 650mV on 0.5Ωcm and 0.2Ωcm Eurosil multicrystalline silicon, with cell efficiencies greater than 18%.

Surface recombination velocities on oxidised multicrystalline silicon were measured for the first time. Surface recombination velocities of steam oxidised 1.5Ωcm substrates were below 150cm/s and showed little injection level dependence.

CHAPTER 1
INTRODUCTION

Despite the continued development of many promising thin film technologies [1,2,3], crystalline silicon remains the dominant material for commercial photovoltaics. Crystalline silicon's success has been attributed to the material's near ideal bandgap (and associated high efficiency potential), elemental abundance, established long term stability, extensive use in microelectronics, and low toxicity [4]. Silicon photovoltaics is an established industry with a significant production volume experiencing rapid expansion.

1.1 Silicon solar cell basics

The theoretical and experimental background for understanding the behaviour of silicon solar cells has been extensively reviewed by Green [5,6,7]. The majority of silicon solar cells are based on a p–n junction diode. Figure 1.1 presents a schematic of a simple silicon solar cell. The cell consists of an emitter of one dopant type and a base region of the opposite doping, with a p–n junction forming at their boundary. Photons of sufficient energy are absorbed by the silicon, transferring their energy to electrons, and exciting them from the valence band to the conduction band (the photovoltaic effect). Each absorbed photon generates an electron in the conduction band and a hole in the valence band.

When no voltage is applied to the cell, minority carriers generated in the emitter and base diffuse to the junction for collection and are driven across it by the strong local electric fields. Crossing the junction, these become majority carriers and move towards the appropriate contact (holes to the rear, electrons to the front). An electric current equal to the sum of the electrons and holes collected flows through the external circuit. This is the short circuit current, I_{sc}.

Applying a load to the cell develops a voltage between the p–type and n–type regions. This voltage causes the flow of an opposing current through the diode superimposed on the short circuit current. In the absence of resistive effects, the current is related to the voltage via

$$I(V) = -I_{sc} + I_o\left(e^{qV/kT}-1\right) \qquad (1.1)$$

where the term I_0 is the diode saturation current which depends upon the dimensions, doping and recombination characteristics of the device.

The typical current voltage curve of a silicon solar cell can be seen in figure 1.2. The intercept of the curve on the voltage axis is the open circuit voltage, V_{oc}. The maximum power of the cell is the maximum product of current and voltage, and is related to the open circuit voltage and short circuit voltage via the fill factor, FF, which is defined as

$$Power_{max} = I_{mp}V_{mp} = FFV_{oc}I_{sc} \qquad (1.2)$$

Cell efficiency is the maximum power of the cell divided by the power of the incident illumination.

1.2 Avenues for improving cell efficiency

Increasing the efficiency of a silicon solar cell requires improvements in the product of short circuit current, open circuit voltage and fill factor. Cell efficiency can be improved by maximising generation while minimising recombination and ohmic losses, that is:

- increasing the fraction of incident light absorbed in the cell
- increasing carrier collection efficiencies
- decreasing the diode saturation current, and
- reducing resistive and other parasitic losses

Cell optimisation often requires trade offs between gains in one of these four areas, and losses in another. For example, reflection losses can be reduced from the front metal contacts with greater contact spacing at the expense of increased resistive losses in the emitter[8].

The short circuit current is directly proportional to the number of excess carriers generated by light absorbed in the cell and their probability of collection. Increasing the amount of light absorbed in the cell requires decreased reflection losses (to increase the quantity of light entering the cell) and long path lengths for the light in the substrate (to maximise the absorption of the light that enters the cell).

Decreased reflection losses are usually achieved with suitably designed coatings on the front and rear of the cell and texturing. Texturing is any form of roughening of the surface of the silicon. Surface roughness reduces reflection losses if light reflected from the surface is directed towards another silicon surface, providing a second opportunity for transmission into the substrate. The area of the contacts on the front surface of the cell also sets a minimum on the possible reduction of reflection losses.

Since silicon is an indirect band gap semiconductor, it is a poor absorber of light at energies approaching the energy band gap for Si (1.124eV). Therefore, the path the light follows in the silicon substrate must be as long as possible to maximise absorption. Path length increases can be achieved by increasing the thickness of the cell, but this requires more silicon (and associated cost) and increases the average distance the carriers have to diffuse to be collected, decreasing the probability of collection. An alternative is to incorporate 'light trapping' which increases the number of times the light crosses the substrate before it escapes the silicon. Some 'light trapping' is easy to achieve in silicon due to its high refractive index. Any light striking an air interface from inside the silicon at greater than 16° from normal incidence is totally internally reflected and 'trapped' in the silicon. The light can be deviated to these angles with almost any degree of surface texturing, with path lengths greater than 40 times the substrate thickness theoretically possible using suitably textured surfaces [9]. This reduces the thickness of silicon required to absorb an equivalent quantity of light, and the carriers can be generated closer to the collection region. Reflection control and light trapping are treated in more detail in chapter 2.

base. Most changes which reduce series resistance losses potentially cause decreases in short circuit current and/or open circuit voltage (e.g. increased substrate and emitter doping, or increased front contact area).

1.3 Choice of crystalline silicon substrate

Three approaches are currently being investigated for crystalline silicon solar cell design: single crystal, multicrystalline and thin–film.

1.3.1 *Single crystal silicon solar cells*

Single crystal silicon is the highest quality silicon, and correspondingly demonstrates the highest cell efficiencies. Growth of single crystal silicon ingots is relatively expensive due to the carefully controlled nature of the growth and the high temperatures required. Czochralski (Cz) silicon is grown by slowly pulling a single crystal seed crystal from a silicon melt. Cz silicon tends to have a high level of oxygen contamination from the crucible, limiting the carrier lifetime in moderately doped material [10]. Higher quality single crystal silicon is produced by float–zoned processing (Fz), during which a molten region of silicon is moved repeatedly along the ingot. Segregation reduces the impurity concentration in most of the ingot, driving the impurities to the ends. Fz wafers with low resistivities less are capable of lifetimes greater than ten milliseconds.

Single crystal silicon solar cell technology has matured to the point where terrestrial cell efficiencies exceed 24% [11] on Fz silicon, approaching the 28.8% upper bound imposed by Auger recombination [7]. The high cell efficiencies are a combination of high bulk lifetimes (with carefully controlled furnace processing), low surface recombination from thermal oxides and increased doping under the metal contacts, and excellent reflection control and light trapping due to texturing. Effective texturing on single crystal silicon can be routinely achieved with anisotropic etches, which are used to selectively etch different crystal orientations to produce grooves or pyramids on the silicon surface.

The high bulk lifetime possible in single crystal silicon has led to surface recombination becoming the major issue when minimising recombination in cells. Suitable surface passivation enables robust optimisation of phosphorus diffused emitters, with near 100% collection of carriers generated in the emitter [12] and high open circuit voltages. Surface recombination has been the dominant mechanism affecting the design of high efficiency single crystal silicon cells for the last ten years. Cells have evolved from the moderate passivation provided by aluminium alloyed rears, through reduced rear contact areas, local diffusions under contacts (PERL and point contact cells) and floating rear junctions.

1.3.2 *Multicrystalline silicon cells*

Multicrystalline silicon was developed as an alternative to single crystal silicon to reduce the cost of the silicon substrate, since the silicon wafer can contribute to as much as one

Most interest is in foreign substrates which are attractive for the potential low cost of some substrates, such as glass, graphite [19] or ceramic [20], combined with the ease of incorporating light trapping and the potential for integrated cell interconnection. These advantages are offset by small grain sizes (without subsequent recrystallisation), reductions in carrier lifetimes and problems with conventional high temperature furnace processing due to the thermal expansion mismatch between the silicon and substrate.

This has led to the development of innovative approaches to cell design to achieve the 15% efficiency minimum generally regarded as necessary for a reasonable balance of systems costs. One of the most interesting developments has been the multilayer silicon solar cell [21,22] where multiple p–type and n–type layers are connected in parallel. Individual layers are engineered to remain thinner than a diffusion length, ensuring high collection probabilities even in low quality material.

Growing silicon on a silicon substrate has the advantage of a template for crystal growth, enabling good crystallographic quality of deposited layers. Since the substrate and deposited layer are silicon, traditional cell processing is possible without concerns for thermal mismatch. Research has moved from approaches involving the deposition of silicon on low cost silicon substrates [23], to the removal of thin layers from more expensive single crystal substrates, and the reuse of the substrate for multiple thin layers [24,25,26]. The efficiency potential of single crystal silicon is high with 21.5% already demonstrated for a thin single crystal cell [27]. The success of these approaches will depend on the cost of the thin layer formation and cell processing since achieving efficiencies greater than 15% appears less challenging.

1.4 Motivation and thesis outline

Research into thin crystalline silicon solar cells is in its infancy, with bulk crystalline silicon unlikely to be displaced from its dominant market share in the next ten years [28]. An effort in multicrystalline silicon is well justified at present, as a significant part of the photovoltaics industry relies on this material. Multicrystalline silicon has the potential to remain a bridge towards thin film silicon.

The major driving force behind improving the efficiency of multicrystalline silicon cells has been maximising bulk lifetime at the completion of cell processing. This has led to cell designs and processes which include phosphorus gettering and aluminium alloying, combined with low processing temperatures. These approaches, combined with improvements in multicrystalline silicon growth, have enabled the demonstration of bulk diffusion lengths in completed cells which are greater than the substrate thickness. This changes the focus from minimising bulk recombination to minimising total (bulk and surface) recombination in the completed device. The flow of this thesis reflects the changes in emphasis as progress was made during the research.

CHAPTER 2
IMPROVING THE OPTICAL PROPERTIES OF SILICON SOLAR CELLS

Maximising the absorption of incident light was identified in the introduction as important for improving the current in silicon solar cells. The early sections of this chapter review the optical properties of silicon and the use of antireflection coatings for controlling reflection losses from silicon. Titanium dioxide is a useful high refractive index material for antireflection coatings on silicon, both for double layer antireflection coatings and for encapsulated cells. Techniques were established for the production of high quality layers with the thermal evaporation vacuum equipment available in the solar group at the ANU.

The latter sections of this chapter investigate texturing of multicrystalline silicon. Lack of a suitable has been identified as a major contributor to the efficiency gap between multicrystalline [7]. An effective texture for texturing multicrystalline silicon was developed with good reflection control and excellent light trapping.

2.1 Solar Spectrum

The distribution of radiation from the sun can be approximated by a blackbody with a temperature of 6000K. The energy at a given wavelength strongly increases in the ultraviolet region of the spectrum, peaking in the visible region and decreasing slowly as the wavelength increases through the near and far infrared. After passing through the atmosphere, this spectrum changes slightly due to absorption and scattering, decreasing in intensity and the peak shifts towards longer wavelengths [29].

The standard used for most non–concentrating measurements is the AM1.5g spectrum. This corresponds to light which passes through the atmosphere at approximately 48 degrees from overhead and includes the diffuse and direct components of the incoming light. The American standard spectral distribution for AM1.5g can be seen in figure 2.1. The illumination standard for one sun cell testing is $1 kWm^{-2}$. Design of the optical properties of a cell must take account of the energy distribution of the incoming light.

2.2 Reflection losses from silicon

2.2.1 *Optical properties of silicon*

For crystalline silicon solar cells, the refractive index of silicon is greater than 3.5 [30] in the useful region of the solar spectrum between 300nm and 1100nm (figure 2.2). Due to this high refractive index, silicon reflects greater than 30% of light incident onto a polished surface. This leads to a corresponding decrease in current and efficiency. It is therefore important to incorporate features which minimise this reflection loss to improve the efficiency of silicon devices.

Silicon is also a relatively poor absorber of light, especially in the near–infrared. This leads to the requirement for relatively thick silicon layers to maximise the amount of light

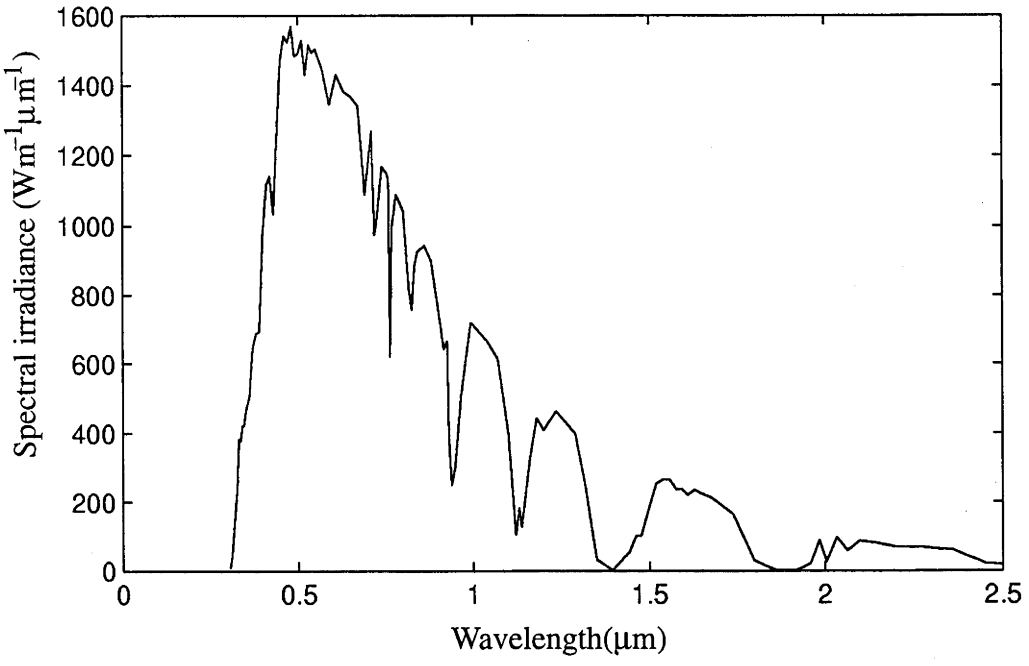

Figure 2.1: *ASTM AM1.5 global spectrum* [29].

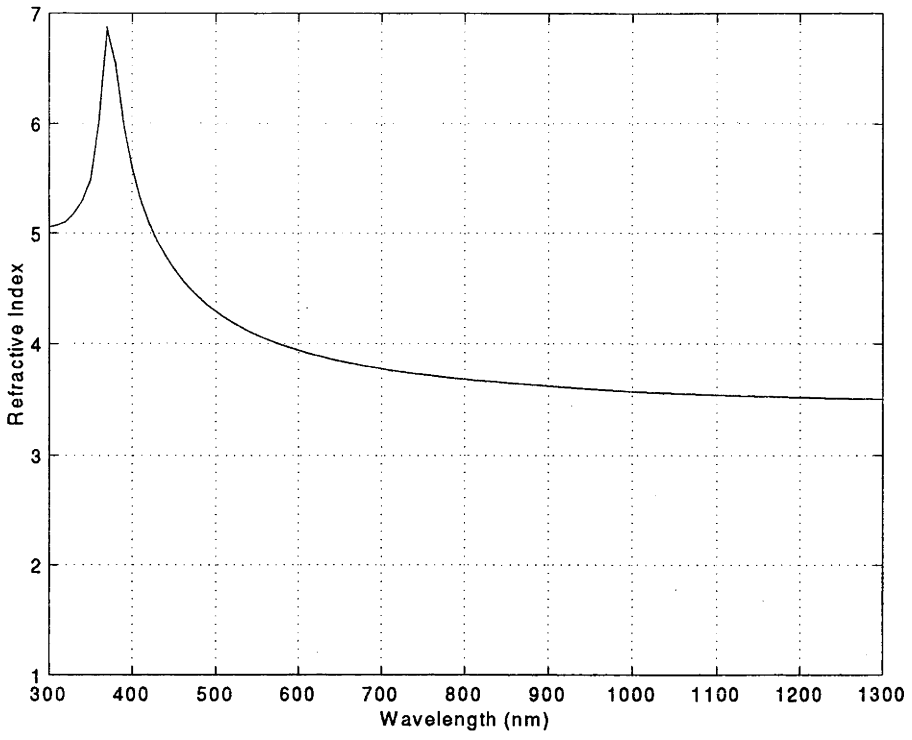

(a)

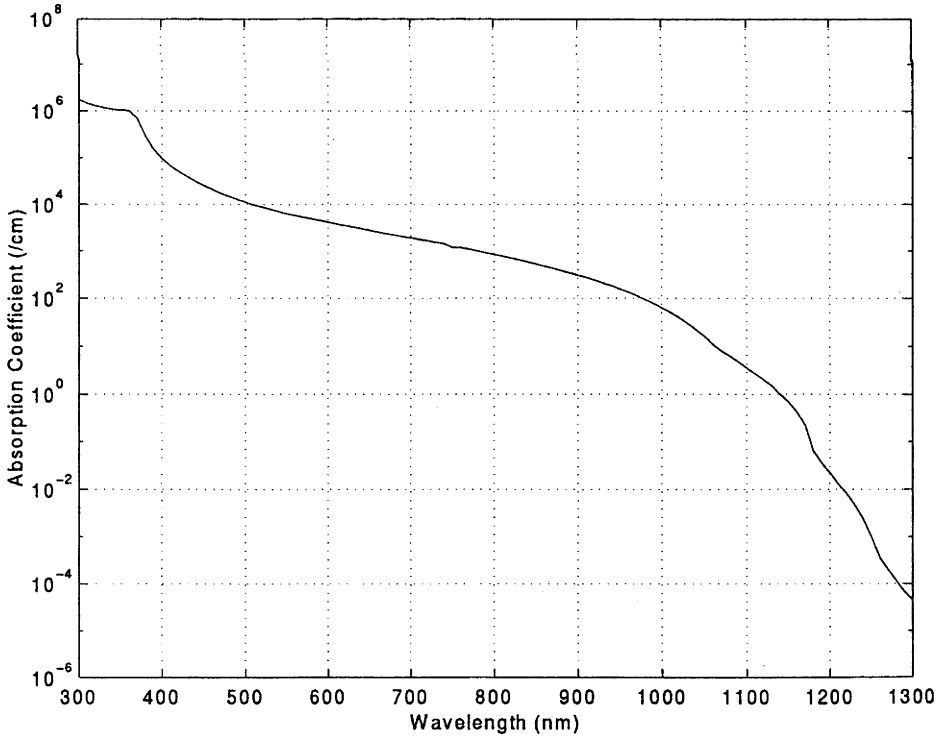

(b)

Figure 2.2: *Optical Properties of Silicon from Green and Keevers [30] (a) Refractive Index (b) Absorption Coefficient.*

absorbed by the solar cell, or the incorporation of 'light–trapping' features to ensure that the light has the greatest possible chance of being absorbed before escaping from the silicon.

2.2.2 *Weighted reflectance*

Since the incident illumination and reflection losses from a silicon solar cell can vary strongly with wavelength, it is important to report reflection losses weighted by the potential for producing current in the cell [31]. The internal quantum efficiency (IQE) of the cell is a measure of the probability of a photon producing a collected photogenerated carrier [6]. The weighted reflectance loss should therefore be expressed as

$$R_{ave} = \frac{\int_0^{\infty} R(\lambda).S(\lambda)\left(\frac{\lambda}{hc}\right).IQE(\lambda)d\lambda}{\int_0^{\infty} IQE(\lambda)S(\lambda)\left(\frac{\lambda}{hc}\right)d\lambda} \qquad (2.1)$$

where S(λ) is the energy distribution of the spectrum (as per figure 2.1) which is converted to a photon distribution by dividing by the energy of a photon (hc/λ).

Ideally, the reflectance would be optimised for the IQE of the cell since this depends on the absorption and recombination characteristics of the device. Since the reflectance work in this chapter was investigated independent from cells, the IQE was assumed to be equal to one from 300nm to 1100nm and zero elsewhere. This approximates the response range of high efficiency PERL cells [32]. This reduces the integral in equation (2.1) to

$$R_{ave} = \frac{\int_{300nm}^{1100nm} R(\lambda).S(\lambda)\lambda d\lambda}{\int_{300nm}^{1100nm} S(\lambda)\lambda\, d\lambda} \qquad (2.2)$$

Weighted reflectance reported in this work was determined by using equation (2.2) unless a different wavelength range was stated.

2.2.3 *Optically thick coatings*

The reflection loss of light normally incident upon a silicon surface with refractive index n_2 is given by

$$R = \frac{(n_2 - n_1)^2 + k_2^2}{(n_2 + n_1)^2 + k_2^2} \qquad (2.3)$$

where n_1 is the refractive index of the layer adjacent to the silicon surface while k_2 is the extinction coefficient of the silicon (assuming that the incident medium is non–absorbing) [33]. The amount of reflection is therefore minimised by keeping the refractive index of adjacent layers as similar as possible. The reflection losses from normally incident light

onto a silicon wafer in air was measured with an integrating sphere and spectrophotometer and presented with the modelled reflection loss from equation (2.3) in figure 2.3. The weighted reflection loss was high at 35%, wasting much of the useful incident illumination. The curves diverged at longer wavelengths due to light which entered the silicon and was reflected from the rear surface without being absorbed. The reflection loss would be greater still if the light strikes at an angle away from the normal (assuming the light is randomly polarised).

The most common technique for reducing the reflection loss from a surface is to apply a material of intermediate refractive index to the surface. The reflection loss from a thick layer (ignoring absorption effects) is then the combined reflection losses from the two surfaces via

$$R = \frac{R_1 + R_2 - 2R_1R_2}{1 - R_1R_2}$$
$$R_1 = \left(\frac{n_1 - n_a}{n_1 + n_a}\right)^2 \quad R_2 = \left(\frac{n_a - n_2}{n_a + n_2}\right)^2 \qquad (2.4)$$

where n_a is the refractive index of the layer applied to the surface. The presence of an encapsulating glass/pottant layer on top of a silicon solar cell substantially reduces the light loss from the silicon. An encapsulating layer (refractive index$\sim$1.46) reduced reflection losses by greater than one third to 23%, as can be by comparing the measured and modelled results in figures 2.3 and 2.4.

A minimum value for the reflection loss from the addition of a single layer is found when the refractive index of the adjacent layer satisfies

$$n_a = \sqrt{n_1 n_2} \qquad (2.5)$$

This can reduce the reflection loss from a surface by 50%. Calculations with equation 2.4 showed that the optimal refractive index for a single layer coating for silicon in air is between 1.9 and 2.0 which reduces weighted reflection losses to below 20%. However, there are not any candidate materials for thick layers with this refractive index. It is therefore necessary to consider thin layers to further reduce reflectivity.

2.2.4 *Optically thin layers (antireflection coatings)*

Interference of light can occur whenever two or more waves of light coherently overlap. The effects of interference cannot be explained by a purely particle nature of light (photon) but rely on the wave nature of light with the electric (and magnetic) fields of the light varying in space. The amplitude of the electric (or magnetic) field of the resulting light wave is governed by the superposition principle, with the amplitude of the electric (or magnetic) fields of the individual waves summed.

2.2.4.1 *Single layer antireflection (AR) coatings*

When a surface is coated with a layer with thickness of the order of the wavelength of the illuminating light, light reflected from the front and light transmitted through the front after

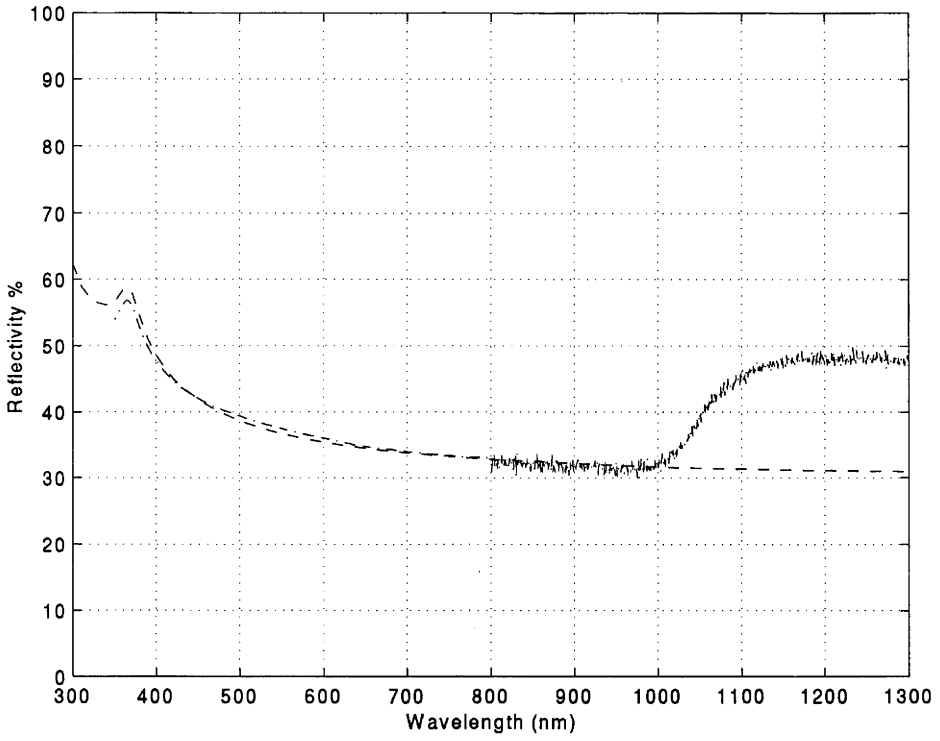

Figure 2.3: *Reflection from a polished silicon wafer.*
—·—Modelled from equation (2.3).
– – – – Measurement with spectrophotometer and integrating sphere.

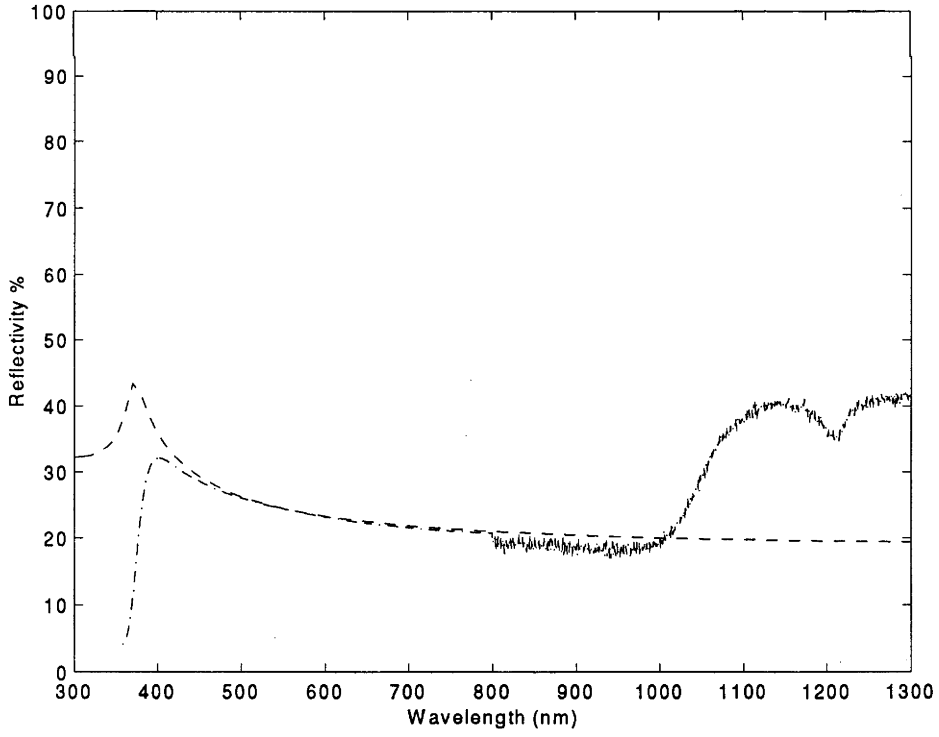

Figure 2.4: *Reflection from silicon encapsulated by Vycor glass and EVA.*
—·—Modelled from equation (2.3).
– – – – Measurement with spectrophotometer and integrating sphere.
The weighted reflectance was reduced below 20%. The decrease in measured reflectivity below 400nm was due to absorption in the EVA.

reflection from the rear of the layer can interfere. When the light reflected from the rear is out of phase with the light reflected from the front, the light interferes destructively, reducing the amount of light reflected. This occurs when the difference between the distances the light travels is an odd multiple of half wavelengths.

The fraction of normally incident light reflected from a layer covered with a thin layer, thickness d, of refractive index n_a, bounded by layers with refractive index n_1 and n_2, is given by

$$R = \frac{r_1^2 + r^2{}_2 + 2r_1r_2\cos 2\delta}{1 + (r_1r_2)^2 + 2r_1r_2\cos 2\delta}$$

$$r_1 = \frac{n_1 - n_a}{n_1 + n_a} \quad r_2 = \frac{n_a - n_2}{n_a + n_2} \quad \delta = \frac{2\pi n_a d}{\lambda} \text{ [34]} \qquad (2.6)$$

The reflection losses vary with wavelength primarily due to changes in the cosδ term, which describes the amount the light interferes. The light interferes destructively producing a minimum reflectance whenever the cosδ term is equal to –1, or equivalently when the thickness of the layer, d, is an odd integer multiple of quarter wavelengths in the thin layer (quarter wavelengths in air divided by the refractive index). This corresponds to the reflected and transmitted light being totally out of phase. In contrast, when cosδ is equal to 1 the light reflected from the front surface and the rear surface of the thin layer are in phase and correspondingly interfere constructively, producing maximum light reflection. It is therefore important to correctly optimise the thickness of the thin layer, in addition to its refractive index, to minimise reflection where the solar spectrum is most intense.

A commonly used single layer antireflection coating is a thermally grown oxide. A 110nm oxide reduces reflection losses weighted over the solar spectrum from around 35% to 14%

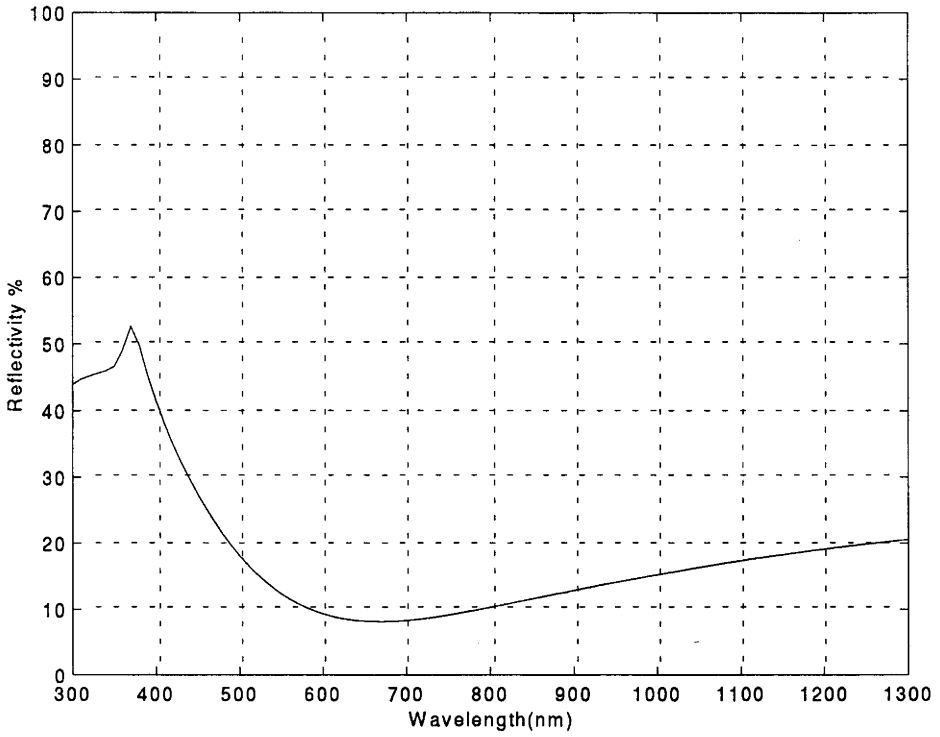

Figure 2.5: *Calculated reflection for 110nm single layer silicon dioxide AR coating on silicon from equation (2.6).*

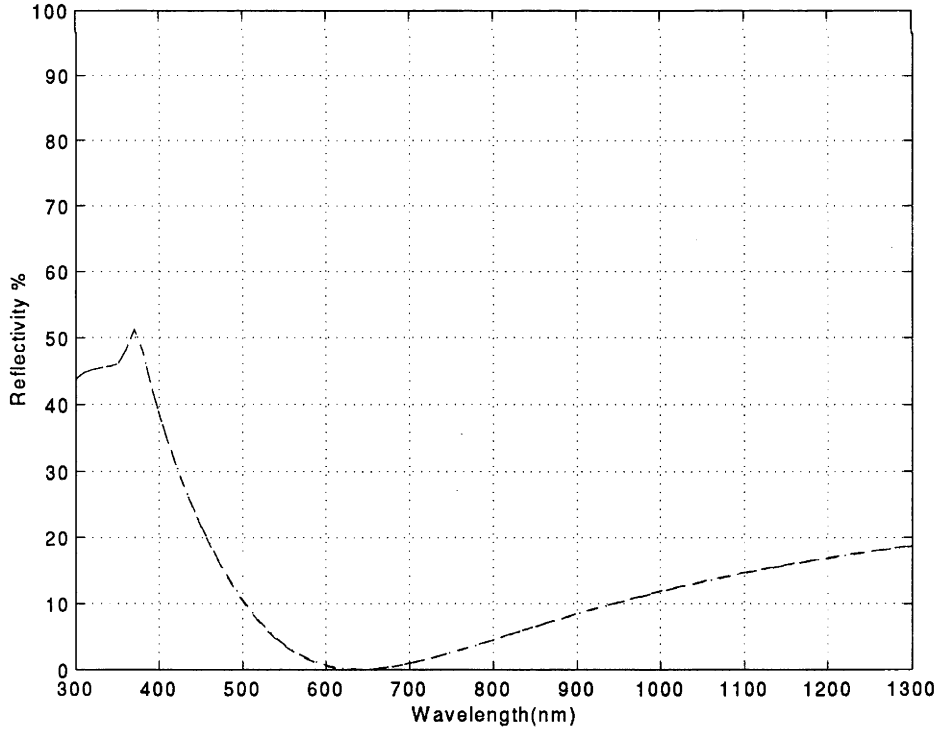

Figure 2.6: *Calculated reflection from a near optimal single layer AR coating (n=1.95) on silicon using equation (2.6).*
Weighted reflectance was reduced to 8% between 300 and 1100nm. The minimum reflectance was near zero at the peak photon flux (600–700nm).

effects by the inclusion of charges trapped in the material. These induce an inversion of the surface and can demonstrate excellent surface passivation [36].

2.2.4.2 *Double layer antireflection coatings*

Stacks of thin layers can further reduce reflection losses provided that the refractive index of each layer deposited decreases. Heavens [34] provides methods for extending the analysis for a single layer to multiple layers.

Double layer antireflection (DLAR) coatings make significant reflection reductions compared to single layer AR coatings. Reflection losses are lower and reduced over a broader range of the spectrum. This can be seen comparing the modelled DLAR coating in figure 2.7 to the optimal single layer AR coating in figure 2.6. The DLAR coating consisted of 110nm of an n=1.4 layer and 60nm of an n=2.4 layer and had a weighted reflectance of 2.5%. Reflection losses were significantly lower at the blue and infrared ends of the spectrum, with reflection losses less than 3% between 450nm and 950nm.

The optimisation of the DLAR coating was robust. Variations of greater than 10% in the thickness of the layers produced weighted reflection losses which were still less than 3%. This corresponded to less than a 0.5% decrease in transmission.

Double layer AR coatings are used for high efficiency single crystal [32] and multicrystalline silicon solar cells [18]. Little further gain is available with the addition of three or more layers.

2.2.4.3 *Thin passivating oxides*

The preceding discussion assumed that the AR coating was deposited directly onto bare silicon. Bare phosphorus diffused silicon has high surface recombination velocities [37] which lead to increased emitter recombination and decreased blue response [6]. Thick thermally grown oxides provide excellent passivation but the low refractive index increases the reflection losses from subsequently deposited high refractive index layers. The oxide layer has to be reduced sufficiently to minimise increased reflection losses.

Figure 2.8 is a contour plot of the reflection from a single layer AR coating with refractive index 1.95 (as in figure 2.6) on top of a passivating oxide layer, varying the thickness of the two layers. The reflection loss for the optimal AR coating thickness increased as the the thickness of the passivating layer increased. The optimal thickness of the AR coating also decreased as the passivating oxide thickness increased.

In the absence of any passivating oxide, the weighted reflectance loss was 8.4% and increased to 9% for just 26nm of passivating oxide. The passivating oxide should therefore be kept below 20nm [6] in order to keep transmission decreases to less than half a percent.

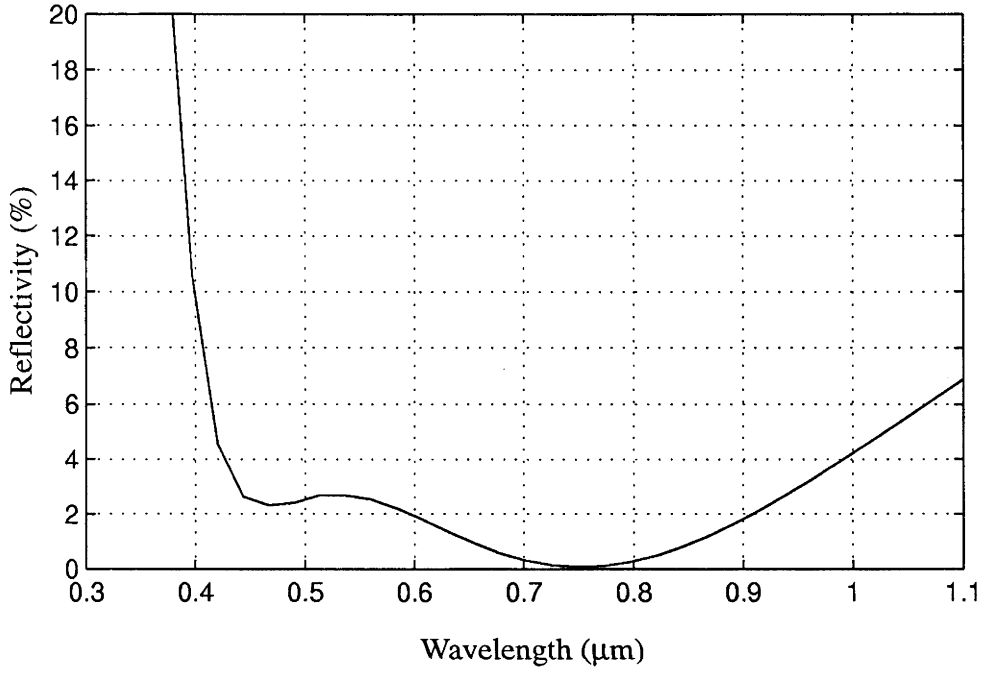

Figure 2.7: *Modelled reflectance from a DLAR (n1=1.4,n2=2.4) coating. The top layer was 110nm and the bottom layer was 60nm. Weighted reflectance was reduced below 2.5% with reflection below 3% from 450 to 950nm.*

2.2.4.4 *Antireflection coatings and encapsulation*

Solar cells are typically encapsulated before deployment in the field in order to protect the solar cells from the effects of weather, to prevent corrosion and to increase the mechanical strength of the module. The presence of the thick layer of glass and pottant bonded to the cell changes the optical properties of the system.

Thermally grown oxides are no longer suitable as an antireflection coating after encapsulation since the refractive index of the encapsulant and the thermal oxide are similar (n~1.5), with reflectance increasing from 14% to 20% upon encapsulation. The choice of optimal refractive index for the thin layer adjacent to the silicon surface should still satisfies equation 2.7, with n_1 replaced by the refractive index of the encapsulant layer. The refractive index required was found to be around 2.4 (figure 2.9) to produce a calculated weighted reflectance of 7.8%, including 3.5% from the glass. This can be reduced to 5.5% with an AR coating on the glass. The encapsulating layer decreases the sensitivity of the reflection losses to non–optimal thicknesses of the AR coating.

Very few candidates exist for high refractive index, non–absorbing materials suitable for antireflection coatings for solar cells. One of the more commonly used materials is zinc sulphide, used for the double layer antireflection coatings in record high efficiency crystalline silicon solar cells [32]. However, sulphide films demonstrate poor resistance to chemical attack and scratching even if baked or deposited at elevated temperatures.

2.2.5 *Titanium dioxide AR coatings*

Metal oxides offer better material properties than sulphide films. An excellent candidate among these is titanium dioxide (TiO_2). Titanium dioxide is structurally hard making it ideal to resist scratching and other mechanical damage. It is also transparent in the visible and infrared spectrum, making it particularly suitable for use on silicon solar cells.

Numerous techniques exist for producing titanium dioxide layers including oxidation of vacuum deposited titanium metal at 400°C–450°C in air or oxygen [38], reactive sputtering or evaporation of titanium in oxygen [39], thermal evaporation of titanium oxides (TiO, Ti_2O_3 and TiO_2) in partial oxygen atmospheres [40] and decomposition of titanium based organo–metallic compounds on heated substrates [41,42,43].

Titanium dioxide can exist in three crystalline forms (the tetragonal forms anatase and rutile and the orthorhombic structure brookite) or can be deposited as a disordered amorphous structure [38]. The resistance to scratching, the refractive index and the density increases through the amorphous, anatase and rutile phases of TiO_2 respectively (brookite is less commonly found). The phase of the TiO_2 depends strongly upon deposition conditions and substrate temperatures [40].

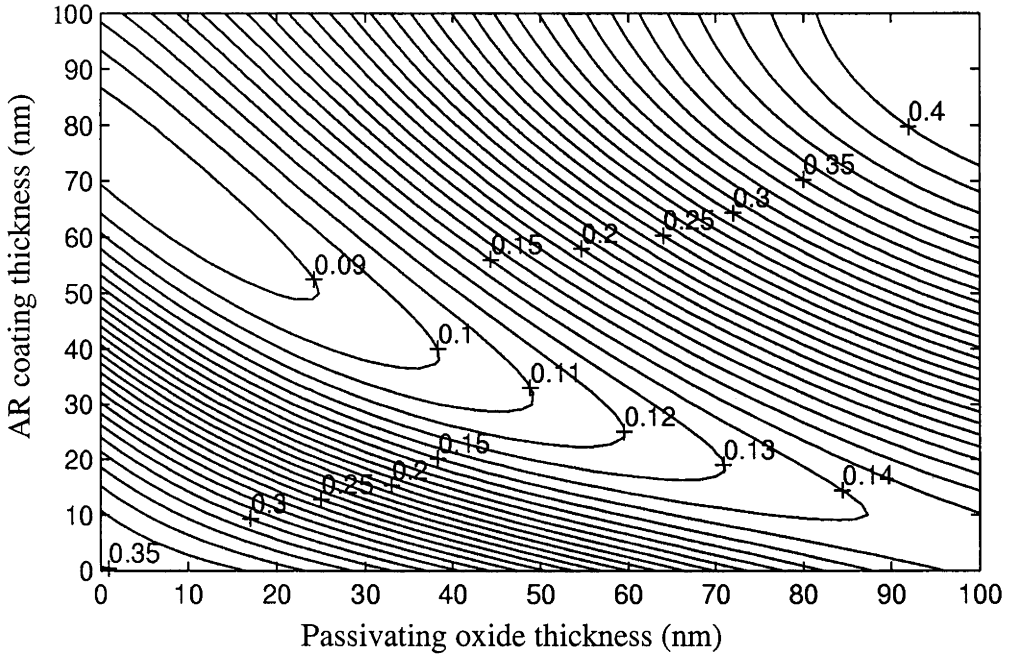

Figure 2.8: *Contour plot of calculated weighted reflection from a silicon surface with passivating oxide under an n=1.95 AR coating.*
Without a passivating oxide, weighted reflectance was 8.5%. The passivating oxide needed to be kept less than 20nm to ensure that transmission did not decrease by more than 0.5%.

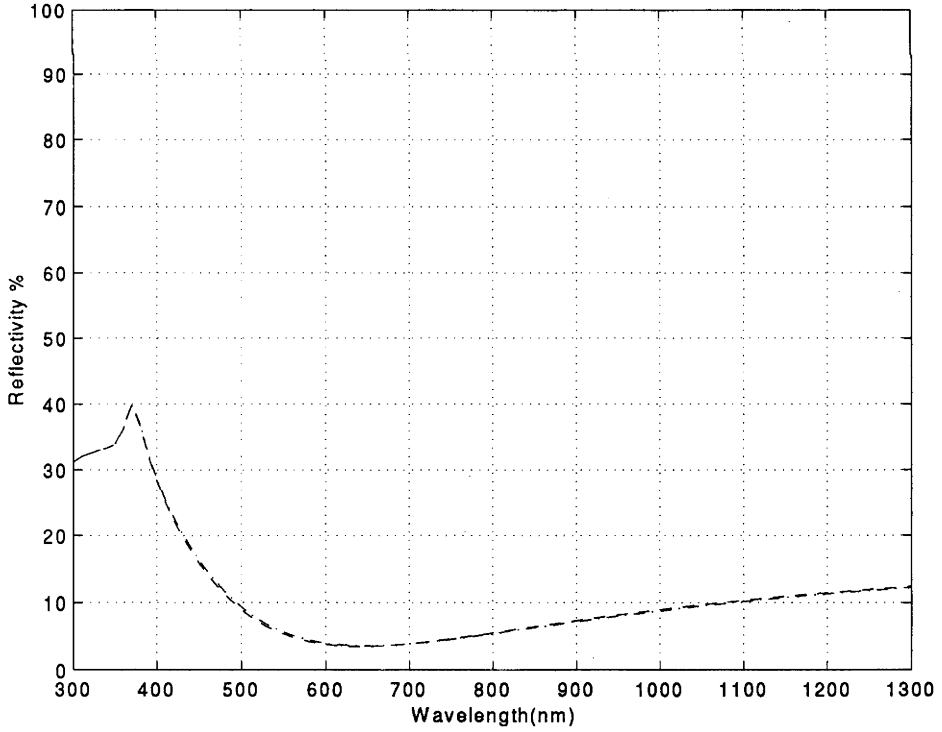

Figure 2.9: *Calculated reflection from near optimal AR (n=2.35) coatings on encapsulated silicon determined from equations (2.4) and (2.6).*
The weighted reflectance was 7.8% with 3.5% due to reflection from the air/glass interface.

2.2.6 *Thermal evaporation of titanium oxides*

Evaporation of titanium oxides to produce titanium dioxide layers was first considered for deposition of TiO_2 following the approach of Pulker *et al* [40]. Titanium dioxide powder was initially used as the evaporation source under vacuum conditions ($<5x10^{-6}$ Torr) onto non–heated substrates (due to the lack of suitable heating arrangements and oxygen sources in the evaporation chamber). Layers evaporated onto glass slides could clearly be seen with the naked eye to be strongly absorbing. This was due to the decomposition of the TiO_2 to lower order oxides with an oxygen to titanium stoichiometric ratio of less than 2.

The introduction of oxygen to the vacuum chamber allowed non–absorbing layers to be deposited. Oxygen was introduced into the chamber via a needle valve, with the oxygen pressure resulting from the balance between the rate of oxygen supply to removal by the vacuum pump. Both titanium monoxide pellets and titanium dioxide powders were used to produce non–absorbing layers on unheated glass slides. Relatively high oxygen pressures greater than 1 mTorr were required to produce non–absorbing layers. Elipsometry measurements of refractive indices were relatively low (between 1.6 and 2 in the visible spectrum), which is too low to provide an effective encapsulated AR coating. This low refractive index was due to poor packing of the deposited titanium dioxide in the amorphous form at the low substrate temperatures. This explanation was supported by softness of the deposited layers which were easily scratched. Uniformity of the layers was poor, with 25% variation in titanium oxide thickness over a 2 inch silicon substrate, indicated by variation in the colour of the antireflection coating.

The deposition of high refractive index layers of titanium dioxide by thermal evaporation required the substrates to be heated. The simplest technique to heat the substrates under vacuum was radiative heating. A suitable radiative heater was developed.

A schematic of the apparatus can be seen in figure 2.10. The substrate heater consisted of a radiative cavity, a tungsten filament halogen lamp and a substrate holder. The radiative cavity consists of a parabolic cross section of polished aluminium 120mm wide by 180mm long sitting on an aluminium base. The parabolic reflector was obtained from a commercially available outdoor floodlight. A 500W tungsten/halogen bulb was aligned along the linear focus of the parabolic cavity. The substrate was clamped to the side of the aluminium base opposite to the cavity and was heated by conduction. The temperature of the cavity base was measured with a K–type thermocouple. Power to the halogen lamp was varied in order to control the temperature of the aluminium base. Temperature could be varied from room temperature to greater than 500°C under vacuum.

Evaporation of titanium monoxide (TiO) onto substrates heated to 380°C produced high refractive index layers with excellent resistance to scratching. Chamber oxygen pressures could be reduced by an order of magnitude to $2x10^{-4}$ Torr before the layers becoming absorbing. The reduced oxygen pressure allowed more uniform layers to be deposited on

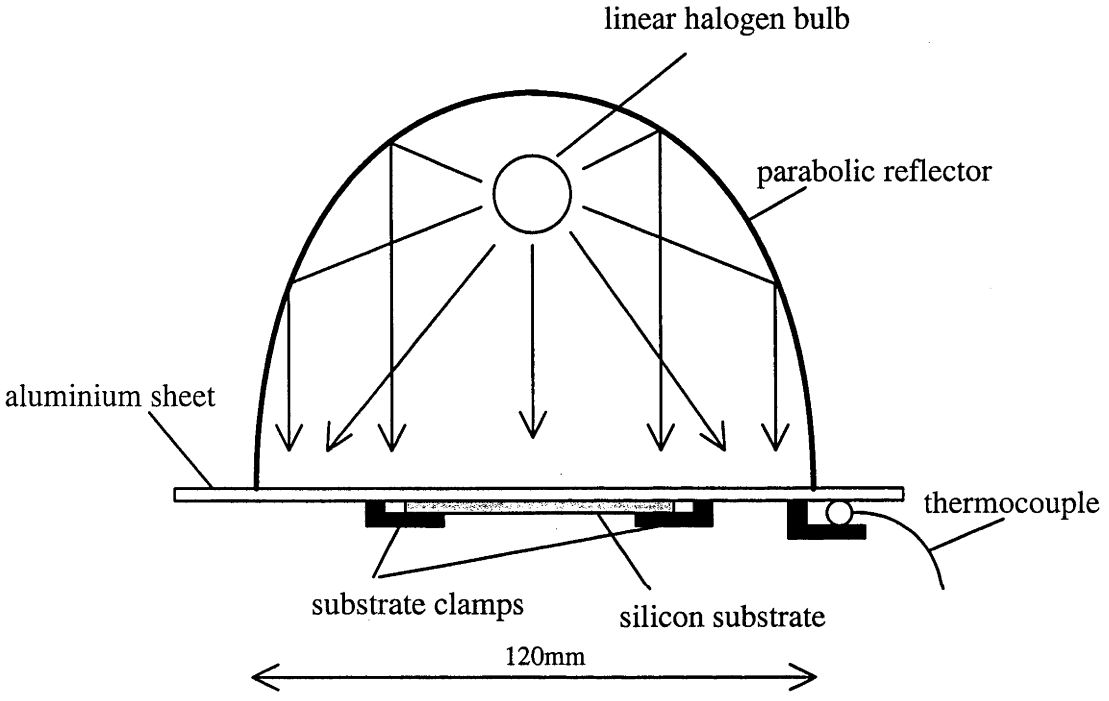

Figure 2.10: *Schematic cross–section of radiative substrate heater. The aluminium sheet was heated by the light from the halogen bulb, with temperature controlled by varying the power to the bulb. The reflector acted as a cavity, containing the light from the bulb. The substrate was clamped to the opposite side of the sheet, where it was exposed to the evaporation source from below. Substrates could be heated to 500°C under vacuum.*

the silicon substrates, with thickness variations caused only by edge effects where the substrate was being supported.

The reflection from a layer deposited at 380°C in oxygen at a pressure of $4x10^{-4}$ Torr was measured with a spectrophotometer. This measurement can be seen in figure 2.11. The reflection loss could not be well fitted with equation (2.6) if the refractive index of the TiO_2 was assumed not to vary with wavelength. TiO_2 has a refractive index which decreases significantly with wavelength between 300nm and 900nm [38,40] and then approaches a constant value for longer wavelengths. Measurements of refractive index for a rutile and anatase film by Hass [38] can be seen in figure 2.12.

The refractive index of the anatase and rutile can be approximated by an exponential decay plus a constant which the refractive index approaches for longer wavelengths (i.e. $n(\lambda)= n_{long\lambda}+C.e^{-(\lambda/\delta)}$ where $n_{long\lambda}$ is the refractive index at long wavelengths and C and δ depend upon the rate of change refractive index with wavelength). These terms were adjusted along with layer thickness to achieve the fit to the reflection curve for the TiO_2 layer measured in figure 2.11. The weighted reflectance between 300nm and 1050nm for the fitted reflectance differs from the real weighted reflectance by 0.2%, primarily due to overprediction of the reflection with the fit at wavelengths less than 400nm. The curves diverge at longer wavelengths (>1050nm) due to light which was not absorbed in the silicon reflecting from the rear of the silicon substrate. The fitted refractive index can be seen in figure 2.12 and falls between the refractive index for anatase and rutile. The thickness of the layer was found to be 60nm.

Layers with the refractive index fitted to the reflection in figure 2.11, could reduce the reflection from an encapsulated (n=1.46) silicon surface to 9.0%. This is greater than the 7.8% calculated for an optimal encapsulated AR coating with constant refractive index 2.4 in section 2.2.4.4. This difference was due to the variation of TiO_2 refractive index with wavelength. Figure 2.13 displays the calculated reflectance curves after encapsulation for a constant refractive index layer with n=2.4 and a layer with the refractive index fit for the evaporated TiO_2 shown in figure 2.11. The layers have similar refractive index and reflection losses at the wavelength where reflection is a minimum. However, the decrease in refractive index at longer wavelengths and the higher refractive index at shorter wavelengths causes increased reflection losses from TiO_2 in both these regions.

The improvement in current with a TiO_2 AR coating and encapsulation was evaluated for aluminium alloyed cells constructed on 1Ωcm Fz substrates. Results for different oxygen pressures are presented in table 2.1. Good current improvements were observed on cells with a thin thermal passivating oxide (~10nm) after titanium monoxide evaporations and encapsulation provided the layers were non–absorbing. Current improvements were close to the 41% improvement predicted from the calculations for encapsulated TiO_2 reflection losses in the previous paragraph. The current increases are greater than predicted, however,

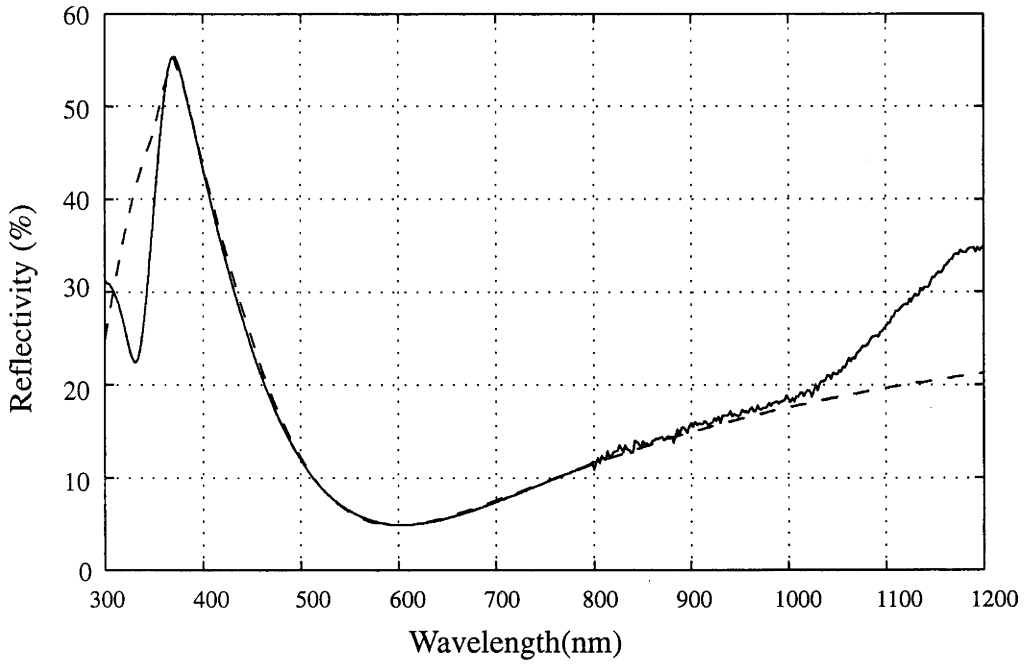

Figure 2.11: *Measured reflection and calculated fit for a thermally evaporated TiO_2 layer.*
——— *Reflection measurement with spectrophotometer and integrating sphere.*
– – – – *Calculated fit using equation (2.6)*
TiO was the source material for the evaporation. The substrate temperature was 380°C and the oxygen pressure $4x10^{-4}$ Torr.

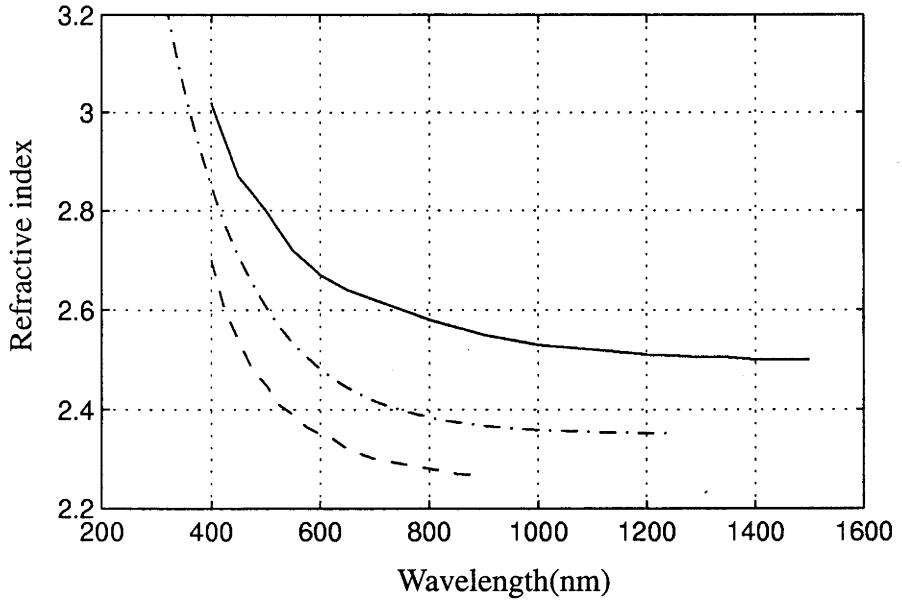

Figure 2.12: *Refractive index for rutile and anatase [38], and the refractive index for the reflectance fit in figure 2.11.*
——— *Rutile*
– – – *Anatase*
—·— *Refractive index for reflection fit in figure 2.11.*

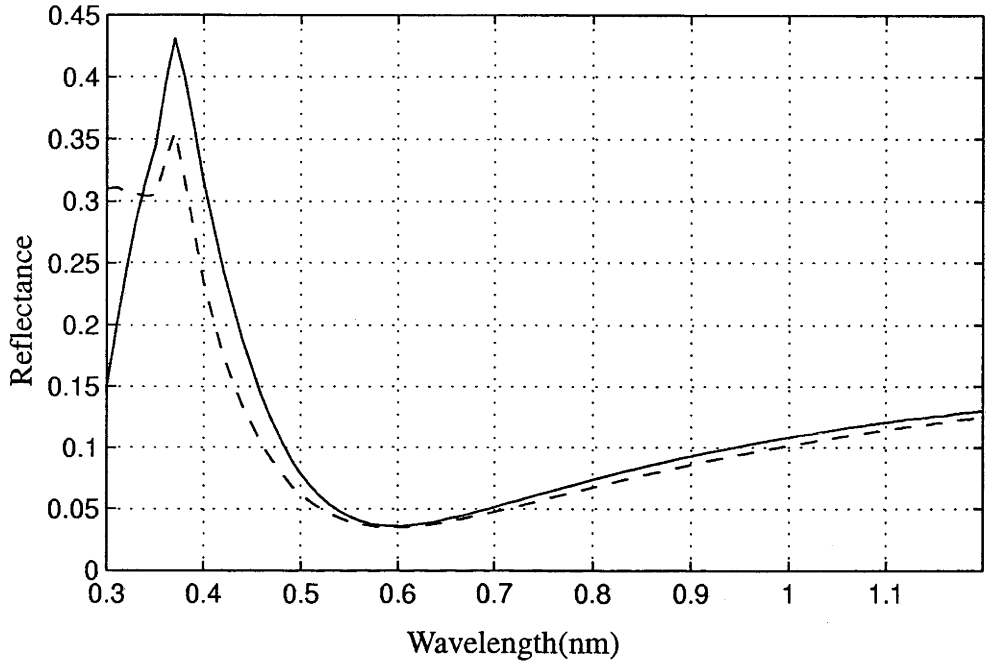

Figure 2.13: *Calculated reflection losses for encapsulated single layer AR coatings on silicon.*
– – – constant refractive index, n=2.4
——— fitted refractive index for TiO_2 (figure 2.12)
The reflection losses were determined using equations (2.4) and (2.6).

due to the narrower response range of the aluminium alloyed cells (IQE<<1@1100nm [6]) and the reduced loss of light reflected from metal fingers after encapsulation [44]. Oxygen pressures below $1x10^{-4}$ created absorbing layers.

Cell	Temperature (°C)	O_2 Pressure (Torr)	Current Increase
S21	380	$4x10^{-4}$	44%
S17b	380	$2x10^{-4}$	42%
S17e	380	$1x10^{-4}$	8% (absorbing)

Table 2.1: *Current improvements for solar cells after titanium monoxide evaporation and encapsulation*

There appeared to be no detrimental effects on single crystal cell performance despite the elevated cell temperature during evaporation. Fill factors were observed to remain constant (within <1%) while voltages increased by up to 10mV, as expected due to the current increase.

Previous work has shown that increasing the pressure of oxygen while substrate temperature and evaporation rate remains constant causes decreases in refractive index [38]. This proposition was supported by measurements of cell currents before and after encapsulation and elipsometry measurements. Elipsometry measurements of refractive index indicated refractive indices between 2.4 and 2.5 at 630nm for $2x10^{-4}$ Torr while refractive indices were between 2.3 and 2.4 at 630nm for $4x10^{-4}$ Torr. As the oxygen pressure decreased during deposition, the difference between the current before and after encapsulation increased. This also indicated that the refractive index of the layer was increasing with decreases in oxygen pressure. Since the layer produced at $4x10^{-4}$ Torr oxygen pressure was near optimal, this pressure and temperature was retained for subsequent depositions.

The thermal evaporation of TiO was used for the deposition of the TiO_2 in single layer AR coatings for encapsulation and the bottom layer of double layer AR coatings on the cells in chapters 5 and 6.

2.2.7 *Titanium dioxide from organo–metallic compounds*

A technique better suited to large area application of titanium dioxide antireflection coatings than reactive thermal evaporation is decomposition of titanium–containing compounds on heated substrates. The economic advantage of the decomposition process is due to the elimination of time–consuming and costly vacuum deposition processes, since the layers are deposited at atmospheric pressure. In early studies, coatings were formed by passing humid air over heated titanium tetrachloride or mixing humid air with titanium tetrachloride vapour [38]. Titanium dioxide was deposited on heated substrates held in the resulting white cloud. The refractive index of the layer depends upon the glass substrate

temperature and varies from 2.25–2.35 at 650nm for substrate temperatures varying from 200–400°C [38].

Other organo–metallic compounds have been used more recently for decomposition into TiO_2. Investigations of liquid tetraisopropyl orthotitanate (TPT) have demonstrated its potential for producing high quality TiO_2 layers [41,42,43]. TPT reacts with water to form TiO_2 and an organic alcohol (propanol). If the reaction occurs in the vicinity of the substrate then a fraction of the TiO_2 adheres forming the antireflective coating.

2.2.7.1 *TPT decomposition and deposition set–up*

Several techniques for the production of uniform layers of titanium dioxide on silicon substrates were investigated. The aim was to produce a uniform layer with high refractive index (>2.2) over a silicon wafer or six inch diameter or greater.

Initial attempts to deposit titanium dioxide relied on a spray deposition process using an artist's air brush. Carrier gas (nitrogen) passed a venturi drawing liquid TPT into the carrier gas from a small reservoir. The carrier gas mixture containing droplets of TPT then passed through a fine nozzle and was sprayed onto the silicon substrate. When the substrate was not heated, a soft white powdery layer formed on the surface of the substrate. This layer was unsuitable for antireflective coatings. If the substrate was heated above 100°C, then the deposited layer showed the characteristic interference fringes of antireflective coatings as the thickness of the layer increased. The elevated substrate temperature assisted in the evaporation of the unwanted propanal reaction by–product produced during the water/TPT reaction, helping to ensure alcohol–free layers.

Trial–and–error variation of carrier gas flow rates allowed good large scale uniformity if the spray nozzle was held around 30cm from the heated substrate. The water vapour naturally present in the air was sufficient for layers to be deposited quickly. Quarter wavelength layers suitable for AR coatings could be deposited in as little as a few seconds. The layers were reasonably resistant to scratching, but were softer than layers formed by thermal evaporation onto heated substrates. However, the layers showed poor small scale uniformity with small dots of thicker TiO_2 (<500μm) forming on the surface where droplets of TPT in the spray deposited on the silicon surface. The area not covered with dots was very uniform in colour indicating good thickness uniformity. Different spray nozzles and carrier flow rates causes different numbers and sizes of the dots to form, but the dots could not be eliminated entirely. Other problems encountered included partial reaction of the TPT in the nozzle of the air brush which caused clogging. The source of the water for this reaction was unclear but may be due to air entering via the venturi or insufficiently dry carrier gas.

To eliminate the formation of dots due to the presence of TPT droplets in the carrier gas, configurations were designed which allowed introduction of the TPT as a vapour using a bubbler similar to that described in previously published investigations [41,42,43]. Carrier

gas (nitrogen) was bubbled through a TPT solution heated in a water bath. The mixture of TPT and carrier gas was then directed onto the substrate surface. The quantity of water available for the reaction was controlled by introducing a water bubbler in parallel with the TPT bubbler and allowing these streams to mix above the substrate. However, the humidity of the air was generally sufficient for good reaction rates and the water bubbler was not required.

A major problem with the configuration described above, was that TPT condensed in the tubes after the heated bubbler. This resulted in liquid flowing along the surface of the tubes and then dripped out the delivery nozzle. Large droplets which dripped onto the heated hotplate or substrate caused several problems. Some of the TPT burnt, leaving brown stains on the substrate while the remainder reacted in the proximity of the droplet and deposited thick layers of TiO_2 locally on the substrate. This problem was subsequently avoided in our laboratory using the approach reported by Hardee and Bard [43] of heating the TPT delivery lines.

To date, this delivery configuration for the TPT has not produced uniform layers over large areas (>10cm^2). Different substrate to nozzle distances and flow rates have demonstrated different degrees of uniformity. Large substrate to nozzle separations were expected to produce better uniformity, but little if any TiO_2 was deposited for large substrate to nozzle distances except for the use of large carrier gas flow rates where spitting of condensed TPT onto the substrate caused the deposition problems outlined above. Lower flow rates and small substrate to nozzle separations (<10cm) led to poor large scale uniformity, with layers varying smoothly with distance from the position of maximum thickness if the nozzle was held still relative to the substrate.

Since the thermally evaporated TiO_2 were of high quality and were satisfactory for small volumes of laboratory scale cells, work on TPT decomposition was discontinued. A commercial atmospheric pressure chemical vapour deposition chamber is being purchased for concentrator cell production. Further investigations of TiO_2 produced by chemical decomposition will be appropriate when this equipment becomes available.

2.3 Texturing

In the preceding discussions, it was assumed that the surface of the silicon was planar. Reflection losses can also be minimised by directing light reflected from the cell towards another cell surface, providing further opportunities for light to be transmitted into the silicon. Changing the topography of the silicon surface to reduce reflection losses is referred to as texturing.

The basic requirements of a good texturing process are that it reduces reflection from the top surface and aids in the retention of long wavelength, weakly absorbed light within the silicon ('light trapping'). Reflection reduction is more important than light trapping for

conventional thick single crystal and multicrystalline wafers. However, light trapping becomes more important for thin (<100μm) substrates produced by processes such as epitaxy or recrystallisation of deposited silicon [45,46]. Devices produced on such thin polycrystalline substrates may become commercially important over the next ten years.

Another benefit of texturing is the deviation of the light from its normal path through the cell. As a result, light is absorbed closer to the front surface of the solar cell. Cells with a front emitter will have an increased short circuit current due to the reduced distance the minority carriers have to diffuse to reach the junction.

2.3.1 *Single crystal silicon texturing*

The use of texturing on single crystalline silicon wafers has led to extremely low reflection losses. The most successful technique, used on record efficiency single crystal silicon solar cells [32], uses selective etchants which etch different crystal orientations at different rates [47].

Early texturing techniques led to the development of the black solar cell, so called for its low reflection losses [47]. Etching (100) oriented silicon wafers in a mixture of KOH, water and isopropanol leads to the surface being covered in a large number of pyramid structures. These result from the selective nature of KOH etching, where etching occurs more rapidly in the (100) direction than the (111) direction. Carbon from the organic isopropanol protects random locations on the wafer surface, preventing etching from occurring. Etching proceeds rapidly on (100) oriented surfaces and stops as (111) surfaces are exposed around the carbon–protected locations on the surface. As a result, intersecting (111) surfaces are left over the wafer surface, creating random pyramid–like structures. This texturing technique is still used in commercial single crystal cell manufacture.

Random pyramids lead to low reflection losses because the entire wafer surface is inclined at 54.7° to the original wafer surface. Light reflected from a pyramid is reflected downward towards another silicon surface which it must strike before it can escape. The surface can also be covered with AR coatings to further reduce reflection losses. The optimisation of the AR coatings changes with the inclination of the surfaces, with thicker AR coatings being required for light perpendicular to the substrate.

Further refinements of the anisotropic etching techniques developed with the use of masking oxides to control the formation of the (111) crystal surfaces. Inverted pyramids or microgrooves can be formed on the silicon surface by opening square holes or long slots, respectively, in the silicon oxide. Inverted pyramids are used on the record high efficiency thick [32] and thin [48] single crystal silicon solar cells.

2.3.2 *Light trapping*

Silicon, an indirect bandgap semiconductor, is a relatively poor absorber of light especially in the near–infrared. Photon absorption at low photon energies requires the absorption of

a phonon to satisfy momentum requirements, which reduces the probability of absorption events [30]. To maximise the chance of light being absorbed in the silicon, the pathlength of the light needs to be made as long as possible. In single junction cells, increasing the thickness of the silicon would require improved diffusion lengths to ensure high carrier collection probabilities. The volume of silicon in the cell should also be minimised to reduce material costs. Other approaches are therefore necessary to keep the light in the silicon until it is absorbed.

Total internal reflection can be used to trap light in the silicon. To escape from a material of high refractive index to one with low refractive index, light must strike the surface at an angle less than the critical angle, or the light will be totally internally reflected. The critical angle is given by

$$\sigma_{critical} = \sin^{-1}\left(\frac{n_{low}}{n_{high}}\right) \tag{2.8}$$

In order to change the path of the light across the cell, the wafer surface must be roughened. The light then deviates from its normal path and may strike the surface at greater than the critical angle. Light trapping appears as a natural consequence of the texturing of silicon for reflection control. Only that fraction of the light which strikes the silicon at less than 16° for weakly absorbed light (n=3.55) can escape. The fraction will vary with the topography of the silicon surface caused by the texturing.

Effective light–trapping can also occur on encapsulated substrates. This is despite the fact that the escape angle of light from silicon to encapsulation material is reduced to around 24° for weakly absorbed light. Light that does escape from the silicon to the encapsulant can also be totally internally reflected at the air/glass interface, where the critical angle is 42°. The effectiveness of the light–trapping after encapsulation will depend upon the surface configuration of the texture. If the front surface is polished (i.e. light trapping features are on the rear surface only) then the light trapping properties with and without encapsulation will be equivalent, since the critical angle of 42° at the air/glass interface is equivalent to the critical angle for silicon in air (16°), after refraction at the silicon/encapsulant interface.

2.3.3 *Multicrystalline silicon texturing*

Anisotropic etching techniques used to texture single crystal silicon solar cells are not as suitable for multicrystalline devices. Crystal grains are randomly oriented and there are few of the (100) surfaces required for effective anisotropic texturing. Random texturing produces texturing on the suitably oriented grains, while virtually no texturing occurs on grains oriented close to (111).

Various texturing techniques have been investigated for use on multicrystalline wafers. These include laser scribing [49,50], plasma etching of photolithographically defined patterns [49,51], defect etching [52] and mechanical grooving [53]. Other approaches

suitable for single crystal and multicrystalline substrates which do not require etching the silicon include textured dielectric coatings deposited by chemical vapour deposition [54]. Mechanical grooving has demonstrated excellent light trapping and reflection results, but appears incompatible with thin substrates. Plasma etching and textured dielectrics are currently too expensive. Defect etching may prove to provide good reflection control after encapsulation.

2.3.3.1 *Total internal reflection from encapsulated silicon*

An effective texture should reduce reflection of incident light by directing reflected light towards another silicon surface. An important point is that solar cells are encapsulated behind glass and a pottant material before deployment in the field. Minimisation of reflection losses from encapsulated solar cells is more important than reflection losses for bare solar cells. There is considerable scope for utilising total internal reflection from the air–glass interface to trap reflected light, and hence decrease reflection losses. The escape angle for light passing from glass (refractive index of 1.5) to air is about 42°. In this context it has previously been pointed out that electroplated metal fingers on encapsulated solar cells, by virtue of their rounded cross section, cause only a third of the reflection loss that simple geometrical calculations would suggest [44]. Much of the light reflected from the fingers is totally internally reflected from the air/glass interface.

A relatively small degree of roughening of a silicon surface is sufficient to reduce reflection losses in encapsulated solar cells. For vertically incident light the silicon surface should be inclined at 21° or more to the horizontal in order to achieve total internal reflection of reflected light at the air/glass interface. For the worst case with light incident at a glancing angle to the glass surface the silicon surface should be angled at 42° to the horizontal. Most of the useful light incident on a solar module lies within an angle of 45° from normal to the glass surface, requiring a silicon surface angle of 35°. Figure 2.14 demonstrates these scenarios schematically.

It is possible to roughen the external surface of the glass instead of the silicon to achieve light trapping and reflection control. A drawback of this approach is that the glass tends to accumulate dirt more readily than does a smooth surface. In this work the external glass surface was assumed to be smooth. For convenience of terminology the glass and the silicon wafers are assumed to be in a horizontal inclination.

2.3.4 *Wet chemical isotropic etching*

In order to eliminate the inherent uniformity problems of using selective etches on multicrystalline silicon, isotropic or uniform etchants were investigated. Isotropic etchants produce features with spherical or rounded features, rather than the planar surfaces characteristic of anisotropic etches. Textures based upon rounded features had not previously been reported in the literature and warranted some attention.

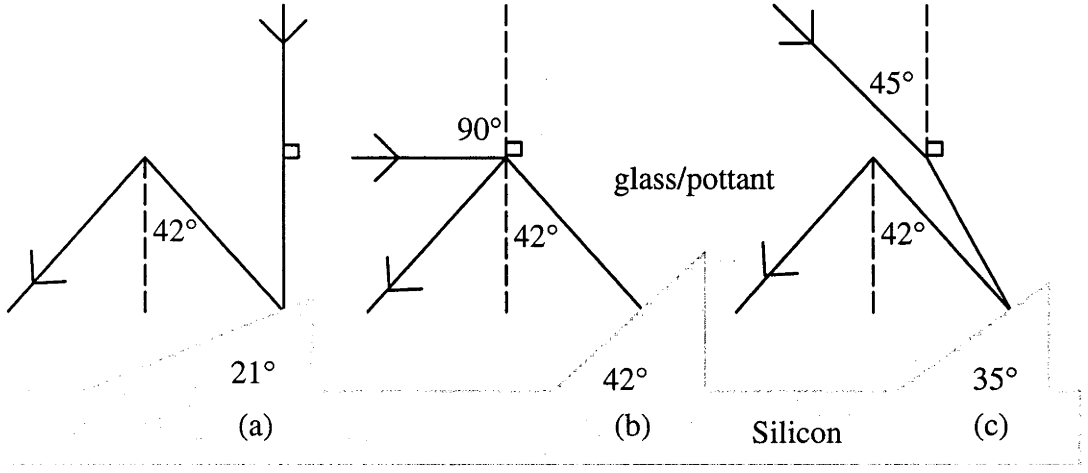

Figure 2.14: *Light deflected from vertical by greater than 42° is totally internally reflected at the air/glass interface.*
(a) Vertically incident light reflected off a surface inclined at greater than 21° will be totally internally reflected.
(b) All light will be totally internally reflected after reflection from a silicon surface inclined at greater than 42°.
(c) All light within 45° of vertical will be totally internally reflected after striking a surface inclined at 35°.

2.3.4.1 *'Tubs' texturing*

The texture structure developed in this work was a network of hemispherical 'tubs'. The process sequence is illustrated in figure 2.15. 'Tubs' were fabricated by growing a 300nm thermal oxide on the wafer then opening a network of small (4 μm) holes in the oxide layer with centres spaced 10μm apart on a rectangular grid. An isotropic etch (comprising $HF/HNO_3/H_3PO_4$) was then used to convert these holes into hemispherical 'tubs'. Etching continued after the hemispheres coalesced until nearly all unetched areas had disappeared. The resulting silicon surface was mostly inclined at a moderate to large angle relative to the original wafer surface. The only areas where this was not the case were in small unetched regions between 'tubs' (5%) and at the bottoms of the 'tubs'. These features can be seen in Figure 2.16, an electron microscope image of a cleaved piece of 'tubs' textured single crystal silicon.

After 'tubs' etching on polished multicrystalline substrates previously undistinguishable grains were clearly discernible, indicating variation in tub etching with grain orientation.

Geometrical calculations (assuming that the 'tubs' have a hemispherical shape) show that about 16% of the surface at the base of the 'tubs' should be inclined at an angle of less than 21° to the original wafer surface. The weighted reflectance at the silicon/encapsulant interface is 19%. After encapsulation, the reflection losses from vertically incident light on the cell with no AR coatings will be 8%. This is comprised of 3.5% from the air/glass interface, 3% from the base regions of the 'tubs', 1% from unetched regions and approximately 0.5% from light lost after being totally internally reflected at the air/glass interface at least once. This is similar to the likely result calculated for a wafer with microgrooves or inverted pyramids.

2.3.5 *Reflectance Measurements from 'Tubs' Textured Samples*

During the early stages of this study, reflectance measurements were made using a Cary 2300 spectrophotometer with an attached $BaSO_4$ integrating sphere. Later measurements were made using a Cary 5 spectrophotometer with an integrating sphere with polytetrafluorethylene (PTFE) coating. PTFE has excellent diffuse reflectance properties providing greater than 99% reflectivity in the range of interest between 350nm and 1400nm. The detectors were PbS in the wavelength range below 800nm and a photomultiplier in the wavelength range above 800nm.

Measurements were calibrated against a 99% reflective PTFE standard. In future, more accurate measurements will be made by obtaining diffuse and specular reference plates with low reflectivity ($\lesssim 10\%$) to enable accurate calibration of absolute reflectances at very low reflectivities. This would assist in avoiding steps in the measured reflectivity as detectors change.

Samples included 1Ωcm single crystal wafers which were polished or had microgrooves, inverted pyramids or 'tubs' etched into the top surface. All wafers were polished on the

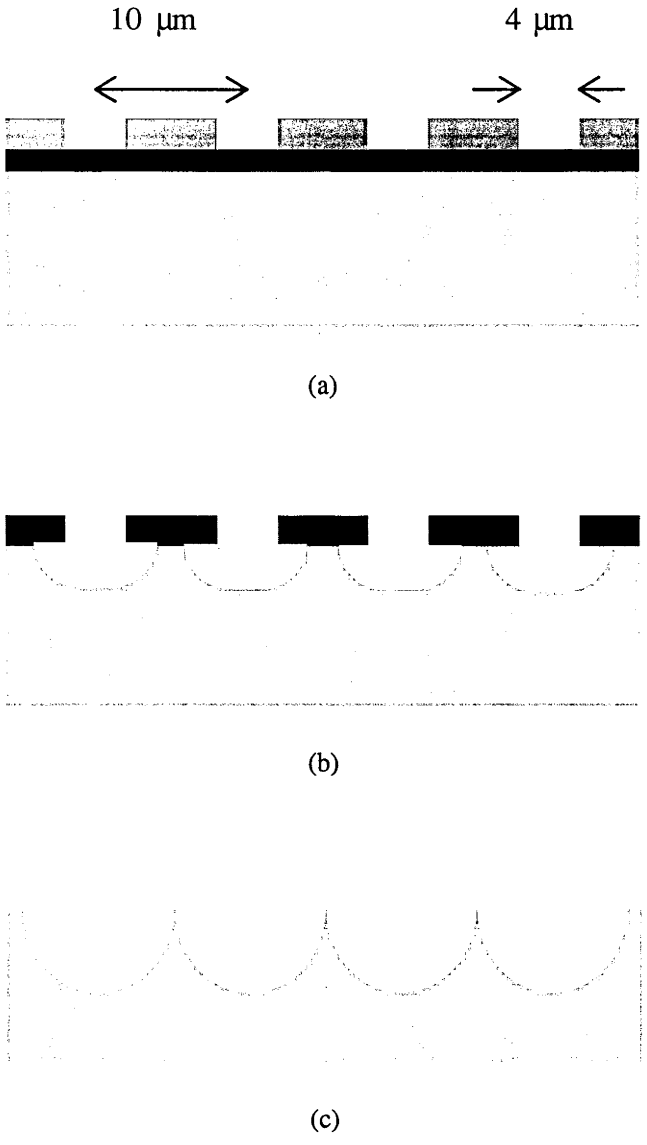

Figure 2.15: *'Tubs' processing sequence.*
(a) 4 μm holes opened through photoresist at 10 μm spacing.
(b) Isotropic etch undercuts oxide.
(c) Holes coalesce leaving silicon surface covered with hemispherical holes.

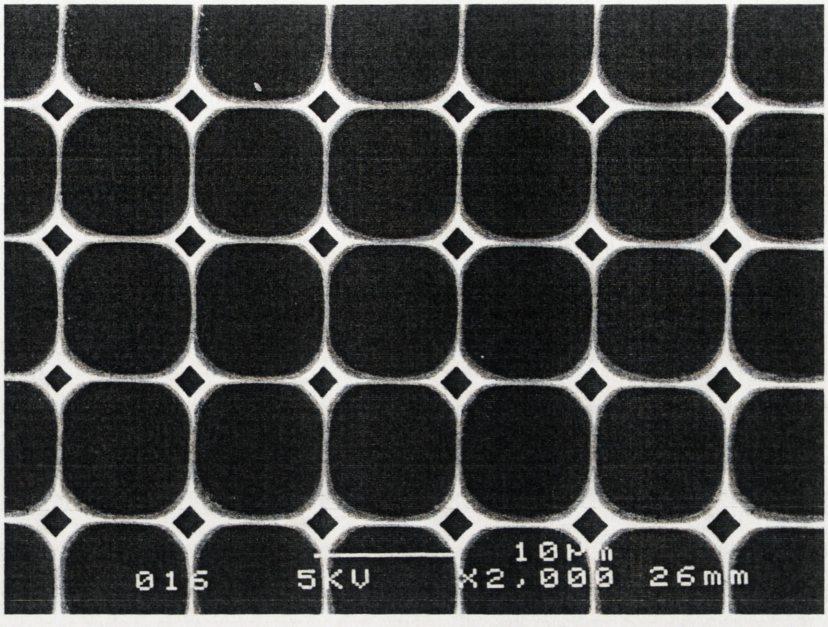

(a)

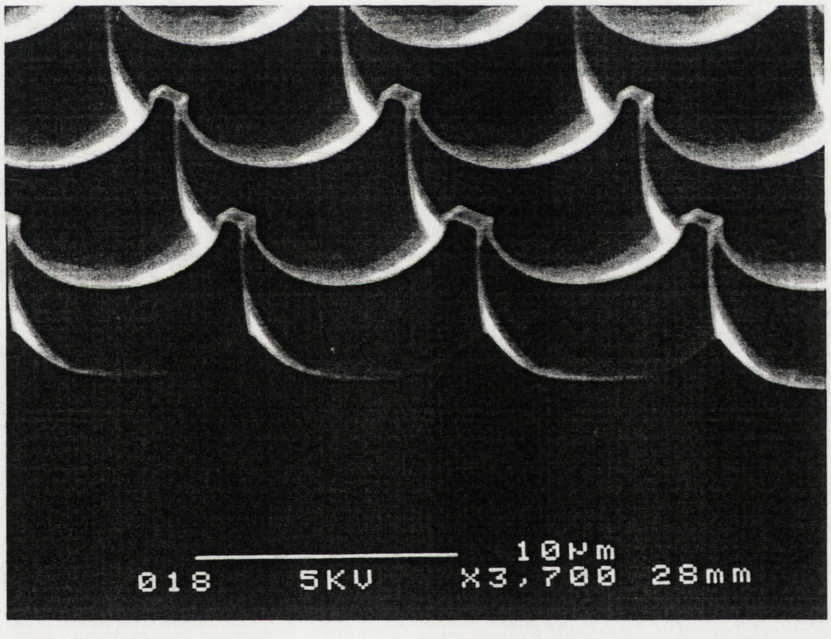

(b)

Figure 2.16: *Images taken with an electron microscope of 'tubs' textured single crystal silicon.*
(a) Image taken at vertical incidence to original wafer surface.
(b) Same sample, viewed towards a cleaved edge at 60° from vertical incidence. Unetched regions appear as diamonds joined by ridges where 'tubs' coalesced. The circle in the base of each 'tub' corresponds in size to the oxide hole through which etching commenced.

rear surface. Single crystal wafers were 250μm thick, while the multicrystalline samples were 310μm thick. A reflector consisting of a 500 nm thick layer of aluminium was evaporated onto the rear surface of most wafers. The reflectivity of aluminium in air has a pronounced dip around 800nm but was greater than 95% beyond 1100nm. Aluminium on silicon has slightly reduced reflectance of approximately 90% at longer wavelengths [6]. This is confirmed for the results from polished wafers (no light trapping). This loss could be reduced by placing a buffer of silicon oxide between the aluminium and silicon [6].

Some of the wafers were then encapsulated behind Vycor glass with an ethyl vinyl acetate (EVA) layer in between. Each of these layers was several mm thick. The vycor glass had a refractive index of about 1.46. Transmission measurements showed it to have negligible absorption in the wavelength range 400nm to 1350nm. EVA transmission measurements indicated strong absorption for wavelengths below 400nm and small absorption peaks at 1200nm and 1375nm, outside the useful range of the solar spectrum for silicon.

2.3.5.1 *Reflection results from 'tubs'*

Texturing controls the reflection of light from unencapsulated silicon wafers by reflecting light towards another silicon surface. Light vertically incident onto the textured regions of microgrooves was reflected at least twice with a small percentage striking the silicon surface three times before loss. 40% of light incident upon inverted pyramids undergoes three reflections before it can escape. 'Tubs' showed considerably poorer reflection control than the anisotropically etched samples before encapsulation. 65% of incident light can strike only one silicon surface. The footprint of light which is reflected from the 'tubs' textured surface twice can be seen in figure 2.17a. The reflection measurements (figure 2.18) demonstrate the superiority of the anisotropic etches on unencapsulated samples with 'tubs' performing poorly.

After encapsulation, reflection losses from the three textured samples were similar in the strongly absorbed wavelengths (figure 2.19). After allowing for the 3.5% of light reflected from the air/glass interface, improvements for inverted pyramids and microgrooves can be attributed to the 25% improvement in transmission across the silicon interface caused by the greater refractive index (than air) of the EVA adjacent to the silicon surface. Geometric calculations supported by the reflection measurements indicated that vertically incident light reflected from the conventional texturing techniques was not totally internally reflected at the air/glass interface due to the angle of reflection from the texturing (less than 39° from vertical) but had already struck two silicon surfaces. Reflection losses from 'tubs' after encapsulation was decreased greatly, becoming comparable with inverted pyramids and microgrooves. Increases in transmission due to the higher refractive index of the encapsulant would only explain a decrease in reflectance to 16%. Much of the reflected light must be deviated through an angle greater than 42° and was then totally internally

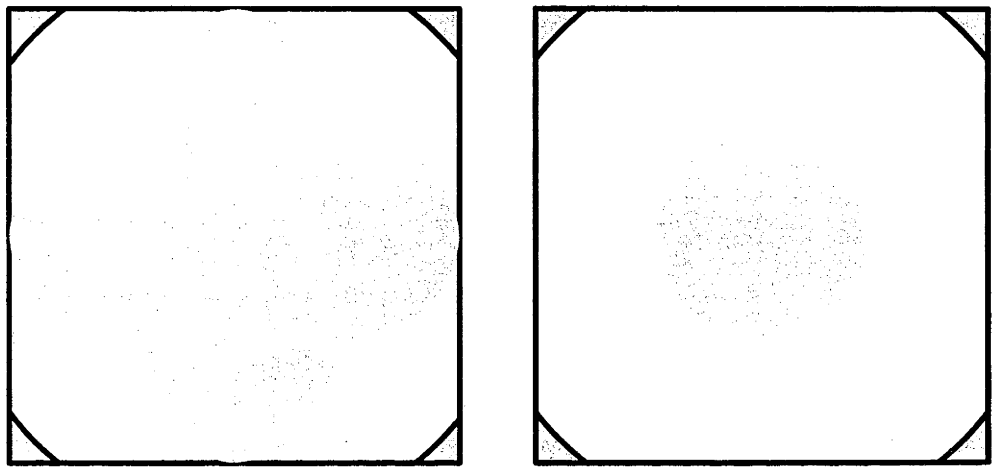

(a) (b)

Figure 2.17: *Footprint of light reflected from 'tubs' textured silicon which can escape without striking another silicon surface determined from geometric calculations.*
(a) Unencapsulated (65%)
(b) Encapsulated (21%)
The regions in the corner are unetched silicon between 'tubs'.

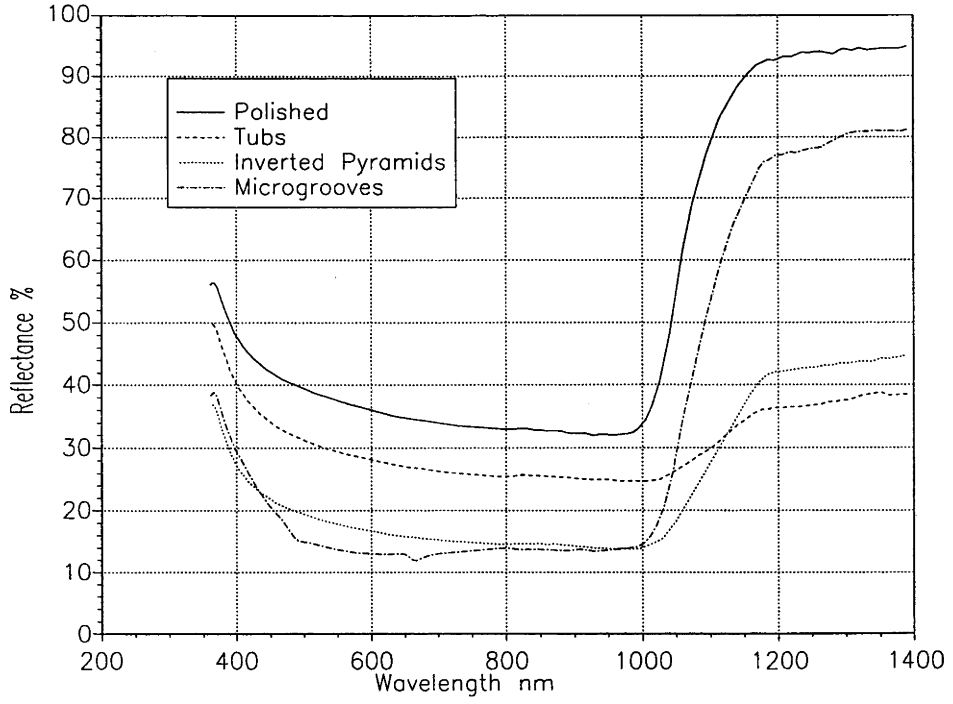

Figure 2.18: *Measured total reflectance as a function of wavelength from unencapsulated polished and textured 1Ωcm single crystal silicon.*

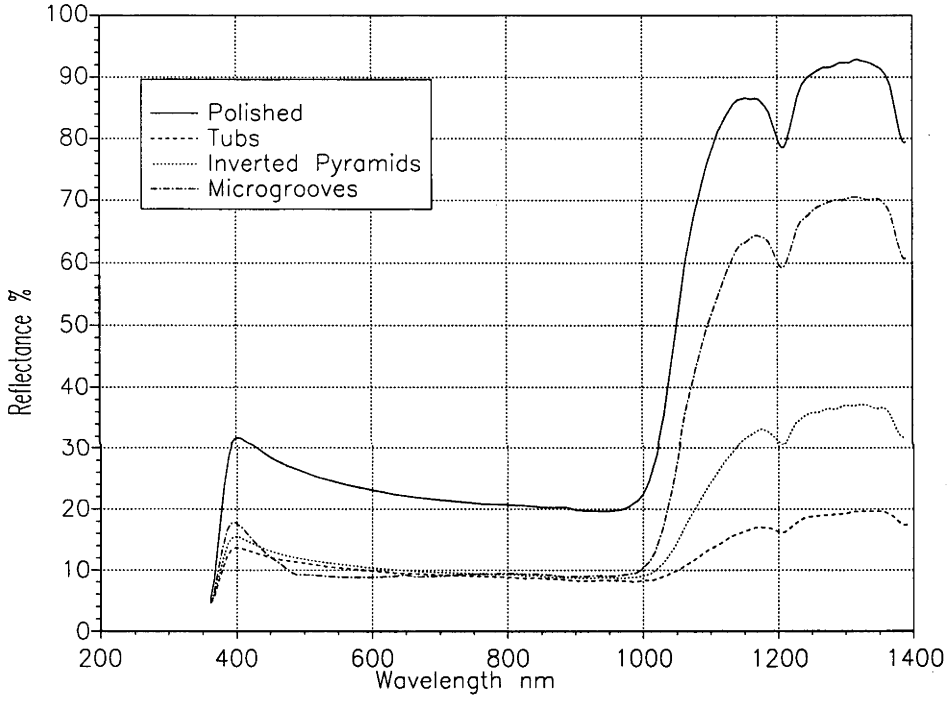

Figure 2.19: *Total reflectance as a function of wavelength from encapsulated polished and textured 1Ωcm single crystal wafers.*

Absorbtion in the EVA caused the dips in reflectance at 1200nm, 1400nm and below 400nm.

reflected at the air/glass interface. As a result, the footprint of light not reflected towards another silicon surface was reduced (figure 2.17(b)). After encapsulation, the average reflectance of 'tubs' in the strongly absorbed wavelengths below 950nm was as good as that achieved using the conventional techniques.

The reflectance measured for each of the textured samples was slightly greater than that predicted by geometric ray tracing. After the masked anisotropic etching, inverted pyramids and grooves were etched slightly with an isotropic etch (HNO_3/NH_4F) to reduce the area of untextured silicon without risk of features coalescing. This procedure rounded the corners and edges of the grooves and pyramids, decreasing the average number of reflections before light escapes. The relatively large size of the unmasked silicon region and the total undercutting of the etch mask between 'tubs' during etching caused the bottom of the 'tubs' to be flatter than hemispherical and the ridges between the tub edges to round. This increased the surface area inclined at less than 21°, and hence would have increased the amount of reflected light which was not totally internally reflected and escaped after one reflection.

2.3.5.2 *Light trapping properties of 'tubs'*

The excellent light trapping properties of 'tubs' can be seen in the measurements of the encapsulated and unencapsulated samples (figures 2.18 and 2.19). 'Tubs' were the best light trapping scheme of the textures tested. This was clear from the low reflection in the infrared region of the spectrum.

Little light was absorbed in the silicon for the wavelengths around 1300nm. Any light which was not reflected was absorbed by parasitic processes, mostly in the aluminium covering the rear of the sample (EVA absorption was also contributing at 1200nm and 1400nm). The better the light trapping, the greater the number of times the light should strike the rear aluminium surface. The polished sample provided poor light trapping, with most of the light striking the rear once before escaping. The reflection in the infrared region was therefore high.

The textured samples all provided some degree of increased light trapping compared to the polished sample. The reflection in the infrared was lower, indicating that light struck the rear surface more often. The light therefore travelled across the substrate a greater number of times resulting in an increased path length compared to the untextured sample. The light traversed the sample most often when 'tubs' texturing was used, with the lowest reflection in the infrared. The microgrooves demonstrated little light trapping while the inverted pyramids provided moderate improvement.

The discussion above only considered how often the light struck the rear surface, which is related to how often the light traversed the substrate. This gives no indication of the distance the light travelled which is the important parameter for absorption of the light in

the silicon. The slope of the reflection in the transition from weak to strong absorption (950nm to 1100nm) gives a better indication of pathlength.

The slope was equal to the change in absorption as a function of wavelength. The absorption is dependent on the pathlength of the light, with the rate of change of absorption with wavelength decreasing with increasing pathlength. The 'tubs' texture, with the smallest slope in this range and the latest onset of the reflection increase, therefore had the longest pathlength in the silicon (with or without encapsulation) and was the better light trapping scheme.

2.3.5.3 *Antireflection Coatings on 'Tubs' Textured Silicon*

Reflection could be further reduced by introducing antireflection coatings above and below the glass/pottant encapsulation layer. Optimisation of a cryolite antireflection coating ($n \simeq 1.3$) on the glass/air interface reduced reflection losses weighted over the usable AM1.5 solar spectrum to 1%. The addition of any uniform layer to the glass surface does not affect the trapping of light in the encapsulant layer in line with the earlier discussion.

An antireflection coating on the silicon surface is a more complex issue. On horizontal encapsulated silicon surfaces, such as unetched regions, the addition of an optimally thick TiO_2 layer (n=2.3) should reduce reflection from the silicon to 5%. However the thickness of TiO_2 evaporated onto the tub walls could differ with the varying slope of the 'tubs', changing the reflective properties. Assuming no improvement from the TiO_2 on the regions of high slope (worst case scenario), a 2% absolute reflection reduction should result (compared to 'tubs' with no AR coating). If reflection on high slopes were similar minimised, absolute reflection should reduce by 4%. This could reduce reflection losses to as little as 2% weighted over the solar spectrum.

2.3.5.4 *Reflection from 'tubs' on multicrystalline silicon*

The excellent reflection and light trapping results for 'tubs' on single crystalline silicon were also evident on multicrystalline substrates (figure 2.20). There was a slight increase in reflection losses from encapsulated 'tubs' on multicrystalline silicon compared to the single crystal silicon sample.

The 'tubs' texturing process highlighted the grain structure of the multicrystalline silicon substrate, which was not clearly visible before texturing. This was primarily a result of the slightly anisotropic nature of the $HNO_3/HF/H_3PO_4$ etch which caused slight variations in the 'tubs' shapes on different grains. Further experience with 'tubs' processing allowed this gap to be reduced by the use of different etch solutions and times. Antireflection coatings also contribute to narrowing this gap. Excellent reflection control can be seen for the completed 'tubs' textured multicrystalline silicon cell in figure 6.6. Importantly, the excellent light trapping performance was also observed for the multicrystalline silicon substrates.

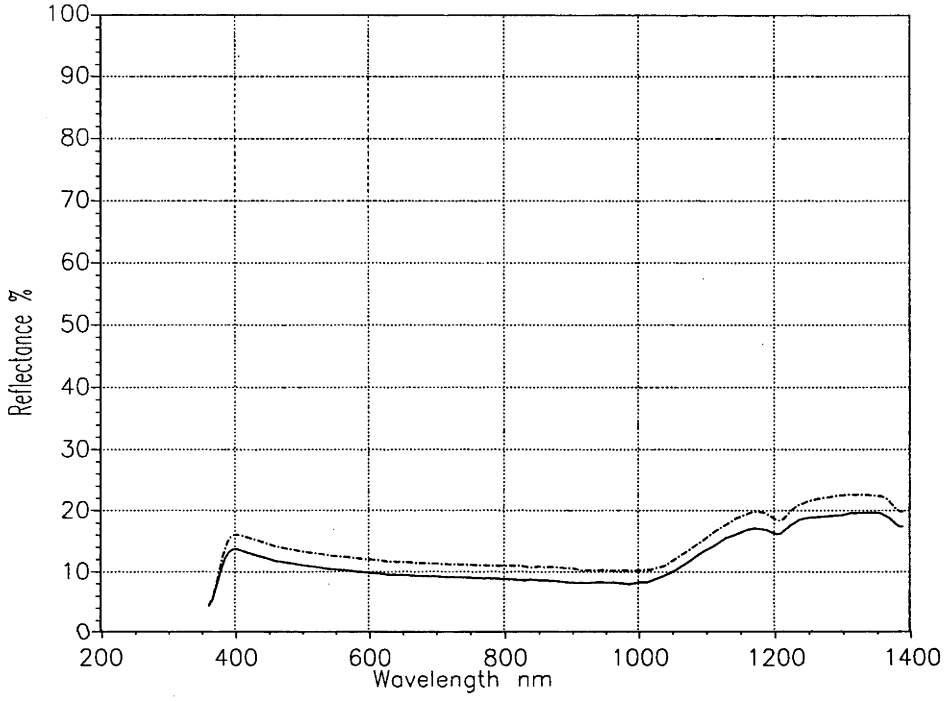

Figure 2.20: *Total reflectance as a function of wavelength from encapsulated 'tubs' textured single crystal and multicrystalline silicon.*

—·— *Multicrystalline silicon*

——— *Single crystal silicon*

2.3.5.5 *Better Packing Arrangements*

Reflection losses from 'tubs' can be further reduced by introducing offset packing arrangements, with etch sites located at the vertices of equilateral triangles rather than squares. This should reduce the silicon area inclined at less than 21° by 25%, increasing the amount of reflected light that is totally internally reflected. This packing arrangement was used for the implementation of 'tubs' on multicrystalline cells described in chapter 6.

2.4 Summary

Silicon is a poor absorber of light and is highly reflective. Suitable optical design is therefore an important component of cell manufacture in order to ensure maximal current generation from the available illumination.

Antireflection coatings significantly reduce reflection losses. Double layer antireflection coatings or antireflection coatings combined with encapsulation can reduce reflection losses below 5% on polished silicon. These require a high refractive index (~2.4) layer close to the silicon.

Titanium dioxide was chosen here for high refractive index antireflection coatings. Good quality layers suitable for laboratory cell production were produced using thermal evaporation from TiO sources, with substrate heating and low oxygen pressures. The layers had high refractive indices and were resistant to scratching. These layers were used for single layer AR coatings under encapsulation with and without texturing reported for cells in chapters 5 and 6, and as the high refractive index layer in DLAR coatings described in chapter 6.

Further reflection losses reductions can be achieved with texturing. A highly effective texture for silicon, known as 'tubs', was developed. The texture used isotropic etches, rather than anisotropic etches, making it well suited for use on multicrystalline silicon. Reflection losses were minimised by producing moderately sloped surfaces, benefiting from total internal reflection from an encapsulant layer. The rounded features produced excellent light trapping, far superior to inverted pyramids or microgrooves. The texture was successfully implemented on high efficiency multicrystalline silicon cells combined with suitable AR coatings, and these results are further described in chapter 6.

CHAPTER 3
MULTILAYER SILICON SOLAR CELLS

3.1 Overview

Interest has been renewed in recent years into the use of polycrystalline silicon to reduce the cost of silicon photovoltaics. Several designs have emerged which step away from more traditional cell designs in order to increase multicrystalline cell efficiency while maintaining low cost manufacturing processes. These approaches include modifying the traditional ingot grown multicrystalline wafer by mechanically texturing the silicon to reduce silicon bulk and increase the volume of the device less than a diffusion length from a junction, such as the POWER solar cell concept [55].

Other approaches being investigated involve growing polycrystalline silicon on a supporting low cost substrate. This enables reduced quantities of silicon to be incorporated into the cell design. Increased flexibility in choosing the quantity of silicon deposited allows for designs which ensure high carrier collection probabilities even on low quality silicon. One design which has generated considerable interest and reports of substantial efficiency advantages over previous designs is the multilayer silicon solar cell, proposed by the Centre for Photovoltaic Devices, University of New South Wales in 1994 [21,22].

3.2 Multilayer Silicon Solar Cell Design

The multilayer structure, has been proposed to achieve moderate efficiencies (> 15%) with very poor quality silicon. Figure 3.1 is a schematic cross section of the proposed device, with stacked p and n layers joined in parallel to layers of like polarity. The thickness of each layer (p or n type) is designed to be less than the carrier diffusion length ensuring a high carrier collection efficiency. The number of layers can be chosen to ensure that most of the solar spectrum is absorbed by the silicon. Thus the short circuit current (J_{sc}) of a multilayer cell can be high even if the diffusion length in the silicon is short (<10 μm). However, the cost of having a large number of junctions is that the cell open circuit voltage (V_{oc}) and fill factor will decline, due to increased bulk and junction recombination.

Although a number of papers have been published comparing the performance of the multilayer solar cell to conventional (single and double junction) designs, a common feature of many of these investigations when modelling device performance is to fix the device thickness several times greater than a diffusion length. This underestimates the potential efficiency of conventional devices, since optimum device thickness for single junction solar cells is less than a diffusion length [56]. As a result, the potential efficiency of the multilayer design on low lifetime silicon then appears much greater than conventional designs. The approach in this work is to optimise the cell thickness, dopant density and number of junctions for a range of silicon qualities and light trapping schemes using a simple analytic model that includes bulk and junction recombination.

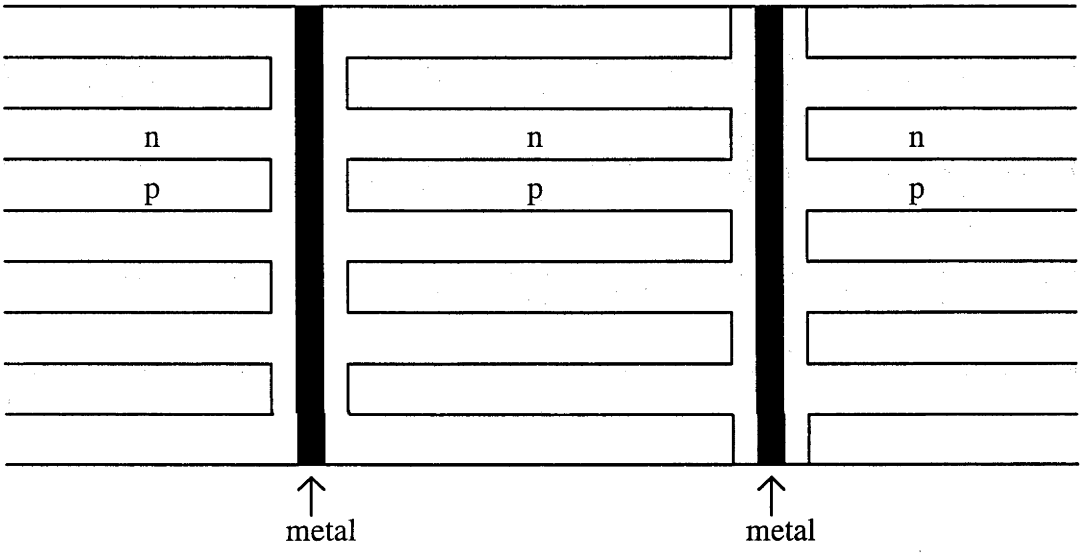

Figure 3.1: *Cross section of an eight junction multilayer solar cell. Like polarity layers are joined in parallel.*

The purpose of this modelling was to assess solar cells based on very low quality (< 50ns lifetime) silicon for which the optimum thickness is likely to be very small (a few microns in some cases). Physical mechanisms like junction recombination and trap assisted tunnelling become very important and light trapping is a critical issue.

3.3 Physical parameters and models

3.3.1 *Recombination mechanisms*

Recombination in conventional (200–400 μm thick) silicon solar cells is generally dominated by bulk and surface mechanisms. Junction region recombination is usually negligible. However, in thin crystalline silicon cells this is may no longer the case for two reasons. The first is that a reduction in cell volume decreases bulk recombination, making depletion region recombination relatively more important. The second is that in many cases, the minority carrier lifetime τ in thin crystalline silicon cells will be low because the silicon is deposited by a low cost process. Cells made on poor quality or irradiated silicon will have a low maximum power point voltage. Since junction recombination is associated with an ideality factor of 2 (in contrast to bulk and surface recombination with an ideality factor of 1) the lower the voltage the greater the proportion of recombination attributable to junction recombination, as can be seen from the approximate equation (3.1)

$$J = -J_{sc} + (J_{B0} + J_{S0})\, e^{(qV/kT)} + J_{J0}\, e^{(qV/2kT)} \tag{3.1}$$

J_{B0}, J_{S0} and J_{J0} are the saturation currents in the base, surface and junction regions respectively and the other symbols have their usual meanings.

In addition to its effect on device voltage (V) junction recombination degrades the cell fill factor because the cell ideality factor rises towards 2. The maximum fill factor in a cell dominated by junction recombination will be about 10% below that of a cell with an ideality factor of 1.

The volume of a depletion region of a solar cell is usually very small compared with that of the base region. However, recombination rates are large since the electron and hole densities are similar in magnitude, in contrast with the base region where there is generally many orders of magnitude difference in the two concentrations. An expression for junction recombination from an abrupt junction at solar cell operating voltages [57,58,59] is

$$J_{J0} = \frac{qn_iW}{\sqrt{\tau_{p0}\tau_{n0}}} \frac{e^{(qV/2kT)}}{q(\psi_d - V)/kT} f(b).\phi \tag{3.2}$$

Here W is the depletion layer width, ψ_d is the built–in voltage, *f(b)* takes account of the location of traps within the energy gap, ϕ is a factor lying between 1/2 and 1 and the other symbols have their usual meaning. A re–analysis of the slightly differing derivations of

junction recombination [57,58] indicates that they bound the actual recombination rate in a junction through differing choice of slope of the potential in the centre of the depletion region. The factor ϕ takes account of this. A value of ϕ=3/4 gives values for J_{J0} between these extremes. For the likely parameter values in solar cells at their maximum power point which have significant junction recombination *f(b)* will take its maximum value of $\pi/2$, which corresponds to the situation where the traps are located near midgap.

W is given by

$$W = \left[(\psi_d - V).2q/\varepsilon\right]^{1/2} \left[1/N_A + 1/N_D\right]^{-1/2} \tag{3.3}$$

An important dependence of junction recombination can be illustrated by assuming that the electron and hole lifetimes are approximately equal. The depletion layer width W is approximately related to the lighter of the acceptor and donor doping densities N_d by the relation

$$W \propto N_d^{-1/2} \tag{3.4}$$

Thus the junction saturation current is approximately given by

$$J_{J0} \propto \tau^{-1} N_d^{-1/2} \tag{3.5}$$

This expression suggests that junction recombination can be decreased by increasing the doping density in the depletion region. This has the effect of reducing the width (volume) of the region of high recombination. An abrupt change in doping type (such as can be achieved with low temperature epitaxy) rather than the more gradual profile obtained, for example, by diffusing phosphorus into a p–type silicon wafer, would also assist in this regard due to the greater electric field (for symmetrically doped junctions) where the recombination rate is greatest. At high doping, improvements in recombination rates are tempered by trap assisted tunnelling, where excessive electric fields enable carriers to tunnel into the junction traps and recombine [60].

Unfortunately it is usually observed experimentally that lifetime has an inverse dependence on doping density above a certain threshold doping level. The threshold doping density is generally in the range 10^{15}–10^{17} cm^{-3}. This experimentally observed dependence can often be fitted by the expression

$$\tau \propto N_d^{-\alpha} \tag{3.6}$$

Combining expressions (3.5) and (3.6) yields

$$J_{J0} \propto N_d^{(\alpha-1/2)} \tag{3.7}$$

Defect recombination yields a range of values of α depending on the method of preparation of the silicon material. If $\alpha > 1/2$ then junction recombination will be suppressed by *reducing* doping density in the vicinity of the junction.

A similar analysis to that above for bulk recombination yields similar expressions to (3.7). For a cell in which the diffusion length is smaller than the width of the quasi neutral regions, such as in an irradiated space cell,

$$J_{B0} \propto N_d^{(\alpha/2 - 1)} \tag{3.8}$$

For a cell in which the diffusion length is larger than the quasi neutral region width, such as in a thin solar cell,

$$J_{B0} \propto N_d^{(\alpha - 1)} \tag{3.9}$$

These recombination processes would require a stronger dependence of lifetime on doping density (values for α of 2 or 1, respectively) than would junction recombination before the conclusion would be reached that doping density should be reduced to minimise bulk recombination.

The inverse dependence of lifetime on doping density above a doping threshold is very well established. It has been observed in FZ and CZ grown silicon [61,62,63,64], cast polycrystalline silicon [65] and ribbon grown silicon [66], as well as in irradiated silicon [67], dopant diffused silicon [68] and gold doped silicon [69,70]. The severity of the effect, the doping threshold, the dependence on doping polarity and synergies with other impurities and defects in the silicon are strongly process dependent.

An inverse dependence of lifetime on doping has many possible origins, including Auger and radiative recombination, trap assisted Auger processes, increased solubility of undesirable impurities in heavily doped silicon, lattice strain caused by the presence of differently sized doping atoms and a range of interactions between doping atoms and defects and impurities. It is perhaps not very surprising that the presence of impurities in doping quantities well above the ppm range should have an effect not only upon carrier mobilities (through scattering from the ionised dopants) but also upon carrier lifetime. The dependence occurs over the whole range of silicon quality, from high lifetime material (τ > 100 μsec) to very low lifetime material (τ < 100 nsec). Poor quality material arising from the presence of large numbers of defects and impurities nevertheless has an inverse dependence of lifetime upon doping density.

Doping densities above the mid-10^{17} cm^{-3} range give rise to bandgap narrowing. It is observed that minority carrier concentrations are greater than expected for the dopant concentrations in this range. Recombination rates therefore cannot be reduced as rapidly as would be expected with increased doping.

In general, higher short circuit currents will be achieved with less heavily doped silicon since both carrier diffusivity and carrier lifetime, and hence diffusion length, will be improved. Choice of optimum doping density in the cell will depend on the exact relationship between lifetime and doping in the silicon used.

3.3.2 *Analytic Model*

A semi–analytic computer program was written to model the multilayer cell. The modelling is one dimensional and the effect of grain boundaries and other two and three dimensional phenomena have been neglected. This is a valid procedure for determining the upper bounds on cell performance as two and three dimensional effects are usually associated with non–ideal cell behaviour. In addition, most two dimensional effects are second order effects, with the obvious exception of grain boundaries. Most modelling of the multilayer structure to date has concentrated on single dimension modelling [71,72,73,74]. Limited two dimensional modelling has been used to investigate the importance of resistive losses in multilayer structures [74,75] but the increased computation complexity limits the potential for determining optimal device structures over large data sets.

The program developed uses the standard analytic expressions for the diode equation, and estimates the current using expressions for carrier generation as a function of cell thickness and carrier collection probability as a function of carrier diffusion length and device dimensions.

Material properties including minority carrier mobilities, band gap narrowing and Auger recombination are taken in accordance with those recently proposed for use with PC–1D [76]. Bandgap narrowing was not included in the junction recombination model since it is not clear if bandgap narrowing persists in depletion regions. Carrier mobilities are assumed to be the same as in conventional silicon doped to the same level. There is evidence that majority carrier mobilities decrease in fine grained polycrystalline silicon [77]. However, this change is minimal at high doping densities, and is strongly associated with the traversal of grain boundaries. This is not an issue in the flow of minority carriers to the pn junction since a cell with adequate efficiency cannot be made in silicon in which minority carriers must traverse grain boundaries to be collected. The set of parameters consistent with $n_i=10^{10}$ at 300K [78] are shown in table 3.1. Surface recombination is not included in the model but is discussed separately in section 3.3.3.

Parameters	Value
Permitted doping density range	10^{16}–10^{19} cm^{-3} (equal for opth polarities)
Carrier lifetimes for Si doped at 10^{18} cm^{-3}	10 and 50 nsec; electron and hole lifetimes assumed equal
Expression for lifetime/doping dependence	$\tau_d=\tau_{@1e18}*(N/10^{18})^{-\alpha}$
α (lifetime/doping dependence parameter)	0, 0.5 or 1
Junctions	One to ten; abrupt
Cell thickness	Variable
Optical properties	–Lambertian light trapping or polished –No external reflection losses at front surface –Rear reflectivity 99% (Internal front reflection for lambertian light trapping 92%)
Illumination	AM1.5G, 100 mW/cm^2, 300K
minority hole mobility [81] $\mu=\mu_{min}+(\mu_{max}-\mu_{min})/ [1+(N/N_{ref})^{\alpha})]$	
μ_{min}	155 cm^2/s
μ_{max}	470 cm^2/s
N_{ref}	1e17 cm^3
α	0.9
n–type bandgap narrowing $\Delta E_g=C_d\ln(N/N_{do})$	
C_d	13.9meV
N_{do}	1.3e17 cm^3
n–type Auger recombination	
C_{nh}	2.3e–31 cm^6/s
minority electron mobility [37] $\mu=\mu_{min}+(\mu_{max}-\mu_{min})/ [1+(N/N_{ref})^{\alpha}]$	
μ_{min}	232 cm^2/s
μ_{max}	1412 cm^2/s
N_{ref}	8e16 cm^3
α	0.9
p–type bandgap narrowing$\Delta E_g=C_a\ln(N/N_{ao})$	
C_a	17.8meV
N_{ao}	2.3e17 cm^3
C_{ph}	9.9e–32 cm^6/s

Table 3.1: Device and material properties for the analytic model.

As doping varies in the model, lifetime is assumed to remain constant, or decrease with increasing doping. Lifetime is assumed to be either 50ns or 10ns at $10^{18}cm^{-3}$ and varies according to the relationship

$$\tau = \tau_{@10^{18}} * \left(\frac{N}{10^{18}}\right)^{-\alpha} \tag{3.10}$$

with α either 0, 0.5 or 1. Constant lifetime is equated by $\alpha = 0$ while $\alpha = 1$ corresponds to lifetime varying inversely with doping. The lifetime doping relationship for 50ns lifetime at $10^{18}cm^{-3}$ doped silicon is shown in figure 3.2 for the three values of α used.

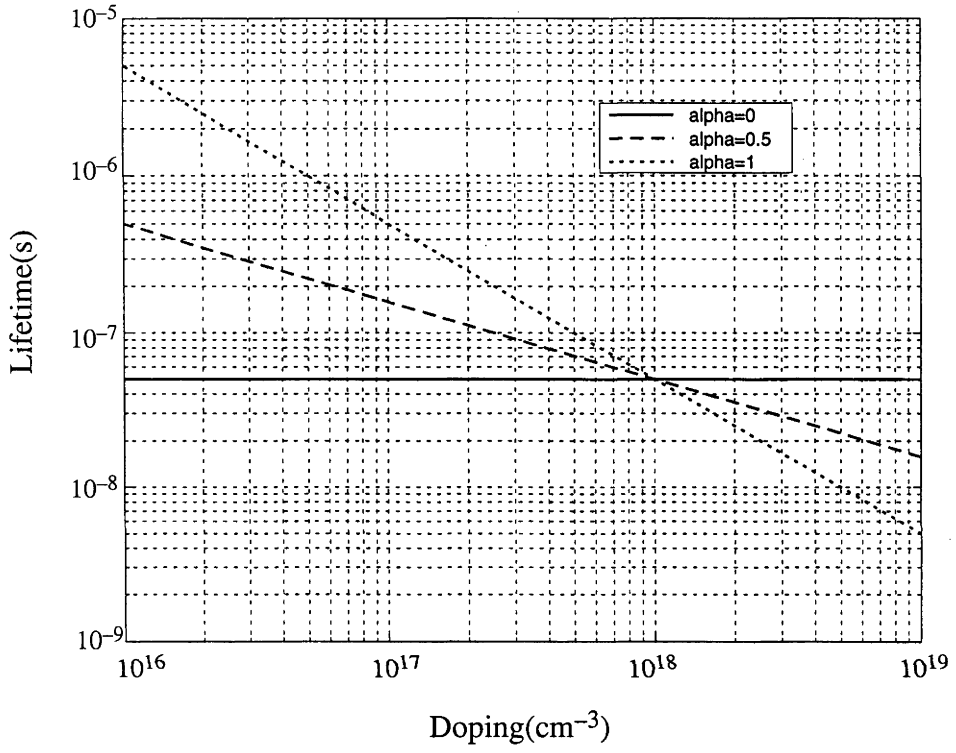

Figure 3.2: *Relationships between lifetime and doping assumed in the analytic model.*

Lifetime at $10^{18}cm^{-3}$ doping is taken as the reference lifetime (50ns or 10ns) then lifetime varies as the inverse of doping (α=1), the inverse of the squareroot of doping (α=0.5) or remains constant with doping (α=0).

The thickness of the n–type and p–type type layers are chosen to keep the collection efficiency of each layer equal. Assuming uniform carrier generation, the collection efficiency of a layer bounded by a single junction and a zero recombination velocity surface is given by

$$Collection\ Probability = \frac{L_x}{W_x} tanh\left(\frac{W_x}{L_x}\right) \tag{3.11}$$

for collection from the back layer of a single or multilayer junction device with no recombination at the rear. W_X and L_X are the thickness and minority carrier diffusion length of the device layer. The corresponding collection efficiency for a layer bounded by two junctions is given by

$$Collection\ Probability = \frac{2L_x}{W_x} tanh\left(\frac{W_x}{2L_x}\right) \tag{3.12}$$

The ratio of n–type and p–type layer thicknesses is determined to be equal to the ratio of their respective diffusion lengths, with the exception of the front and rear layers, which are half the usual thickness. Collection probabilities of carriers photogenerated in the depletion region are assumed to be unity due to the strong electric field present in the junction.

Carrier generation was determined by a third degree polynomial fit of the logarithm of width to the carriers generated for the $100mWcm^{-2}$ AM1.5G spectrum by PC–1D for eight silicon thicknesses between 0.5 and 100 microns. This generation information is obtained for silicon with a back surface reflector or Lambertian rear textured surface.

Recombination is separated into contributions from the wafer bulk, with an ideality factor of one, and the depletion regions with ideality factor 2. Bulk recombination contributions from a layer depend on the layer boundary condition. The bulk recombination contribution from the front or back layer of the single or multilayer cell is for (S=0)

$$J_B = \frac{qD_x n_i^2}{L_x N_x} tanh\left(\frac{W_x}{L_x}\right) \tag{3.13}$$

while the contribution from a typical layer in the multilayer device, bounded by junctions, is

$$J_B = \frac{2qD_x n_i^2}{L_x N_x} tanh\left(\frac{W_x}{2L_x}\right) \tag{3.14}$$

The width of the layers increases slightly as the operating voltage of the cell increases from short circuit conditions due to narrowing of the depletion region, leading to an effective ideality factor marginally greater than one.

Acceptor and donor level doping are chosen to be equal. Unequal doping levels offers no obvious advantage for improving cell efficiency under the assumptions made for this investigation. Unequal capture cross sections can be enhanced by asymmetric junctions leading to saturation of traps in the depletion region and a reduction in space–charge region

recombination [58]. It appears unlikely that the dominant traps in silicon would be strongly asymmetric since p–type and n–type silicon typically have similar lifetimes. There would be benefit in differing the doping in different layers to optimise bulk recombination if the relationship between lifetime and doping differed in n–type and p–type material. These relationships will need to be determined for experimental devices to be optimised.

As doping levels increase in the device, the resulting narrowing of the junction leads to increased electric fields in the depletion region. Sufficiently strong electric fields enhance the capture cross section of traps in the depletion region. A weak model of trap assisted tunnelling, approximating the true potential with a linear potential over the junction width, is incorporated to keep the model equations analytic. The conventional Shockley–Read–Hall (SRH) expression for recombination via traps was shown by Hurkx et al. [60] to become

$$R_{trap} = \frac{pn - n_i^2}{\frac{\tau_p}{1+\Gamma_p}\left[n + n_i \exp\frac{E_{ti}}{kT}\right] + \frac{\tau_n}{1+\Gamma_n}\left[p + n_i \exp\frac{-E_{ti}}{kT}\right]} \qquad (3.15)$$

where E_{ti} is the difference between the trap and intrinsic energy levels. This differs from usual SRH theory by the terms $(1+\Gamma_X)$, where Γ_X, the field enhancement function, effectively reduces the lifetime. For smaller values of the electric field and near mid–gap traps the field enhancement term is approximated by

$$\Gamma_n = \Gamma_p = 2\sqrt{3\pi}\frac{|F|}{F_\Gamma} exp\left[\left(\frac{|F|}{F_\Gamma}\right)^2\right] \qquad where \qquad F_\Gamma = \frac{2\pi\sqrt{24m^*(kT)^3}}{qh} \qquad (3.16)$$

and the effective electron mass m* is 0.25 times the free electron mass. Junction recombination is increased by the factor $(1+\Gamma_X)$ when trap assisted tunnelling contributions are included. This approximation underestimates the tunnelling contribution according to Hurkz model [60] but is sufficient to provide a lower bound to the junction region recombination.

Solutions to the analytic equations described by the model are found as lifetime, doping, number of junctions, lifetime doping dependence and the light trapping scheme are varied. When device thickness is varied, a maximum efficiency is observed with efficiency decreasing for very large and very small device thicknesses. The optimal thickness is determined to within 0.1 microns by iterative calculations of efficiency and the device efficiency is then reported for the optimal thickness.

3.3.3 *Surface Recombination*

Surface recombination can affect devices in two ways: by increasing saturation currents (decreasing output voltage) and by decreasing short circuit currents. Single junction devices will be more severely affected than the multilayer cell by both these contributions [79]. The fractional contribution of surface recombination to the saturation current will be greater in a single junction device due to its smaller device volume and greater

degradation of open circuit voltage will result for a given surface recombination velocity. In addition, only the layers adjacent to the surface in the multiple junction device will have decreased carrier collection efficiency in contrast to all (two) the layers in a single junction device.

Low lifetime material is less affected by the effects of surface recombination than higher quality silicon. The effect of the surface on a solar cell's performance is characterised by the non–dimensional variable (SL/D). Provided this dimensionless variable is much less than one, the surface causes little degradation on solar cell performance as shown in figure 3.3. Single junction devices will require surface recombination velocities less than 10^4cm/s for 10–100ns material or efficiencies will drop dramatically. Bare silicon has a surface recombination velocity of about 10^5cm/s [80] so some surface passivation will be necessary.

Good passivation can be achieved with high temperature passivating oxides even with extremely high doping levels. King and Swanson [81] observe near constant surface recombination velocities of $1.6\text{x}10^3$cm/s on boron doped substrates between 10^{17} and 10^{19}cm^{-3} while phosphorous doped silicon is observed by Cuevas et al. [37] and King et. al. [82] to vary from 10^2 to 10^3cm/s over the same range. While high temperature processing will be unsuitable for silicon deposited on most substrates, it demonstrates that recombination velocities sufficiently low are possible. The effectiveness of the low temperature passivation developed in future will therefore be an important aspect in determining optimal cell design.

Several promising low temperature passivation techniques exist. Plasma enhanced chemical vapour deposition (PECVD) of silicon dioxide and silicon nitride provides effective passivation of silicon surfaces and act as antireflective coatings [83]. The passivating layers are deposited at less than 300°C followed by a 20 minute photoanneal at 350°C. Ionised species can be introduced to an oxide passivated surface with a corona discharge to demonstrate extremely low surface recombination velocities [84]. Techniques must be developed to maintain deposited charge over the useful lifetime of cells.

Recombination at the surface can be reduced by creating a region with increased doping concentration near the surface. The high–low Emitter solar cell [85] demonstrated the potential of this structure to reduce recombination. Another example is the well known back–surface field used to minimise the effects of rear surface recombination. Recombination is reduced by the injection of carriers from the highly doped region near the surface toward the lower doped region, away from the surface. This decreases the dark saturation current and improves photogenerated carrier collection. The high optimal doping of the bulk in low lifetime devices limits the doping difference between high and low regions but scope still exists for reducing surface recombination.

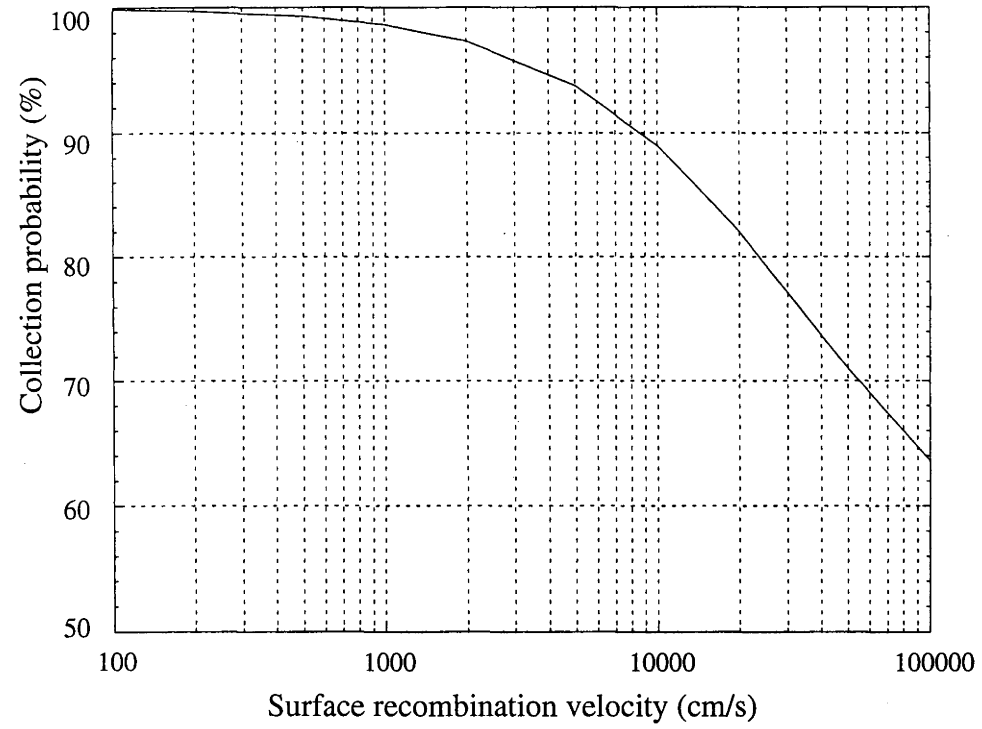

(a)

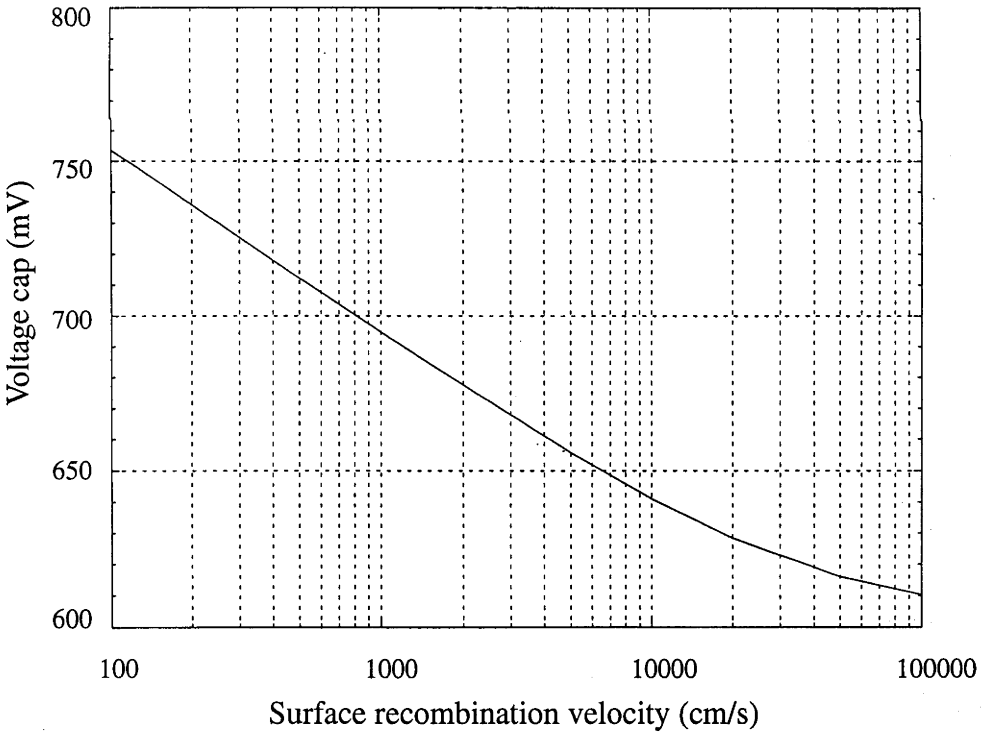

(b)

Figure 3.3: *Effect of surface recombination on 50ns $10^{18}cm^{-3}$ doped silicon. Ratio of layer width to diffusion length 0.3. Diffusivity=$5cm^2/s$.*
a) Average layer collection probability from single junction device assuming uniform generation relative to a device with S=0 surface.
b) Voltage cap imposed by recombination at front and rear surfaces with $J_{SO}=J_{BO}(S)-J_{BO}(S=0)$. Band gap narrowing as per analytic model.

Provided the effective surface recombination velocity can be reduced below several thousand centimetres per second, performance in neither device should reduce by more than a few percent (relative) when compared to the model (where S=0).

3.4 Modelling results

Cell efficiency is the product of three cell characteristics, short circuit current, open circuit voltage and fill factor, each of which are affected by variations in the cell parameters used.

Results obtained from the analytic model for multilayer devices can be compared to results obtained from the solar cell modelling package PC–1D when trap assisted tunnelling (not included in PC–1D) and surface recombination are ignored. A layer of the multilayer device, consisting of half of the p and n regions adjacent to a junction is simulated. The layer is illuminated by light at a reduced intensity to produce an average photogeneration rate in the layer equal to the average photogeneration rate in the full device. Carrier collection efficiencies, open circuit voltages, efficiencies, fill factors and short circuit currents agree between the two models to within 1% giving us considerable confidence in the analytic model.

The very small optimised thickness of the simulated devices causes device efficiencies to become very sensitive to the level of light trapping incorporated in the device. Two extremes of light trapping are simulated to bound the levels of light trapping likely in a real device. Ideal Lambertian light trapping with a perfect rear reflector is commonly assumed to be an upper bound when simulating light trapping. This level of light trapping is approached only by the best light trapping schemes. As a lower bound, polished silicon with a perfect rear reflector is assumed (no light trapping).

3.4.1 *Lifetime independent of doping (α=0)*

If lifetime is assumed not to vary with doping, the modelling indicates optimal device doping for devices with three or more junctions is in the range of $10^{18}cm^{-3}$. Recombination is minimised by the increased doping levels reducing the reverse saturation current and the width of the junction leading to greater open circuit voltages and fill factors (until trap assisted tunnelling dominates). Short circuit current is slightly reduced due to decreased carrier mobility.

The optimum doping varied for the single junction devices, because the device efficiency depended more strongly on the quality of the light trapping. Poor light trapping results in lower optimal doping levels to increase mobility in order to maintain longer diffusion lengths necessary to achieve good collection of carriers in thicker devices. When Lambertian light trapping is included, optimum doping levels for conventional devices are similar to the doping levels of the multilayer devices.

When no light trapping is included the multilayer solar cell demonstrates a clear advantage over conventional devices. The extra silicon thickness required to maintain high carrier

generation leads to decreased carrier collection efficiencies in single junction devices while the multilayer solar cell maintains higher short circuit currents. The highest efficiencies are produced with seven or eight junction devices, with a 25 micron device generating 16.7% efficiency for a lifetime of 50ns and a 17 micron device capable of 13.1% at 10ns (figure 3.4). These efficiencies are 2% (absolute) better than those generated by single junction devices.

The multilayer cell loses this advantage when effective light trapping is incorporated. Thinner devices are capable of maintaining high levels of carrier generation with high carrier collection efficiency leading to significant improvements in short circuit current. Optimum efficiencies are demonstrated with two junctions, with 19.8% for a 5 micron two junction device with 50ns lifetime and 16.5% for a 3.3 micron 10ns lifetime device (figure 3.5). Despite the small total device thickness, the individual layers are thicker than in the optimised multilayer devices. Efficiencies of devices with one to five junctions vary by less than 0.6%.

This conclusion differs markedly from previously published predictions [71–75] primarily because the device thickness is allowed to be freely optimised. Pinning of the device dimension at greater than 10 microns reduces the efficiency of devices with few junctions because only carriers within a diffusion length of the junction are collected leading to low carrier collection efficiencies. Thinner devices allow carriers to be collected throughout the device, more than offsetting the loss in total carrier generation.

As the number of junctions increases in the devices simulated, short circuit current and device thickness increase, while open circuit voltage and fill factor decrease. This information is summarised in figure 3.6 for 50ns lifetime devices with Lambertian light trapping doped to $10^{18}cm^{-3}$. Optimum width increases with the number of junctions, but the thickness of the individual layers comprising the device decreases, leading to increases in carrier collection efficiency. The increased device thickness leads to increased carrier generation, combining with the improved carrier collection to increase short circuit current. The cost of the increased thickness and number of junctions is increases in bulk and junction recombination. To first order, the bulk recombination increases proportionally to the device thickness and junction recombination proportionally to the number of junctions. These cause a decrease in open circuit voltage. Fill factor also reduces due to the lower operating voltages and increased ideality factor resulting from an increased ratio of junction to bulk recombination at the maximum power point. With effective light trapping, the net effect is a decrease in efficiency as the number of junctions increases beyond two.

3.4.2 *Doping dependent lifetime ($\alpha \neq 0$)*

When lifetime varies inversely with doping (α=0.5 or 1), optimal doping levels reduce. Increases in doping no longer decrease junction recombination and diffusion lengths

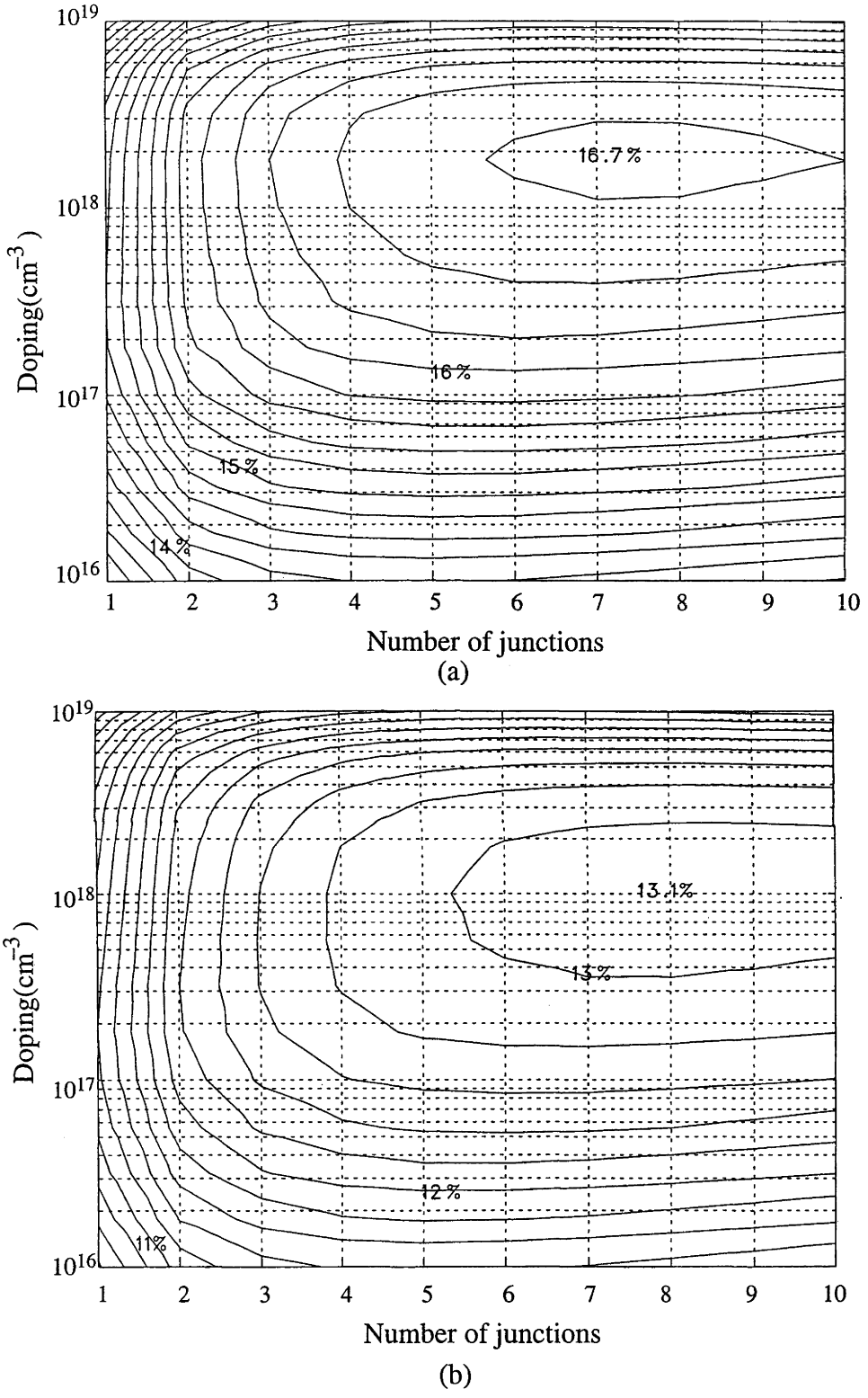

Figure 3.4: *Contour plots of efficiency versus number of junctions and doping for polished silicon layers with lifetime invariant with doping. Contour intervals for all contour plots are 0.2%.*

a) 50ns lifetime. Peak efficiency 16.7% (V_{oc} 600mV, J_{sc} 35.7mA/cm^{-2}) for a 25 micron, seven junction multilayer device doped to 1.8x10^{18}cm^{-3}.

b) 10ns lifetime. Peak efficiency 13.1% (V_{oc} 538mV, J_{sc} 33.8mA/cm^{-2}) for a 17 micron eight junction multilayer device doped to 10^{18}cm^{-3}.

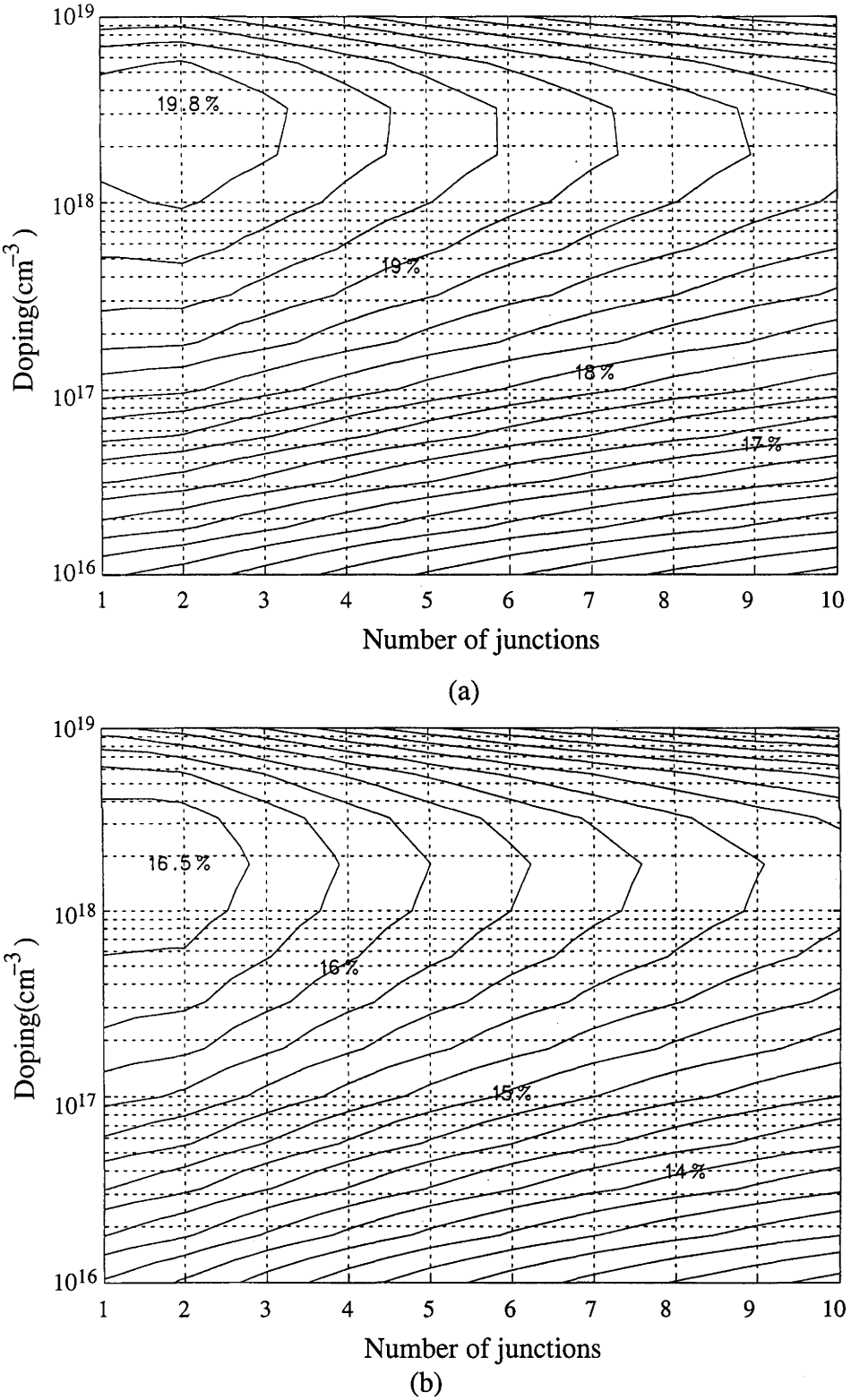

Figure 3.5: *Efficiency of silicon layers with Lambertian light trapping with lifetime invariant with doping.*

a) 50ns lifetime. Peak efficiency 19.8% (V_{oc} 652mv, J_{sc} 37.8mA/cm^{-2}) for 5 micron double junction device doped to 3.2x10^{18}cm^{-3}.

b) 10ns lifetime. Peak efficiency 16.5% (V_{oc} 603mV, J_{sc} 36.2mA/cm^{-2}) for 3.3 micron double junction device doped to 1.8x10^{18}cm^{-3}.

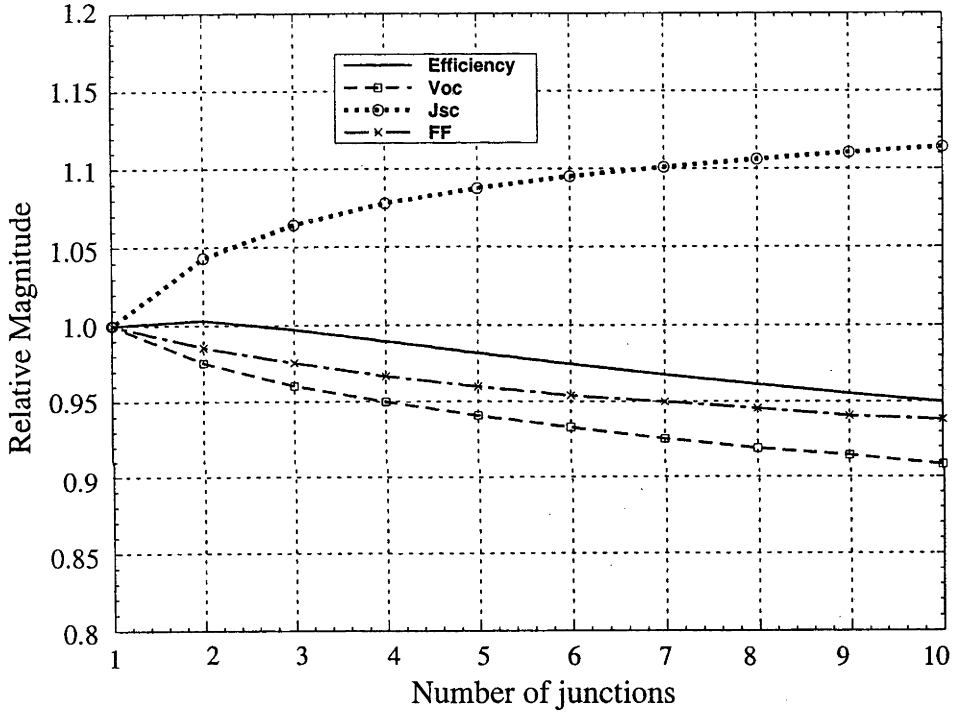

Figure 3.6: *Trends for device characteristics as the number of junctions is varied for $10^{18}cm^{-3}$ doped 50ns silicon layers with Lambertian light trapping, compared to a single junction device.*
Width is optimised for maximum efficiency. Increased short circuit current and decreased fill factor and open circuit voltage are observed for increasing numbers of junctions.

decrease more rapidly due to the reductions in both lifetime and mobility. Bulk recombination decreases more slowly with increases in doping than when lifetime is doping invariant. Optimum doping levels reduce to between $10^{16}cm^{-3}$ and $10^{17}cm^{-3}$.

The optimum number of junctions for polished devices reduces from seven or eight (for $\alpha = 0$) to five (for $\alpha = 0.5$). The lower doping levels leads to diffusion lengths sufficiently long to maintain high carrier collection efficiencies with fewer junctions at the thicknesses required to maintain high carrier generation. Efficiencies of 17.8% are modelled on 33μm, 160ns silicon at $10^{17}cm^{-3}$ doping and 15.3% on 30μm, 75ns $5.6x10^{16}cm^{-3}$ doped silicon (figure 3.7) with five junction multilayer devices. (The higher lifetimes are due to the lifetime/doping dependence and correspond to 50ns and 10ns at $10^{18}cm^{-3}$ doping respectively.) The variation in optimal efficiencies between devices with one junction and optimised multilayer devices is reduced to 1% (absolute). The efficiency improvement is due to increases in short circuit currents due to the greater diffusion lengths (resulting from higher lifetime at lower doping) and improved fill factor as the ratio of junction to bulk recombination at maximum power point decreases with lower doping and fewer junctions.

The optimal number of junctions reduces to one with effective light trapping when α equals one half. The variation in the optimal efficiency between devices with one to ten junctions remains around 1%. Single junction devices demonstrate efficiencies of 20.3% for 4.8μm, 120ns, $1.8*10^{17}cm^{-3}$ doped silicon and 18% for 3.9μm, 42ns, $5.6*10^{16}cm^{-3}$ doped silicon (figure 3.8). The longer diffusion lengths at low doping enable single junction devices to maintain good current collection efficiency at thicknesses sufficient to absorb most photons likely to generate carriers. Increases in the number of junctions and thickness offer little gain in current and decreases in fill factor and open circuit voltage caused by the increased recombination lead to lower efficiencies in the multilayer devices than the conventional devices.

When lifetime is varied as the inverse of doping (α=1) in the model, efficiencies fall for all devices as the doping levels increase (Figure 3.9). This is not surprising considering bulk recombination and junction recombination will increase and diffusion lengths will decrease under these circumstances. This observation is independent of the relative lifetime. This suggests that if lifetime varies this strongly with heavy doping in any doping range in the low quality materials used for these devices, doping should be minimised rather than maximised for more efficient devices.

4. Discussion

To provide perspective, some aspects of related work on the multilayer structure are discussed. In particular, this discussion focuses on the assumptions made by the different theoretical evaluations on the efficiency potential of multilayer and conventional devices.

Green et al. [21] calculated the performance of conventional and multilayer thin cells for 50ns lifetime materials. The stated assumptions were a Lambertian light trapping scheme

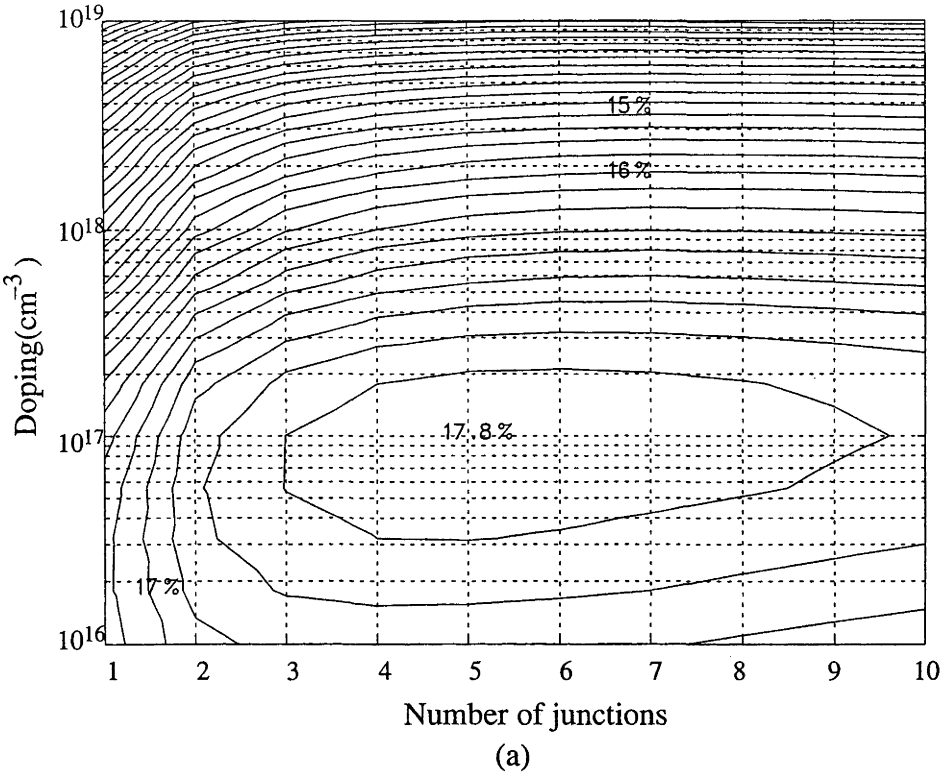

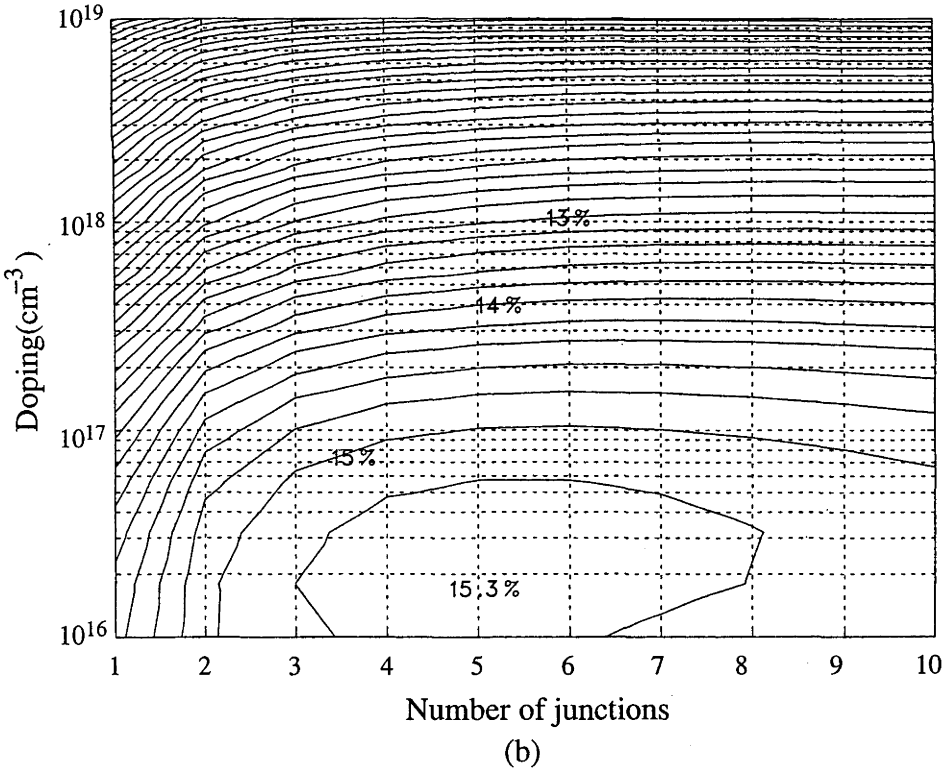

Figure 3.7: *Device efficiency for polished silicon layers when lifetime is assumed to decrease with increasing doping as* $\tau=\tau_{@1e18}\cdot(N/10^{18})^{-0.5}$ *(i.e.* $\alpha=0.5$*)*
a) 50ns @ $10^{18}cm^{-3}$*. Peak efficiency 17.8% (*V_{oc} *593mV,* J_{sc} *37.1mA/cm*$^{-2}$*) for a 33 micron five junction multilayer device doped to* $1x10^{17}cm^{-3}$ *(*$\tau=160ns$*).*
b) 10ns @ $10^{18}cm^{-3}$*. Peak efficiency 15.3%% (*V_{oc} *530mV,* J_{sc} *36.8mA/cm*$^{-2}$*) for a 30 micron five junction multilayer device doped to* $1.8x10^{16}cm^{-3}$ *(*$\tau=75ns$*).*

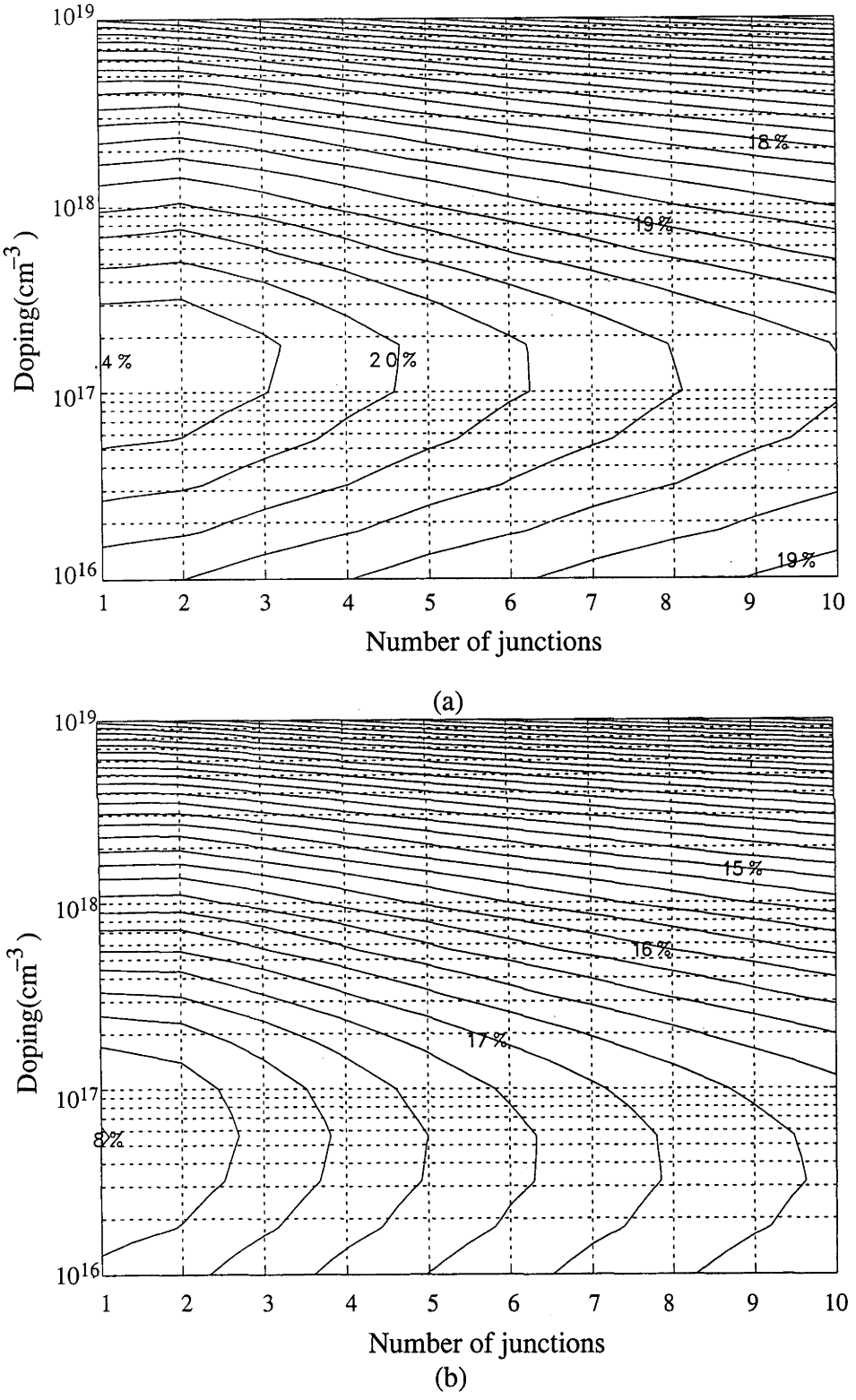

Figure 3.8: *Device efficiency with lifetime varying with doping (α=0.5) and Lambertian light trapping.*
a) 50ns @ $10^{18}cm^{-3}$. Best efficiency 20.4% (V_{oc} 651mv, J_{sc} 37.9mA/cm^{-2}) for 4.8 micron single junction device doped to $1.8x10^{17}cm^{-3}$ (τ=120ns).
b) 10ns @ $10^{18}cm^{-3}$. Best efficiency 18% (V_{oc} 599mV, J_{sc} 37.3mA/cm^{-2}) for 3.9 micron single junction device doped to $5.6x10^{16}cm^{-3}$ (τ=42ns).

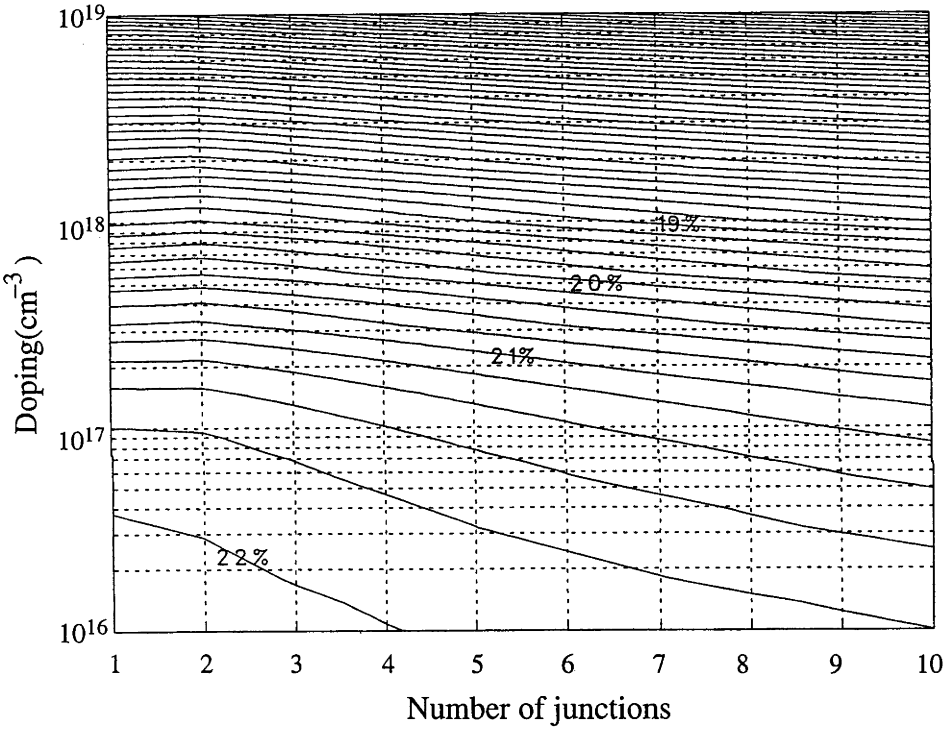

Figure 3.9: *Modelled device efficiencies with lifetime varying inversely with doping (α=1) with Lambertian light trapping. Lifetime at $10^{18}cm^{-3}$ is 50ns. Efficiencies were highest when doping is minimised.*

and a voltage cap (imposed by surface recombination) of 650 mV. It appears that trap assisted tunnelling is not included and reflection losses are zero. The limiting efficiency was calculated to be 15.1% and 20.5% for a 2.5μm single junction and a 25μm multilayer structure respectively. However, it is easy to show that a single junction cell can reach 19% under these assumptions. A 3.5 micron 10^{18} doped single junction device modelled on PC–1D has 19% efficiency with short circuit current 36.6mA, open circuit voltage 633mV (reduced from 660mV by 650mV voltage cap), and 0.82 fill factor at 300K with band gap narrowing [76] included. This agrees well with the analytic models prediction of 19.2%. The 20.5% multilayer efficiency potential is higher than the model's prediction of 19.5% (650mV voltage cap and no trap assisted tunnelling included). It is not clear if bandgap narrowing or junction recombination were included in Green's calculation.

Green and Wenham [71] compared the efficiency of 10 micron multilayer and single junction devices with 10 ns lifetime and 6% reflection losses. The 10 micron device thickness is clearly to the advantage of the multilayer device since the thickness is greater than a diffusion length. Optimising the thickness of the single junction device under the same assumptions improves open circuit voltage and short circuit current increasing efficiency from 10.7% [31] for a 10μm device to 15.4% (V_{oc}=620mV, J_{sc}=32.1mAcm^{-2})for a 2 micron thick device. Values for multilayer devices of 17.3% [71] are higher than those predicted by the analytic model (14.5% for 8 junction, 10μm device (V_{oc}=551mV, J_{sc}=36.8mAcm^{-2}) but reasons for these efficiency differences are impossible to determine without information on current, fill factor and open circuit voltage.

Sproul et al. [72,73] and Wenham et al. [74] analysed the multilayer cell and concluded that it has a large potential advantage over conventional thick cells for low quality silicon. The same claim can be made for a thin conventional cell. The authors have failed to optimise efficiency of conventional cells for either doping density or cell thickness. Failure to allow these variables to be optimised creates a situation in which the multilayer cell is viewed favourably.

An unquantified claim is made by Sproul et al. [72] as to the superiority of a multilayer device over a thin single junction device when metals forming precipitates in the junction region are present. According to Sproul, the multilayer cells is more severely affected by these 'non–ideal' junction effects but failure to optimise the thickness of the single junction device leads to underestimates of the potential of the single junction device. According to the model, the single and double junction device with effective light trapping are more efficient than the multilayer device. The extra junctions in the multilayer device would lead to greater decreases in efficiency when 'non–ideal' impurities cause increased junction recombination and the conventional junction devices would remain more efficient.

When discussing the effect of horizontal grain boundaries on multilayer and conventional cells Sproul et al. [73] fix the conventional and multilayer cell thickness at 10 μm despite

assuming a diffusion length of 4 μm. The small thickness (less than a diffusion length) of an optimised single junction cell will reduce the probability of incorporation of a horizontal grain boundary within its structure. The multilayer cell will have a greater chance of a horizontal grain boundary being located within a depletion region, with probable serious consequences. The claim is made that a multilayer cell will have a "far greater tolerance to grain boundaries, in terms of current collection, than conventional single junction devices". The pictorial figure presented to support this claim belies the truth of this claim provided that the thickness of the single junction device is chosen to be appropriately small.

There may be significant problems with junction shunts down grain boundaries in heavily doped silicon ($N \sim 10^{18} cm^{-3}$) with small grain sizes. In such silicon the junction depletion width during cell operation will be small (<50nm). There will be defects within grain boundaries traversing the junction, offering possible conduction paths through the junction. This may be enhanced by preferential segregation of dopant along the grain boundaries. The length of grain boundary intersecting the junction will be large if the grain size is small. Multilayer cells will be more susceptible to junction shunting than conventional cells due to the increased number of junctions. For example, if the average grain size is 20 μm and there are 10 p–n junctions then there will be about 10,000 cm of grain boundary intersecting junctions per square centimetre. This is thousands of times larger than in conventional multicrystalline silicon solar cells, which shunt more regularly than single crystal silicon cells.

Rau and Goldbach [75] produced calculations purporting to show that the multilayer structure has a large advantage over a single junction cell. However, junction recombination, an important source of recombination, was entirely omitted, leading to the conclusion that a cell with 20 layers or more would be the optimum design since voltage and fill factor did not decrease with increased numbers of junctions. In addition, cell thickness was fixed at 20 μm when the diffusion length was only 10 μm, leading to a low current in a single junction cell. Other significant problems reducing the usefulness of this paper were setting the diffusivity independent of doping density, failing to optimise efficiency for doping density and apparently neglecting bandgap narrowing.

A more recent publication of multilayer solar cell modelling by Edmiston et al. [79] investigates the behaviour of four junction multilayer silicon solar cells on 10 ns lifetime, 10 micron substrates. Two important points emerge from the paper: the need for excellent light trapping to maintain moderate cell efficiencies and the importance of junction recombination as the mechanism limiting device efficiency. Considerable discussion concentrated on variations in the modelled efficiency when different trap assisted tunnelling models or reduced junction recombination rates are considered. The resulting large variation in device efficiency (12–15%) demonstrates a need for further studies of

junction recombination in heavily doped and fine grained polycrystalline silicon to determine the magnitude of depletion region recombination as the limiting mechanism on cell efficiency.

The variation in the value of Φ between 1/2 and 1 in equation 3.2 is due to differences in the approximations of the electric field in the junction. Calculations by Corkish and Green [86] indicate that a value of Φ=1/2 rather than Φ=3/4 in equation 3.2 would therefore be appropriate, since this provides a more accurate representation of the electric field at the point of maximum recombination. The use of 3/4 leads to an overestimate of junction recombination of 33%. Unfortunately, the original software used for modelling is no longer supported, but the key results in figures 3.4 and 3.5 were recalculated. It was found that the mulitple junction cells in figure 3.4 increased in efficiency by 0.5% while the double junction cells in figure 3.5 increased in efficiency by 0.4%. This was primarily due to an increase in fill factor as the fraction of recombination due to junction recombination decreased. The overal trends remained, with the multilayer cells optimal for poor light trapping and double junction cells optimal with excellent light trapping.

An apparent weaknesses in the modelling of junction recombination in the developed model was highlighted by Green [87]. The insertion of an intrinsic layer in the junction can decrease electric field strengths in the junction, enabling optimisation of junction recombination when bulk doping is high by minimising junction tunnelling. Unfortunately, the model could not be modified at the time of publication of Green's work, due to discontinuation of the license of the program used for the modelling. However, it is likely that the efficiency of both conventional and multilayer cells would improve with the addition of intrinsic layers and is unlikely to greatly affect the relative performance of the different structures. This was the case for earlier models developed with no tunnelling.

An important influence on device behaviour not simulated by one dimensional models is resistive losses. Several publications have used two dimensional modelling to determine the possible resistive losses in the multilayer device [75,79]. Resistive losses are predicted in the range of 5% (relative) for $10^{18}cm^{-3}$ doped 10 micron devices with 1000 micron spaced contacts despite reinjection of carriers to deeper layers. These losses could be reduced by incorporated very thin (50nm) heavily doped ($10^{20}cm^{-3}$) layers to the surfaces (or centre of imbedded layers). This would reduce the sheet resistivity below 200$\Omega/\square$, increase the majority carrier mobility across grain boundaries [77] and improve the passivation of the surfaces. These layers could be similarly incorporated into the surface of single junction or emitter–wrap through devices to minimise resistive losses. The potential to incorporate these layers will depend on the ability to control the silicon deposition process. The proposed sheet resistivity is similar to that used in the emitter of high efficiency single junction designs where resistive losses are minimal.

The modelling predicts very small optimal thickness for optimised conventional devices in the range of 3–6 microns. While a 3 μm cell is very thin compared with wafer based cells it is thicker than the individual layers required in a multilayer cell on similarly poor quality material. The fact that only single p and n layers need be deposited is a major advantage. A multilayer cell will require the sequential deposition of several n and p layers, followed by two laser scribes aligned to each other interspersed with two further doped silicon depositions for the purposes of sub–cell interconnection [71]. Monolithic interconnection of subcells to form a module carries the risk of module shorting due to a shunted junction or the limiting of module performance by the worst sub–cell unless further steps are taken such as the incorporation of bypass diodes. Constructing devices approaching the modelled efficiency limits will be very challenging.

According to the model, the multilayer cell could have a significant performance advantage (1–2% absolute) over a single junction cell if the light trapping scheme used was poor. However, in this case the efficiency of multilayer cells would also be severely degraded and would likely fall well below 15% when reflection and other manufactured device losses are included, which would jeopardise their usefulness from an economic point of view [74]. With effective light trapping, little difference is apparent between the thin conventional and multilayer cells modelled.

3.5 Summary

This work investigated the theoretical efficiency limits for conventional and multilayer silicon solar cells on low lifetime silicon. In contrast to previous work, the thickness of the devices were optimised for maximum efficiency for a range of doping levels and numbers of junctions.

Both conventional and multilayer thin silicon solar cells have the potential to utilise poor quality material yet achieve efficiencies above 15%. With good light trapping and device thickness optimised for efficiency, conventional one and two junction devices provide the highest efficiencies in the model. On the other hand, the multilayer cell (with about seven pn junctions) has a 2% and 1% absolute efficiency advantage over single and double junction cells respectively, if the light trapping scheme is poor.

Low quality silicon has not been thoroughly investigated to determine the relationship between lifetime, minority carrier mobility and doping. If lifetime in such a material is found to be inversely related to doping, then the optimal doping level and number of junctions modelled is reduced compared to that expected if lifetime is invariant with doping. In this case the difference between conventional and multilayer devices becomes even narrower with single junction devices optimal when light trapping is included for higher cell efficiencies. The properties of the silicon eventually used in practice will strongly affect the optimal design parameters.

The multilayer solar cell appears to be a good design to maintain high cell efficiencies on poor quality silicon when surface recombination is high or light trapping schemes are poor. Effective light trapping schemes for thin polycrystalline silicon are yet to be proven and if devices must be thicker than a diffusion length, the multilayer device can maintain higher short circuit currents. However, low quality silicon, low temperature passivation and light trapping schemes in thin silicon layers are still under investigation. The superiority of one cell structure over another is still an open question pending more detailed information and understanding of material parameters.

CHAPTER 4
LIFETIME MEASUREMENTS OF MULTICRYSTALLINE SILICON USING QUASI–STEADY STATE PHOTOCONDUCTANCE

4.1 Lifetime measurements

Recombination in silicon is characterised by the carrier lifetime [5]. Recombination rates are proportional to the number of excess carriers and inversely proportional to the carrier lifetime.

Numerous techniques now exist for the measurement of carrier lifetimes in silicon [88]. To prevent contamination of wafers during subsequent processing, contactless measurements techniques are particularly useful. These usually rely on optical illumination for the generation of carriers, with the measurement of excess carriers possible by a variety of techniques.

The most common and widely used approach is photoconductivity decay (PCD). This was first developed as a contacted technique in 1955 [89]. Excess carriers are generated by optical excitation and the decay of the excess conductivity is monitored by current flow through the sample. The conductivity can also be measured without contacts with an RF bridge circuit, relying on the change in permeability of the sample due to the changes in conductivity.

Other contactless techniques also exist for measuring the excess carrier concentration, independent of conductance. These include measurements of free carrier absorption with changes in excess carrier concentration or more sensitive measurements can be made using microwave reflectance. These are used for many scientific investigations of recombination in silicon today [90,91]. Accurate measurement of low lifetime materials requires extremely fast illumination and detection circuits, with associated costs.

4.2 Steady–state photoconductance

An alternative, economical approach to determine the lifetime of a silicon sample was recently developed by Sinton *et al* [92]. Unlike transient PCD lifetime measurements, the sample is illuminated with a near steady state source, which produces a photogenerated excess of carriers. Under steady–state illumination, the generation rate of excess carriers is equal to the rate of recombination of the excess carriers since the excess carrier concentration does not vary with time. Therefore the total recombination in the sample can be equated to the total photogeneration. By measuring the illumination of the sample with an optical detector, the photogeneration rate, and therefore the recombination rate in the sample can be determined. By measuring the conductance with a RF bridge circuit, the excess carrier density can also be determined.

The steady–state approach eliminates the need for high speed electronics reducing the cost of the system.

4.2.1 *Contributions of surface and bulk recombination to effective lifetime*

During steady state photoconductance measurements, photogeneration is balanced by the total recombination in the sample. Recombination includes contributions from bulk recombination and recombination at the surfaces.

Therefore, the effect of surface recombination on the photoconductance in the sample must also be considered. The excess carrier concentration in low level injection can be determined by solving the minority carrier diffusion equations with appropriate boundary conditions which account for surface recombination.

The minority carrier diffusion equation is a balance between generation and recombination and the diffusive flow of carriers. For a p–type substrate, the excess electron carrier concentration, Δn, is given by [5]

$$-D_e\frac{d^2\Delta n}{dx^2} = Gen. - Rec.$$

$$-D_e\frac{d^2\Delta n}{dx^2} = G(x) - \frac{\Delta n}{\tau_e} \qquad (4.1)$$

where D_e is the minority carrier electron diffusivity and τ_e is the electron carrier lifetime.

For the case of uniform generation, (G(x)=constant) such as illumination with infrared light, the general solution for this equation is given by

$$\Delta n(x) = C_1 cosh\left(\frac{x}{l_e}\right) + C_2 sinh\left(\frac{x}{l_e}\right) + G\tau_e \qquad (4.2)$$

where l_e is the minority carrier diffusion length $\sqrt{D_e\tau_e}$.

The values for the constants, C_1 and C_2 depend on the conditions at the surfaces of the sample. The boundary conditions are determined by the balance of carriers recombining at the surface and carriers diffusing to the surface to replace the carriers which have recombined.

$$Sf_e\Delta n(0) = De\frac{d\Delta n(0)}{dx} \qquad \text{at the front surface } x = 0$$

$$Sr_e\Delta n(W) = -De\frac{d\Delta n(W)}{dx} \qquad \text{at the rear surface } x = W \qquad (4.3)$$

where S_{fe} and S_{re} are the surface recombination velocities at the front and rear surface respectively. Combining these boundary conditions combined with equation (4.2) the carrier distribution can be obtained.

$$\Delta n(x) = G.\tau_e\left[1-\frac{\left(\frac{Sr_e.l_e}{D_e}\right)cosh\left(\frac{x}{l_e}\right) + \left(\frac{Sf_e.l_e}{D_e}\right)cosh\left(\frac{x-W}{l_e}\right) + \left(\frac{Sr_e.l_e}{D_e}\right)\left(\frac{Sf_e.l_e}{D_e}\right)\left(sinh\left(\frac{x}{l_e}\right)-\left(\frac{Sf_e.l_e}{D_e}\right)sinh\left(\frac{x-W}{l_e}\right)\right)}{\left(\frac{Sf_e.l_e}{D_e} + \frac{Sr_e.l_e}{D_e}\right)cosh\left(\frac{W}{l_e}\right) + \left(\frac{Sf_e.l_e}{D_e}\frac{Sr_e.l_e}{D_e} + 1\right)sinh\left(\frac{W}{l_e}\right)}\right] \qquad (4.4)$$

The photoconductance, σ_L, can be determined from the integral of the excess carrier concentrations weighted by the carrier mobility.

$$\sigma_L = q\int_0^W \left(\mu_n \Delta n(x) + \mu_p \Delta p(x)\right) dx \tag{4.5}$$

In low level injection, the excess carrier concentration has little effect on mobility. Therefore μ_n and μ_p can be considered constant in the sample and charge conservation dictates that the excess number of electrons and holes are equal, so that

$$\sigma_L = q(\mu_n + \mu_p)\int_0^W \Delta n(x)dx = q(\mu_n + \mu_p)\Delta n_{ave} W \tag{4.6}$$

At higher injection levels, changes in mobility with injection level can allowed for. The total photogeneration, J_{ph} in the sample is equal to the total recombination. Recombination can be expressed in terms of the average excess carrier concentration and an effective minority carrier lifetime τ_{eff} as

$$J_{ph} = GW = \frac{q\Delta n_{ave} W}{\tau_{eff}} \tag{4.7}$$

The effective lifetime which will be extracted from the photoconductance measurement is given by combining equations (4.6) and (4.7) so that

$$\tau_{eff} = \frac{\sigma_L}{GW(\mu_n + \mu_p)} \tag{4.8}$$

The effective lifetime can be related to the bulk lifetime and the surface recombination velocities via equation (4.4) and (4.6) so that

$$\begin{aligned}\tau_{eff} &= \frac{\Delta n_{ave}}{G} \\ &= \frac{1}{G}\int_0^W \Delta n(x)dx \\ &= \tau_e\left[1-\left(\frac{l_e}{W}\right)\frac{\left(\frac{Sf_e.l_e}{D_e}+\frac{Sr_e.l_e}{D_e}\right)\sinh\left(\frac{W}{l_e}\right)+2\left(\frac{Sf_e.l_e}{D_e}\right)\left(\frac{Sr_e.l_e}{D_e}\right)\left(\cosh\left(\frac{W}{l_e}\right)-1\right)}{\left(\frac{Sf_e.l_e}{D_e}+\frac{Sr_e.l_e}{D_e}\right)\cosh\left(\frac{W}{l_e}\right)+\left(\frac{Sf_e.l_e}{D_e}\frac{Sr_e.l_e}{D_e}+1\right)\sinh\left(\frac{W}{l_e}\right)}\right]\end{aligned} \tag{4.9}$$

It is difficult to establish obvious trends from this equation, except under the extremes of the recombination behaviour, such as when bulk recombination is minimal or when $S_x l_x/D_x$ approaches zero.

4.2.2 *Effective lifetime dominated by surface recombination ($w/l<<1, Sl/D>1$).*

An interesting case is the effective lifetime which will be determined when the diffusion length is much greater than the substrate thickness and the surface recombination velocity is relatively large.

$$\tau_{eff} = \frac{W}{Sf + Sr} + \frac{W^2}{3D_e}\left(\frac{Sf^2 + Sr^2 - Sr.Sf}{(Sr + Sf)^2}\right) \tag{4.10}$$

The particular cases of identical surface recombination velocities at both surfaces and the surface recombination velocity zero at one surface was examined by Cuevas and Sinton

[93]. When the surface recombination, S is the same at both surfaces, expression (4.10) reduces to the much simpler expression

$$\tau_{eff} = \frac{W}{2S} + \frac{W^2}{12D_e} \tag{4.11}$$

while when one surface has zero recombination velocity the expression simplifies to

$$\tau_{eff} = \frac{W}{S} + \frac{W^2}{3D_e} \tag{4.12}$$

In equations (4.11) and (4.12), the second term places a lower limit on the bulk lifetime due to surface recombination since carriers in the bulk need to diffuse to the surface to recombine. If one surface is well passivated, carriers near the low recombination surface have to diffuse across the entire substrate thickness to recombine. When the sample has two high recombination velocity surfaces, the lifetime limit is four times lower with the carriers having to diffuse across at most half the substrate thickness. Typical substrate characteristics (W≈300μm, D≈30cm/s) produce lower lifetime limits due to surface recombination of 2.5μs and 10μs for the cases of two and one high recombination velocity surface respectively. This was confirmed with experimental lifetime measurements.

By assuming no recombination is occurring in the bulk, effective lifetime measurements can provide an upper limit to the surface recombination velocity in the sample. Figure 4.1 shows the relationship between effective lifetime and surface recombination velocity for substrates with one and two high recombination velocity surfaces predicted by equations (4.12) and (4.11). Reasonable determinations of surface recombination velocities can be expected from lifetime measurements below 10^4cm/s. Above 10^4cm/s, the diffusion limit lower bound prevents separation of surface recombination velocities without highly accurate measurements of effective lifetime. This is not critical since this range of surface recombination velocities will place similar bounds on device performance (see section 6.3.1).

4.2.3 *Effective lifetime with low surface recombination (Sl/D<1,w/l>>1).*

At lower surface recombination velocities, the fraction of total recombination occurring in the bulk of the sample is likely to be important. Equation (4.9) can be simplified if the recombination at each surface is relatively low *(Sl/D<1)* to the expression

$$\frac{1}{\tau_{eff}} = \frac{1}{\tau_{bulk}} + \frac{Sf + Sr}{W} \tag{4.13}$$

Consequently, the effective lifetime can be limited by the bulk or surface. The components due to the surface and the bulk can be separated by measuring samples with differing thickness. This approach is used in section 6.7 to determine the surface recombination velocity of steam oxidised multicrystalline silicon samples.

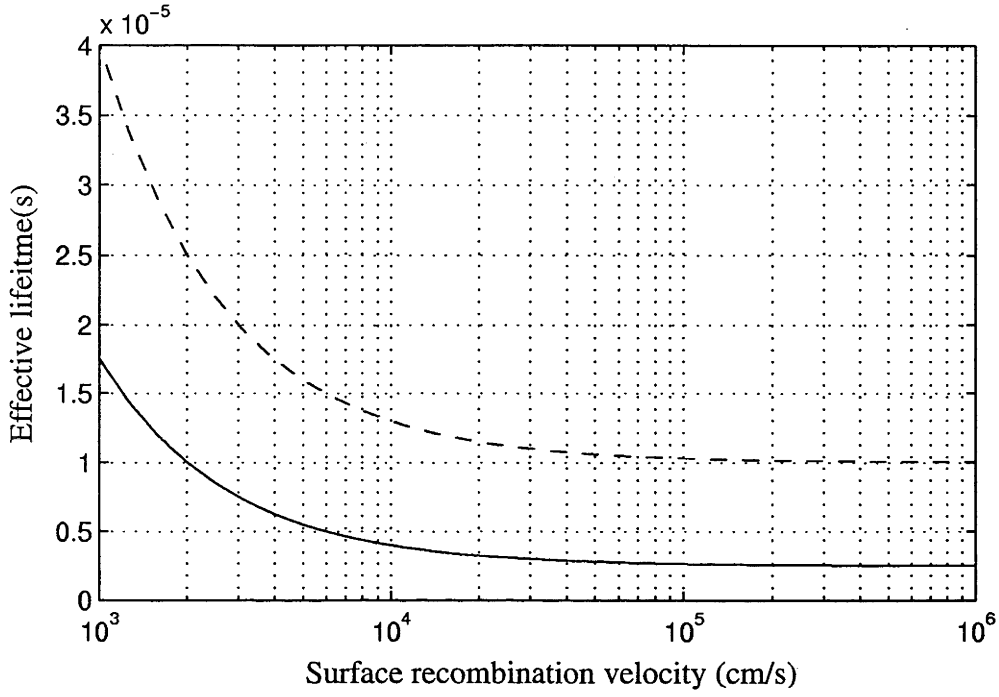

Figure 4.1: *Modelled effective lifetime on substrates limited by surface recombination.*
——— *both surfaces high S*
– – – *one surface zero S*
The substrate thickness is 300μm and the diffusion coefficient is 30cm/s. The lower bound for effective lifetime at high surface recombination velocities is due to diffusion processes. Above 10^4cm/s, it is difficult to differentiate surface recombination velocities with effective lifetime measurements. At lower surface recombination velocities, bulk recombination is likely to affect the effective lifetime.

4.3 Quasi–steady state photoconductance

In practise, photoconductance measurements are made with a light source with a slowly varying light intensity, hence the term quasi–steady state photoconductance (QSSPC). There are benefits in using a non–steady state light source to illuminate the sample for photoconductance measurements. The first benefit is minimising heating of the sample by using a relatively short light pulse. Continuous illumination leads to heating of the sample and the conductance detector. The magnitude of this heating varies with different illumination levels, leading to changes in the recombination and mobilities in the sample and in the calibration of the detector.

The second benefit is the determination of the injection level dependence of the effective lifetime of the sample in a single measurement, by varying the light intensity during the measurement. This allows identification and measurements of saturation currents from emitters, injection level dependent surface recombination velocities and non–ideal bulk recombination.

4.3.1 *Effect of non–steady state illumination*

While there are clear benefits for using a non–steady state light source, it is important to establish the influence of the time dependence of the photogeneration on the measured effective lifetime.

Unless otherwise specified, the light source used for the quasi–steady state photoconductance measurements was a commercially available Xenon flash, designed for photographic purposes. The flashes produced a rapidly increasing light intensity to maximum illumination, followed by an approximately exponential decay of the light intensity to a level ten to twenty times lower than the maximum illumination level. A typical measurement of the light excitation is shown in figure 4.2. The decay constant for the light was 2.3ms.

Since the illumination is not steady state, the changes in intensity with time during the light decay may have an effect on the effective lifetime determined from quasi–steady state measurements. This can be simply modelled for the case of lifetimes independent of injection level. The excess carrier concentration is governed by the following equation

$$\begin{aligned}\frac{d}{dt}(\Delta n(t)) &= -\frac{\Delta n(t)}{\tau_{eff}} + Gen(t) \\ &= -\frac{\Delta n(t)}{\tau_{eff}} + G_0 exp\left(-\frac{t}{\tau_{decay}}\right)\end{aligned} \qquad (4.14)$$

where τ_{eff} is the effective lifetime, τ_{decay} is the decay constant of the light for t>0 and G_0 is the light intensity at the start of the decay (t=0). This equation has solutions

$$\Delta n(t) = G_0\left(\frac{\tau_{eff}\cdot\tau_{light}}{\tau_{light}-\tau_{eff}}\right)e^{\frac{-t}{\tau_{light}}} + C_1 e^{\frac{-t}{\tau_{eff}}} \qquad for\ t>0 \qquad (4.15)$$

with the value for C_1 determined by the conditions when the decay of the light commenced.

The light could be approximated by a steady state condition of constant illumination I_0 or no illumination before t=0 as shown in figure 4.2 with the real illumination included for comparison. For case (a), $\Delta n=G_0\tau_{bulk}$ for $t\leq 0$ with $C_1=-G_0\tau_{eff}.\tau_{eff}/(\tau_{light}-\tau_{eff})$. while for case (b), $\Delta n=0$ for $t\leq 0$ and $C_1=-G_0\tau_{light}.\tau_{eff}/(\tau_{light}-\tau_{eff})$. The quasi–steady state lifetime is determined by the excess carrier concentration divided by the generation rate at a given time

$$\tau_{qsspc}(t) = \frac{\Delta n(t)}{G(t)}$$

$$= \frac{\Delta n(t)}{G_0 exp\left(\frac{-t}{\tau_{light}}\right)}$$

$$\tau_{qsspc}(t) = \tau_{eff}\left(\frac{\tau_{light}}{\tau_{light}-\tau_{eff}}\right)-\tau_{eff}\left(\frac{\tau_{eff}}{\tau_{light}-\tau_{eff}}\right)e^{-t\left(\frac{1}{\tau_{eff}}-\frac{1}{\tau_{light}}\right)} \qquad \text{(case a)}$$

$$\tau_{qsspc}(t) = \tau_{eff}\left(\frac{\tau_{light}}{\tau_{light}-\tau_{eff}}\right)-\tau_{eff}\left(\frac{\tau_{light}}{\tau_{light}-\tau_{eff}}\right)e^{-t\left(\frac{1}{\tau_{eff}}-\frac{1}{\tau_{light}}\right)} \qquad \text{(case b)} \qquad (4.16)$$

The second term vanishes within a few effective lifetimes of the start of the decay provided that the effective lifetime of the material is much less than the decay constant of the light. Therefore information within the first few bulk lifetimes of the start of the decay should be discarded. However, even after discarding this initial information, the finite decay of the light leads to an overestimate of the effective lifetime by the factor $(\tau_{light}/\tau_{light}-\tau_{eff})$ relative to the real effective lifetime. The resulting error as a function of effective lifetime is shown in figure 4.3. The error is small while the the effective lifetime is much smaller than the decay constant of the light while the error increases to an overestimate of 10% at 200μs with rapid increases in the error as the effective lifetime approaches the decay constant of the light (2.3ms).

4.3.2 *Equipment for quasi–steady state photoconductance measurements*

The apparatus for quasi–steady state photoconductance measurements is relatively simple. The required equipment is a source of illumination, a detector for the quantity of illumination and a detector for the samples conductance. This equipment was obtained from Sinton Consulting [94]. A photograph of the equipment can be seen in figure 4.4.

As mentioned above, the illumination was usually provided by a commercial Xenon flash. This was capable of producing light intensities on the sample approaching 1000 suns. The illumination was kept uniform over the sample and the detector by the use of diffuse neutral density filters, and the intensity could be adjusted by suitable combinations of filters.

The illumination level was monitored by a backside–contact solar cell [95] in series with a low resistance, which has a linear response between short circuit and illumination. This produces a response of 8.95mV per sun. This limits the detector to intensities less than 60 suns without the the use of an aperture to scale the illumination on the solar cell.

The generation in the sample has to be adjusted for the reflectance of the sample. This is usually a fairly coarse estimate based upon the thickness of the sample and the type of

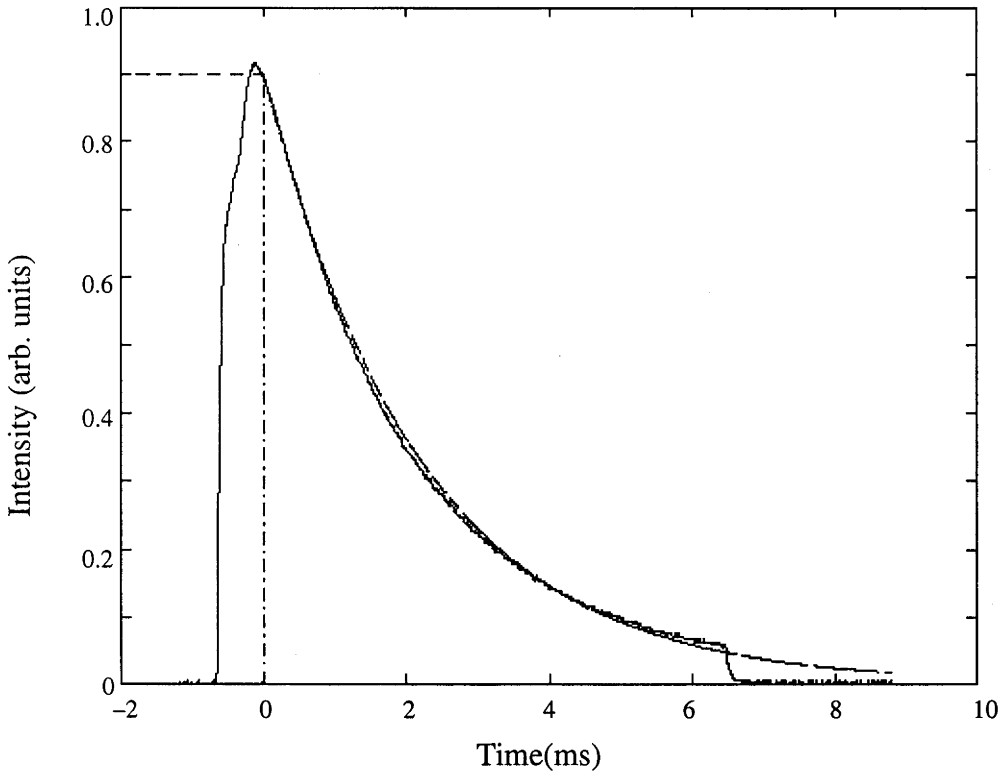

Figure 4.2: *Modelled light intensity to determine effect of time dependence of light decay on effective lifetime measurement.*
——— *real light response*
— — — *steady state illumination before t=0 (case a)*
—·— *light off before t=0 (case b)*

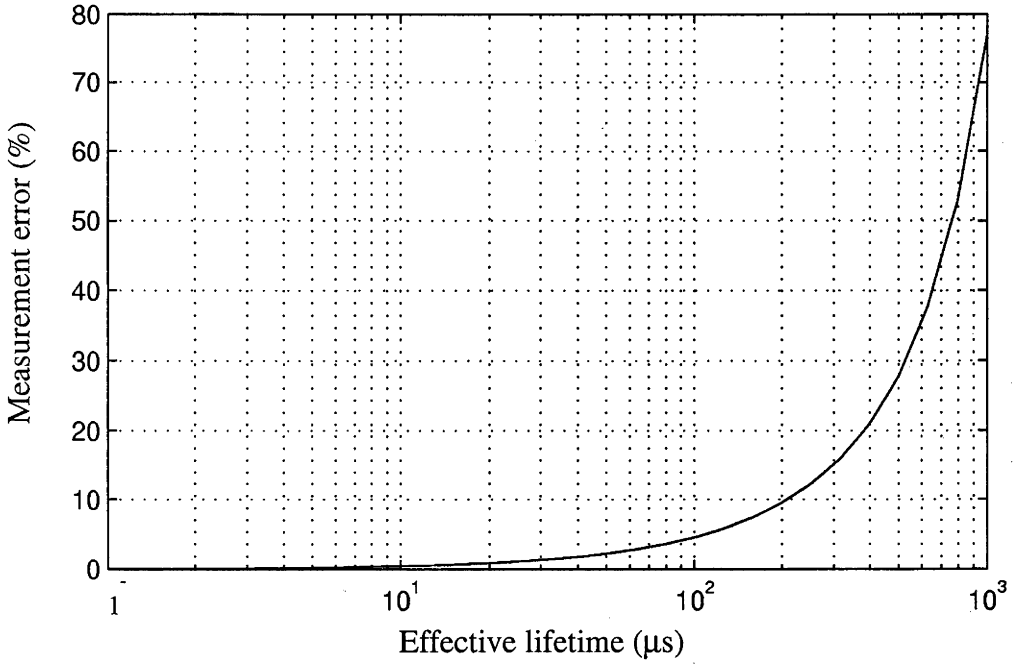

Figure 4.3: *The error in measured lifetime due to the finite decay constant of the light.*

The curve is calculated from equation (4.16). The decay constant for the light was 2.3ms. Errors due to the time dependence of the light are less than 10% for effective lifetimes less than 200μs. Errors increase rapidly at higher lifetimes.

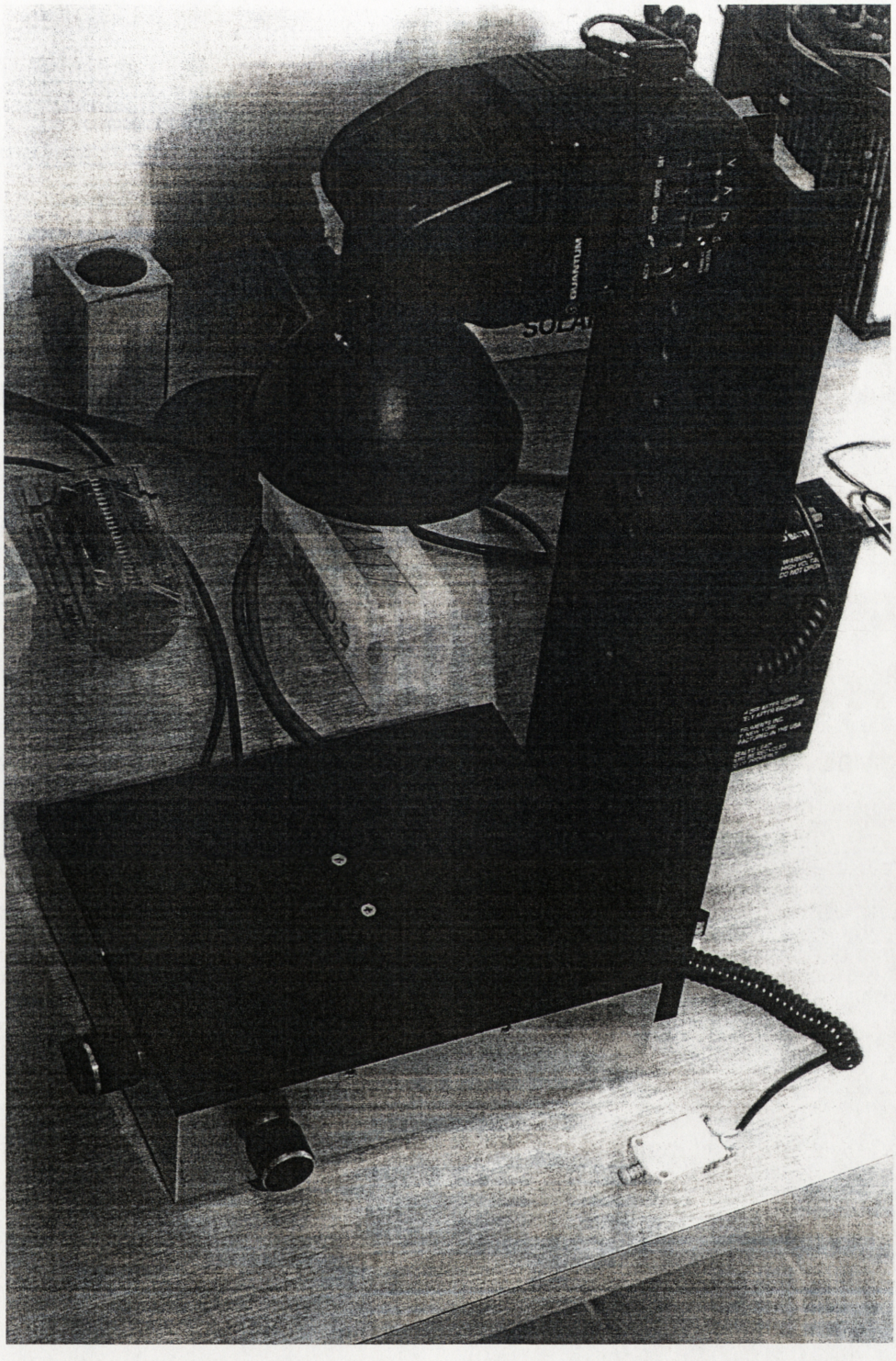

Figure 4.4: *Quasi–steady state photoconductance equipment.*
The sample is placed above the 3cm^2 coil to the left of the screws, which is protected by a plastic cover. The output conductivity signal was balanced by adjusting the capacitance and the resistance of the bridge circuit. The sample was illuminated by the flash mounted above the sample. Diffusers were used to provide uniform illumination despite the proximity of the flash. The intensity of the illumination was measured with a solar cell to the right of the screws. The conductance and illumination signals were measured with a digital oscilloscope, and then downloaded for analysis.

antireflection coatings and texturing. The estimate was likely to vary from the real generation rate by up to 5%, and contributed to equivalent errors in the final measured lifetime. 5% errors in effective lifetime have little effect on the prediction of cell performance (<2mV in V_{oc}) though limit the ability to separate bulk and surface effects for low effective lifetimes (section 4.2.2). More precise results, if warranted, could be obtained with reflectivity measurements of the sample with a spectrophotometer and integrating sphere.

The photoconductance was measured with an RF bridge, with a $3cm^2$ coil coupled to the sample. The circuit was balanced before measurement to increases the sensitivity of the measurement of the (usually) smaller excess conductivity. The conductance signal was calibrated with the use of samples of known resistivity and thickness. The signal from the detector varied linearly with changes in conductance. The illumination and conductance signals were measured with a digital oscilloscope, and transferred to computer for analysis.

4.3.3 *QSSPC measurements of single crystal silicon samples*

Initial investigations of the QSSPC technique concentrated on single crystal p–type substrates. Single crystal silicon was expected to be well behaved compared to multicrystalline silicon, due to the absence of grain boundaries and lower impurity and defect concentrations.

Effective lifetime measurements of silicon substrates with QSSPC quickly established that effective lifetimes can be strongly injection level dependent. The most common injection level dependence observed during QSSPC measurement was due to recombination in heavily phosphorus doped surfaces, used for emitters or for surface passivation. An example of the measurement of a phosphorus passivated 0.4Ωcm Fz substrate can be seen in figure 4.5.

The effect of the diffused region can be theoretically determined by replacing the surface recombination velocity S in equation (4.13) with the surface recombination velocity equivalent to the emitter saturation current from a diffused region, $J_o.(Na+\Delta p)/qn_i^2$ [96] which is dependent on the excess carrier concentration, $\Delta p = \Delta n$.

$$\frac{1}{\tau_{eff}} = \frac{1}{\tau_{bulk}} + \frac{2J_o(N_a + \Delta n)}{qn_i^2 W} \qquad (4.17)$$

The injection level dependence of a diffused region was therefore characterised by a linear relationship between inverse effective lifetime and excess carrier concentration at higher injection levels, as seen in figure 4.5. The dark saturation current could be determined from the slope of the effective lifetime provided the substrate doping and thickness were known. The intercept of the line of best fit of inverse effective lifetime versus excess carrier concentration is given by

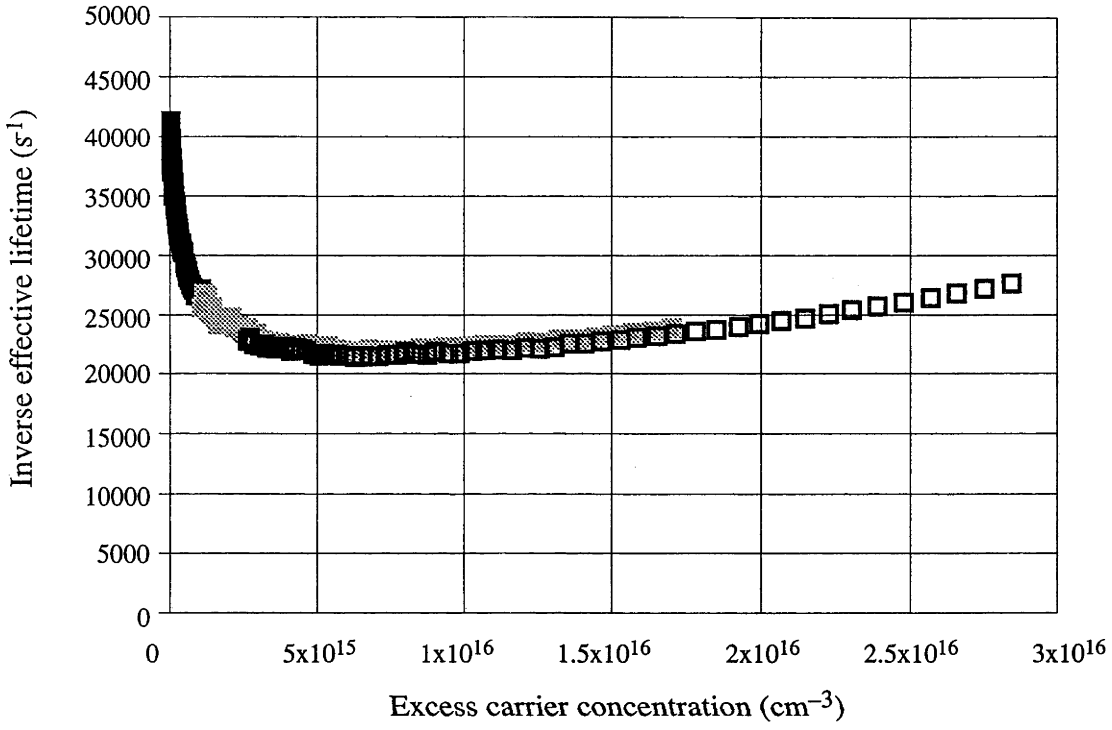

Figure 4.5: *QSSPC effective lifetime measurements of 230μm 0.4Ωcm Fz substrate with phosphorus diffused surfaces.*

The effective lifetime of the Fz substrate demonstrated injection level dependence throughout the measurement range. At higher injection levels, the saturation current in the diffused regions dominated causing the linear relationship between inverse effective lifetime and injection level. At lower injection levels, the measured effective lifetime decreased, possibly due to differences in the lifetimes of electrons and holes in the SRH formulation of recombination.

$$\frac{1}{\tau_{eff}} = \frac{1}{\tau_{bulk}} + \frac{2J_o N_a}{qn_i^2 W} \qquad (4.18)$$

so that the emitter recombination must be subtracted from the effective lifetime to determine the bulk lifetime. If the second term dominates due to large J_o and/or doping, extraction of the bulk lifetime will be unreliable.

Equation (4.17) was expected to extend to low excess carrier concentrations. In practice, the effective lifetime typically remained linear for excess carrier concentrations greater than ten percent of the substrate doping. However, at lower injection levels, the inverse effective lifetime tended to remain constant or increased as the excess carrier concentration decreased. This typically occurs during measurements of Fz and Cz single crystal substrates with good phosphorus diffused surface passivation.

This behaviour could be due to the transition from low injection to high injection recombination behaviour in the Shockley–Read–Hall (SRH) formulation of recombination via traps. Recombination in the SRH model is given by

$$U = \frac{np - n_1 p_1}{\tau_{po}(n + n_1) + \tau_{no}(p + p_1)} \qquad (4.19)$$

where τ_{no} and τ_{po} are the electron and hole lifetime parameters of the traps and n_1 and p_1 are the equilibrium electron and hole concentrations if the Fermi level was at the energy level of the trap [57]. The SRH formulation reduces to $U=\Delta n/\tau_{no}$ (assuming traps close to midgap) for very low injection levels changing to $U=\Delta n/(\tau_{no}+\tau_{po})$ at very high injection levels, with the region of transition depending upon the values for the electron and hole lifetimes, substrate doping and trap energy level.

Fitting effective lifetimes modelled with PC–1D indicated that the difference in the electron and hole lifetime may be quite large. A modelled fit of the measured recombination is shown in figure 4.6. The recombination at high excess carrier concentrations was dominated by recombination in the diffusions ($J_o=5\text{x}10^{-14}\text{Acm}^{-2}$), but the fraction due to the surface decreased as the injection level decreased, indicating that the increased recombination should be due to a decrease in the bulk lifetime at lower injection levels. Assuming the traps are located near midgap, the hole lifetime needs to be 40 times greater than electron lifetime (which is of order of 35μs) to fit the observed behaviour. The effective lifetime would be expected to approach a constant limit as injection levels decrease further. Confirmation of this requires measurements at injection levels below the sensitivity of the current QSSPC equipment. This injection level dependent behaviour due to SRH recombination has been observed for a wide variety of substrates [97].

Alternate possibilities for the variation in effective lifetime at low injection level include shunting and junction recombination [Green priv comm]. Shunting of the floating junctions would lead to increased recombination as carriers which are transported across the junction by the resistive shunt recombine. A shunt resistance of 100ohm cm^2 would

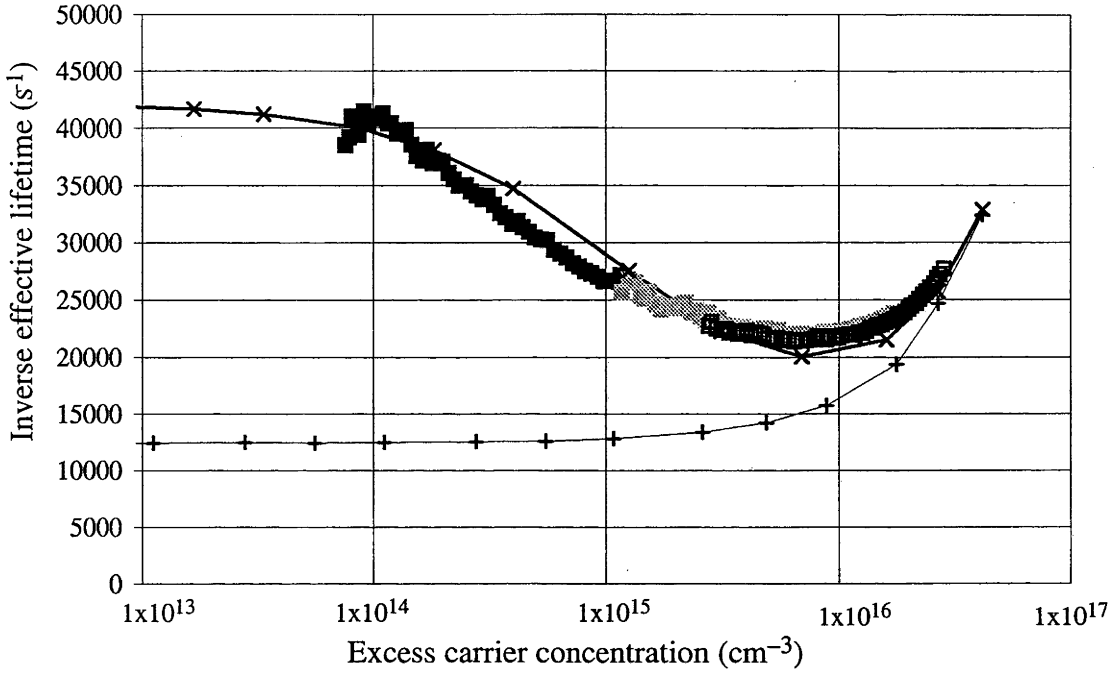

Figure 4.6: *PC–1D modelling of recombination in the 0.4Ωcm ($4x10^{16}cm^{-3}$ doped) Fz substrate in figure 4.5.*

■ □ *QSSPC measurement (low/medium/high)*
—×— *PC–1d model with SRH recombination and diffused region recombination*
—+— *PC–1d model with diffused region recombination (no SRH)*

The Fz sample had particularly low lifetime due to contamination from coprocessed multicrystalline silicon samples. Decreases in the effective lifetime at lower injections levels appear due to differences in the electron and hole lifetimes in the SRH model of trap recombination. The low level lifetime (electron) was 35μs while the hole lifetime was greater than 1ms. The effective lifetime would be expected to become injection level independent at lower injection levels. Recombination at greater than $10^{16}cm^{-3}$ excess carrier concentration was dominated by recombination in the phosphorus diffused regions ($J_{oe}=5x10^{-14}Acm^{-2}$).

be necessary for the observed decrease in effective lifetime at low injection levels in figure 4.6. This is much lower than the shunt resistances observed even in completed (metallised) cells on float zone substrates, which typically have resistances greater than 1000ohm cm^2. Therefore, shunts do not appear to be the likely cause of the injection level dependence.

Junction recombination would also need to be enhanced significantly compared to equation 3.2 for the observed decrease in lifetime to be caused by junction recombination. Assuming identical lifetimes for electrons and holes, junction recombination would need to be approximately 200 times greater than that predicted by equation 3.2. The hole lifetimes would need to be 4 10^4 times smaller than the electron lifetime, which appears unlikely. If the injection level dependence was due to junction recombination or shunting, it would be expected to limit the lifetime to $W^2/12D$ (1.6 μs) at low injection levels. More sensitive measurements may allow this to be determined.

This has implications for the bulk lifetime determined from fitting equation (4.17) to the linear region of the effective lifetime measurement. The bulk lifetime will reflect the high injection lifetime at the injection levels where the effective lifetime response was linear, not the low injection lifetime at the intercept.

4.3.4 *Heating effects during QSSPC measurement*

By using a light with short pulse duration, the heating effects of the illumination was reduced. The effect of the heating on QSSPC measurements was investigated by observing the change in equilibrium conductance of samples before and after illumination.

The flash was placed closed to the sample to maximise the illumination and the potential heating of the substrate. Flashes decreased in intensity from 600 to 30 suns over the 7ms duration of the flash. The background conductance signal was observed to decrease by ΔS=18mV on 0.3Ωcm substrates and ΔS=8mV on 1Ωcm substrates due to decreases in mobility with temperature. The conductance signal returned to equilibrium with a decay constant of 1–2 seconds, several orders of magnitude longer than the flash.

These changes in background conductivity would be sufficient to affect the measured excess photoconductivity in low lifetime materials. The change in background conductance is greatest at the end of the flash where the excess carrier concentration is smallest. The change of 18mV corresponded to an underprediction of excess carrier concentration by $1.2x10^{14}cm^{-3}$ at the end of the measurement of the 0.3Ωcm Fz substrate, equivalent to an effective lifetime of 0.5μs at 30 suns. This would strongly affect measurements of substrates with lifetimes of the order of microseconds and smaller.

The change in background conductivity can be accounted for during analysis of the effective lifetime. Since the substrate required seconds to return to equilibrium, the substrate can be assumed to lose no heat during the illumination. Heat was provided by the illumination, so the change in temperature with time was equal to the total change in

temperature during the flash multiplied by the integral of the illumination to that time divided by the integration of the illumination over the full duration of the flash. The change in conductance was relatively small compared to the background and can be assumed to be linear with respect to temperature change so that the fractional change in conductance is equal to the fraction of the total illumination to that time. The conductivity signal is adjusted accordingly (by zero at the start to ΔS at the end) and the analysis then proceeds as usual.

4.4 QSSPC measurements of multicrystalline silicon

The analysis from section 4.3.1 indicated that quasi–steady state illumination should provide an accurate measurement of effective lifetime provided that the effective lifetime was much shorter than the decay constant of the illumination. Quasi–steady state photoconductance measurements should therefore be particularly well suited to measurements of low lifetime material, such as multicrystalline silicon. This relies on the assumption that the recombination behaviour is well described by a single recombination parameter, the steady–state effective lifetime.

From experience, the measured effective lifetimes of multicrystalline silicon substrates as a function of injection level fell into two categories. Most substrates demonstrated similar behaviour to the single crystal silicon substrates. Some substrates however, particularly those more heavily doped, were well behaved only above a threshold carrier concentration, and showed rapid increases in measured effective lifetime as injection levels dropped below the threshold. These different outcomes from effective lifetime measurement will be discussed in the next two sections.

4.4.1 *QSSPC versus PCD measurements of multicrystalline silicon*

The majority of the multicrystalline silicon substrates from Eurosolare measured in this investigation demonstrated similar behaviour to that observed for the single crystal silicon substrates. Substrates were lightly phosphorus diffused and oxidised before measurement. A typical example can be seen in figure 4.7. At higher excess carrier concentrations, diffused region saturation currents dominated producing the linear relationship between injection level and inverse effective lifetime while at lower excess carrier concentrations the effective lifetime typically decreased due to changes in the SRH lifetime with changes in injection level.

Despite the general similarity in behaviour, differences between multicrystalline silicon and single crystal silicon appeared when comparing QSSPC and PCD effective lifetime measurements. QSSPC and PCD measurements of effective lifetimes at one sun illumination of some high lifetime 1.5Ωcm gettered multicrystalline silicon substrates with lifetimes around 200μs and a 1Ωcm float zone substrate can be seen in Table 4.1. The effective lifetimes measured with QSSPC were greater for the Fz substrate as predicted by

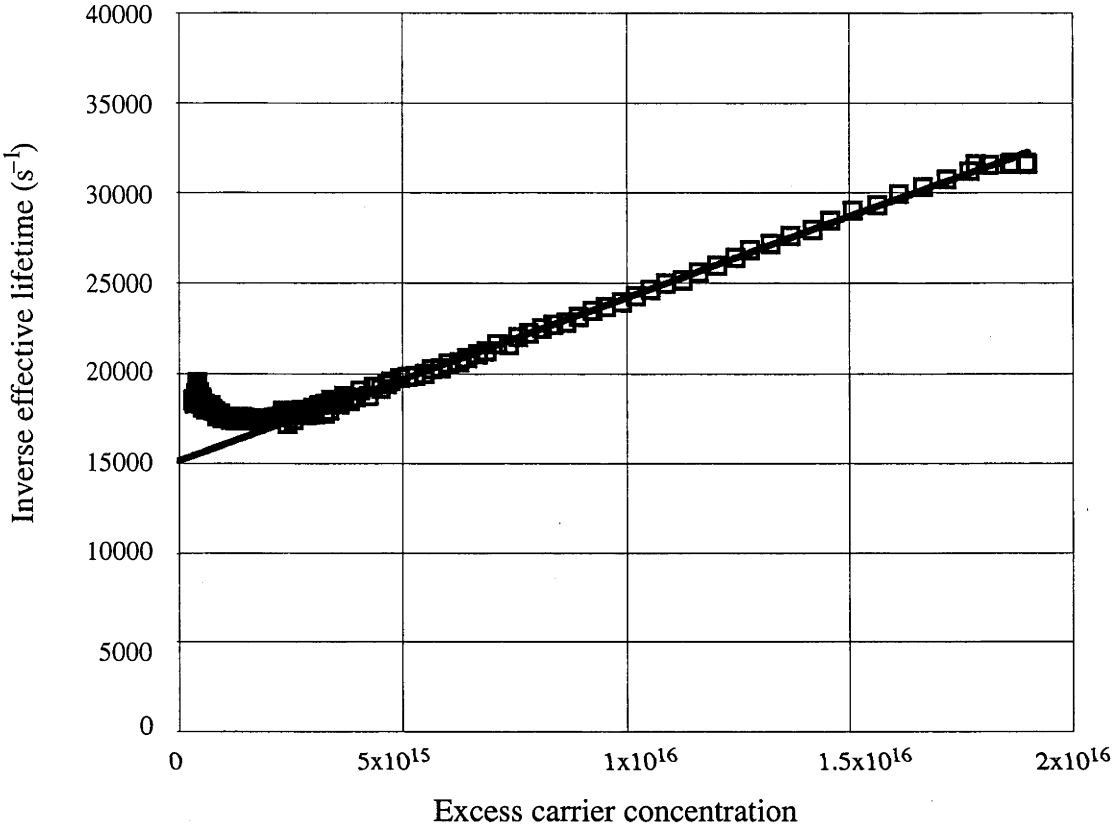

Figure 4.7: *QSSPC effective lifetime measurement of 220μm 1.5Ωcm multicrystalline silicon substrate with oxidised phosphorus diffused surfaces.*
Illumination was varied from 80 suns down to half a sun. The multicrystalline substrate showed similar behaviour to the Fz substrate in figure 4.5. The diffusions had a combined saturation current of $2x10^{-13}Acm^{-2}$, causing the linear relationship between inverse effective lifetime and injection level. The effective lifetime decreased slightly at lower injection levels.

equation (4.16), with the QSSPC technique expected to overpredict effective lifetimes by about 10%.

Substrate	QSSPC effective lifetime (μs)	PCD effective lifetime (μs)
Fz 1Ωcm	180	170
Multi 1.5Ωcm	190	260
Multi 1.5Ωcm	120	220
Multi 1.5Ωcm	180	250

Table 4.1: *Comparison of PCD and QSSPC lifetimes for single crystal and gettered multicrystalline silicon.*

The quasi–steady state measurement of the Fz substrate overpredicted effective lifetime compared to the PCD measurement by about 10%, as predicted from theory. However, the effective lifetimes from PCD measurements of multicrystalline silicon were much greater than with QSSPC, with the PCD measurement dominated by the lifetime in the better grains.

The opposite behaviour was observed with the multicrystalline silicon substrates, with the PCD lifetime 30% to 80% higher than that measured with QSSPC. This was due to the grain to grain variation of the lifetime of multicrystalline silicon substrates. During the PCD measurement, the conductance was dominated by the carrier concentration in the better grains, which have greater numbers of excess carriers after the illumination and these carriers decay more slowly. Consequently the measured effective lifetime by the PCD technique more closely reflected the lifetime in the better grains. In contrast, the quasi–steady state measurements produced an area averaged effective lifetime over the area measured. (This comparison ignores lateral current flow which is reasonable with typical grain dimensions in the material (5–10mm) much greater than the substrate diffusion lengths ~800μm.)

This can examined theoretically for the idealised case of half of the substrate having double the injection level independent effective lifetime of the remainder of the substrate, which has an effective lifetime τ_g. The effective lifetime for the QSSPC measurement is given by

$$\begin{aligned}\tau_{qsspc} &= \frac{\Delta n_{ave}}{G(t)} \\ &= \frac{\frac{1}{2}\left(2\tau_g G_o e^{-t/\tau_{light.}}\right) + \frac{1}{2}\left(\tau_g G_o e^{-t/\tau_{light.}}\right)}{G_o e^{-t/\tau_{light.}}} \\ &= \frac{3\tau_g}{2}\end{aligned} \qquad (4.20)$$

which is equal to the area averaged effective lifetime. The PCD lifetime can be expressed as

$$\tau_{pcd} = -\frac{\Delta n_{ave}}{\left(\frac{d\Delta n_{ave}}{dt}\right)}$$
$$= \frac{\frac{1}{2}\left(G_o 2\tau_g e^{-t/2\tau_g}\right) + \frac{1}{2}\left(G_o \tau_g e^{-t/\tau_g}\right)}{\frac{1}{2}\left(G_o e^{-t/2\tau_g}\right) + \frac{1}{2}\left(G_o e^{-t/\tau_g}\right)}$$
$$= \frac{2\tau_g e^{-t/2\tau_g} + \tau_g e^{-t/\tau_g}}{e^{-t/2\tau_g} + e^{-t/\tau_g}} \qquad (4.21)$$

which is only equal to the area averaged lifetime at t=0, and is higher for all subsequent times. A comparison of the inverse effective lifetimes expected in the two modelled cases can be seen in figure 4.8. For all injection levels, the QSSPC measurement is equal to the area averaged effective lifetime. At the start of the PCD decay, the effective lifetime is also equal to the area averaged lifetime, but as the excess carrier concentration decreases the effective lifetime increases towards the lifetime of the better grain. The resulting relationship between effective lifetime and injection level is similar to that expected for a diffused substrate, rather than the constant effective lifetime in the individual grains. Extracting effective lifetimes from late in the decay or at the intercept with $\Delta n=0$ in the model would lead to a 50% greater effective lifetime from the PCD measurement than from QSSPC. Measurements of real multicrystalline silicon samples would be complicated by the greater number of grains with differing lifetimes all contributing to the effective lifetime measurement.

The restrictions of the transient PCD method can be avoided with mapping of lifetime over the substrate, followed by area averaging, as used by Nagel *et al.* [98]. However, this is time consuming and not suited to the high throughput required for process monitoring. Quasi–steady state photoconductance therefore appears to be better suited for effective lifetime measurements of multicrystalline silicon.

4.4.2 *Trapping effects during QSSPC measurements of multicrystalline silicon samples*

Some of the substrates demonstrated effective lifetimes during quasi–steady state measurements which rapidly increased below a threshold excess carrier concentration, while demonstrating normal injection level dependence above this threshold. A typical measurement with this effect in a 0.2Ωcm substrate can be seen in figure 4.9. The threshold excess carrier concentration can correspond to levels greater than one sun illumination, restricting the usefulness of the measurement for cells at usual operating conditions. The prevalence of the trapping tended to increase with substrate doping and for low effective lifetimes: common in 0.2Ωcm substrates and rare in 1.5Ωcm.

The photoconductance signal measured during the illumination was distinctly different to that observed for other substrates. Rather than following the exponential decay of the illumination, Figure 4.10 shows that the conductance decreased more slowly during the illumination. When the illumination was switched off, the conductance decayed with a relatively long decay constant, compared to substrates without the transient effect with

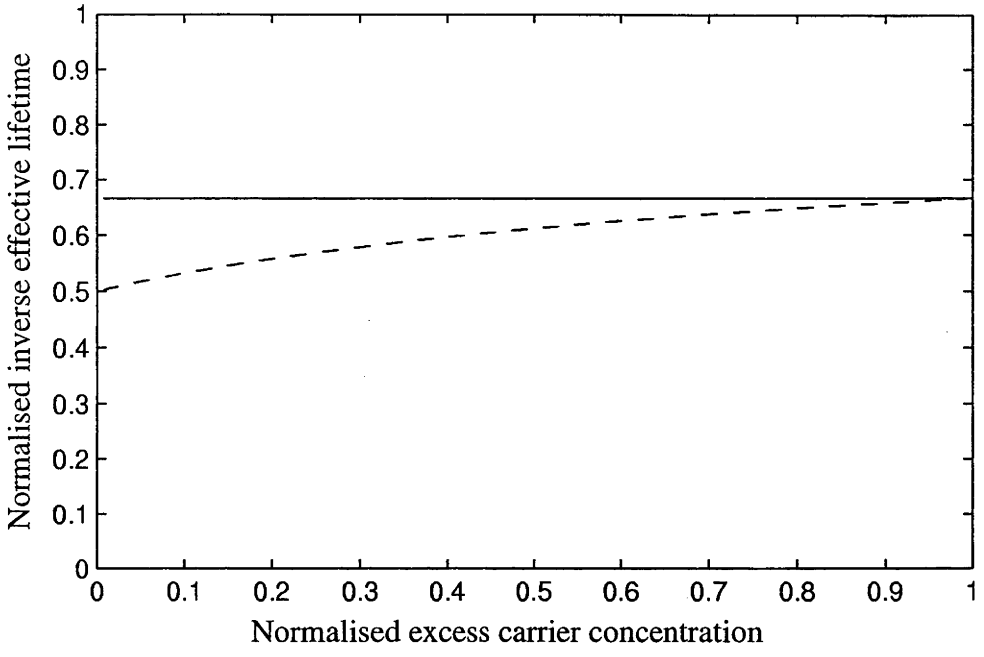

Figure 4.8: *Modelled QSSPC and PCD inverse effective lifetimes for simple two grain/two lifetime model.*

— — — *PCD*

——— *QSSPC*

The model consisted of two grains with equal area with the good grain double the lifetime of the worse grain (no injection level dependence). The inverse effective lifetime was normalised to the lifetime in the worse grain. The effective lifetime from the quasi–steady state measurement is equal to the area averaged effective lifetime. The PCD effective lifetime is equal to the area average at t=0 ($\Delta n_{norm}=1$), but approaches the lifetime of the better grain at lower excess carrier concentrations. This would lead to the false conclusion of better lifetimes and worse emitter saturation currents on multicrystalline silicon when using PCD measurements.

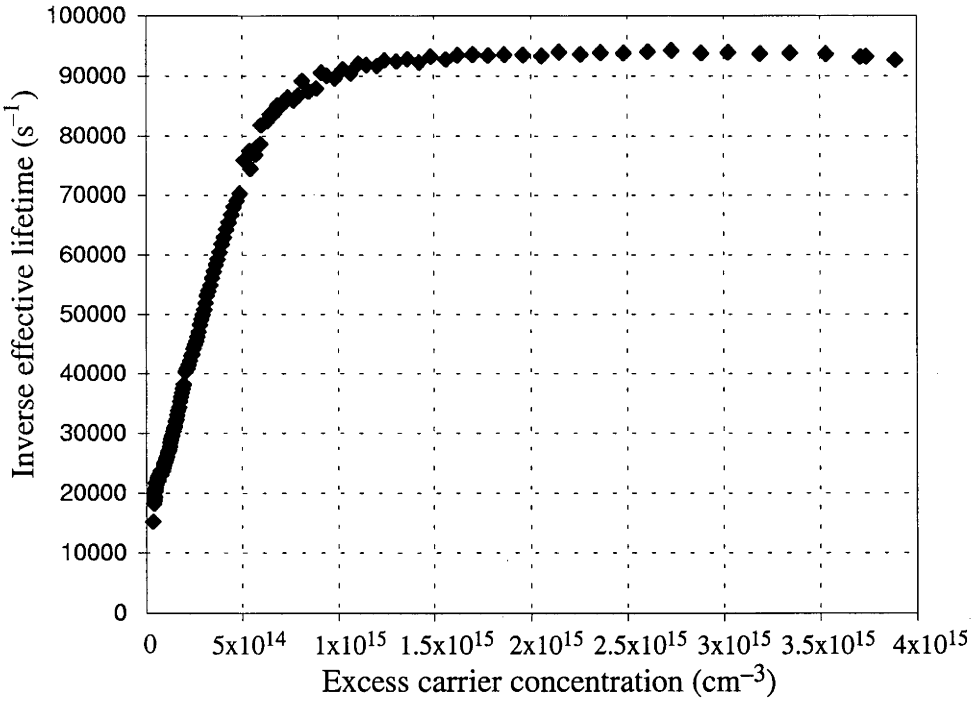

Figure 4.9: *Characteristic QSSPC measurement of multicrystalline silicon sample with transient behaviour at low injection levels.*
This behaviour was common in 0.2Ωcm substrates. The transient behaviour was characterised by normal lifetime measurement above a threshold injection level, with rapidly increasing lifetime below the threshold. Despite the relatively high lifetime for a 0.2Ωcm substrate (10.5μs), the transient behaviour affected the measurement at illumination levels equivalent to up to 10 suns.

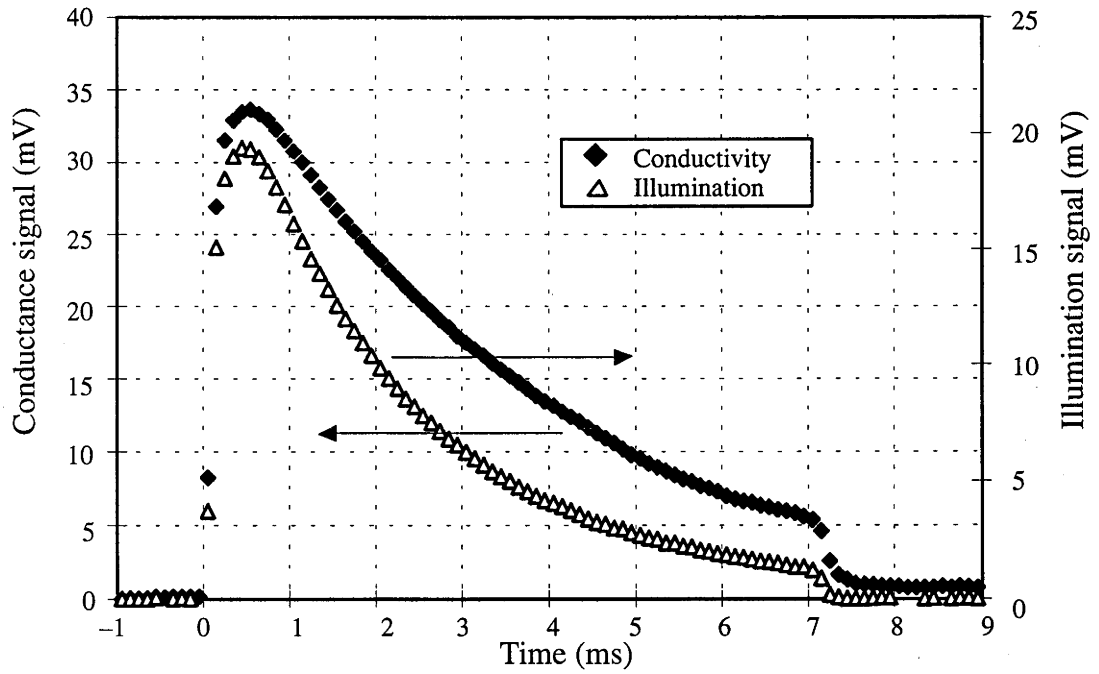

Figure 4.10: *Conductance and illumination outputs during QSSPC measurements with transient behaviour.*
Measurements of samples which demonstrated transient behaviour were characterised by conductance signals which decayed more slowly than the illumination, and slowly decayed to equilibrium after the illumination was switched off.

comparable effective lifetimes. This behaviour suggested the presence of processes with characteristic time constants greater than the effective lifetime.

4.4.2.1 *Trapping effects during transient photoconductance decay measurements*

It has long been recognised that the presence of large numbers of shallow traps can affect the measurement of lifetime during photoconductance decay measurements [88]. Shallow traps with emission lifetimes greater than the effective lifetime can lead to erroneously high effective lifetimes during PCD measurements.

A schematic of the energy levels involved can be seen in figure 4.11. The traps lead to an overprediction of lifetime due to the emission of minority carriers from the shallow traps. In p–type silicon, the shallow traps have a relatively fast rate of electron capture, while the hole capture rate is very slow. The shallow traps therefore fill with electrons quickly while the substrate is under illumination. Once the light is switched off, a large percentage of these electrons are emitted from the trap into the conduction band at a rate exponentially decreasing in proportion to the emission rate. This is effectively a source of generation, and the excess carrier concentration in the conduction band is increased in proportion to this 'generation' rate. If the emission lifetime is longer than the bulk lifetime, the excess carrier concentration will initially decay at the rate of the bulk lifetime followed by a more slow decay proportional to the rate of emission of electrons from the trap. The transient lifetime at the lower injection levels will therefore reflect the emission lifetime, rather than the bulk lifetime.

The presence of such traps should not affect steady state measurements of effective lifetime since the concentration of electrons in the shallow traps will be in steady state, with the rate of electron capture into the trap equal to the electron emission (ignoring the small hole capture rate of the trap which contributes to the effective lifetime). The trapping effects can therefore be eliminated from PCD measurements by illuminating the sample with a bias light with constant illumination and generating a relatively small number of additional excess carriers during the transient measurement. The change in the rate of capture and emission in the trap then no longer affects the lifetime measurement. The rate of decay of the excess carriers is the differential lifetime, $\delta U/\delta \Delta n$ [99,100] rather than the effective lifetime ($=U/\Delta n$) and is only equal to the effective lifetime if the effective lifetime is not injection level dependent, as expected in very low level injection.

4.4.2.2 *Trapping in QSSPC photoconductance measurements*

The shallow traps which cause problems during transient photoconductance decay measurements can provide a qualitative explanation of the transient behaviour observed in figures 4.9 and 4.10.

During the initial increase in illumination, the trap fills with electrons. As the illumination levels start to decrease, the excess electron concentration in the conduction band decreases. The emission and capture from the shallow traps are initially almost balanced. As the

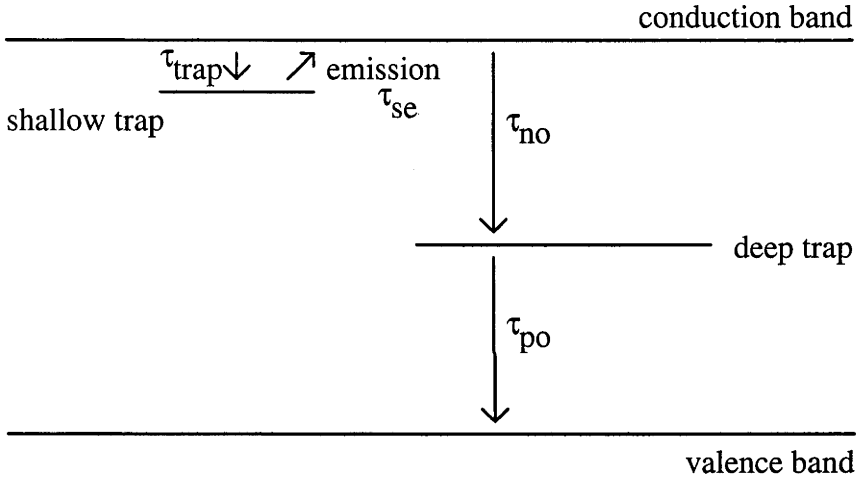

Figure 4.11: *Schematic of dominant carrier processes in p–type silicon with shallow and deep traps.*

During steady state illumination, the shallow traps have little effect on recombination due to the long hole lifetime, with electrons trapped at the same rate as electrons are emitted. During a PCD or QSSPC measurement, the electron concentration in the conduction band decreases, and the rate of emission from the trap can exceed the rate of capture. This leads to a net flow of electrons from the trap into the conduction band, and a greater concentration of electrons in the conduction band than would be present in the absence of the shallow traps.

excess concentration in the conduction band decreases further, the rate at which electrons are emitted from the trap exceeds the rate at which electrons are recaptured, producing a net flow of electrons to the conduction band from the shallow traps. As the excess carrier concentration in the conduction band continues to decrease due to recombination via the deep traps, the net transfer of electrons from the trap to the conduction band increases with fewer electrons available to be captured by the shallow traps. Eventually the rate of release from the shallow traps decreases as the electron concentration in the shallow traps is depleted. After the illumination source is turned off, the remaining electrons continue to decay from the trap. The shallow traps therefore acted as a supplementary source of generation to the photogeneration as the light intensity decreased.

Since only the generation from the light was measured for determining the effective lifetime, net 'generation' from the traps will lead to an overprediction of effective lifetime via

$$\begin{aligned}\tau_{qsspc} &= \frac{\Delta n_{ave}}{G_{light}} \\ &= \frac{\tau_{eff}\left(G_{light} + G_{trap}\right)}{G_{light}} \\ &= \tau_{eff}\left(1 + \frac{G_{trap}}{G_{light}}\right)\end{aligned} \tag{4.22}$$

The net generation from the trap can therefore be determined if the effective lifetime was assumed to be independent from the injection level. Figure 4.12 is the trap generation rate required to cause the observed behaviour of the effective lifetime over the range of carrier injection levels during the QSSPC measurements of the 0.2Ωcm sample in figure 4.9. The trap generation rate increased as the measurement proceeded with the decrease in the electron concentration in the conduction band, before peaking and decreasing exponentially as the traps deplete. The peak generation rates were high, corresponding to illumination levels equivalent to two suns illumination and therefore affected the QSSPC measurement at quite large excess carrier concentrations. Integrating the net trap generation rate with respect to time indicated that less than $5\text{x}10^{16}$ traps/cm^3 released electrons during the measurement. This was less than the substrate doping (10^{17}cm^{-3}) but greater than the excess carrier concentration during measurement.

If this number of traps were filled during the QSSPC measurement, then the excess holes concentration was much greater than the excess electron concentration. The QSSPC theory then breaks down since equation (4.6) relied on the assumption of equal average excess electron and hole concentrations.

The presence of shallow traps provided a qualitative explanation of the transient behaviour observed during QSSPC measurements. Since most research concentrated on high efficiency multicrystalline cells, the trapping was not of major concern in this work. In substrates where trapping did occur, effective lifetime measurements were restricted to

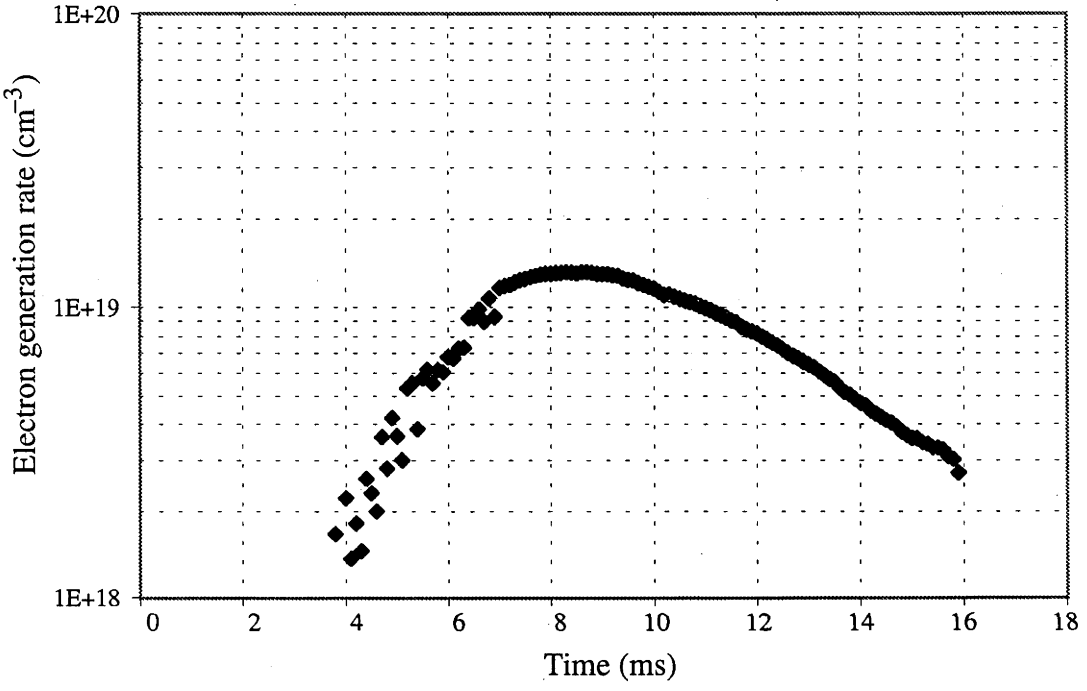

Figure 4.12: *Calculated electron generation rate from traps during QSSPC measurement of 0.2Ωcm substrate.*
The electron generation rate from the shallow traps was determined from equation (4.22) for the 0.2Ωcm multicrystalline substrate measured in figure 4.9. The generation rate rises as the excess carrier concentration in the conduction band drops, then decreases as the traps are depleted. Despite the high peak rate of trap generation which is equivalent to 2 suns illumination, the total number of traps which contributed to the generation was less than $5x10^{16}cm^{-3}$.

higher light intensities, maintaining carrier concentrations above the trapping threshold. The resulting effective lifetime therefore often reflected injection levels greater than those the cell would experience under one sun illumination.

4.4.3 *Summary of QSSPC measurements on multicrystalline silicon*

Quasi–steady state photoconductance measurements appeared a useful tool for effective lifetime measurements of multicrystalline silicon. The effective lifetime measured with QSSPC was the area weighted average, compared to the transient photoconductance decay which approached the lifetime of the best grains. QSSPC measurements are over a range of injection levels, allowing the injection level dependence of the effective lifetime to be observed and the identification of non–ideal recombination.

The major limitation of the technique was transient effects in some substrates, possibly due to shallow traps. This restricted lifetime measurements to greater than the threshold carrier concentration, which may be greater than the cell's injection level under one sun illumination.

4.5 Effect of symmetric illumination

As suggested in section 4.4.2, slowly decaying trapping effects appear to severely affect the QSSPC measurements of effective lifetime of some multicrystalline silicon substrates with the potential for substantial overpredictions of lifetime. The overprediction of lifetime was due to the release of trapped carriers generated at higher illumination levels, which can produce sufficient numbers of carriers to affect the conductance under later, lower levels of illumination.

It was anticipated that some the trapping affects could be avoided by using a light pulse which increased, rather than decreased, in light intensity with time. Under an increasing light intensity, the rate at which carriers are entering the traps should be greater than the rate at which carriers are reinjected into the conduction band, so that the trap acts as a net recombination site rather than a generation site. Effective lifetime should then be underestimated, unlike the exponential decay where the trapping led to overprediction of effective lifetime. A combination of increasing and decreasing light intensity should bound the real effective lifetime.

A disco light strobe was used as the light source. It produced a light intensity which increased for several milliseconds, before peaking and then decreasing in intensity over several milliseconds (figure 4.13). The symmetric light pulse could be approximated by a Gaussian distribution, except at high light intensities where the real illumination intensity varied more slowly. The Gaussian distribution had a 1/e half width of 2.1ms.

4.5.1 *Modelling symmetric illumination*

When no trapping occurs, the excess carrier concentration and the effective lifetime as a function of time can be determined from the balance of generation and recombination.

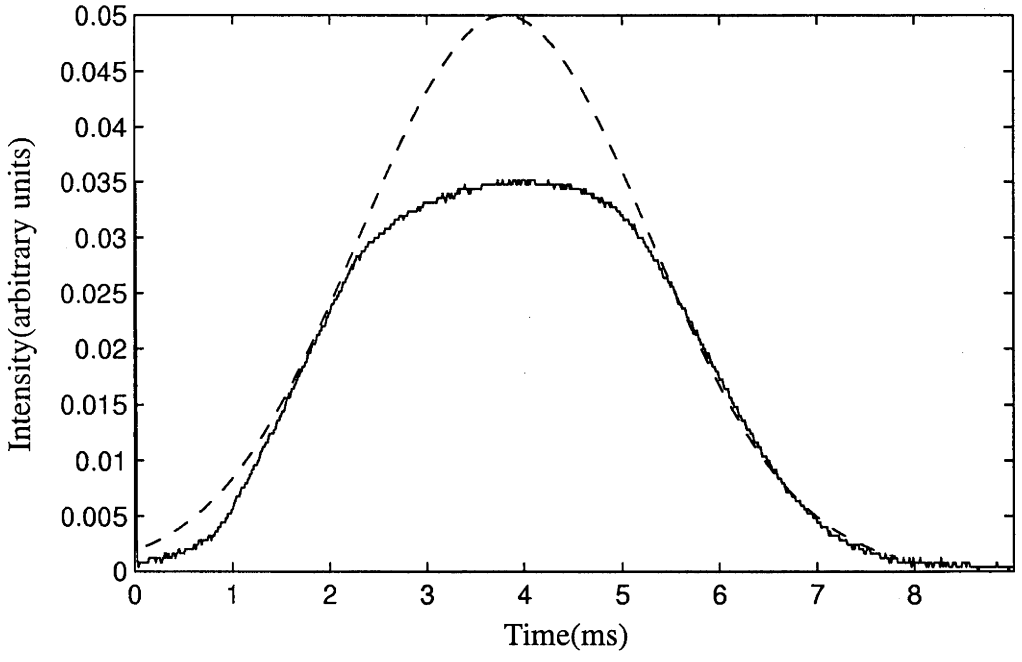

Figure 4.13: *Light intensity for symmetrical illumination and Gaussian model.*
——— *real light source*
– – – *Gaussian model*
The real light source had an approximately symmetric intensity, rising in intensity for 4ms before decreasing with a similar shape for a further 4ms. The Gaussian model is a reasonable approximation for the light, except at maximum intensity where the real light source had a more slowly varying intensity.

$$\frac{d}{dt}(\Delta n(t)) = -\frac{\Delta n(t)}{\tau_{eff}} + G(t)$$

$$= -\frac{\Delta n(t)}{\tau_{eff}} + G_{max}exp\left(\frac{-(t-t_{max})^2}{\tau_{gauss}^2}\right)$$

$$\Delta n(t)) = \frac{\sqrt{\pi}\, G_{max}\tau_{gauss}}{2} erfcx\left(\frac{-(t-t_{max})}{\tau_{gauss}} + \frac{\tau_{gauss}}{2\tau_{eff}}\right) exp\left(\frac{-(t-t_{max})^2}{\tau_{gauss}^2}\right)$$

$$\tau_{qsspc}(t) = \frac{\Delta n(t)}{G(t)} = \frac{\sqrt{\pi}\,\tau_{gauss}}{2} erfcx\left(\frac{-(t-t_{max})}{\tau_{gauss}} + \frac{\tau_{gauss}}{2\tau_{eff}}\right)$$

$$\tau_{qsspc}(t) \approx \tau_{eff}\left[\frac{1}{1-\frac{(t-t_{max})2.\tau_{eff}}{\tau_{gauss}^2}}\right] \quad if \frac{-(t-t_{max})}{\tau_{gauss}} + \frac{\tau_{gauss}}{2\tau_{eff}} is\ large \qquad (4.23)$$

for Gaussian illumination where G_{max} is the maximum generation rate, t_{max} is the time of maximum generation and τ_{gauss} is the 1/e half width of the Gaussian. The final approximation for the QSSPC lifetime is accurate provided the term $\left(\frac{-(t-t_{max})}{\tau_{gauss}} + \frac{\tau_{gauss}}{2\tau_{eff}}\right)$ is large. The error in the approximation was less than 1% for effective lifetimes less than 100μs and illumination times up to double τ_{gauss}.

During Gaussian illumination, equation (4.23) predicts that the QSSPC lifetime will be an underprediction of the effective lifetime as the illumination intensity increases, since the excess carrier concentration lags the illumination increases. As the excess carrier concentration increases, the excess carrier concentration in the wafer is less than would be expected for the equivalent intensity of illumination under steady state conditions. This is due to the response time of the substrate, which is characterised by the effective lifetime. The converse is true during the decrease in excess carrier concentration with the excess carrier concentration greater than expected under steady state, and overprediction of effective lifetime results. The measured lifetimes during the ramp up and ramp down of the light bound the real effective lifetime. The size of the error is directly related to the bulk lifetime and the time from maximum illumination intensity, as expressed in the relation in the brackets on the last line of equation (4.23). Figure 4.14 demonstrates the calculated increased spread in the measured effective lifetimes (as the light intensity increases and decreases) due to increases in substrate effective lifetime.

4.5.2 *Measurements with symmetric illumination*

QSSPC measurements of a variety of samples with different effective lifetimes were made with the symmetric light pulse. Due to differences in the illumination spectrum and uniformity, effective lifetimes measured with the symmetric light pulse were usually slightly greater than with the exponentially decaying light pulse.

Effective lifetime measurements were made on low (0.1Ωcm) and high (0.4Ωcm) lifetime Fz samples. The 0.1Ωcm substrate was poorly passivated with native oxides while the

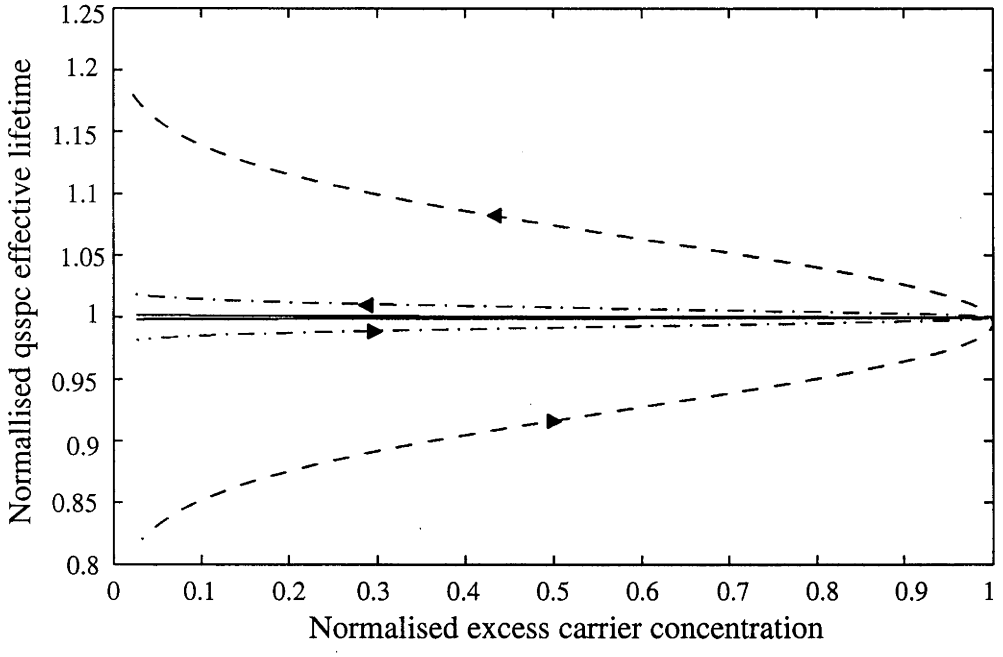

Figure 4.14: *Normalised effective lifetime versus normalised excess carrier concentration with Gaussian light intensity distribution for 1μs, 10μs and 100μs effective lifetimes from equation (4.23).*

— — — 100μs
— · — 10μs
——— 1μs

The arrows indicates the direction of change with time. The half of the curve below one corresponds to the region of increasing illumination with underpredictions of effective lifetime while the top half corresponds to decreasing illumination levels and underpredictions of effective lifetime. The effective lifetime is accurately measured at the point of maximum excess carrier concentration. The spread of the measurements decrease as the illumination approaches maximum and as effective lifetimes decrease.

0.4Ωcm substrate had phosphorus diffused surfaces. The effective lifetime measurements for the symmetric and normal exponentially decaying flash can be seen in figures 4.15 and 4.16, for the 0.1 and 0.4Ωcm substrates respectively. In each case, the behaviour was well explained by the modelled calculations. For the 0.1Ωcm substrate, the effective lifetime was relatively low (9μs). Consequently, the spread in the measured effective lifetimes was a small percentage of the effective lifetime, and the spread increased at low excess carrier concentrations (t further from t_{max} in equation (4.23)).

The 0.4Ωcm Fz substrate displayed a wider spread in measured effective lifetimes, due to the larger effective lifetime (250μs at $2x10^{15}cm^{-3}$). The shape of the symmetric illumination measurements differed slightly from the model, particularly at higher injection levels. Near the maximum injection levels for the symmetric light, the measured lifetimes for the increasing and decreasing illumination finished in a relatively sharp point compared to the model. This was due to the more slowly varying intensity of the real illumination near maximum illumination compared to the great intensity change in the Gaussian model (figure 4.13). The rate of change of the light intensity was less than the Gaussian model, leading to more rapid approach to the real effective lifetime. This was confirmed by modelling the light intensity near maximum illumination with a sine, rather than Gaussian, distribution.

At low light intensities, the measured lifetimes for decreasing light intensity did not mirror the effective lifetimes for increasing intensity. This was due to the injection level dependence of the lifetime below one sun illumination ($\sim 2x10^{15}cm^{-3}$) which can be seen in the measurements with the exponential decaying QSSPC. Consequently, the measured effective lifetime as the light intensity decreased was not as great as it would have been if the effective lifetime was constant.

The Fz samples effective lifetime measured at the maximum injection level with the symmetric pulse were consistently higher than the normal exponentially decaying light, despite the fact that the exponential decay should overpredict the effective lifetime. This was probably due to differences in the relative intensity of the light over the detector and the sample with the different illumination types or to differences in the spectrum of the lamps.

In the extreme where lifetimes were strongly injection level dependent, the lifetimes measured with the symmetric light pulse continued to bound the real effective lifetime, with underprediction of lifetime during the increase in light intensity and overprediction during the decrease. This can be seen for the Cz substrate in figure 4.17, with the measured lifetime with the higher intensity measurement bounding the lower intensity measurement. The normal QSSPC measurement was again slightly higher than the symmetric measurements due to the illumination differences, but demonstrated similar injection level dependence.

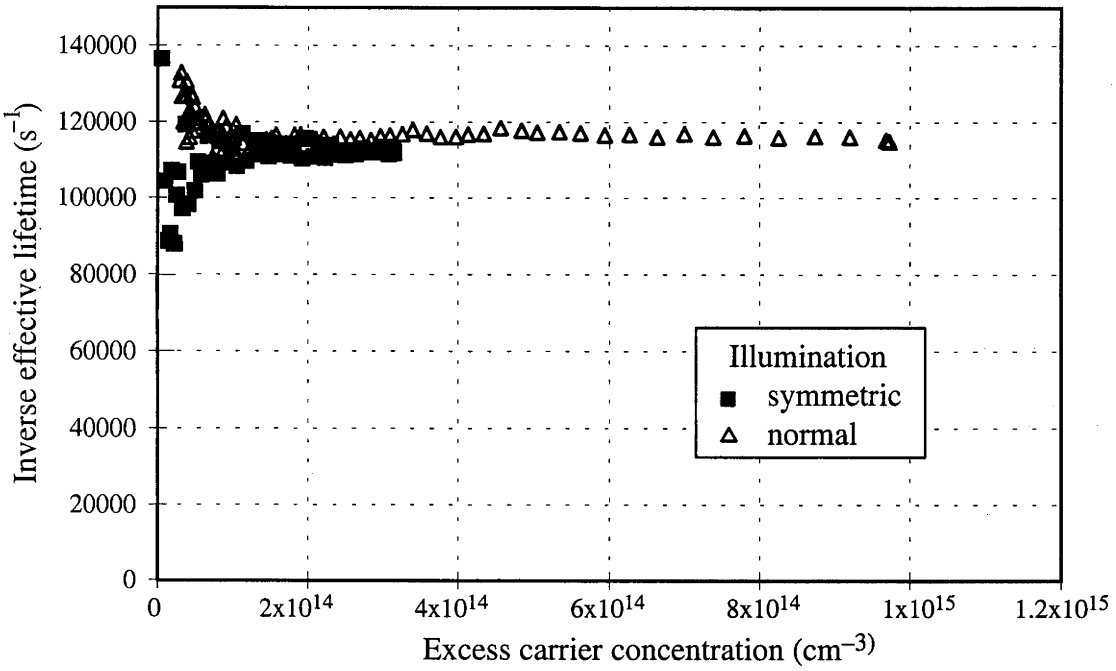

Figure 4.15: *Normal and symmetric QSSPC measurements of 0.1Ωcm Fz substrate, with native oxides on the surface.*
The 0.1Ωcm substrate has a low effective lifetime around 9μs. The spread in the lifetimes with the symmetric illumination was small due to the low effective lifetime, increasing at low illumination levels, as predicted by the model.

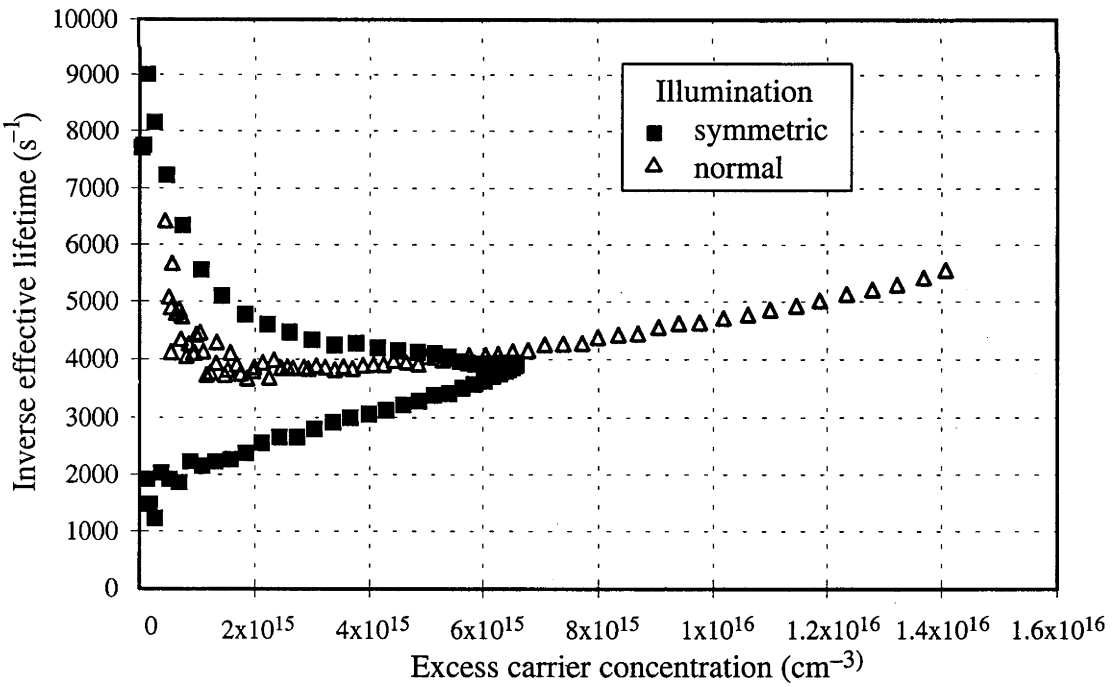

Figure 4.16: *Normal and symmetric QSSPC measurements of 0.4Ωcm Fz substrate, with lightly phosphorus diffused surfaces.*
The effective lifetime of the 0.4Ωcm Fz substrate varied with injection level, decreasing at high injection levels due to emitter recombination, with a maximum effective lifetime of 250μs around one sun illumination ($1.5x10^{15}cm^{-3}$). The high lifetime led to large differences in effective lifetime during increasing and decreasing excess carrier concentration with the symmetric illumination.

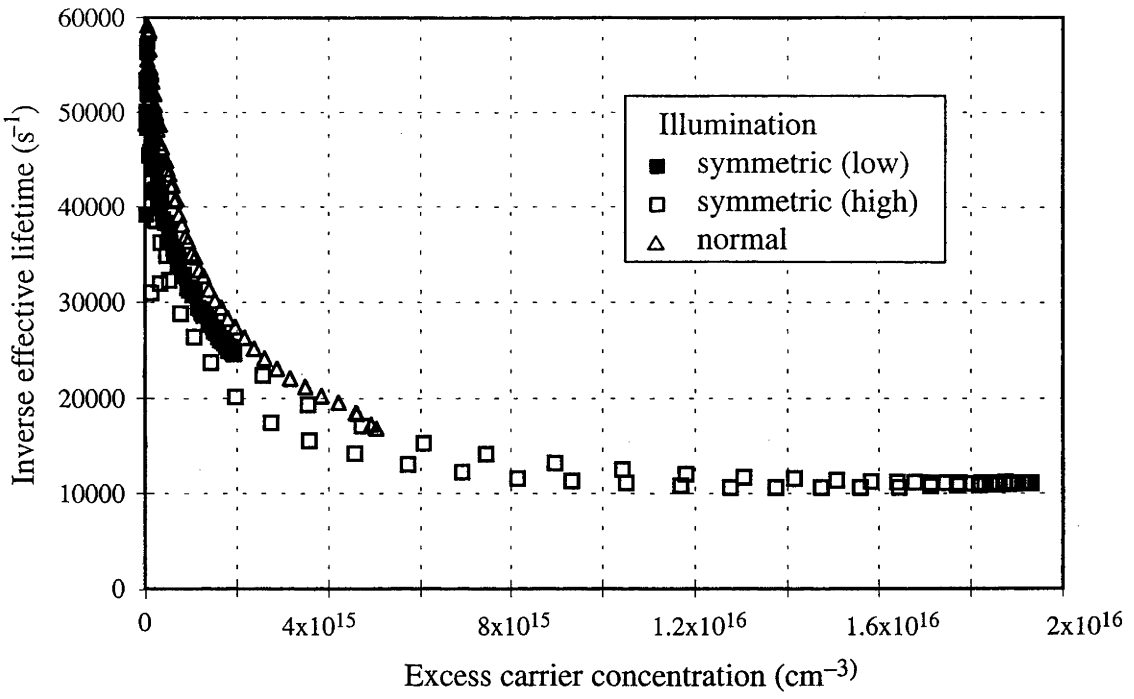

Figure 4.17: *QSSPC measurements of 0.5Ωcm Cz silicon substrate, with phosphorus diffused surfaces.*
The Cz substrate demonstrated a strongly injection level dependent lifetime, increasing with excess carrier concentration.

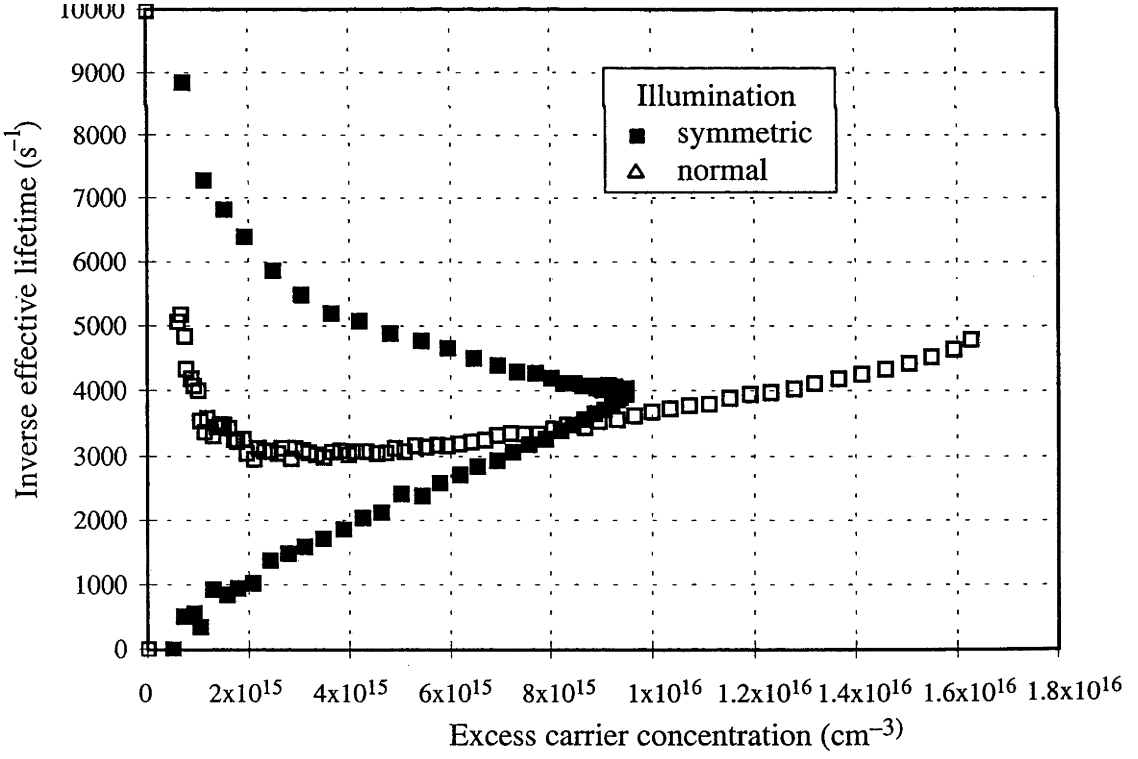

Figure 4.18: *Symmetric and normal QSSPC measurements of high lifetime, gettered 1.5Ωcm multicrystalline silicon substrate with phosphorus diffused surfaces.*
The behaviour of the high lifetime 1.5Ωcm multicrystalline silicon substrate is similar to the 0.4Ωcm Fz substrate (figure 4.16). The long lifetime leads to large variations in lifetime between increasing and decreasing light intensity.

Multicrystalline silicon substrates which were well behaved for normal QSSPC measurements showed behaviour similar to the model (allowing for deviations similar to those outlined above for the 0.4Ωcm Fz substrate). A high lifetime 1.5Ωcm multicrystalline silicon substrate was measured with the symmetric and exponential decaying light (figure 4.18). The behaviour of the multicrystalline substrate was similar to the 0.4Ωcm Fz substrate in figure 4.16.

Interestingly, the symmetric light pulse did not eliminate the trapping effects during the increase in light intensity on substrates where trapping effects was observed with normal QSSPC measurements, such as the 0.5Ωcm substrate in figure 4.19. The effective lifetime measured during the increase in light intensity, closely matched that during the decrease in light intensity.

This observation challenges the earlier hypothesis in section 4.4.2 that the injection level dependence of the effective lifetime at low injection levels was due to transient shallow trapping effects. During the increase in light intensity, the fraction of traps containing electrons should be increasing. Therefore the traps should be acting as a net sink of electrons from the conduction band, leading to an underprediction of the steady state effective lifetime (in addition to the underprediction due to the increase in excess carrier concentration). However, during the rise in light intensity, the effective lifetime remained lower than the effective lifetime at high injection levels, demonstrating the same injection level dependence as during the decrease in light intensity.

4.5.3 *Summary*

QSSPC lifetime measurements using the symmetric light pulse were predicted to bound the steady–state effective lifetime, with underpredictions of effective lifetime during the increase in excess carrier concentration and overpredictions during the decrease in light intensity. This was confirmed for the single crystal and well behaved multicrystalline silicon substrates, with the spread of the bounds decreasing as effective lifetime decreased as predicted by the model.

The symmetric illumination did not produce the expected results for the substrates with the apparent trapping effects at low injection levels. The lifetime during both the increase and decrease in illumination demonstrated the strong increase in effective lifetime as excess carrier concentrations decreased. This challenges the theory that the behaviour was due to transient effects from shallow traps.

4.6 Future investigations of the trapping effects during QSSPC measurements of multicrystalline silicon

The results of the QSSPC measurements with the symmetric light pulse of the substrates with the apparent lifetime improvement at low injection levels, opened questions as to the cause of the lifetime increase. Was the behaviour due to trapping effects during the

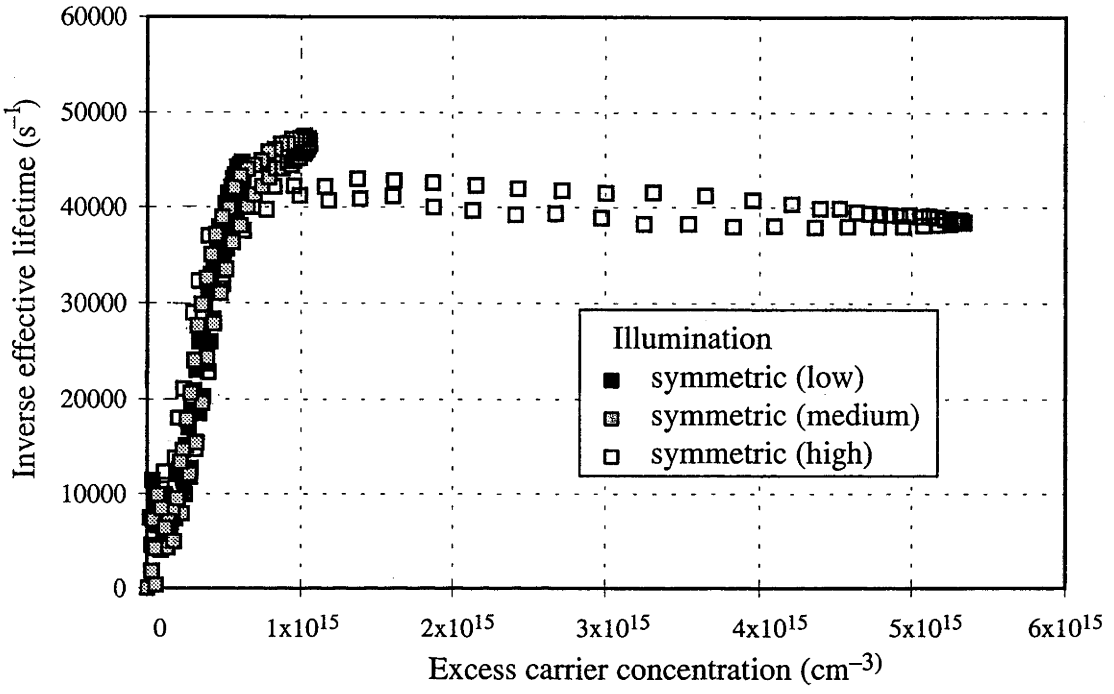

Figure 4.19: *Lifetime measurement with symmetric illumination of 0.5Ωcm multicrystalline silicon substrate with strong trapping.*
The trapping effects commenced at around 10 suns illumination. The use of symmetric illumination was an attempt to reduce or eliminate the effects of trapping from effective lifetime measurements of multicrystalline silicon. Surprisingly, the trapping effects did not disappear during the increase in light intensity with symmetric illumination.

measurement, problems with conductivity measurement on some multicrystalline silicon substrates or genuine recombination behaviour?

The first consideration will be to determine if the behaviour was due to the transient nature of the QSSPC measurement. Since continual illumination leads to heating of the substrate and the conductivity detector, steady–state measurements with a constant light source are not practical. The use of arrays of pulsed light emitting diodes appears to be a better option for producing a brief source of illumination with constant intensity. The pulses need to be sufficiently long that the substrate can approach steady–state during the illumination and spaced sufficiently that the substrate can return to equilibrium when the illumination is switched off. Each pulse would allow measurement of the effective lifetime at one injection level. Varying the intensity of the pulses would allow an injection level dependence to be determined. Development of a suitable LED array and associated circuitry is under way. This may also prove suitable for increasing the range of effective lifetimes (i.e. lifetimes >200μs) which can be accurately measured with QSSPC since this technique can produce pulses enabling the sample to approach steady–state conditions for any substrate with appropriate pulse shapes.

If the behaviour proves not to be due to transient effects, then effective lifetime measurements with different techniques would be appropriate to determine if the lifetime behaviour is genuine, rather than an artefact of the photoconductance measurement technique. If so, the challenge becomes identifying the mechanism producing the strongly injection level dependent behaviour. Otherwise, further investigation of the inductive coupling technique for measuring multicrystalline silicon substrates may be in order.

CHAPTER 5
PROCESSING DEPENDENCE OF THE LIFETIME OF MULTICRYSTALLINE SILICON

5.1 Introduction

Lifetimes in multicrystalline silicon are typically of the order of 10μs or less [13], much lower than that which can be achieved in single crystal silicon. Therefore the diffusion length of the substrate is often of the order of the substrate thickness or less. Consequently the cell parameters are extremely sensitive to changes in bulk lifetime. It is therefore critical to maintain and maximise bulk lifetime during cell processing.

The electronic quality of multicrystalline silicon is affected by the presence of a range of impurities commonly incorporated during crystal growth, such as oxygen, carbon and metallic impurities, and also has increased concentrations of crystallographic defects, such as grain boundaries and dislocations. These can all contribute to decreasing the bulk lifetime.

The lifetime of multicrystalline silicon can be strongly affected by high temperature thermal steps, such as those which occur during solar cell processing, due to changes in the interaction of these impurities and defects within the crystal structure. Some processes can be beneficial to the bulk lifetime, including impurity gettering steps such as phosphorus diffusions and aluminium alloying, while others can lead to lifetime degradation [15]. The impact of these processes depends upon the initial concentration of impurities and defects in the materials and therefore the effects of higher temperature processing can vary greatly between material from different sources.

The nature of the crystal growth can also lead to spatial variation in the electronic quality of the substrates, due to differences in the concentrations of impurities and defects throughout the ingot [13]. This differs strongly from the situation with single crystal silicon where variations in electronic quality between wafers from different regions of the same ingot, or even between ingots, tend to be small.

5.1.1 *Process monitoring with quasi–steady state photoconductance*

Despite the fact that the lifetime of multicrystalline silicon can vary greatly during the process sequence, little work has been published on the topic [101,102]. Studies on the effects of various processing steps on multicrystalline silicon are often conducted separate from the processing sequence [103,104,105] or rely on final cell characteristics to determine the effect of the process step being investigated [106,107,108].

By using a contactless lifetime measurement technique, the lifetime of the substrates can be tracked during the entirety of the process . A number of potential benefits arise from taking this approach. Most importantly, interactions between different processing steps can be observed. Lifetimes can be mapped after each step and related to the final cell lifetime

and cell performance. Substrate to substrate variations can be tracked throughout the sequence.

Quasi–steady state photoconductance is well suited to contactless measurements of multicrystalline silicon [92]. Measurements are made over a relatively large area ($3cm^2$) and produce an area–averaged effective lifetime. The measurement relies on the absolute size of the measured signal, rather than the rate of decay of the signal, so it does not require fast, expensive electronics in the detector or light source to achieve accurate results. Measurements are made over a range of illumination levels, allowing the injection level dependence of the recombination to be determined and different recombination mechanisms and non–ideal behaviour to be identified.

5.1.2 *Multicrystalline silicon source*

The multicrystalline silicon used in all the investigations described here was provided by Eurosolare. Eurosolare multicrystalline silicon is a high quality material produced by directional solidification [13]. This growth technique leads to many of the impurities present in the melt segregating to the top of the ingot during crystallisation. The wafers used in this investigation were all sourced from the central core of the ingot, where contamination from the crucible is small and the growth is well ordered in long columnar grains. Grain sizes are of the order of a few square millimetres to a square centimetre. Eurosolare material has a low oxygen impurity level ($\sim 10^{17}/cm^3$) and has a dislocation density ($5x10^4$–$10^5/cm^2$) which is relatively low for multicrystalline silicon [103].

5.2 Process Monitoring experiments

Substrates were monitored with quasi–steady state photoconductance measurements during a variety of processing sequences and substrate resistivities to determine the effects of different processes on material lifetimes.

5.2.1 *High Temperature versus Low Temperature Processing*

A concern when processing multicrystalline silicon substrates is the effect of high temperatures on the bulk lifetime. The traditional approach to processing multicrystalline (and also Cz) silicon has relied on relatively low temperatures (<950°C) during cell processing [16,18,106]. This is in direct contrast with high efficiency Fz single crystal silicon solar cell processing where temperatures greater than 1000°C are routinely used during oxidations.

The effects of high temperature (>1000°C) oxidations during processing versus moderate temperature (900°C) oxidations were investigated here for a range of substrate resistivities following a simple cell processing sequence.

5.2.1.1 *Experiment*

0.2Ωcm, 1Ωcm and 1.5Ωcm wafers (100mm x 100m) from Eurosolare were diced into smaller substrates 50mm x 33mm on each of which two $4cm^2$ cells were manufactured.

Cells were divided into two processing streams. A 1Ωcm Fz wafers was included as a control in each stream. Substrates in one stream (MP8) followed a sequence typical for high efficiency single crystal silicon solar cells. A masking oxide was grown at 1100°C in a TCA/oxygen ambient. The 4cm^2 emitter area was defined through the masking oxide using photolithography, before emitter formation at 840°C. The masking oxide and the phosphorus glass were removed and a passivating oxide was grown at 1000°C for 2 hours with TCA in oxygen followed by a 30 minute anneal in argon. The 110nm passivating oxide also acted as a crude antireflection coating.

The second batch (MP7) was processed using steam oxidations at 900°C to replace the higher temperature oxidations. The steam was provided by bubbling 100L/hr oxygen through a bubbler containing deionised water at 85°C. The masking oxide was grown for 2 hours while the passivating oxide was grown for 100 minutes, followed by a 30 minute anneal in argon at 900°C. The final steam oxidation resulted in a layer which was too thick on the phosphorus diffused emitter and was etched back in dilute HF to the optimal oxide thickness (110nm) after metallisation.

Measurements of the effective lifetime of the substrates were made after each processing step. Substrates were annealed in forming gas (5%H_2/Ar) at 400°C for 20 minutes to improve the passivation quality of the surface oxides.

Front metallisation consisted of thermally evaporated Cr/Pd with photolithographic liftoff followed by silver electroplating, while the oxide was removed from the entire rear of the multicrystalline cells and contacted with aluminium. The Fz cells had 1 or 0.4mm holes opened at 4mm spacing through the rear oxide to reduce rear recombination and metallised with 10nm Ga/25nm Pd liftoff followed by full area evaporation of 1μm of aluminium. Cells were then annealed in forming gas before measurement of current–voltage characteristics.

5.2.1.2 *Results*

The results of the lifetime measurements for the 1.5Ωcm substrates are presented in figure 5.1. These substrates demonstrated the highest lifetime of the three substrates with several samples having lifetimes greater than 50μs after the phosphorus diffusion. The lower temperature processing sequence produced lifetimes which were approximately double those of the higher temperature sequence. Lifetimes were observed to increase dramatically after phosphorus diffusion, followed by a decrease similar in magnitude after the final oxidation.

The cell characteristics exhibited a strong relationship with the final lifetime measured before metallisation. Figure 5.2 shows that voltage and current increased as the effective lifetime increased. The voltage, current and efficiency of the best low temperature cell are included in table 5.1 This substrate had a final measured lifetime of 32μs, compared to 64μs after the phosphorus diffusion. The best high temperature cell was 0.6% (absolute)

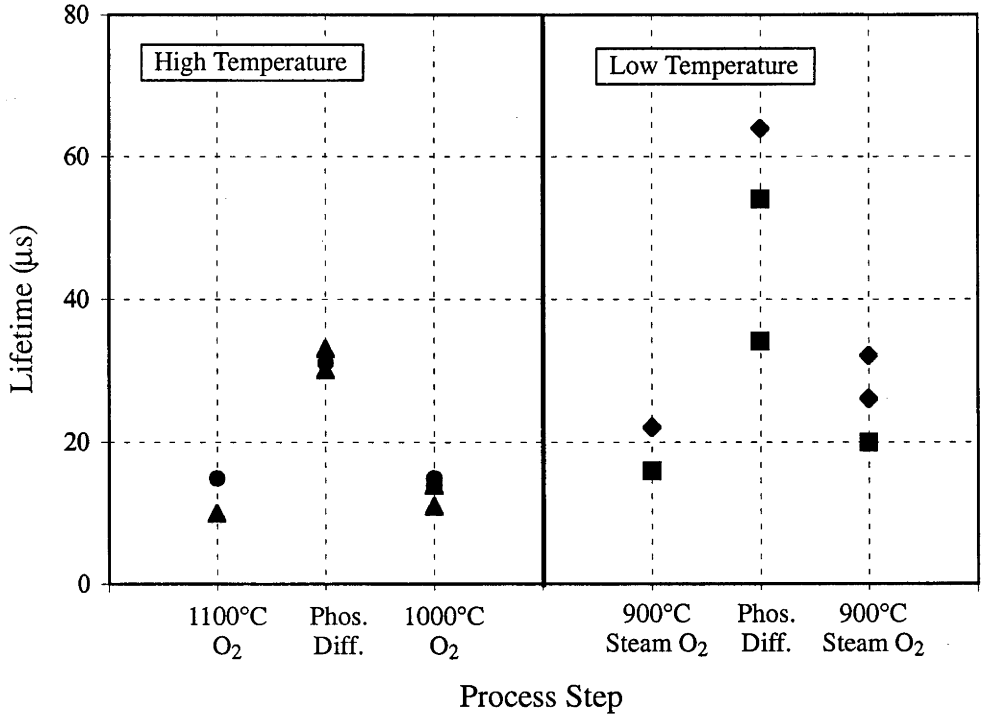

Figure 5.1: *Measured effective lifetimes of 1.5Ωcm substrates during comparison of high and low temperatures during processing.*
Each symbol represents a different sample. There are two symbols (sometimes overlapped on the graph) for each sample after the initial oxidation, since there were two cells on each substrate. The effective lifetime increased during the phosphorus diffusion, and degraded during the subsequent oxidation. Better lifetimes were demonstrated with low temperature processing.

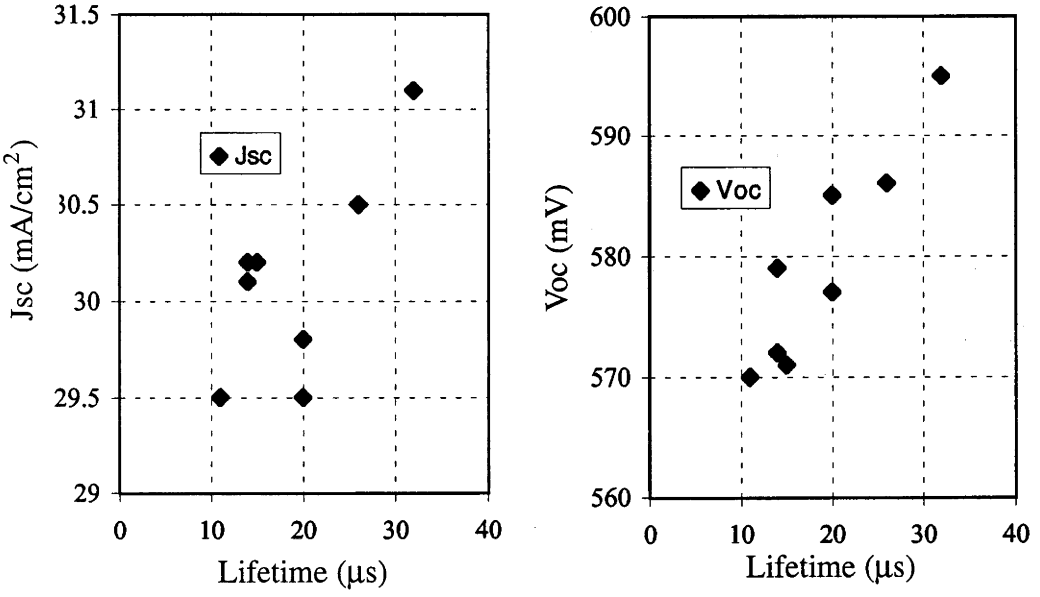

Figure 5.2: *Open circuit voltage and short circuit current as a function of final measured effective lifetimes for 1.5Ωcm substrates during comparison of high and low temperature processing.*
Cell characteristics were observed to improve with increased measured lifetime.

less efficient with an efficiency of 13.8% (V_{oc} 578mV, J_{sc} 30.1mA/cm^2 and FF of 79%). Another cell had similar current and voltage, but dropped to 13.5% due to a lower FF (77%). These cells both had final lifetimes of 14μs, down from 33μs and 31μs respectively after the phosphorus diffusion.

The behaviour of the thin 1Ωcm (220μm) and the thicker (350μm) 0.2Ωcm substrates was similar during high temperature and low temperature processing. The effective lifetimes after each processing step are displayed in figures 5.3 and 5.4. The lifetime of the 1Ωcm substrates improved by approximately 50% during the phosphorus diffusion. The effective lifetime then returned to a similar lifetime during the second oxidation to that measured after the first oxidation . The 0.2Ωcm substrates demonstrated similar improvements after the phosphorous diffusion, but the degradation in lifetime after the final oxidation was variable, sometimes degrading to the lifetime after the initial oxidation while other substrates showed no degradation during the oxidation.

Substrate	Final lifetime (before metal)	Process	V_{oc}(mV)	J_{sc}(mA/cm^2)	Efficiency(%)
1.5Ωcm	32μs	Low Temp	595	31.1	14.4
1Ωcm	20μs	High Temp	592	30.0	14.0
0.2Ωcm	8μs	Low Temp	630	29.0	13.9

Table 5.1: *Best cell efficiencies during comparison of high temperature and low temperature processing.*

The efficiency of the low temperature processed cells was clearly superior on the 1.5Ωcm substrates. There was little difference between high and low temperature processing for the 1 Ωcm and 0.2Ωcm cells.

Cell voltage and current versus the final measured lifetime for the 220μm 1Ωcm substrates are presented in figure 5.5. The 1Ωcm cell characteristics also demonstrated trends of improving cell performance as a function of increasing effective lifetime. The best 1Ωcm cell performance is shown in table 5.1 This corresponded to the cell in figure 5.3 which had the highest final effective lifetime. The low temperature processed substrate which exhibited similarly high lifetime after the initial oxidation broke before the phosphorus diffusion. The lower lifetime cells had efficiencies around 13%.

Breakages during the final metallisation restricted the range of lifetimes in the completed 0.2Ωcm cells to between 6μs and 8μs. The range was too small to provide useful information on the relationship between cell characteristics and effective lifetime. The completed 0.2Ωcm cells had good voltages: all cells produced open circuit voltages greater than 620mV, with the best 635mV. The best cell was processed at low temperature, with the cell performance summarised in table 5.1 This cell had a high fill factor of 79%. The fill factors on the 0.2Ωcm cells were often poor due to the presence of shunts. The best cell processed at high temperature had better voltage and current (V_{oc} 635mV, J_{sc} 28.5mA/cm^2) but was restricted by lower fill factor (0.75) and produced an efficiency of 13.5%.

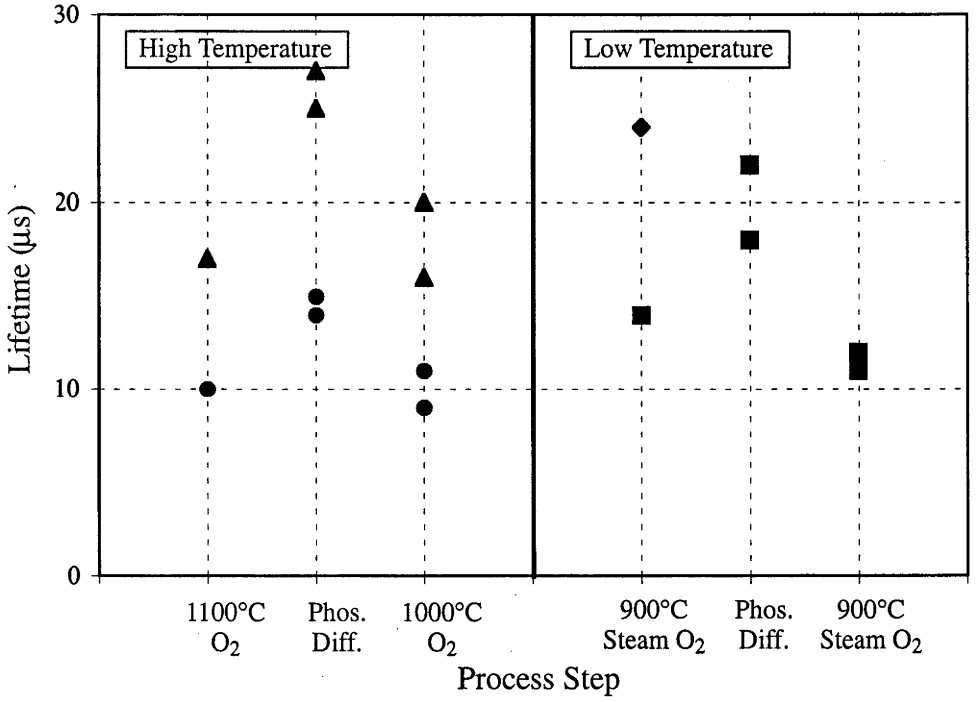

Figure 5.3: *Measured effective lifetimes for 1Ωcm substrates after each furnace step during comparison of high and low temperature processing.*
Each sample is represented by a different symbol, with two symbols for each of the two cells on the sample after the phosphorus diffusion. The effective lifetime increased after the phosphorus diffusion, degrading close to original levels after the second oxidation. Similar behaviour was observed for high and low temperature processing.

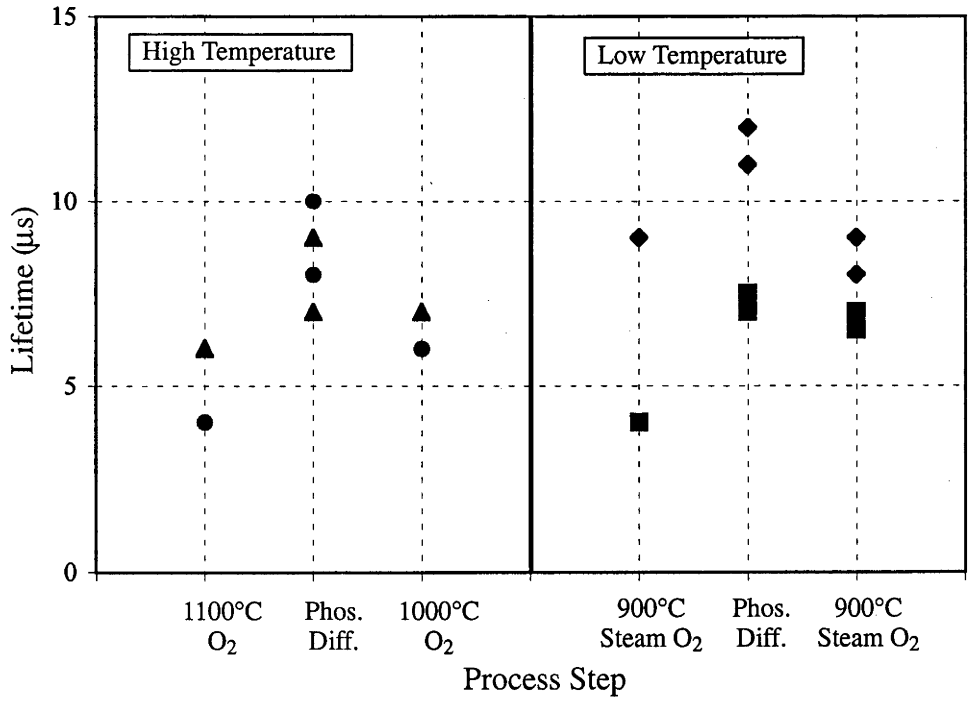

Figure 5.4: *Effective lifetimes for 0.2Ωcm substrates comparing high and low temperatures during processing.*

Each sample is represented by a different symbol, with two symbols for each of the two cells after the phosphorus diffusion. Behaviour was similar to that observed for 1Ωcm substrates except that lifetimes often degraded less during the final oxidation.

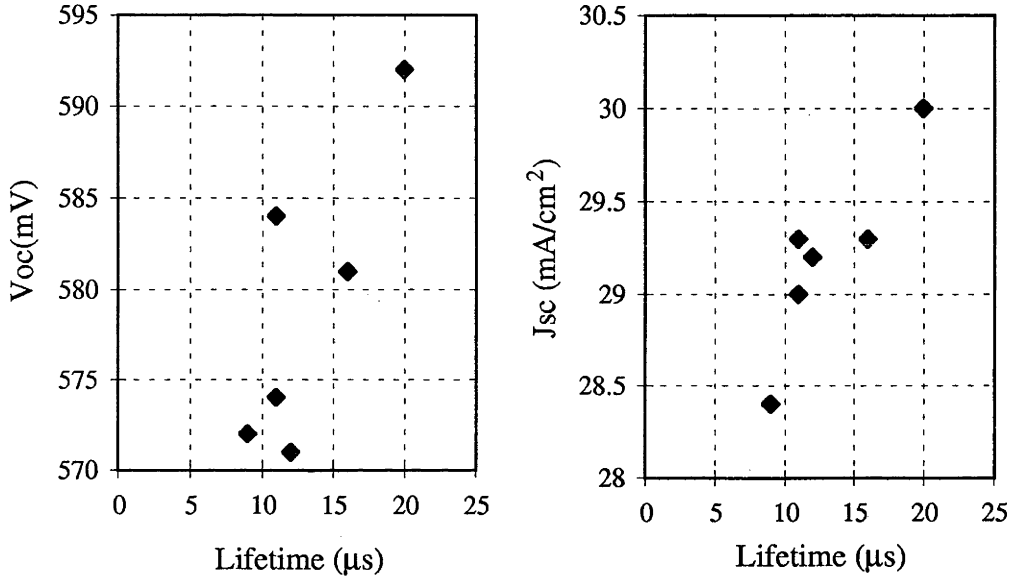

Figure 5.5: *Short circuit current and open circuit voltage as a function of final measured effective lifetimes for 1Ωcm substrates during comparison of high and low temperature processing.*
Cell characteristics followed a general trend of improvement with increased measured lifetime.

The 1Ωcm Fz substrates included in the processing streams had effective lifetimes greater than 100μs after each processing step in both the high temperature and low temperature processing streams. The effective lifetime increased to 170–180μs after the phosphorus diffusion. The cells which received the high temperature oxidation increased in effective lifetime to 400μs, while the cells which received the steam oxidation remained unaltered (170μs). The cells with 0.4mm contacts on 4mm spacing both produced voltages of 670mV and the two cells exhibited currents of 33.5 and 32.9mA/cm^2 for high and low temperature processing respectively. The cells with 1mm on 4mm contacts had 10mV lower voltages and currents of 32.2 and 32.1mA/cm^2 for high and low temperature processing respectively. Fill factors were poor due to series resistance problems with the Ga/Pd rear contacts. Fill factors were 0.74–0.76 on the 1mm on 4mm and 0.71–0.73 on the 0.4mm on 4mm rear contacted cells. This restricted Fz cell efficiencies to between 15.4 and 16.2%. More typical PERC fill factors around 80% would have produced efficiencies of 18.0% on the better Fz cells.

5.2.1.3 *Discussion*

The multicrystalline substrates displayed a consistent pattern of improvements in the effective lifetime after the phosphorous diffusion and subsequent reduction in effective lifetime after the final oxidation.

The improvements in effective lifetime observed after the phosphorus diffusion can best be attributed to phosphorous gettering of impurities from the multicrystalline samples, rather than simply improvements in the front surface passivation from the phosphorus diffusion. Mobile impurities diffusing randomly in the silicon bulk are more soluble in the phosphorus diffused silicon and will collect in the emitter [109]. The emitter is less sensitive to impurities and their associated lifetime degradation than the bulk, since it is thinner and already limited by Auger recombination.

Two pieces of evidence support this suggest that the improvements in effective lifetime were the results of improvements in bulk lifetime due to phosphorus gettering in the multicrystalline samples. The first is the comparison of results for the Fz and multicrystalline silicon substrates. The multicrystalline samples were all limited to less than 20μs after the initial oxidation. If surface recombination at the silicon/oxide interface was the dominant recombination mechanism in the multicrystalline silicon, then the lifetime of the Fz sample would be expected to be similarly limited, especially given the reduced thickness of the Fz substrates (which was 270μm compared with 350μm for the 0.2 and 1.5Ωcm multicrystalline substrates). However, the Fz samples had substantially higher effective lifetimes (>100μs). Measurements of oxidised Fz and multicrystalline silicon silicon samples (presented in section 6.7) indicated that surface recombination velocities are similarly low on Fz and multicrystalline silicon. This indicated that bulk recombination was limiting the effective lifetimes.

The second piece of evidence supporting the above conclusion was the degradation in effective lifetimes after the second oxidation. The quality of the surface passivation is expected to remain the same at the rear (same oxidation) while the quality of the passivation on the emitter should be improved. This was the case for the Fz substrates after the final oxidation, supporting the theory that they were limited by the quality of the surface passivation. In contrast, the effective lifetime of the multicrystalline substrates decreased after the oxidation despite the expected improvement in surface passivation quality, indicating that the multicrystalline substrates were limited by bulk processes.

This degradation of lifetimes after the second oxidation to levels closer to the lifetimes after the first oxidation indicated that impurities gettered during the phosphorous diffusion were released back into the bulk during the subsequent oxidation. This degraded the bulk lifetime, decreasing the measured effective lifetime.

Gee *et al.* [110] observed similar behaviour in Cz silicon by extracting diffusion lengths from internal quantum efficiency measurements. Cz samples were observed to decrease in lifetime after post–phosphorus diffusion oxidations. The decrease in lifetime in the post–diffusion oxidation was attributed by these authors to an increase in Fe–B pairs. The increase in impurity concentration was attributed to either redistribution of the previously gettered Fe from the emitter, contamination during the oxidation or dissolution of iron precipitate from the bulk. The second option (contamination) can be discounted in our experiments due to the high lifetimes maintained in the Fz samples.

This behaviour of the multicrystalline silicon during the phosphorus diffusion and subsequent oxidation was recognised due to the use of process monitoring. Without measuring the lifetime during the processing sequence, the only information which would be extracted would be the final lifetime (via cell or substrate measurement). The gettering behaviour and subsequent lifetime degradation could not have been observed.

The final measurements of effective lifetime provided useful predictions of the relative performance of the multicrystalline silicon cells. Figures 5.2 and 5.5 illustrate that both the open circuit voltage and the short circuit current of the 1.5Ωcm and 1Ωcm substrates increased as the final effective lifetime improved. The relative performance of the cells could therefore be predicted before metallisation.

Despite the successful qualitative prediction of relative cell behaviour with the final measured effective lifetimes, the effective lifetimes measured with QSSPC after the final oxidation did not accurately predict cell voltage. Cell voltages were substantially lower (25–30mV). Cell performance was modelled with and without rear metallisation using PC–1D with bulk lifetimes similar to the better measured final effective lifetimes to evaluate the effect of rear surface recombination. The results are summarised in table 5.2.

resistivity	thickness	τ_{bulk}	no rear metallisation			full rear metallisation		
			τ_{eff}	V_{oc}	J_{sc}	τ_{eff}	V_{oc}	J_{sc}
1.5Ωcm	350μm	30μs	30μs	622mV	32.9	14μs	611mV	32.0
1Ωcm	220μm	20μs	20μs	630mV	32.4	7μs	614mV	31.0

Table 5.2: *Effect of rear metallisation on cell effective lifetime modelled with PC–1D.*

The presence of the rear metallisation led to a substantial decrease in effective lifetime. The effective lifetime of the thicker 1.5Ωcm substrates was halved while the effective lifetime of the thinner 1Ωcm substrate was decreased by 65%. There was a corresponding decrease in cell voltage and current.

Despite the fairly low lifetimes of the substrates, the rear metallisation was contributing significantly to the total recombination in the cells. The modelled effective lifetime decreased substantially in both substrates with full rear metallisation due to the increased recombination at the rear surface. The cell diffusion length approached the substrate thickness, so carriers could diffuse from the junction to the rear and recombine. The lifetime after the oxidation provided useful qualitative information because the subsequent metallisation was similar on the cells (which it was in this case) and bulk recombination was still a significant contributor to total recombination at these lifetimes. However, more accurate predictions of cell behaviour would have required a more complete picture of cell recombination. Therefore, the effective lifetime after the rear metallisation would be more useful in predicting the cell behaviour. Measurements of effective lifetime after metallisation were used in the work described in chapter 6 to determine the effect of metallisation on reduced rear contact and rear locally diffused cells.

5.2.1.4 *Conclusions*

Process monitoring with QSSPC measurements proved to be a useful tool for examining the behaviour of the multicrystalline substrates during high and low temperature processing. This method allowed the gettering behaviour of the phosphorus diffusion and the subsequent lifetime degradation to be observed. This behaviour would not have been recognised without process monitoring. The effective lifetimes after the final oxidation provided qualitative prediction of the relative cell performances.

The 1.5Ωcm substrates benefited from low temperature processing, with higher cell efficiencies achieved with processing at 900°C. This was predicted by the results from the process monitoring, during which substantially higher effective lifetimes were measured in substrates subjected to low temperature processing. The more heavily doped 0.2Ωcm and 1Ωcm substrates were less sensitive to temperature, producing similar lifetimes and cell performance regardless of the processing temperature. Cell efficiencies peaked around 14% with the simple cell design.

5.3 Thin passivating oxides

Thick passivating oxides are a poor choice for controlling reflection from a silicon surface in air and offer no reflection benefit if the cells are encapsulated under glass. The analysis in section 2.2.4.3 showed that better reflection control should be achieved with very thin passivating oxides (<20nm), covered with a high refractive index coating (~2.3) such as titanium dioxide, whether encapsulated under glass or with a second antireflection coating.

The lifetime measurements in the previous section suggest that higher lifetimes might be achieved if the final passivating oxide growth could be avoided, since cell lifetimes degraded significantly during the final oxidation. It was therefore desirable to investigate the potential for avoiding the lifetime degradation and improving cell efficiency by retaining the phosphorous glass from the phosphorous diffusion rather than growing thin oxides.

5.3.1 *Experiment*

Two 0.2Ωcm and 1.5Ωcm multicrystalline silicon and 0.4Ωcm Fz substrates were processed. Processing followed the initial sequence described in section 5.2.1.1. A masking oxide was grown in steam at 900°C for 2 hours, followed by emitter formation from a solid source at 840°C for 20 minutes through two 2x2cm^2 areas opened through the masking oxide. One substrate from each pair then had the phosphorus glass removed, retaining the thick rear oxide, and was then oxidised for 40 minutes at 900°C to produce a thin passivating oxide on the emitter. This was followed by a 2hour drive–in at 1000°C in argon to anneal the oxidation and increase the depth of the phosphorus emitter. The second substrate in the pair had the phosphorus glass retained and did not receive the 1000°C anneal. Lifetimes were measured with QSSPC after the phosphorus diffusion and the oxidations.

Cells were then metallised using Cr/Pd liftoff followed by Ag electroplating on the front. The rear contacts were aluminium through 0.6/2mm holes in the rear oxide for the 1.5Ωcm and 0.4Ωcm cells, while the 0.2Ωcm substrates had 100% of the rear contacted with aluminium.

5.3.2 *Results*

Lifetime measurements for the 1.5Ωcm substrates demonstrated the same trends as were observed in the comparisons of high and low temperature processing. The effective lifetime improved in both substrates from 12–17μs to 28–42μs during the phosphorus diffusion. The substrate selected for the thin oxide/drive–in decreased in effective lifetime to the levels observed after the initial oxidation (15–16μs). The cells which had not received the second oxidation had significantly higher effective lifetimes, voltages and currents. The cells with the phosphorus glass retained had voltages of 596mV and 586mV, despite the lack of an AR coating, and efficiencies of 11.6% and 11.0%. Addition of a TiO_2

AR coating improved the efficiencies of the better cell to 15.8%, improving the voltage further to 606mV. The cells with the thin oxide performed worse, with an efficiency of 10.2% and 10.0% (without AR coating) and open circuit voltage of 565mV and 560mV.

The 0.4Ωcm Fz substrates demonstrated different behaviour. The effective lifetime measurements for these substrates are compiled in figure 5.6. The lifetime after the initial oxidation was less than 70μs (injection level dependent, decreasing at lower carrier concentrations). This *decreased* during the phosphorus diffusion to less than 50–60μs (though demonstrating weaker injection level dependence). The substrate which had the thin oxide grown on the emitter had an inverse effective lifetime which was linear with injection level with an intercept of 190μs and linear slope corresponding to a J_0 of $3x10^{-14}A/cm^2$. The efficiency of the cells with the thin oxide were 13.8% and 14.0% with open circuit voltages of 668 and 670mV. The cells which were not oxidised had an efficiency of 12.7 and 12.8% with open circuit voltages of 630mV and 628mV.

Difficulties in measuring the low resistivity substrates (due to the small signal with the original QSSPC equipment and high substrate conductivity) prevented useful lifetime information being extracted from measurements of the 0.2Ωcm substrates after the oxidations. The wafer with the thin oxide proved to have the better performance, with open circuit voltages of 632mV and 617mV and an efficiency of 11.2% and 10.5%. The best cell improved further with a TiO_2 AR coating to an open circuit voltage of 639mV and an efficiency of 15.3%, with current improving from $22.5mA/cm^2$ to $30.3mA/cm^2$ (34.7%). The cells which did not receive the second oxidation had efficiencies of 9.3 and 8.7% (low due to poor fill factors), with open circuit voltages of 596 and 594mV. The worst of the 0.2Ωcm cells had a 'soft' fill factor, which can be seen in figure 5.7. This corresponded to the substrate which had a strongly injection level dependent lifetime after the phosphorus diffusion (figure 5.8), in contrast to the other 0.2Ωcm substrates where lifetimes typically varied little with injection level.

5.3.3 *Discussion*

The advantages of eliminating the second oxidation step were immediately apparent on the 1.5Ωcm substrates. The changed process demonstrated higher voltage than any of the 1.5Ωcm cells in the previous section (with the thicker passivating oxide) despite the lower current with the thin oxide (without AR coating). This can be directly attributed to the improved final effective lifetime (>40μs) which was maintained by avoiding the final oxidation. These lifetimes were greater than the final lifetime of the best cells in the previous section, but on the lower end of lifetime range after the phosphorus diffusion (30–70μs). The cell which received the thin oxide/drive–in had substantially lower final lifetime due to the final oxidation (despite higher lifetime after the phosphorus diffusion) and, correspondingly, the cells had 25mV lower open circuit voltage.

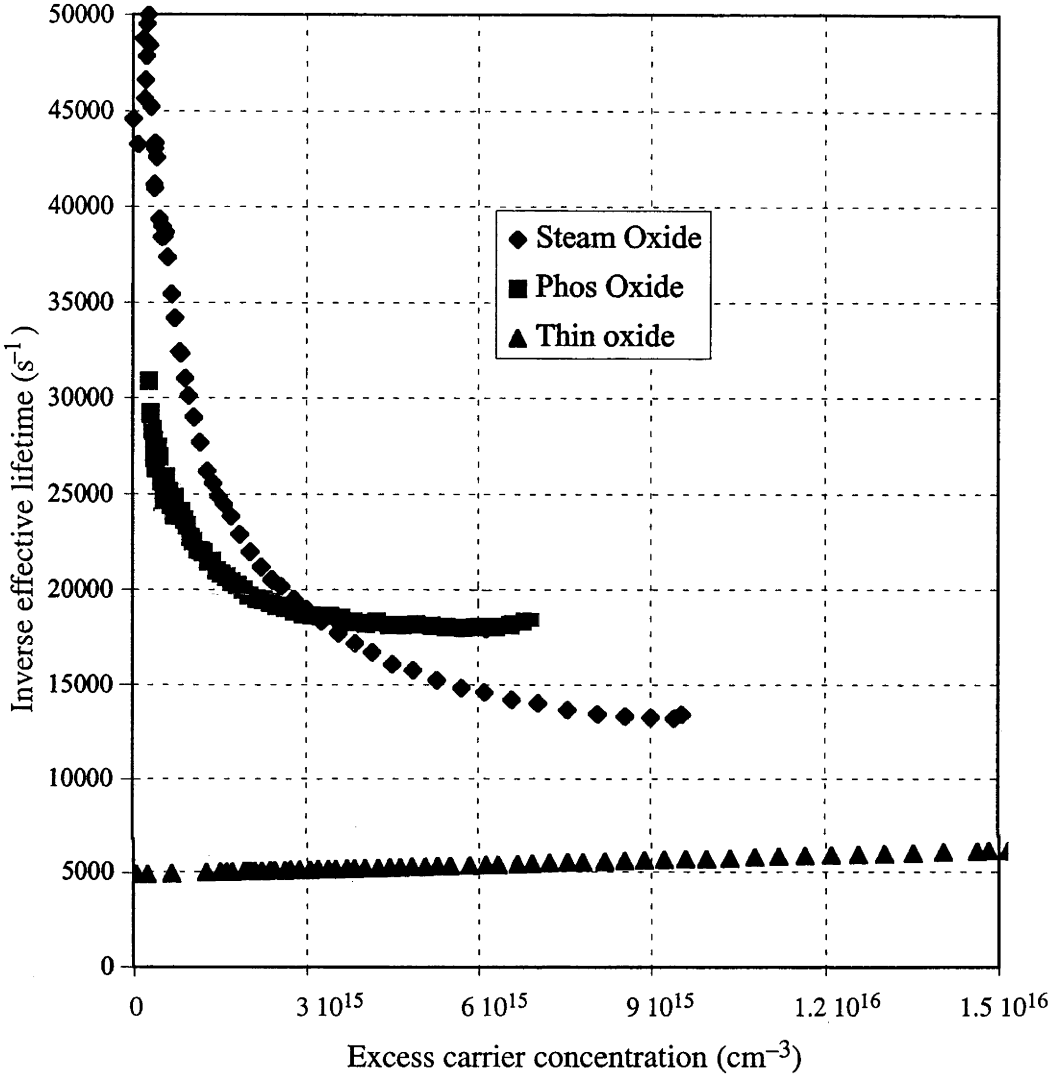

Figure 5.6: *Measured effective lifetime of the 0.4Ωcm Fz sample after each processing step during thin oxide processing.*
The Fz sample was strongly affected by surface recombination. The steam oxide had a strong injection level dependence, decreasing from 460cm/s at $10^{15}cm^{-3}$ to 180cm/s at $10^{16}cm^{-3}$. The phosphorus diffusion limited the effect of injection level dependence to the rear oxidised surface. The dark saturation current of the emitter with phosphorus glass ($>1.2x10^{-13}A/cm^2$) decreased recombination at lower injection levels and increased it at higher injection levels. The growth of the thin oxide led to a dramatic decrease in total recombination, decreasing the emitter saturation current to $3x10^{-14}A/cm^2$.

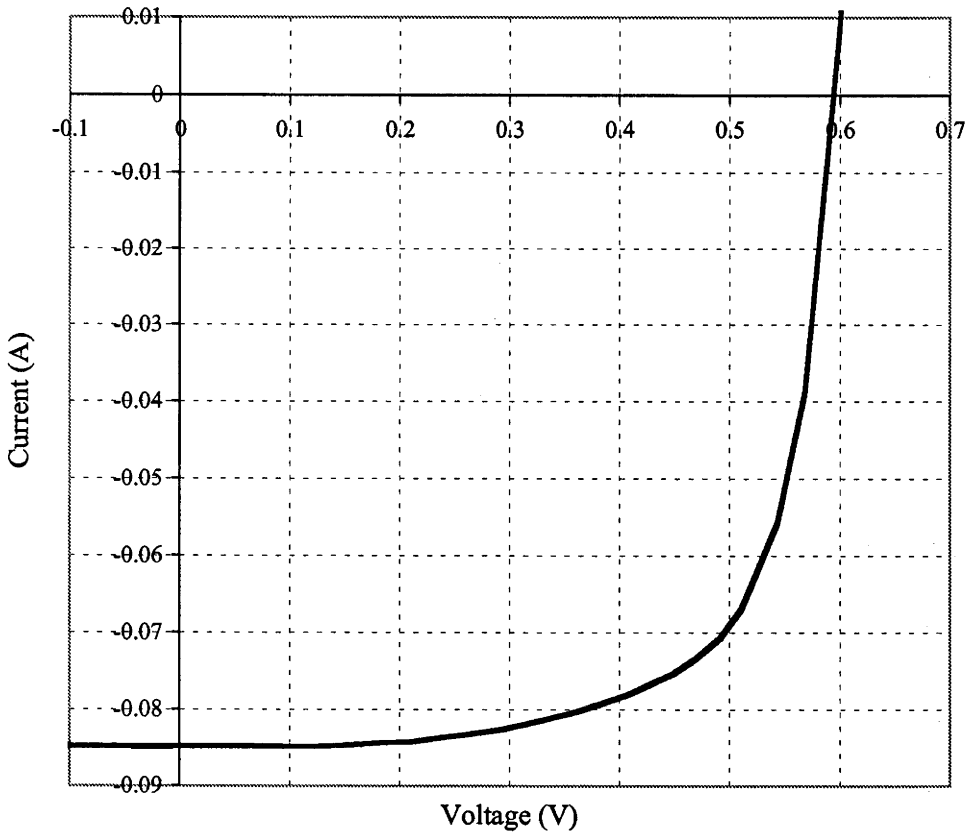

Figure 5.7: *I–V curve of the worse 0.2Ωcm substrate with thin oxide. The cell demonstrated a poor fill factor (0.69) despite good shunt and series resistances.*

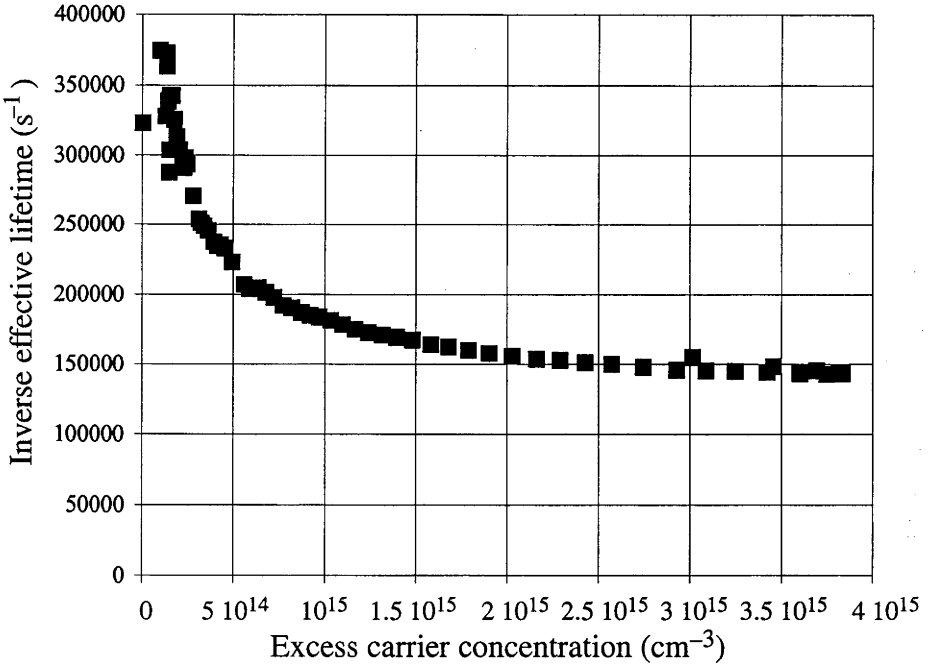

Figure 5.8: *Injection level dependent lifetime of the worse 0.2Ωcm substrate with the 'soft' fill factor.*

The cell with the 'soft' fill factor, had a strongly injection level dependent lifetime after the phosphorus diffusion, unlike the other substrates. The light intensity was much greater than one sun (5–50suns) to increase the signal strength.

The 0.4Ωcm Fz wafers were observed to have the opposite behaviour to the 1.5Ωcm substrates with the substrate which received the thin oxidation proving more efficient than the cells which received only the phosphorus diffusion. This was expected from the lifetime results where the lifetime after the thin oxidation improving to 190μs, compared to 50μs observed after the phosphorus diffusion.

The lifetime measurements indicated that the Fz samples were strongly influenced by surface recombination (figure 5.6). After the initial oxidation, the effective lifetime was strongly injection level dependent, varying from 70μs at $10^{16}/cm^3$ carrier concentration down to 33μs at $10^{15}/cm^3$. This corresponds to an oxide surface recombination velocity varying from around 180cm/s at $10^{16}/cm^3$ to 460cm/s at $10^{15}/cm^3$ (assuming a bulk lifetime around 250μs). This is similar to the injection level dependent behaviour observed for dry oxidised 0.5Ωcm Fz substrates by Glunz *et al* [90], except at roughly double the recombination velocity. The higher recombination rate may be due to the poorer passivation provided by a non–annealed steam oxide. After the phosphorus diffusion, the lifetime decreased at high injection levels to around 55μs at $10^{16}cm^{-3}$ but increased at lower injection levels. Qualitatively, this indicated that the effective surface recombination velocity of the emitter fell between the values of the oxide recombination velocities at 10^{15} and 10^{16} if the bulk lifetime didn't change or that the bulk lifetime improved with the phosphorus diffusion with the surface recombination due to the emitter was correspondingly higher. The J_0 of the emitter was therefore more than $1.2x10^{-13}Acm^{-2}$. After the thin oxidation/drive–in, the measured emitter saturation current was $3x10^{-14}Acm^{-2}$ (equivalent to a surface recombination velocity of 75cm/s at $\Delta n=0$). The behaviour of the Fz substrate was dominated by recombination at the surfaces, rather than the bulk lifetime, with the improved quality of the thin oxide emitter passivation combined with the deeper emitter to reduce emitter recombination (compared to the phosphorus glass from the solid source diffusion).

The evidence that the 0.4Ωcm substrates were limited by surface recombination points to the 1.5Ωcm substrates being limited primarily by the bulk lifetime, since the lifetimes decreased during the final oxidation, when the surface passivation improved. Lifetimes were substantially lower than would be expected from the surface passivation quality indicated by Fz substrates, even allowing for the reduced substrate doping. The substrate behaviour also fitted with the hypothesis that impurities are controlling the lifetime in the 1.5Ωcm samples with the phosphorus diffusion gettering impurities which were released during the subsequent oxidation/drive–in.

Interestingly, the 0.2Ωcm substrates demonstrate similar behaviour to the 0.4Ωcm substrates, with the cells with the thin oxide outperforming the cells not oxidised. Little difference was expected in the behaviour of the 0.2Ωcm substrates, with little or no degradation in effective lifetime observed during the oxidation in the comparisons of high

and low temperature processing (see figure 5.4). Unfortunately, lifetimes could not be extracted from the final measurements of the samples. After the phosphorus diffusion, the substrate which was not re–oxidised demonstrated non–ideal recombination with the effective lifetime decreasing at lower injection levels, unlike the samples with the thin oxide (figure 5.8). The completed cell also demonstrated non–ideal behaviour with a 'soft' fill factor and low voltage despite good series and shunt resistances (figure 5.7). Therefore the poor result in that substrate may be a reflection on the recombination behaviour in that substrate, rather than the cell process. Attempts were made in later investigations to compare substrates from adjacent wafers in the ingot when using small sample groups to minimise the effects of substrate to substrate variations.

The cell with the thin oxide demonstrated an open–circuit voltage of 639mV with the addition of the AR coating. The excellent voltage is a direct consequence of the relatively heavily doped ($10^{17}cm^{-3}$) substrate, with low bulk lifetimes of the order of 5μs required. At the time, this was one of the best open–circuit voltages which had been observed for a multicrystalline silicon substrate. The best voltage of 643mV had been achieved on a thin epitaxially grown substrate [111].

The immediate improvement in cell efficiency for the 1.5Ωcm substrates can be attributed to monitoring the lifetime during the process sequence in the previous section. Analysis of the final cell lifetime or completed cell characteristics would not have revealed the high lifetimes which were demonstrated after the phosphorus diffusion and the subsequent degradation of the lifetime. Observation of this behaviour enabled the simple change in the sequence to be identified which led directly to an improvement in efficiency.

5.4 Aluminium BSF

Aluminium alloyed back–surface field cells are the most common high efficiency cell design for multicrystalline silicon, including the current record efficiency multicrystalline silicon solar cells from Georgia Tech [18]. Aluminium alloying provides the high rear surface doping advantages of a back surface field and low rear contact resistance.

A potentially more important benefit from the use of aluminium alloying is the gettering benefit of aluminium. Aluminium has long been recognised as an impurity getter [112], and has been used to improve the lifetime in single crystal and multicrystalline silicon solar cells [15,105,113]. Impurities are more soluble in the aluminium melt [114] and heavily Al doped silicon, trapping the mobile impurities in the p^+ region at the rear, where the lifetime is already limited by the heavy doping.

The effects of aluminium alloying on the effective lifetime during cell processing and the completed cell characteristics of Eurosolare multicrystalline silicon substrates was investigated.

5.4.1 *Experiment*

The 1.5Ωcm substrates received the most extensive examination. Substrates were first oxidised in steam at 900°C for 2 hours. The cells were then diffused from either a solid source or a liquid $POCl_3$ source, aiming for a resistivity around 180 Ω/□. The masking oxide was then removed from the rear and 1μm of aluminium was thermally evaporated onto the cell rear under vacuum. Most substrates had the phosphorous glass removed, and a thin passivating oxide was grown at 900°C for twenty minutes in a dry oxygen ambient, followed by a drive–in in argon at 1000°C for two hours (batch MP9,MP11) or 900°C for one hour (MP11) to alloy/diffuse the aluminium into the cell rear. The phosphorous glass was retained for passivation purposes on a selection of substrates and the alloying/diffusion was conducted at 900°C for one hour (MP9).

Breakages of the thin (220μm) 1Ωcm substrates restricted their investigation. The samples were oxidised in steam, before the $POCl_3$ diffusion (no solid source diffusion investigated). After removal of the rear oxide, the cells then had 1μm of aluminium evaporated on the rear under vacuum. The substrates were then processed in batch MP9 with half the substrates retaining the thin oxide on the front and alloyed at 900°C for one hour or a thin passivating oxide was grown at 900°C for twenty minutes in a dry oxygen ambient, followed by a drive in argon at 1000°C for two hours.

The 0.2Ωcm substrates were processed in batch MP9, with emitters formed from either the solid source or liquid source.

Lifetimes were measured after the phosphorus diffusion and after the aluminium alloy, with excess Al etched in orthophosphoric acid to reduce the background conductance of the samples. The cells had aluminium evaporated onto the rear and Cr/Pd fingers on the front using photolithographic liftoff followed by silver electroplating. The cells were finally annealed in forming gas for 20 minutes at 400°C.

5.4.2 *Results*

The lifetime of the 1.5Ωcm substrates during the aluminium alloying sequence can be seen in figures 5.9 and 5.10. As was observed during the earlier experiments, the effective lifetime increased during the phosphorus diffusion to the range of 15–45μs. Unlike the behaviour during post–diffusion oxidations in the earlier sections, the lifetime of the substrates was observed to improve on most substrates during the subsequent aluminium alloy step. The exception was during the thin oxide growth followed by 1000°C oxidation after the solid source diffusion in batch MP9 where a decrease in lifetime was observed. The same processing sequence produced a slight lifetime improvement after the Al alloying on the 1.5Ωcm substrates in batch MP11.

The 1Ωcm substrates demonstrated different behaviour during processing (figure 5.11). The effective lifetimes of the substrates which received the higher temperature (1000°C)

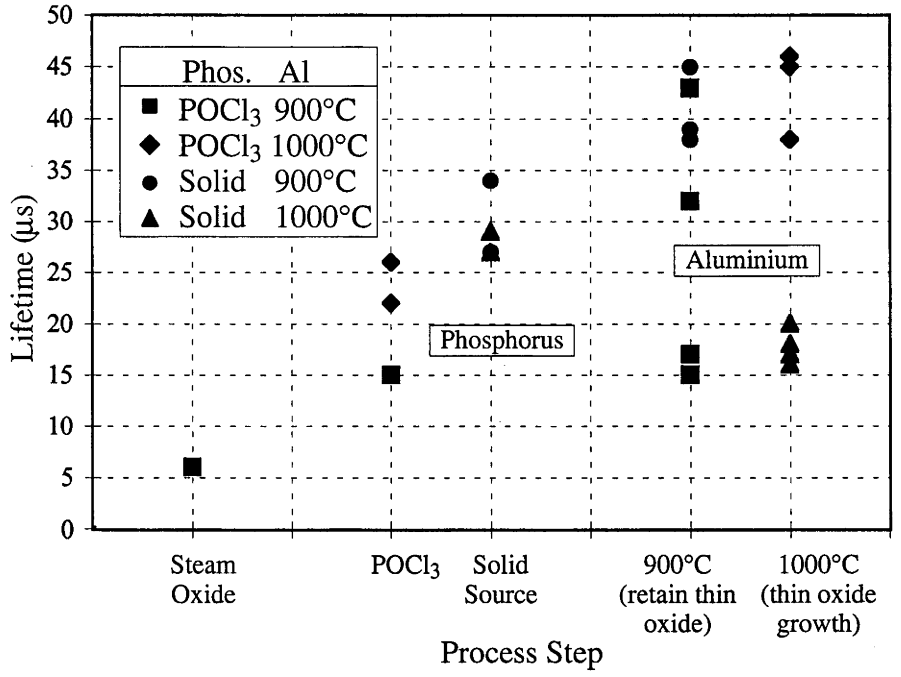

Figure 5.9: *Measured effective lifetimes during processing of aluminium alloyed 1.5Ωcm substrates in batch MP9.*
Lifetimes were maintained or improved after the phosphorus diffusion during the oxidation/alloy step (except solid source diffusion followed by 1000°C alloy) enabling high lifetimes to be demonstrated on most substrates.

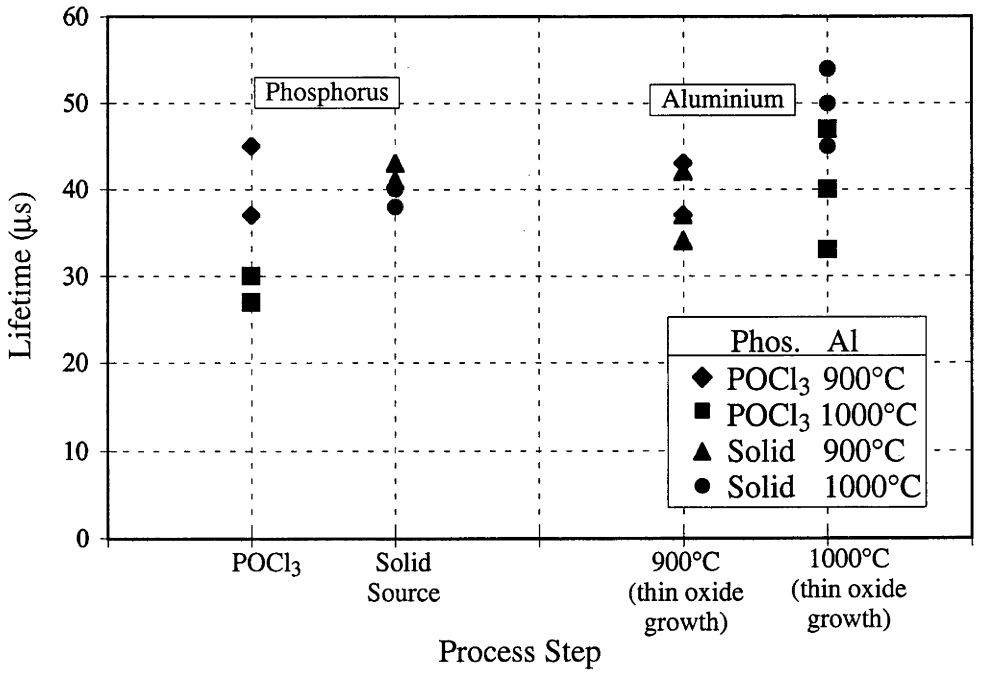

Figure 5.10: *Lifetime during processing of aluminium alloyed 1.5Ωcm substrates in batch MP11.*
High lifetimes were maintained on all substrates during the final high temperature step by including aluminium BSF formation.

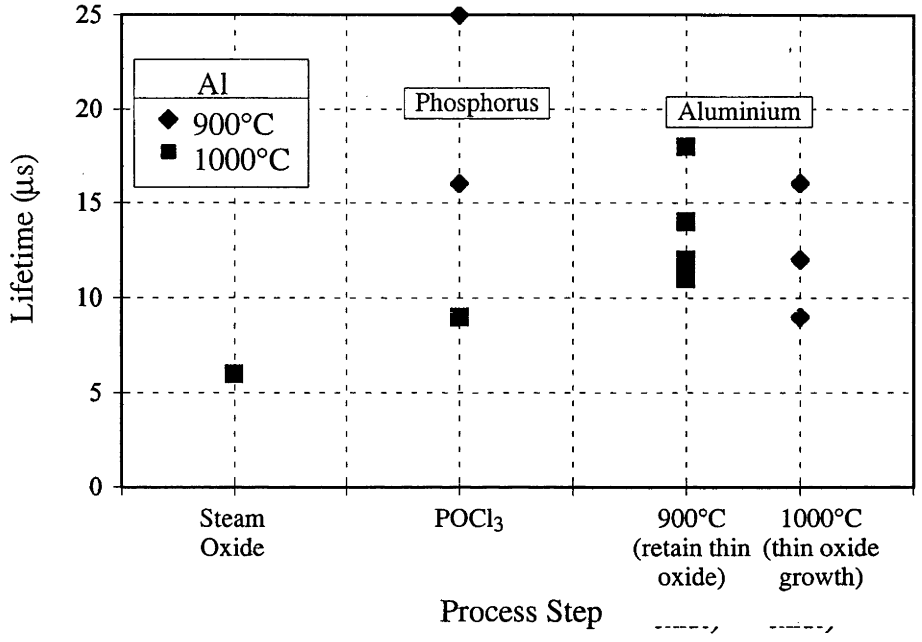

Figure 5.11: *Effective lifetimes of thin (220µm) 1Ωcm substrates during aluminium alloy process sequences.*

The effective lifetime of the substrates which received the higher temperature alloy demonstrated improvements in effective lifetime after the alloy while the substrates with the lower temperature alloy decreased in lifetime. Since the thin cells are more strongly influenced by the rear, this difference may be attributable to the poorer rear surface passivation afforded by the lower temperature alloy.

alloy improved while the lower temperature alloy decreased in effective lifetime. After the high temperature processing had been completed, the effective lifetimes of the substrates lay in a band from 9 to 18μs.

The cells demonstrated strong trends of improved current and voltage with improved final effective lifetime for the 1.5Ωcm and 1Ωcm cells in batch MP9. The relationships between the final lifetime and cell characteristics can be seen in figures 5.12 and 5.13. Cells from batch MP11 were not completed due to difficulties during metallisation/liftoff.

The aluminium alloy process increased the voltage of the 1.5Ωcm substrates further. The best cell demonstrating a voltage of 600mV, short circuit current density of 27.6mA/cm^2 and fill factor of 0.77 for an efficiency of 12.6%. This was demonstrated on the substrate with a final lifetime of 46μs, after a 900°C aluminium alloy when the $POCl_3$ oxide was retained. The $POCl_3$ oxide was too thick (~40nm) for an optimal antireflection coating, reducing the potential for further efficiency improvement. The best cell with a regrown oxide had a slightly lower lifetime of 42μs. The thin oxide was grown on the emitter after removal of the phosphorus glass followed by 1000°C aluminium alloy. This 12.0% efficient cell had an open circuit voltage of 591mV, current density of 27.6mA/cm^2 and slightly low fill factor of 0.73. The lower efficiency was primarily due to the poor fill factor. This cell had the potential to reach 17% efficiency with the addition of the AR coating and encapsulation with the expected 42% current increase. (A cell in a later batch processed without lifetime monitoring produced an efficiency of 17% with a open circuit voltage of 595mV, J_{sc} 35.9mA/cm^2 and FF of 79.3% up from an efficiency of 11.2% and just 584mV before AR coatings). A better fill factor (0.78) on the 1.5Ωcm cells with suitably thin oxides could have produced cell efficiencies greater than 18%. A similarly processed cell with solid source diffused emitter (rather than $POCl_3$) had a higher final lifetime (46μs) but broke during metallisation. The best cell with the solid source glass retained had lower current, voltage and efficiency (table 5.3) than the cells with $POCl_3$ glass or the thin oxide due to the poor effective lifetime.

Cell ID	V_{oc}(mV)	J_{sc}(mA/cm^2)	FF	Eff(%)	Lifetime(μs)	Oxide
MP9 1.5c	600	27.6	0.77	12.6	46	$POCl_3$ glass
MP9 1.5a	591	27.9	0.73	12.0	42	thin oxide
MP9 1.5gg	576	25.2	0.73	10.5	18	solid source glass

Table 5.3: *Better aluminium BSF 1.5Ωcm cell results from batch MP9 from each different front oxide.*

Improvement in 1.5Ωcm cell performance was due to the better final effective lifetimes in the Al–BSF cells. The best performance was from the cell with the $POCl_3$ glass retained. Shunting in the thin oxide cell prevented similarly high efficiency.

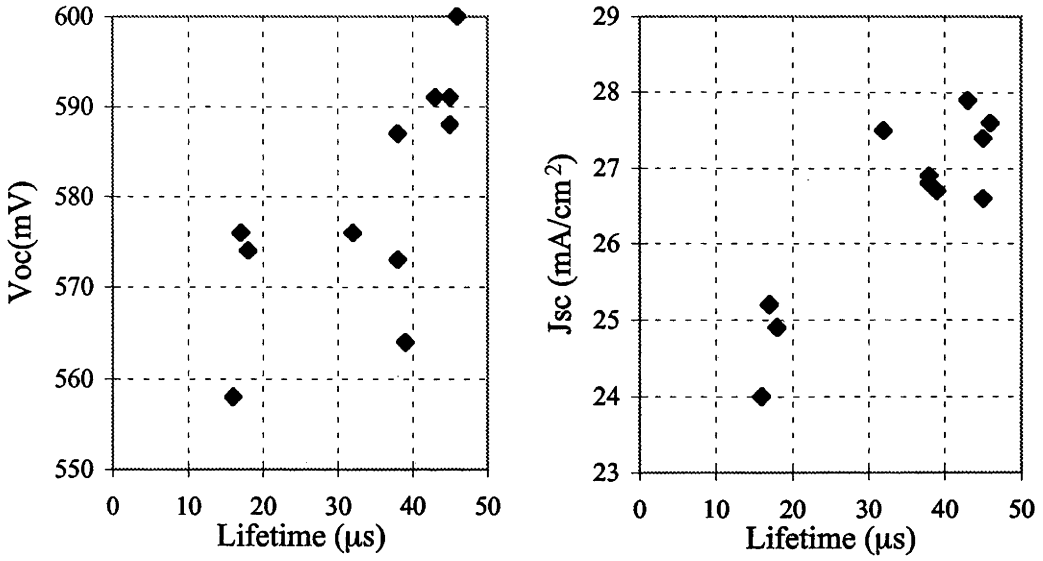

Figure 5.12: *1.5Ωcm cell characteristics versus final measured lifetime during aluminium alloying (batch MP9).*
The trend of improving current and voltage as a function of improved final lifetime was observed for the 1.5Ωcm substrates.

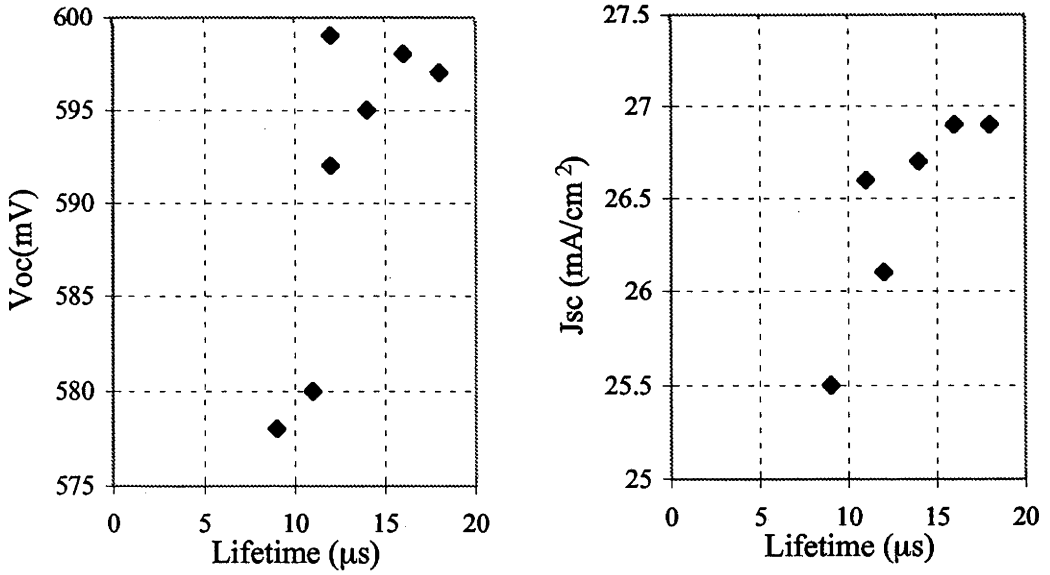

Figure 5.13: *1Ωcm cell characteristics versus final measured lifetime during aluminium alloying (batch MP9).*
The open circuit voltage and the short circuit current of the thin 1Ωcm substrates improved with increases in the lifetime measured after the aluminium alloy.

Similar behaviour and efficiencies were observed for the 1Ωcm substrates. The best cell was a $POCl_3$ diffused cell with the oxide retained, alloyed at 900°C with final lifetime of 16μs. This cell had a voltage of 598mV, an excellent fill factor of 0.78 and an efficiency of 12.5%. The thick $POCl_3$ oxide again limited the potential efficiency improvement with AR coating/encapsulation. Of the cells with the thin oxide, the cell with the best efficiency had a relatively poor lifetime (11μs) and poor voltage (580mV). Its efficiency was higher than cells with better lifetimes (14–18μs) due to the better fill factor (0.78). These cells had voltages over 595mV, but poor fill factors (<0.75) limited efficiencies to 11.9%.

Cell ID	V_{oc}(mV)	J_{sc}(mA/cm^2)	FF	Eff(%)	Lifetime(μs)	Oxide
MP9 1d	598	26.9	0.78	12.5	16	$POCl_3$ glass
MP9 1aa	580	26.6	0.78	12.0	11	thin oxide
MP9 1b	595	26.7	0.75	11.9	14	
MP9 1bb	597	26.9	0.74	11.9	18	

Table 5.4: *Better aluminium BSF thin 1Ωcm cell results from batch MP9 from the different front oxides.*

The cell with the $POCl_3$ glass retained had the best efficiency. Poor fill factors limited the efficiency of the cells with thin oxides with the better effective lifetimes.

Overall, the fill factors of the aluminium alloyed cells were poor. Most 1.5Ωcm cells decreased in fill factor during the forming gas anneal by 1 to 5% due to decreased shunt resistances. In all but the best cell, fill factors were less than 0.73. Most of the 1Ωcm cells had improvements in fill factor during the forming gas anneal due to decreased series resistance, but fill factors still varied from 0.77 to 0.79 in the better cells while other cells had relatively low fill factors (0.74–0.75) due to shunting (R_{sh}~100Ω).

Little useful information was obtained from the 0.2Ωcm substrates. The lifetimes of the 0.2Ωcm substrates were difficult to measure due to the poor sensitivity of the early QSSPC equipment). Lifetimes were in the 5–7μs range after the phosphorus diffusions, but demonstrated strong injection level dependence and trapping after the alloying process. The cell results were extremely poor, with all the 0.2Ωcm cells demonstrating poor fill factors due to shunting with the best fill factor 0.63. Most cells had fill factors less than 0.5. The shunting caused low open circuit voltages voltages in all the cells. The short circuit currents, however, were good for 0.2Ωcm substrates with short circuit current densities greater than 23mA/cm^2 (without AR) on all the cells.

5.4.3 *Discussion*

The inclusion of the aluminium alloyed back surface field provided immediate improvements in the performance of the 1.5Ωcm substrates. The benefit of the presence of aluminium during the final oxidation/drive–in was apparent during the process

monitoring experiments. Figures 5.9 and 5.10 show that the high lifetimes observed after the phosphorus diffusion were typically maintained or improved during the subsequent high temperature step, unlike the samples in earlier sections where lifetime was degraded during the final oxidation.

The effective rear surface recombination of an aluminium alloyed surface is worse than an oxide passivated surface, indicating that the measured lifetime improvement was due to improved bulk lifetimes. Therefore, the effective lifetime improvements can be attributed to the aluminium helping to maintain or improve the bulk lifetime. Extending our earlier hypothesis that gettered impurities released from the emitter during the final oxidation were limiting the cell lifetime, the aluminium appears to be gettering the released impurities, preventing the lifetime degradation.

Similar behaviour was observed in Cz silicon be Gee *et al.* [110]. Diffusion lengths in Cz samples were observed to decrease when samples were oxidised after the phosphorus diffusion. This degradation was eliminated by including aluminium on the cell rear during the final oxidation.

1.5Ωcm cell performances were correspondingly better due to the increased effective lifetime. Figure 5.12 displays the trend of improvements in cell characteristics with increased lifetime. This produced the first 1.5Ωcm cell in this investigation with an open circuit voltage of 600mV without AR coating.

The results for the thin 1Ωcm substrates were interesting, with similar effective lifetimes measured after the final processing step (9–18μs) as were measured during the comparisons of high and low temperature processing (9–20μs). Despite the similar measured lifetime after processing, the voltage of the aluminium alloyed cells were 10mV higher (allowing for the current differences). The difference is best explained by the post processing metallisation. The 100% metallisation dramatically increased rear surface recombination rates in the simple cells used for comparing high and low temperature processing (see table 5.2). The aluminium alloyed cells, in contrast, were less sensitive to rear metallisation with the BSF obscuring the rear from the minority carriers. Consequently, the current and voltage of the aluminium alloyed cells were higher than the high/low temperature cells for an equivalent post–processing lifetime. Post–metallisation measurements of cell lifetimes are therefore also important to determine total recombination in completed cells.

The best 1Ωcm and 1.5Ωcm cells both had $POCl_3$ glass retained (table 5.3 and 5.4). The cells with the $POCl_3$ glass were noticeably darker than bare silicon with the naked eye. This was due to the excessive thickness of the $POCl_3$ glass (~30–40nm). The $POCl_3$ glass was too thick to gain the optimal current boost from an antireflection coating (see section 2.2.4.3). Therefore, the deposition of a thinner glass was necessary for the maximum current increase afforded by antireflection coatings. This could be achieved with better

control of the $POCl_3$ glass pre–deposition (lower oxygen concentration) or stripping the regrown oxide with the final effective lifetime benefiting from the presence of the aluminium (as was demonstrated with other cells in the batch).

While the aluminium was clearly of benefit to maintain the bulk lifetime during the final oxidation, it is likely to be limiting the effective lifetime through rear surface recombination. 400 μm 1 Ωcm Fz samples which received a similar aluminium treatment at the ANU decreased in effective lifetime from 340μs after a phosphorus diffusion to 42μs, with a completed cell voltage of 620mV [92]. The effective diffusion length was reduced to the cell thickness, indicating large recombination velocities at the rear Al doped surface. The effective surface recombination velocity for the 1Ωcm Fz sample can be determined from the effective lifetime via equation (4.12). This corresponds to an effective surface recombination velocity of 1600cm/s or a J_0 of $1.7x10^{-12}A/cm^2$. Any gettering benefits from the aluminium were swamped by increases in rear surface recombination.

The recombination at an aluminium back surface field is typically high. Attempts to produce 20% efficient single crystal silicon solar cells relied on thick heavily doped substrates to minimise the effects of rear recombination [113]. Current 18.6% [18] and previous 18.2% [115] record efficiency aluminium alloyed 0.65Ωcm multicrystalline silicon solar cells have been limited by the recombination velocity at the rear surface. Efficiency improvements resulted from decreases in rear surface recombination. Effective surface recombination velocities are decreased from 10^4cm/s ($J_o=6.7x10^{-12}Acm^{-2}$) to 2000cm/s ($1.3x10^{-12}Acm^{-2}$) by increasing the aluminium thickness from 1 to 10μm [18,115]. Low surface recombination velocities (<200cm/s or $J_0=7x10^{-13}Acm^{-2}$) have been demonstrated with aluminium alloyed cells on 3Ωcm substrates [116]. This was achieved by alloying very thick screen printed layers of aluminium (37μm). Thick layers of aluminium were not practical with ANU processing equipment (thermal evaporation and vertical furnace orientation of substrates), indicating that the thinner aluminium BSF was likely to be limiting the performance of cells if further lifetime gains were achieved, even with the increase in depth of the profile with diffusion of aluminium at higher temperatures More detailed information on the breakdown in effective lifetime between rear surface and bulk recombination could be determined from analysis of IQE measurements from completed cells [117], if available.

The effective lifetimes for the 1.5Ωcm substrates were all below 55μs. This limit implies an effective rear surface recombination velocity of 1000cm/s, corresponding to a J_0 of $1.8x10^{-12}A/cm^2$. This was similar to the J_0 determined for the 1Ωcm Fz substrate.

The lifetimes for the thinner (220μm) 1Ωcm substrates also appear to be affected by the rear surface recombination after BSF formation. The effective lifetimes of the substrates were limited to below 20μs. The reduced substrate thickness increased the effect of rear recombination on the total cell recombination. An effective lifetime of 20μs on the thin

1Ωcm substrates corresponded to an effective rear surface recombination velocity of 1500cm/s, if the recombination was dominated by the rear surface. The effective rear surface recombination velocity of the rear alloy was also expected to increase slightly compared to the 1.5Ωcm substrates due to the increased substrate doping, with the J_0 ($1.6x10^{-12}A/cm^2$) of the alloyed layer similar. Substrates with higher lifetimes after the phosphorus diffusion decreased in effective lifetime while the substrate with the lower lifetimes improved. Aluminium was improving the bulk lifetime, but rear surface recombination was then dominating due to the reduced substrate thickness.

The effective surface recombination values determined from the Fz and multicrystalline samples appear low compared to the 10^4cm/s values reported by Rohatgi *et al* [115] for 1μm of aluminium, partly (though not entirely) due to lower substrate doping. King *et. al.* [118] measured similar values of dark saturation current ($2.4x10^{-12}A/cm^2$) for two hour Al diffusions at 1000°C, after adjusting the J_0 determined from their modeling for the updated value of the intrinsic carrier concentration ($10^{10}cm^{-3}$@300K [78]). The values for 900°C, however, differ by a factor of two. This may be due to the etching of the aluminium from our samples before measurement. The more lightly doped 900°C BSF may be semi–transparent to minority carriers, and therefore sensitive to the recombination rate at the surface. PC–1D modeling using typical 1 hour 1μm Al diffusion profiles [119] indicated the potential for changes in the J_0 of the BSF with the rear surface recombination velocity changing from 10^5cm/s to 10^6cm/s in the 900°C diffusion, whereas there was no change in J_0 with the higher temperature diffusion profiles. This again underlined the importance of considering the effects of post–processing metallisation on the recombination in the finished cells.

PC–1D modelling of aluminium alloyed cells demonstrated that QSSPC measurements were dominated by the effects of the rear recombination, with little variation in effective lifetime with changes in emitter saturation current since equation (4.13) is dominated by the surface recombination velocity of the worse surface. Therefore, while the quasi–steady state measurement provided useful comparative information on total recombination and cell voltages, current collection information is complicated by the spectral dependence of absorption and the weak dependence of effective lifetime on the quality of the better passivated surface. Despite this, current was clearly strongly dependent on the measured lifetime (figures 5.12 and 5.13) with bulk lifetime variations dominating any differences in the emitter quality.

Little useful information could be extracted for the 0.2Ωcm substrates. Noise and substantial trapping swamped the effective lifetime measurements with the low substrate lifetimes and high background conductivity. Cell performances were severely hindered by shunting. Fill factors were extremely poor, varying from a high of 0.63 with most cells falling between 0.4 and 0.5. Cell voltages were restricted by the shunting. Currents were

relatively good, though the oxide was again too thick for an optimal AR coating. The shunting problem was not restricted to this batch, with all subsequent batches of aluminium alloyed 0.2Ωcm cells also shunted. A likely explanation for this phenomena was shunting paths developing along grain boundaries due to preferential diffusion of the Al during the alloying process, since 0.2Ωcm substrates without alloying were less prone to shunting. Aluminium alloying was subsequently avoided on 0.2Ωcm substrates.

5.4.4 *Aluminium BSF Conclusions*

Including an aluminium BSF in the cell design helped improve the performance of 1Ωcm and 1.5Ωcm multicrystalline cells. The presence of the aluminium enabled the growth of thin thermal oxides since impurities released from the emitter were gettered by the aluminium, preventing lifetime degradation. Cell current can be improved with the lower reflection losses afforded by the thin oxides (combined with suitable AR coatings). Efficiencies were greater than 12.0% with thin oxides with the potential for greater than 17% with AR coating. The cell performances were affected by recombination at the rear aluminium BSF. Fill factors were disappointing due to shunting in many cells.

5.5 Gettering

The earlier process monitoring experiments demonstrated that excellent lifetimes could be obtained after the use of phosphorus diffusions and aluminium alloying. Both these processes are known to be excellent impurity getters. This indicated that impurities play an important role in the lifetime of the Eurosolare substrates.

The gettering process consists of three important steps [120]. Firstly the impurities must be released from their bound location in the crystal structure. These sites include dislocations, precipitation complexes and grain boundaries. Impurity release can be achieved at elevated temperatures where the impurity receives sufficiently energy to escape and become a mobile interstitial impurity.

Subsequently, the impurity must diffuse though the crystal to the gettering site. Since diffusion is strongly temperature dependent, increased temperatures assist the diffusion process. Sufficient time must be allowed for the impurities to diffuse to the catchment region and not simply redistribute within the crystal. Otherwise, there is the potential for increasing recombination in the new location [121] (e.g. redistributing impurities from grain boundaries to the crystal bulk).

The mobile impurities then need to be caught at a catchment site where they will not affect device performance or where they can be easily removed. The impurities may be trapped by the increased solubility of the impurity in a heavily doped region, such as a phosphorus diffusion or aluminium alloyed layer or by the presence of increased numbers of precipitation sites. The presence of the capture regions must do no harm to the

recombination in the cell. In high efficiency solar cells, the gettering layer is typically removed to prevent the gettered impurities from redistributing through the substrate during subsequent processing steps. In less efficient cells, gettering regions may not reduce cell efficiency and can be retained.

The choices for gettering techniques are surprisingly numerous. The gettering process relies on the segregation of the impurity from the bulk to the catchment region. The most common getters used for solar cell processing are phosphorus diffusions and aluminium alloying. The effectiveness of phosphorus is due to the increased substitutional solubility of impurities in the heavily doped region [109]. Other less effective n–type getters include dopants such as arsenic or antimony [122]. Aluminium alloying is effective due to the presence of the molten aluminium, with impurities segregating into the melt [114]. Other p–type dopants, such as boron, are less effective than n–type dopants due to poor substitutional solubility [109]. Gettering processes involving precipitation include surface abrasion [123] or laser damage [124], silicon nitride or polysilicon deposition [125] and ion implantation [126,127].

The benefit of phosphorus pre–gettering on Eurosolare substrates was investigated. Phosphorus gettering was chosen because it is a simple process, already used in the cell processing sequences for emitter formation. It was a proven clean process in the ANU laboratory, with high voltages (>690mV) demonstrated on Fz wafers using $POCl_3$ diffused emitters. Aluminium alloying carried the risk of contamination during the evaporation process and reduced cleaning options before the high temperature furnace steps.

5.5.1 *Gettering experiments*

$100cm^2$ wafers were diced into $15cm^2$ substrates for processing. These included 0.2Ωcm and 1.5Ωcm substrates. Samples were etched in HF/HNO_3 solution to remove the surface damage and contamination. The samples then received the gettering treatment of a heavy phosphorus diffusion. The heavy phosphorus diffusion was then etched in HF/HNO_3 to remove the gettering layer and associated impurities.

A range of gettering times and temperatures were investigated, including brief diffusion at 850°C for half an hour, and longer diffusions at 850°C, 900°C and 1000°C for three hours. After etching the gettering diffusion, the substrate was lightly diffused for 20 minutes at 875°C to produce a diffusion of 100–200Ω/□, followed by a 10 minute oxidation to provide better surface passivation. Samples were then annealed in forming gas for 20 minutes at 400°C before measurement.

Measurements were initially made with QSSPC. If the lifetime proved to be greater that 200μs, where QSSPC begins to overpredict lifetimes by 10%, transient photoconductance decay measurements were also acquired.

After lifetime measurements, some substrates had the in–situ grown oxide removed, and a new thin oxide grown for 21 minutes at 900°C, followed by a 40 minute anneal in argon, to improve the surface passivation quality. The samples were then annealed in forming gas at 400°C before measurement.

5.5.2 *Results*

The lifetime results after the light phosphorus diffusion are summarised in table 5.5

Sample ID	Material	Resistivity (Ωcm)	Gettering (time,temp.)	QSSPC τ_{eff}(μs)	PCD τ_{eff}(μs)
c	multi	0.2	none	10	
cc	multi	1.5	none	40	
a	multi	0.2	850C, 0.5h	13	
aa	multi	1.5	"	70	
b	multi	0.2	850C, 3h	12	
bb	multi	1.5	"	94	
Fz–b	Fz	1	"	120	
d	multi	0.2	900C, 3h	15	
dd	multi	1.5	"	180	250
A	multi	1.5	"		280
B	multi	1.5	"	190	260
C	multi	1.5	"	200	220
D	multi	1.5	"	120	220
E	Fz	1	"	180	170
G	multi	1.5	1000C, 3h		200
H	multi	1.5	"	40	
I	multi	1.5	"	60	
J	multi	1.5	"		180
K	Fz	1	"	400	330

Table 5.5: *Measured effective lifetime after various gettering times and temperatures*

The measured lifetime was typically injection level dependent. An example of the injection level dependence can be seen for a multicrystalline silicon sample in figure 5.14. Consequently, the lifetime was extracted at the injection level which corresponded to one sun illumination (i.e. open circuit voltage conditions). This was typically of the order of $10^{15}cm^{-3}$, which was often close to the maximum effective lifetime.

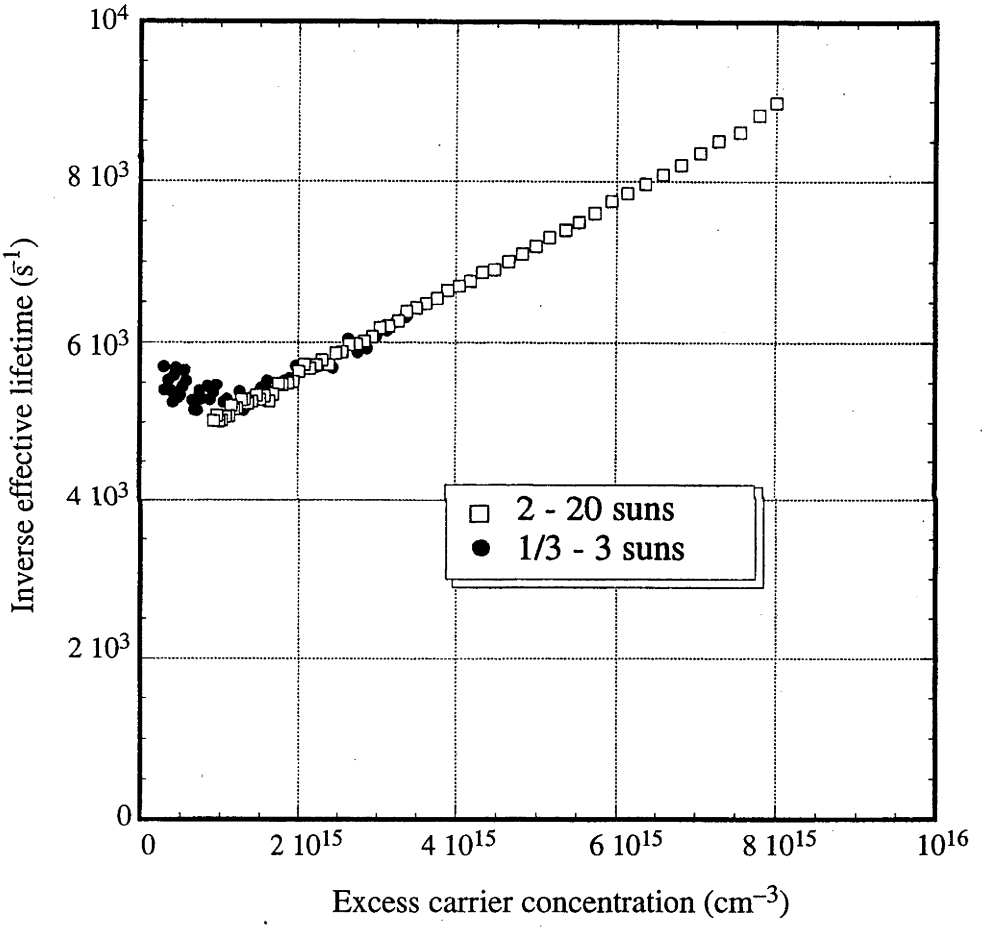

Figure 5.14: *Effective lifetime of a 1.5Ωcm multicrystalline substrate (dd) from quasi–steady state photoconductance measurements.*
Two ranges of light intensities were shown to demonstrate the injection level dependence of the effective lifetime. The effective lifetime corresponding to one sun illumination was 180μs.

The substrates which were reoxidised increased in effective lifetime. The 1Ωcm Fz substrate (E) increased in PCD effective lifetime from 180 to 320μs while the 1.5Ωcm substrate (B) increased from 260 to 330μs.

5.5.3 *Discussion*

Phosphorus gettering has led to dramatic improvements in the lifetime of the 1.5Ωcm multicrystalline substrates. The sample which received no gettering had an effective lifetime of 40μs. This compared favourably to the results for earlier experiments without gettering, where the lifetimes after the phosphorus diffusion were between 30 and 70μs. Many substrates demonstrated lifetimes greater than 200μs after gettering.

Lifetime improvements from the phosphorus diffusion were apparent for most gettering times and temperatures. The shortest getter at 850°C for half an hour (followed, after etching, by a similar diffusion for surface passivation) led to an effective lifetime of 70μs while 3 hours at the same temperature produced an effective lifetime of 94μs.

The best gettering results were achieved for samples gettered for 3 hours at 900°C. All substrates demonstrated a PCD measured effective lifetime around 200μs after the gettering treatment, with lifetimes up to 280μs, while QSSPC lifetimes varied from 120 to 200μs. The comparison of PCD and QSSPC measurements in section 4.4.1 indicated that the QSSPC measurement provides a better reflection of the area averaged lifetime while the PCD lifetime was influenced by the lifetime in the better grains.

The poorer results from the highest temperature gettering process were not surprising, given the sensitivity of the 1.5Ωcm substrates to higher temperature processing in the comparison of high and low temperature processing. The better substrates demonstrated lifetimes around 200μs though slightly lower than the identical substrate processed at 900°C (280μs), while substantially lower lifetimes of the order of 50μs were demonstrated on other substrates (compared to 260μs on identical substrates). The higher temperature processing damaged the effective lifetime compared to lower (900°C) processing. Segregation coefficients also decrease at higher temperatures [120], potentially reducing gettering effectiveness.

Previous investigations of gettering with phosphorus have led to similar conclusions of an optimal gettering temperature for multicrystalline silicon. The fabrication of the current record efficiency multicrystalline silicon cells on 0.65Ωcm HEM material consisted of a half hour diffusion at 900°C, followed by etch–back to optimise the emitter resistivity and remove impurities. This gettering produced lifetimes in the range of 35–145μs [128]. Gettering performance dropping sharply 50°C either side of the optimal condition. Combined with aluminium gettering, lifetimes improved from 10μs on the as–grown material up to 135μs on completed Al–BSF cells.

High lifetimes have also been reported by other researchers in multicrystalline silicon from Eurosolare [103]. Samples received gettering treatments of four hours at 900°C. After gettering 1cm^2 mesa diodes demonstrated diffusion lengths up to 1200μm (the substrate thickness) with an average diffusion length of 600μm over 9 diodes compared to an average of 250μm before gettering (370μm on better substrates). The importance of low oxygen content was noted, with lifetime degraded during gettering on samples with high oxygen content ($|O_i|>10^{17}cm^3$).

The J_0 of the oxidised lightly diffused surface on the 1Ωcm Fz wafers varied from 10^{-13}A/cm^2 to $3x10^{-14}$A/cm^2 (the best J_0 corresponding to a sample with particularly low sheet resistivity of 400Ω/ □), decreasing as the effective lifetime of the wafers increased from 120μs to 330μs. The measured effective lifetimes closely match that predicted by effective lifetime dominated by the surface ($1/\tau_{eff}=2J_oNa/qn_i^2W$) for J_0 greater than $5x10^{-14}$A/cm^2, departing from the effective lifetime for the lowest J_0 ($3x10^{-14}Acm^{-2}$, measured 330μs, surface 440μs). Despite the low values for the emitter saturation current, the surfaces play a dominant role in recombination, limiting the effective lifetime. The bulk lifetime is therefore substantially higher than the measured effective lifetimes.

The emitter diffusion limited the multicrystalline samples in a similar way. The 1.5Ωcm substrates have slightly lower effective surface recombination for the same J_0 due to the lower substrate doping, so the lifetime limit imposed by the surface was expected to be 100% higher for the same emitter diffusion due to the lower substrate doping and the increased substrate thickness. Typical substrate lifetimes were of the order of 50% higher than the Fz substrates with similar phosphorus diffusions, with surface recombination, though not dominating recombination in the same manner as on the Fz substrates, contributing significantly to total recombination.

This was supported by the samples which had the phosphorus glass removed and were reoxidised at 900°C for 20 minutes. The J_0 of the Fz wafer decreased from $5x10^{-14}Acm^{-2}$ to $3x10^{-14}Acm^{-2}$ leading to an increased effective lifetime of 320μs, up from 180μs. The multicrystalline silicon substrate also increased in effective lifetime as the surface passivation improved, though not as dramatically as the Fz substrate. Surface recombination was playing an important role in the total recombination of the substrates indicating potential for even greater bulk lifetimes.

More satisfactory investigations of the benefits of gettering could be made with the use of low temperature passivation rather than light phosphorus diffusions to reduce the effects of surface recombination. The light phosphorus diffusion will getter some of the impurities from the bulk. Consequently, the as–sourced samples have received a degree of phosphorus gettering when measured while the gettered samples have been subjected to a second gettering step after the long diffusion getter of interest. Alternate passivation schemes may provide less contaminated information. Ethanol–iodine solutions have been

shown to produce good passivation of silicon surfaces [129], but the absorption of the iodine solution is likely to affect QSSPC measurements. HF passivation [130] appears to be a suitable candidate without the absorption problems of iodine, but handling is complicated by the dangers of HF spills. Schmidt and Aberle [91] demonstrated that plasma deposited silicon nitride layers offer excellent passivation even on relatively low resistivity wafers (~1Ωcm) but layers which provide good passivation are likely to be difficult to remove after deposition[131] limiting the potential for further processing of the gettered substrate. Further investigations are required to find a suitable candidate.

Despite the potential lifetime benefit, the use of long phosphorus pre–gettering is not viewed favourably for commercial cell fabrication due to the high thermal budget and long furnace times. Recently, the use of pre–gettering anneals have generated some interest [121,132]. Brief, rapid high temperature anneals (>1000°C,<3min) are used to release impurities from their non–interstitial recombination sites followed by a gettering step to remove the mobile impurities. Such processing has the potential for reducing the duration of the gettering step, with the gettering time limited only by the diffusion of impurities, not their release. If impurity diffusion is the limiting mechanism, long gettering times may be unavoidable. Long phosphorus gettering still warrants investigation to determine potential upper limits on cell performance.

5.6 Conclusions from process monitoring experiments

Process monitoring has proven to be a useful tool in determining the effects of different process conditions on the performance of multicrystalline silicon solar cells which would not have been able to be determined from completed cell characteristics.

In particular, changes in effective lifetime during different steps of the cell process sequence were observed. Substrates benefited from the formation of the emitter due to partial gettering of impurities. Subsequent process steps were found to be important, with oxidations leading to the release of impurities back into the bulk with consequent lifetime degradation. In contrast, aluminium alloying maintained or improved the effective lifetime despite the large surface recombination velocities at the rear. The observation of the gettering behaviour of the aluminium and phosphorus provided the impetus for phosphorus gettering experiments which led to dramatic improvements in the lifetime of the 1.5Ωcm multicrystalline silicon substrates.

The final effective lifetimes also proved to be a useful indicator of final cell performance. Cell voltage and current were observed to increase with increasing final measured lifetime. There is potential for optimisation of a process without completing cell metallisation, provided the metallisation process does not unduly affect cell recombination. As minority carrier diffusion lengths increased, recombination at the rear metallisation will increasingly become important and needs to be included in the monitoring measurements.

Observation of the behaviour of the multicrystalline substrates during processing enabled improvements in the cell processing sequence to be identified which led to rapid improvements in cell efficiency from 14% with the simplest process sequence to greater than 17% with thin oxides and aluminium BSF.

The success of the phosphorus gettering led to the pursuit of higher efficiency and advanced device structures, as presented in the next chapter.

CHAPTER 6 HIGH EFFICIENCY MULTICRYSTALLINE SILICON SOLAR CELL DESIGNS

6.1 Introduction

The performance of multicrystalline silicon solar cells is substantially lower than single crystal silicon solar cells, both in the laboratory and commercial manufacture. This is due to the lack of suitable texturing and lower material lifetimes.

An effective texture suitable for multicrystalline silicon was reported in chapter 2. The early experimental work presented in this chapter investigates the advantages and problems of incorporating the 'tubs' texture described in section 2.3.4.1 into the cell processing sequence.

Improvements in material quality reported in chapter 5 and by others [98,103,133] offer the opportunity for further improvements in multicrystalline silicon cell performance. Rear surface recombination was identified in the previous chapter as an important contribution to cell recombination in the multicrystalline silicon substrates with better lifetimes. The importance of rear recombination has increased further with the higher lifetimes which can be achieved with phosphorus gettering. The bulk of this chapter presents modelling of the effects of rear surface recombination on cell performance and experimental results on the implementation of cell designs to reduce rear surface recombination.

6.2 'Tubs' texturing

Initial investigations of high efficiency approaches concentrated on the implementation of texturing on multicrystalline substrates. Texturing provides a number of potential benefits for cell performance, as outlined in chapter 2, including reduced reflection losses, light trapping and absorption of light closer to the front collecting junction. Texturing has been identified as a major contributor to the performance gap between multicrystalline and single crystal silicon solar cells [7].

Experiments were conducted to determine any changes in the cell processing sequence required to include 'tubs' texturing. 'Tubs' texturing required an additional oxidation step for an etch mask and photolithography to define the holes through the masking oxide. Cell performances were compared to those from earlier cells which did not receive texturing.

6.2.1 *Experiment*

'Tubs' texturing was first investigated with simple 100% rear contacted cells with thin emitter oxides on 1.5Ωcm multicrystalline silicon substrates.

Substrates were cleaned by etching in 10/1 HNO_3/HF for 2 minutes then oxidised in steam for 2 hours at 900°C. 2μm holes triangularly packed on 15μm spacing were opened

through the front oxide over the 2x2cm^2 cell areas (except under the finger contacts) using photolithography. The silicon was etched through the oxide holes using 30/1 HNO_3/HF until the etch pits coalesced and only small peaks of unetched silicon remained. The etching completed in $4^1/_2$ to $5^1/_2$ minutes (depending, in part, on hole size after photolithography) with regular visual inspection of the substrate with a microscope towards the completion of etching. The remaining masking oxide was then removed in 10% HF.

A masking oxide for the phosphorus diffusion was then grown in steam for 2 hours at 900°C, before the 2x2cm^2 emitter areas were opened through the masking oxide using photolithography. The emitter was diffused using a solid source for 20 minutes at 850°C producing a sheet resistance of 150Ω/□. The masking oxide was removed before growth of a thin oxide for 21 minutes at 900°C followed by a 40 minute anneal in argon.

The front metal fingers were restricted to the untextured areas of the cells using aligned photolithography. High viscosity photoresist was needed to ensure coverage of the sharp peaks between the 'tubs', therefore long exposures were necessary to expose the front metal grid. Cr/Pd contacts were applied with liftoff. Aluminium contact was made to the entire rear after the removal of the rear oxide and the front contacts were silver plated. The cells were then sintered in forming gas for 15 minutes at 300°C before measurement.

Cells then had a TiO_2 AR coating deposited with thermal evaporation before being remeasured. Tabbing and encapsulation followed before final measurement.

6.2.2 *Results*

Cell performances were good for the simple design. Cell efficiencies varied from 12.2 to 13.9% without AR coating. The best cell had an open circuit voltage of 597mV, fill factor of 80% and current of 29.2mA/cm^2. Addition of the TiO_2 AR coating led to improvements in cell currents from 16 to 21% while encapsulation led to further improvements of 4.5 to 6.5%, with the biggest improvements on the substrates which had the smallest increase after the TiO_2 deposition. Combined current improvements from the AR coating and encapsulation were 22 to 26%.

Cell voltage increased by 6–7mV on all the cells in line with the current increases. Fill factors dropped on some cells during the tabbing process while other cells increase slightly in fill factor due to the open circuit voltage improvement. The best cell achieved 17.0% (+22% compared to cell prior to TiO_2/tabbing) with open circuit voltage of 602mV(+1%), FF of 78.5%(–2%) and current of 35.9mA/cm^2(+24%).

6.2.3 *Discussion*

An important role of this experiment was to develop suitable protocols for the incorporation of 'tubs' texturing on multicrystalline silicon. Early cells with 'tubs'

texturing were severely decorated during electroplating due to poor photoresist coverage of the sharp peaks between the features (see Figure 2.16). This led to poor currents because of the increased front metal coverage and poor fill factors due to shunts across the perimeter of the cells.

These problems were reduced by using photoresist with higher viscosity and slow spin speeds and restricting the texturing to the cell area to minimise the risk of shunting due to decorations across the cell border. This in turn led to difficulties exposing the front contact grid in the bottoms of the 'tubs' leading to a discontinuous grid after liftoff. This problem was solved by developing a texturing mask where holes were only exposed on the cell area between the fingers (figure 6.1.).

Cell efficiencies before the addition of TiO_2 were higher than equivalent cells without texturing from the previous chapter. This was due to the slight improvement in reflection for the unencapsulated 'tubs' textured substrates. The weighted transmission with the bare 'tubs' textured substrates was around 75% (depending on the 'tubs' overlap) compared to 65% for polished silicon (see figure 2.18). Therefore the current and efficiency of the 'tubs' textured substrates was expected to be around 15% higher than the untextured substrates (not including finger reflection losses).

Since the reflectance of the textured substrates was less than that of polished silicon, the percentage decrease in reflectance with the addition of the TiO_2 and encapsulation was less for the 'tubs' textured substrates. Textured cell current improved by between 22% and 26%, compared to up to 45% improvement for polished wafers.

The current results reflected the potential of 'tubs' texturing for improving cell performance. Despite the high recombination velocities at the rear from the 100% metal coverage, the current from the better cells (35.9mA/cm^2 and 35.6mA/cm^2) was the best to date in a TiO_2 encapsulated cell, compared to the best polished cell (35.2mA/cm$^{2)}$ which had an aluminium alloyed rear. The voltage was lower than in the earlier polished Al alloyed cells, due to the higher rear surface recombination without alloying, leading to an equivalent cell efficiency of 17.0%.

6.2.4 *'Tubs' textured Al–BSF cells*

The potential to improve cell performance by including the higher efficiency characteristics of aluminium BSF cells with 'tubs' texturing was next investigated.

6.2.4.1 *Experiment*

Three 1.5Ωcm substrates were processing following a similar protocol to the previous section (6.2.1) for 'tubs' textured cells, modified to include Al–BSF formation. 1μm of aluminium was evaporated onto the rear of the cell when the masking oxide was removed after the phosphorus diffusion. A thin oxide was grown for 21 minutes at 900°C followed by a 2 hour anneal at 1000°C to alloy/diffuse the aluminium.

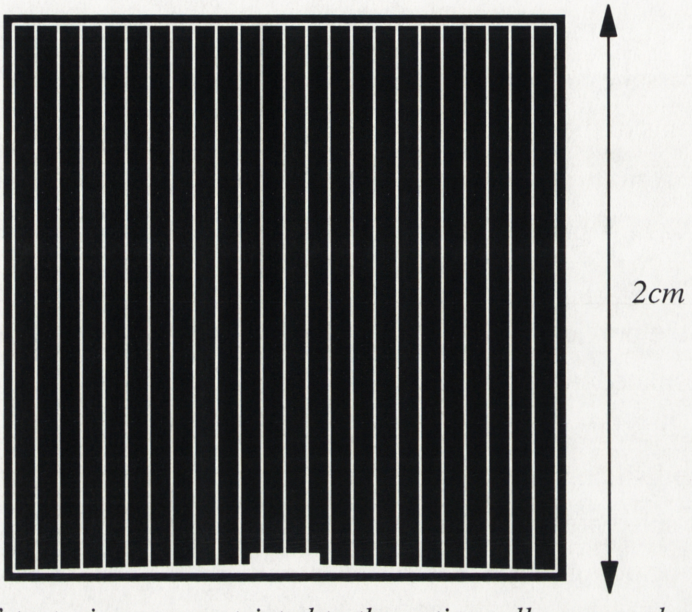

Figure 6.1: *'Tubs' texturing was restricted to the active cell area, excluding the front metal contacts.*
The area in black was textured. The regions under the metal contacts were not textured to ensure clear photolithography with the thick photoresist required to prevent decoration. Texturing was restricted to the cell area to minimise the risk of shunts across the cell perimeter due to poor photoresist coverage on the peaks between 'tubs'.

After TiO_2 deposition and encapsulation, a MgF_2 AR coating was added to reduce reflection losses from the glass.

6.2.4.2 *Results*

The aluminium collected in a lump on the rear of some cells during alloying, epitaxially depositing excess silicon in this region. These lumps were broken free with tweezers to allow subsequent photolithography and heat sinking during cell measurement. One substrate cracked during this procedure.

The remainder of the batch produced the first four cells with efficiencies greater than 17%. Cell efficiencies varied before AR coating/encapsulation from 13.4 to 14.4% due to current variations from 28.5 to 30.6mA/cm^2. Voltages were relatively tightly bound between 594 and 603mV, while fill factors varied from 0.78 to 0.79. Addition of the TiO_2/encapsulation/MgF_2 boosted the cell efficiencies beyond 17%, with decreased spread between 17.1 to 17.7% Currents varied from 36.3 to 37.4mA/cm^2 with the greater increases on the substrates with the poorest initial currents. Voltages increased 5–6mV with the current increase while fill factors dropped slightly (<1%) during tabbing.

6.2.4.3 *Discussion*

The combination of 'tubs' texturing and Al–BSF led to further improvements in cell efficiency due to the increase in cell current. The current in all the cells was better than the previous best result (35.9mA/cm^2, previous section) for the encapsulated 'tubs' textured 1.5Ωcm cells without Al alloyed rear. The 4% boost can be attributed in part to the improved bulk lifetime and rear surface passivation with the Al–BSF, but is also due to the decreased reflection (2–2.5%) from the glass afforded by MgF_2. Cell efficiencies were correspondingly higher with efficiencies as high as 17.7%. This is an impressive efficiency for a cell without phosphorus pre–gettering.

The high efficiencies are driven by the excellent current results from the cells. 37.4mA/cm^2 was the highest current produced by a multicrystalline cell during this research. The high current can be attributed to the low reflection losses and improved absorption closer to the front surface with the 'tubs' texture, with 35.9mA/cm^2 the best current produced for an equivalent Al–BSF cell without texturing.

The narrowing of the spread of currents after the AR coatings/encapsulation points to variations in the reflectivity of the 'tubs' textures before encapsulation. This was also observed in reflectance measurements from a later batch of cells (Figure 6.23). Reflectivity from bare 'tubs' textured cells varied in weighted reflectance by up to 4%. This was due to variations in the shapes of the 'tubs' from grain to grain due to the slightly anisotropic nature of the HF/HNO_3 etch and differences in the size and degree of overlap of the 'tubs'. The reflection losses before encapsulation are sensitive to the shape and size of the 'tubs'. The addition of the AR coating and encapsulation reduces the spread in reflection losses.

Better analysis of the benefits of texturing could be achieved by analysing the internal quantum efficiency measurements of cells with and without texturing [117]. This would assist in providing information on the breakdown in current improvement between reflection decreases, light trapping and enhanced absorption near the front surface.

6.3 Phosphorus gettering and rear surface recombination

Advancements in multicrystalline silicon manufacture have led to dramatic improvements in material quality over recent years. Additional enhancement of minority carrier lifetimes can be achieved by phosphorus gettering in materials with low defect densities [18,103,105]. Gettering experiments in chapter 5 have also enabled the demonstration of diffusion lengths in multicrystalline silicon which can be significantly greater than the typical cell thickness. Recombination at the rear surface of the cell can therefore strongly influence the cell performance. When surface recombination velocities at the rear surface of the cell are high, further increases in diffusion length provide little improvement in the cell characteristics because carriers recombine at the rear, limiting improvements in voltage and current.

Conducting the photogenerated current from the solar cell requires contact to be made to the silicon substrate. Metal contacts to silicon have very high surface recombination velocities, greater than 10^5cm/s [134], and they are of clear concern when minimising recombination in narrow base (cell thickness less than diffusion length) cells.

6.3.1 *Effect of rear surface recombination on cell performance*

The dark saturation current due to recombination in the emitter of a silicon solar cell can be reduced below 10^{-13}A/cm^2 with suitably chosen diffusion parameters and surface passivation. Therefore, solar cells with optimised emitters have demonstrated open circuit voltages on single crystal silicon greater than 700mV [11,135]. This is significantly greater than the voltage which can currently be achieved with multicrystalline silicon solar cells, indicating that the recombination limiting the cell voltage is occurring in the base and at the cell rear.

The open circuit voltage limit imposed by a p–type substrate with thickness W and effective rear recombination velocity, S_{eff}, can be determined from the expression

$$V_{oc} = \frac{kT}{q} ln\left(\frac{J_{sc}}{Jo_{base}}\right) \tag{6.1}$$

where the dark saturation current density, Jo_{base} is given by [5]

$$Jo_{base} = \frac{qn_i^2 D_e}{L_n N_a}\left[\frac{\left(\frac{S_{eff}L_n}{D_e}\right)cosh\left(\frac{W}{L_n}\right) + sinh\left(\frac{W}{L_n}\right)}{cosh\left(\frac{W}{L_n}\right) + \left(\frac{S_{eff}L_n}{D_n}\right)sinh\left(\frac{W}{L_n}\right)}\right]. \tag{6.2}$$

Here q, L_n and D_e are the electron charge, diffusion length and diffusivity respectively, while N_a is the acceptor doping level and n_i is the intrinsic carrier concentration.

The voltage cap imposed by base recombination for a range of material lifetimes and surface recombination velocities can be seen in Figure 6.2 for a 300μm 0.5Ωcm substrate. The surface recombination velocity is varied from 100cm/s (typical of thermal oxides [90]) to 10^6cm/s (typical of metal contacts) while lifetime is varied from 10μs to 1ms with the 10μs to 100μs range typical of high quality multicrystalline substrates. The short circuit current density, J_{sc}, is assumed to be 35mA/cm^2 which is achievable in high efficiency multicrystalline silicon solar cells.

Rear surface recombination has little effect on the open circuit voltage of the cells until the base diffusion length approaches the cell thickness (lifetimes>20μs). Carriers injected at the junction can then diffuse across the base and recombine at the cell rear. If $S_{eff}L_n/D_e>>1$, then further increases in bulk lifetime provide little improvement in open circuit voltage (<7mV) since the recombination is dominated by processes occurring at the rear surface.

Improvements in open circuit voltage therefore require decreases in the effective surface recombination velocity at the rear surface to less than 10^4cm/s, substantially less than can be achieved with 100% metal contacts.

The same conclusions are reached when modelling cell efficiency with PC–1D. 300μm 1Ωcm devices were modelled for a range of rear surface recombination velocities and bulk lifetimes to determine the combined effect of these two parameters on cell efficiencies. Reflective losses were assumed to be 5%. Resistive losses, which can depend on three dimensional effects, were not treated. The results of this modelling are presented in figure 6.3.

Figure 6.3. can be best explained by breaking the graph down into three separate sections. In region 1, lifetime is less than 20μs. The cell diffusion length is less than the substrate thickness. Therefore recombination at the rear surface has little effect on cell behaviour. Efficiency improvements depend only upon improving the bulk lifetime in the completed devices.

In region 2, diffusion lengths are greater than the substrate thickness and recombination at the rear surface is high. The efficiency has reached a plateau with little change in efficiency with variations in lifetime and surface recombination velocity. The efficiency of the device is pinned by recombination at the rear surface. Cell voltage is limited since carriers injected at the junction diffuse to the rear surface and recombine, while current is limited to the carriers photogenerated in the front half of the device since carriers in the rear half of the device diffuse to the rear and recombine.

Therefore, to obtain further efficiency improvements it is necessary for the device parameters to fall in region 3. Recombination at the rear surface is sufficiently low that

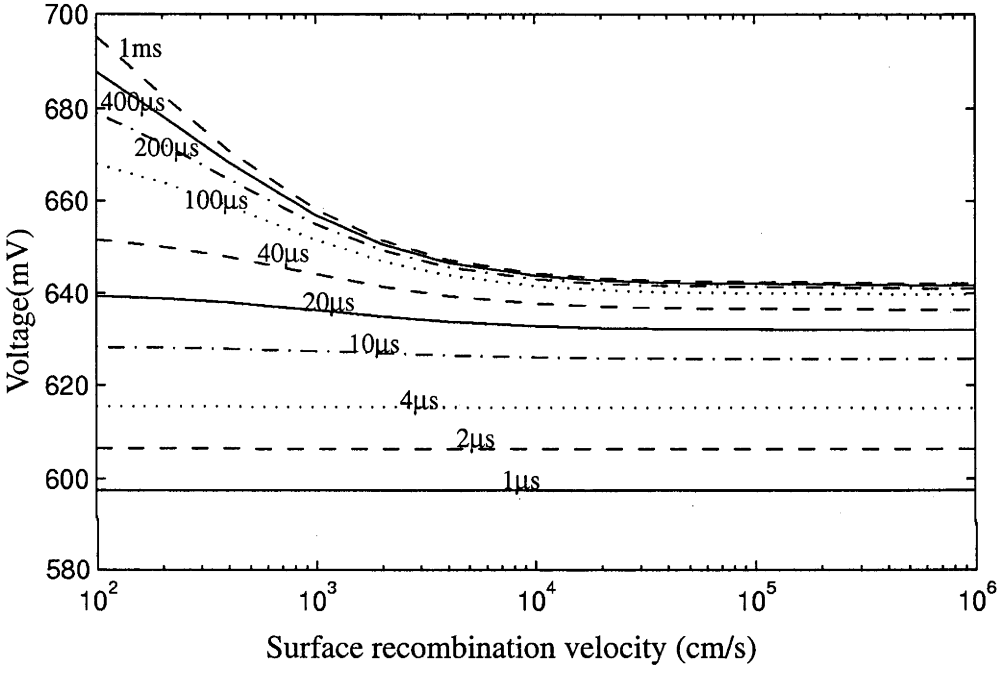

Figure 6.2: *Modelled effect of rear surface recombination on open circuit voltage from equation 6.2.*
The substrate is 300µm thick with a resistivity of 0.5Ωcm. Rear surface recombination can be seen to have little effect on cell voltage for lifetimes less than 20µs. If rear surface recombination velocities are large (>10^4cm/s), little improvement in voltage can be achieved with further improvements in lifetime. Improvements in cell lifetime can only lead to improved voltage if the rear surface recombination velocity can be reduced to below 10^4cm/s.

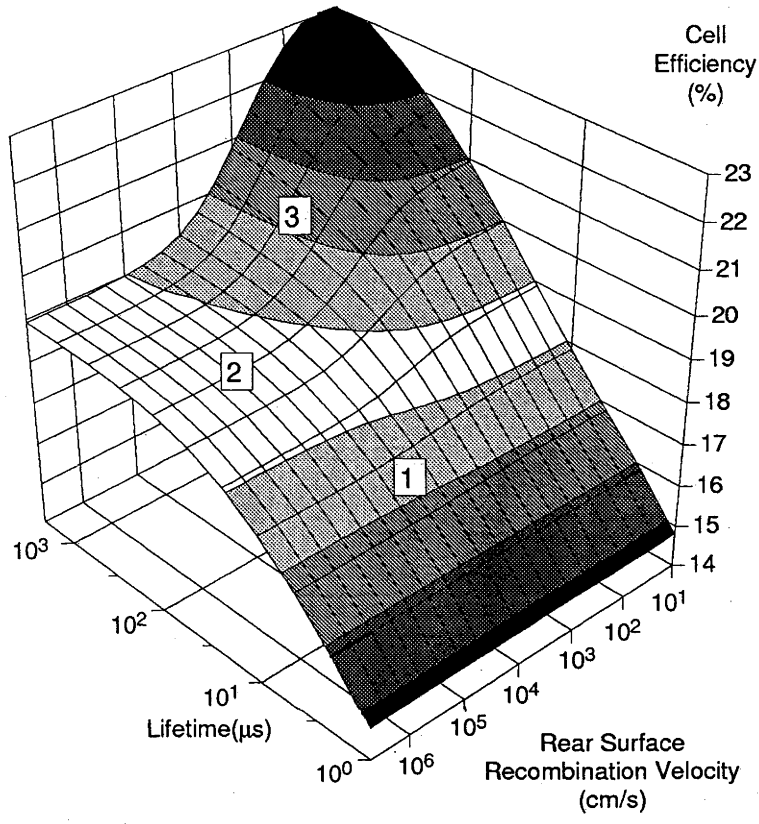

Figure 6.3: *PC–1D modelling of the effect of rear surface recombination on 300μm 1Ωcm cell efficiencies.*

The results fall into three distinct sections. In region 1, the cell efficiency is limited by the bulk lifetime with diffusion lengths less than the substrate thickness. Rear surface recombination has little or no effect on cell performance. In region 2, the diffusion length is greater than the substrates thickness and rear surface recombination rates are high. Cell efficiency is limited by recombination at the rear surface. In region 3, the cell efficiency is dependent on both the cell lifetime and the rear surface recombination velocity. The diffusion length is greater than the substrate thickness and the surface recombination velocity is below 10^4cm/s. Efficiency gains can be achieved at the cost of decreased bulk lifetime provided rear surface recombination is decreased.

both bulk and rear surface recombination have similar contributions to the device behaviour. Efficiency improvements can result from improvements in bulk lifetime or by rear surface passivation.

Importantly, improvements in rear surface recombination velocity can be made at the expense of decreasing bulk lifetime while still obtaining efficiency gain. This allows for the possibility of high temperature processing to obtain good surface passivation provided the resulting decrease in bulk lifetime is not excessive. This differs from the traditional approach to multicrystalline silicon solar cell processing where lifetime degradation is the major concern.

An alternative to reducing the rear surface recombination velocity is to vary the substrate thickness. The expression for the dark saturation current, equation (6.2), can be simplified for high rear surface recombination velocities in the extreme cases of cell thickness to

$$Jo_{base} = \frac{qn_i^2 D_e}{N_a L_n} \quad for\ Ln \ll W$$

$$Jo_{base} = \frac{qn_i^2 D_e}{N_a W} \quad for\ Ln \gg W \qquad (6.3)$$

Figure 6.4 is a plot of the voltage limit imposed by the base for cells with high rear surface recombination velocities (S=10^6cm/s) for a range of cell lifetimes and material thicknesses from 100μm to 1mm. For the thinnest cells, the voltage is independent from the bulk lifetime with carriers diffusing from the junction to the rear to recombine. Improvements in bulk lifetime offer no improvements in cell voltage. Cell voltage improves as the cell thickness increases as the carriers find it harder to diffuse to the rear with the reduced gradient in carrier concentration. This trend continues for a given lifetime until the cell thickness approaches the diffusion length and the voltage depends more upon the cell lifetime.

Therefore, to maximise the voltage potential, the cell thickness needs to be greater than the diffusion length so that carriers cannot diffuse from the junction to the rear and recombine. In such long base cells, the dark saturation current only decreases as the inverse square root of lifetime, unlike thinner cells with a well passivated rear where saturation decreases as the inverse of lifetime. Consequently, lifetime improvements lead to smaller improvements in cell voltage.

A consequence of the the high recombination velocity at the rear is that carriers generated in the back half of the cell preferentially diffuse to the rear and recombine, rather than to the junction for collection. Therefore, carrier collection efficiencies in cells with high rear surface recombination will be poor, leading to relatively low currents. As cell lifetimes increase, cells need to increase in thickness to maximise cell performance leading to increased material costs.

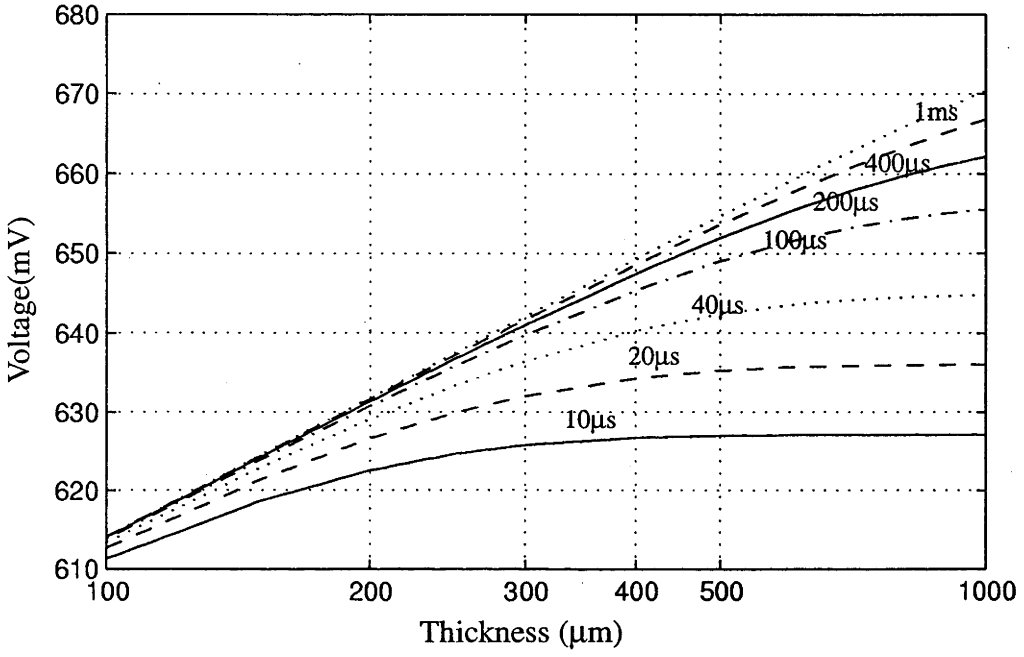

Figure 6.4: *Open circuit voltage cap of 0.5Ωcm cell imposed by high rear surface recombination as a function of cell thickness.*
For small substrate thicknesses, the recombination is dominated by recombination at rear surface and is independent of bulk lifetime. As the cell thickness increases to greater than a diffusion length, the cell voltage is dependant upon the bulk diffusion length. Maximising voltage requires cell thicknesses greater than two diffusion lengths.

Reduced surface recombination at the rear surface is therefore a better alternative for high efficiency cells.

6.3.2 *Cell structures to reduce rear surface recombination*

To achieve high open circuit voltages, effective rear surface recombination must become an important component of the cell design. To date, rear surface passivation of multicrystalline silicon solar cells has almost exclusively relied upon increased doping under total area rear metal contacts. This decreases the amount of recombination by decreasing the minority carrier concentration near the rear surface. This heavily doped region is known as the back surface field, for historical reasons [7]. The region of high doping can be produced by alloying aluminium into the rear of the cell or by diffusing boron.

The majority of multicrystalline silicon solar cells currently manufactured consist of a $n^+/p/p^+$ structure. The rate of recombination at the rear metal contacts of multicrystalline silicon solar cells is reduced by the increased doping level under the metal contact (back surface field). The entire heavily doped rear of the substrate is contacted by metal. Multicrystalline cells which hold the current record efficiency [18] and cells which have demonstrated high open circuit voltages (>640mV) [106,107,111] use this cell structure.

Cells with an aluminium alloyed rear were the first single crystal silicon solar cells to achieve efficiencies greater than 20% [113]. Aluminium alloyed cells are the most common design for high efficiency multicrystalline silicon solar cells. The gettering benefit provided by the aluminium on multicrystalline is well established [15], helping to maintain high minority carrier lifetimes in the multicrystalline silicon. The high minority carrier lifetimes provided by aluminium alloying have led to aluminium alloyed cells holding the multicrystalline silicon solar cell efficiency records since 1990 [16] with the current record efficiency 18.6% for a $1cm^2$ cell [18].

Despite the impressive results produced by aluminium alloying, the minority carrier lifetime in the current record efficiency cell has improved to levels where cell efficiency is limited more by surface recombination at the aluminium alloyed surface than by bulk recombination. Recombination velocities in recent record efficiency cells are of the order of $2x10^3$ to 10^4cm/s. This severely limits the open circuit voltage of cells with lifetimes of the order of 100μs. Low surface recombination velocities (<200cm/s) have been demonstrated on high resistivity 3Ωcm substrates [105] but similarly low levels have not been demonstrated on lower resistivity wafers. Analysis of single crystal aluminium alloyed cells have indicated that cells with thickness less than half a diffusion length (necessary for high current collection efficiency) will be limited to about 655mV [56]. Higher voltages are only possible in low resistivity cells with thickness greater than a diffusion length, sacrificing current for voltage.

Similar problems are likely to apply to cells with boron diffused rear surfaces. Boron diffused multicrystalline silicon cells are likely to have lower minority carrier lifetimes in the absence of the gettering benefit of aluminium. Despite this, high open circuit voltages (640mV) have been achieved on 0.2Ωcm multicrystalline silicon substrates [106,107] with boron diffused rear surfaces. However, rear surface recombination is not a major contributor to total cell recombination in these cells with voltages indicating diffusion lengths of the order of 100μm, much less than the substrate thickness.

Slightly higher voltages have been obtained with multicrystalline cells produced by liquid phase epitaxy [111]. 643mV was demonstrated on a 26μm epitaxial layer grown on a heavily doped multicrystalline substrate. This structure has the potential for voltages approaching the Auger limit [6] independent of the epitaxial layer doping and thickness provided that the diffusion length in the epitaxial layer is much greater than the epitaxial layer thickness. Single crystal silicon epitaxial layers have produced voltages of 663mV on heavily doped substrates [46], indicating that recombination in the epitaxial layer is limiting the efficiency of the multicrystalline silicon epitaxial cell.

The inability of back surface fields to further reduce rear surface recombination led to the development of the PERC structure [135], a novel single crystal silicon solar cell design, a decade ago. Recombination was decreased by reducing the area of the rear contacts. The regions between the contacts were well passivated with thermally grown silicon oxides. This development led to the first conventional (front emitter) silicon solar cells with open circuit voltage greater than 700mV. The short circuit current also improved due to the decreased rear surface recombination. Cells also benefited from improvements in NIR response due to improved internal rear surface reflection since aluminium covered oxidised silicon surfaces reflect up to 98% of incident light while aluminium alloyed cells reflect less than 70%. The improved NIR response was more pronounced on textured cells with light trapping. The widely spaced reduced area contacts increased contact and spreading resistance losses leading to slightly reduced fill factors. The net result was an efficiency gain over cells with a total area back–surface field with single crystal silicon cell efficiencies peaking at greater than 22% [17,135].

The suitability of reduced area contacts to reduce rear surface recombination on multicrystalline silicon solar cells was therefore investigated in section 6.5 in this research. Since multicrystalline silicon electronic quality is extremely sensitive to different processing steps and temperatures, the primary challenge is to maintain high minority carrier lifetimes without the gettering benefits of aluminium alloying. The processing sequences for multicrystalline silicon may differ from those required to produce similar cells on single crystal silicon.

Further improvements in single crystal single cell efficiency were obtained with the development of the PERL cell structure, where boron is diffused under the reduced area

rear metal contacts. The localised back surface field reduced recombination at the metal contacts and decreased contact resistance losses. Cells with the PERL structure hold the current single crystal silicon efficiency record of 24% [11]. The efficiency gain was obtained at the expense of increased processing complexity, requiring additional masking oxidations and the boron diffusion step. The PERL cell design on multicrystalline silicon was also investigated in this research and is treated later in section 6.6.

6.4 Long base cells

In the previous chapter, the 0.2Ωcm substrates demonstrated very high voltages due to the heavy doping of the substrate. The potential for voltage and efficiency gains from phosphorus gettering and 'tubs' texturing of the 0.2Ωcm substrates was investigated.

Even with phosphorus gettering, the 0.2Ωcm substrates have demonstrated lifetimes below 15μs, corresponding to diffusion lengths less than 175μm. Since the 0.2Ωcm substrates are relatively thick (380μm), rear surface recombination will have very little influence on cell performance. Consequently, this is a long base cell and the cell rear can be designed to maximise fill factor without concern for losses in voltage or current. This would usually point towards introducing a heavily doped region under the rear to minimise contact resistance, but shunting difficulties with Al alloying on the 0.2Ωcm substrates, risk of lifetime degradation with boron diffusions and the already relatively heavily doped substrate, lead to the choice of a simpler design with 100% Al contact to the substrate.

6.4.1 *Experiment*

Half the 0.2Ωcm substrates received phosphorus pre–gettering for three hours at 900°C followed by etching in HF/HNO_3 to remove the heavily diffused regions. A texture masking oxide was grown in steam for 2 hours at 900°C, followed by photolithography and texturing as described in section 6.2.1. After texturing, the masking oxide was removed and a phosphorus diffusion mask grown was grown in steam for 2 hours at 900°C. Solid source phosphorus diffusions for 20 minutes at 850°C produced sheet resistivities of 160–180Ω/□. A thin passivating oxide was grown for 21 minutes at 900°C followed by an anneal/drive–in at 900°C for 40 minutes. Cells were then metallised with Cr/Pd on the front using aligned photolithography and liftoff and the entire rear was deposited with evaporated aluminium. Cells were then Ag electroplated, sintered in forming gas for 20 minutes at 400°C and measured.

The best substrate then had a TiO_2 AR coating added, followed by tabbing, encapsulation and MgF_2 deposition. The cells were measured after each additional step.

6.4.2 *Results*

Cell performance varied greatly for both the gettered and the ungettered substrates. The efficiency of the bare gettered cells varied from 12.9 to 14.1%. The voltage on the better

cells was 652mV, dropping to 636mV on the worst cell. Currents were similar varying from 25.8 to 26.6mA/cm^2. The fill factor on the best cell was 82.2%. The worse cells demonstrated 'soft' fill factors dropping to 78.6% despite similar series resistance at open circuit voltage to the better cells. The fill factors, despite being very high for multicrystalline cells, contributed to half (4.5%) the total efficiency variation (9.3%).

The ungettered substrates also demonstrated high voltages of 618 to 640mV, and currents similar to the gettered substrates (25.3–26mA/cm^2). Fill factors however were mostly poor despite good shunt and series resistances, with fill factor varying form 0.787 on the better cells but dropping to 0.65 on the worst. Consequently, efficiencies were lower, varying from 10.7 to 13.0%.

The addition of the TiO_2 AR coating on the best cells increased current by 25%, increasing a further 2.5% with encapsulation. The MgF_2 increased the current by a further 2.5% to 34.9 and 35.0mA/cm^2. The current increase boosted the voltage by 7mV to 659mV, while the fill factor decreased slightly during TiO_2 deposition and tabbing to 0.814 and 0.804. Cell efficiency increased to 18.6% on both cells. The IV curve of one of the better cells is displayed in figure 6.5. The two best cells shared a relatively large grain (~3cm^2) but each cell contained more than 10 grains of varying sizes.

Reflectivity measurements were made on the best cells using a spectrophotometer and integrating sphere. The reflectance as a function of wavelength can be seen in Figure 6.6. The weighted reflectance relative to the AM1.5 global spectrum between 400 and 1050nm was 5.2%.

6.4.3 *Discussion*

The performance of the long base cells was surprisingly good. The best gettered substrate produced efficiencies of 18.6% for 4cm^2 devices. The high efficiency can mostly be attributed to the exceptionally high open circuit voltages and the low reflectivity from the 'tubs' textured substrate.

The excellent cell voltages are primarily due to the high substrate doping. Cell voltage increases with p–type substrate doping for long base cells provided the product De/Na.Ln decreases with doping. The dark saturation current for this cell is 2.55×10^{-13}Acm^{-2}. This indicates a minimum effective diffusion length of 125μm assuming no other recombination sources. A typical emitter saturation current contribution of 5×10^{-14}Acm^{-2} was calculated to increase the minimum bulk diffusion length to 150μm.

Cell efficiency was also assisted by the high device current, despite the short diffusion lengths in the 0.2Ωcm material. This was due to the very low reflectance from the encapsulated 'tubs' textured samples. The weighted reflectance was 5.2%, with a minimum reflectance of 3%. This is particularly remarkable, given that the coverage of the silver fingers was 3.5% (28μm on 800μm spacing). Encapsulation decreased the

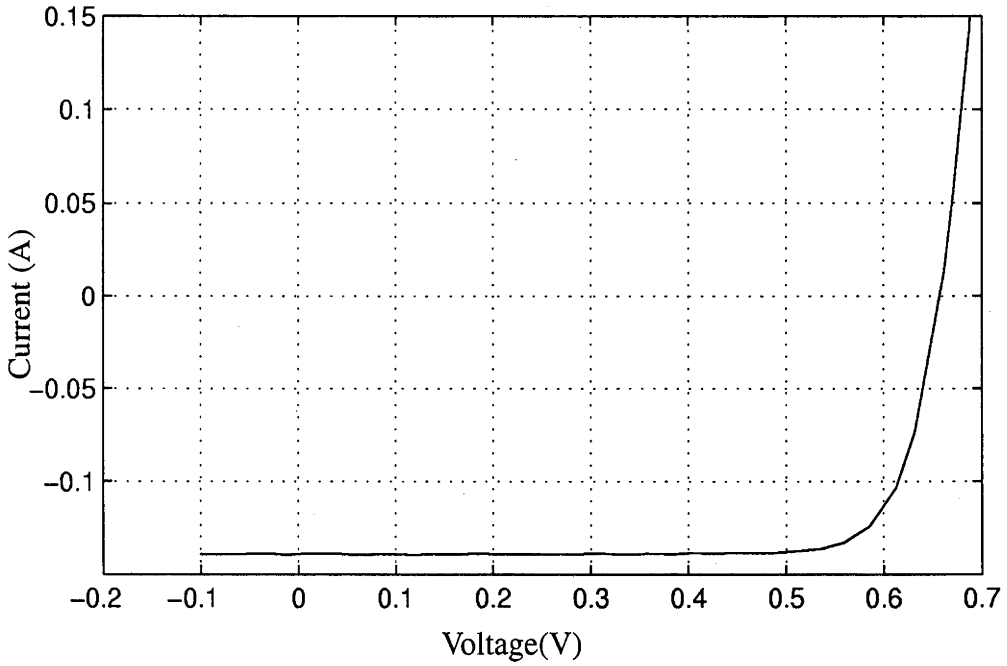

Figure 6.5: *Measured IV curve for the 18.6% efficient 'tubs' textured gettered 0.2Ωcm cell.*
The cell has demonstrated the highest recorded open circuit voltage for a multicrystalline silicon solar cell (659mV). Current is high due to the low reflection losses and light coupling due to the 'tubs' texturing.

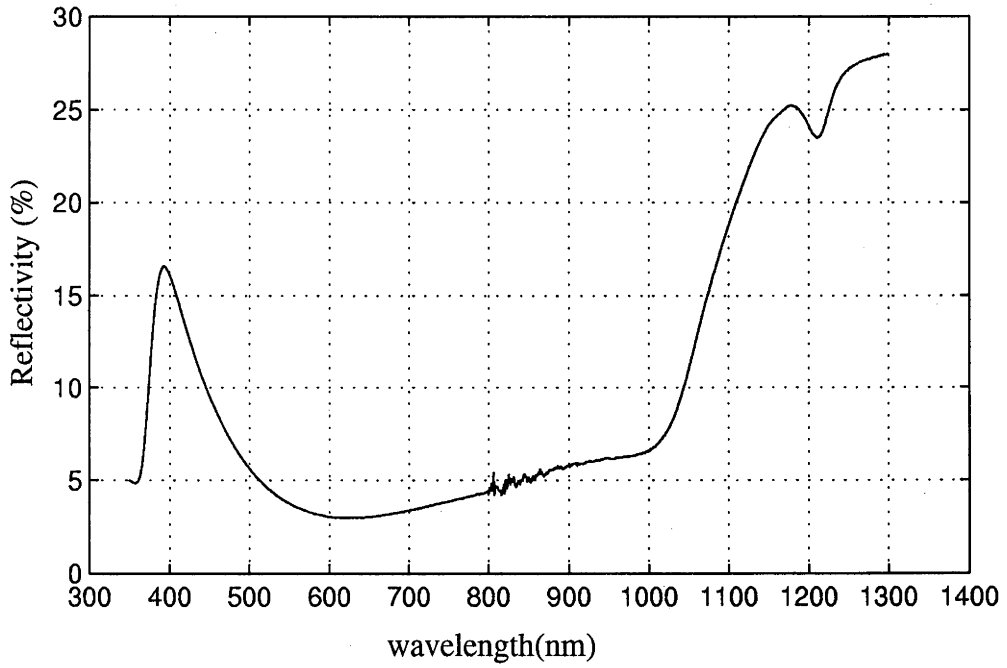

Figure 6.6: *Reflection losses from the 18.6% efficient 0.2Ωcm cell.*
The cell was 'tubs' textured with a TiO_2 AR coating added to the silicon, and MgF_2 on the glass. The minimum reflectance is 3% at 620nm with a weighted reflectance of 5.2% between 400m and 1050nm. The light trapping is excellent. The drop in reflectivity below 400nm and the small dip in the reflectivity at 1200nm are due to absorption in the EVA.

reflection losses from the metal fingers with much of the light reflected from the grid totally internally reflected onto the silicon at the glass/air interface. Encapsulation decreases reflection losses for semicircular cross section fingers to just 35% of the coverage area [44].

The fill factors of the better cells, despite being greater than 80%, were disappointing considering the cell design with high substrate doping and 100% rear metal coverage.

The better devices were simulated with PC–1D. Reflection losses were assumed to be 5%, as per the reflectance measurements. Accurate prediction of cell performances with a polished front surface required an increased substrate resistivity of 0.25Ωcm. A bulk diffusion length of 156μm, corresponding to a lifetime of 13μs produced a cell voltage of 659mV and cell currents of 34.9mA/cm^2. This was extremely close to the measured cell characteristics, and the bulk lifetime was close to the maximum achieved during gettering experiments (15μs). Attempts to accurately model the cell performance with the nominal 0.2Ωcm substrate resistivity proved difficult. Bulk diffusion lengths need to be shorter to accurately predict open circuit voltage due to the higher substrate doping. Consequently, current dropped to 33.1mA/cm^2. However, the modelling neglected the effects of texturing which would be expected to lead to enhanced absorption near the front surface and higher currents than would otherwise be expected for a given diffusion length. Internal quantum efficiency measurements would offer more insight into the effect of the texturing on cell current.

The excellent efficiency and cell performance with the long base 0.2Ωcm cells raises some interesting questions about the suitability for such substrates to improve cell performance in a commercial setting. The more heavily doped substrate clearly has the potential for improving the voltage of cells even with a simple cell design. The major concern would be the potential loss of cell current. The current in commercial screen printed cells is already limited by heavy emitter doping necessary for good contacts. Consequently, the cell current is primarily generated toward the red end of the spectrum. Decreases in cell diffusion length would therefore be expected to have a greater impact on the current of a screen printed cell than a cell with better blue response. The trade off between these two effects for screen printed cells would determine the potential efficiency benefit. The trend towards development of selective emitters for industry [136,137] could favour the use of more heavily doped substrates. The laser grooved buried contact cells developed by UNSW [138] used by BP Solar for their Saturn modules should have a blue response sufficient to benefit from more heavily doped substrates.

6.4.4 *Non–ideal fill factors in 0.2Ωcm cells*

The fill factors of most of the 0.2Ωcm cells were poor. Typical examples of this can be seen in cells s58b and s57aa in figure 6.7. The cells had a near linear increase in current between 100–400mV and the maximum power voltage. The IV curve of the cells demonstrated good shunt resistances in reverse bias (>1000Ω) and relatively low series resistance near

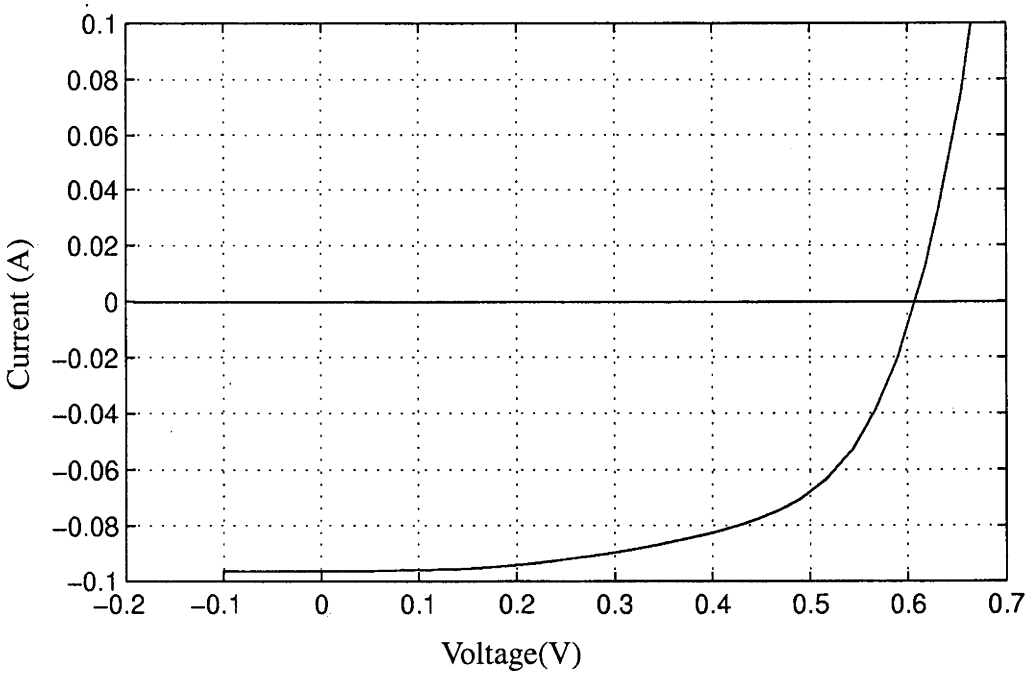

(a)

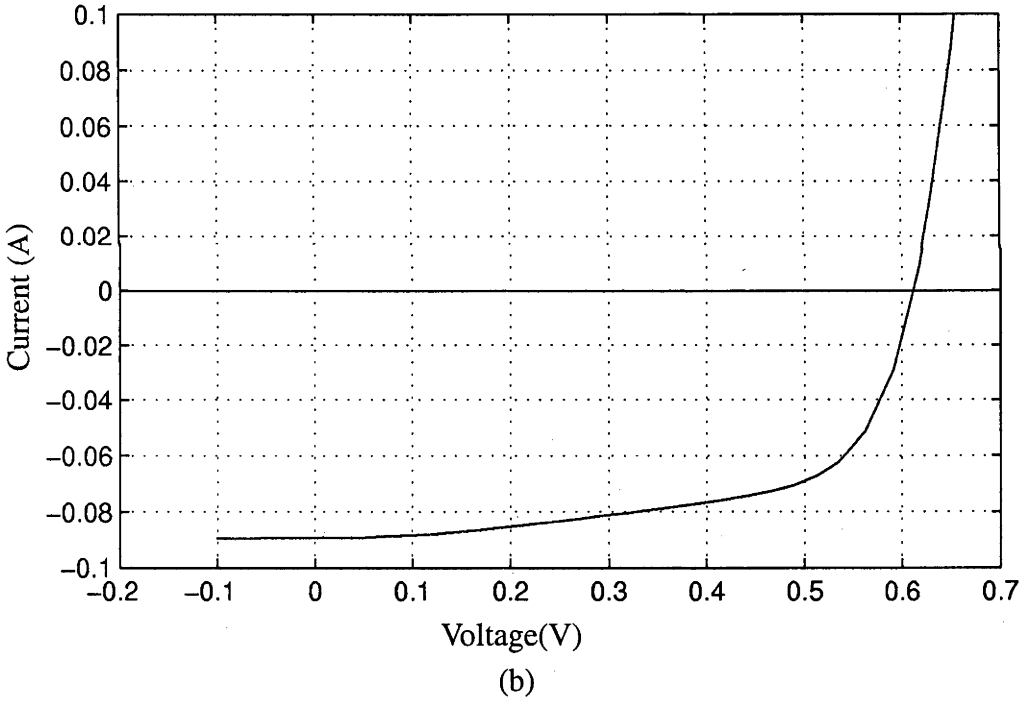

(b)

Figure 6.7: *0.2Ωcm cells with poor fill factors.*
a) Cell ID s58b V_{oc}*=606mV,* I_{sc}*=96.8mA and FF=59.4%*
b) Cell ID s59e V_{oc}*=611mV,* I_{sc}*=89.4mA and FF=63%*
The poor fill factors are characterised by a linear slope between 100–200mV and the knee of the curve. Cells typically have excellent shunt resistances in reverse bias. Despite their similar shapes, the poor fill factors have different causes. (a) is caused by distributed series resistance while (b) is caused by a shunt in series with a schottky–like diode.

open circuit voltage. The poor fill factors were independent from the quality of the cell current and voltage.

Further information on the behaviour of the substrates was obtained by investigating the cell's IV characteristics at different light intensities. Illumination intensity was varied from one seventh of a sun, to one sun to one and a half suns. This led to decreases in fill factor on s58b from 69.6, to 59.4% and finally 56.4%. Behaviour of s59e was markedly different, with fill factors increasing from 34% to 67%. Clearly, two different mechanisms were at work.

The improvement in fill factor with illumination on s59e pointed towards shunt like behaviour in the cell (despite the lack of a shunt in reverse bias). Currents in the dark and illuminated IV curves were similar below 500mV with differences in the curves at higher voltages caused by series resistance losses (Figure 6.8). Qualitatively, the shape of the curves where they overlap is similar to that expected from a shunt. However, figure 6.9 demonstrates that the curves could not be modelled with a shunt resistance in parallel with the cell. The reverse current was very small indicating a shunt resistance greater than 2000Ω in reverse bias.

It appeared that a shunt would have provided a better explanation of the low current behaviour if a small voltage was required to 'turn on' the shunt in forward bias. This combined with the excellent shunt resistance in reverse bias pointed towards a diode in series with a shunt resistance. A model of a shunt in series with a diode (figure 6.10) was fitted to the low current region of cell s59e. The result of this modelling can be seen in figure 6.11. There was excellent agreement between the cell current and the model below 500mV. The cell recombination behaviour in the absence of the shunt can be found by subtracting the model from the dark IV curve. The cell demonstrated ideality factors which increased from 1.7 at 450mV to 1.35 at 550mV before series resistance effects dominate and the slope of the curve decreases beyond 600mV. The fill factor increased with increases in illumination since the fraction of the total current through the shunt at maximum power decreased and the maximum power current therefore increased as a fraction of the short circuit current.

The shunt/diode behaviour was the primary cause of poor fill factors in the 0.2Ωcm substrates. The shunt resistance varied greatly between substrates leading to large differences in fill factors (table 6.1) The shunt resistance can be sufficiently small to significantly reduce the open circuit voltage of the device. Subtracting the shunt/diode current from the illuminated IV curve leads to the conclusion that the 35Ω shunt had little

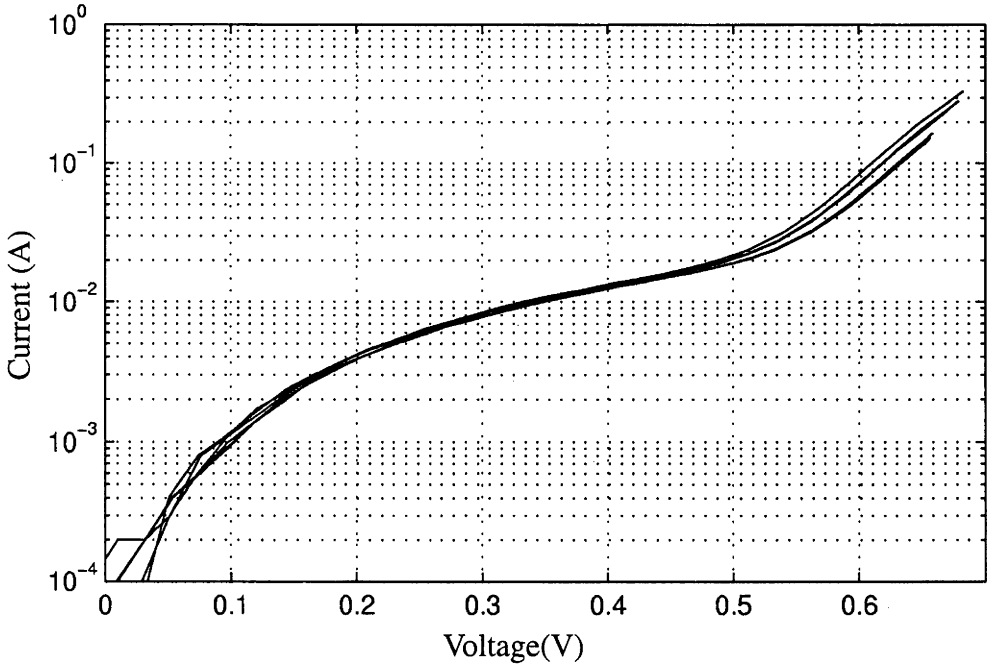

Figure 6.8: *IV curves for cell s59e at different illumination levels. The curves are shifted by the short circuit current. The curves correspond to the dark and 1/30, 1/7, 1, 1 1/2, and 2 sun illumination. The IV curves are similar for voltages below 500mV. Slight differences appear at higher voltages due to series resistance losses.*

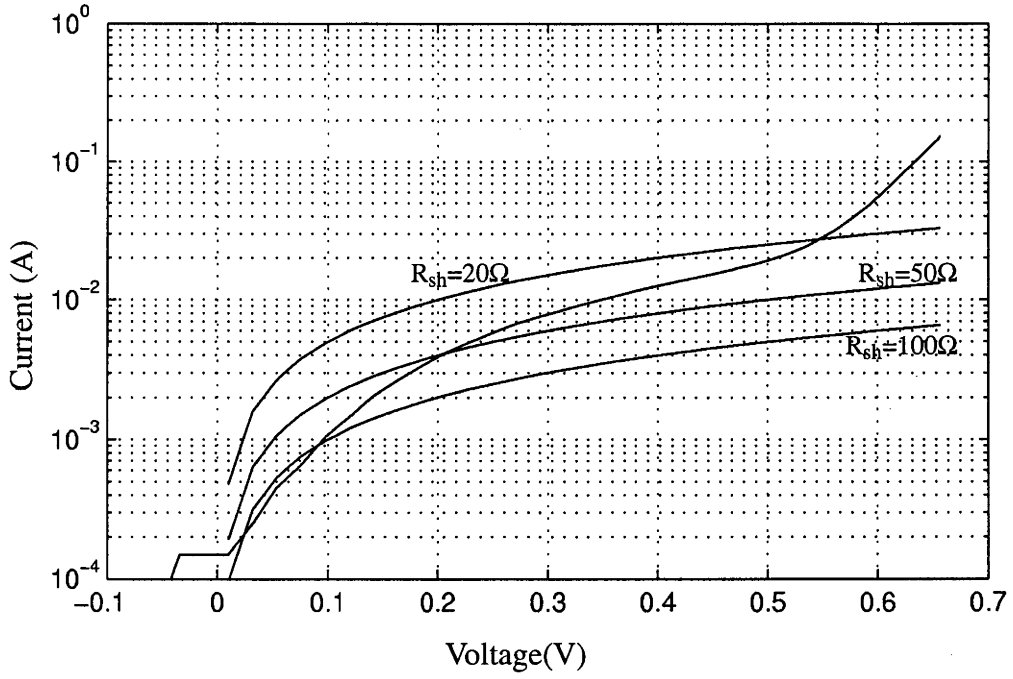

Figure 6.9: *Comparison of dark IV curve for s59e and modelled shunt behaviour. The forward bias current of cell s59e at low currents is not well modelled by pure shunt resistance. In reverse bias, the cell demonstrates currents less than 0.5mA at 1V (i.e. R_{sh}>2000Ω)*

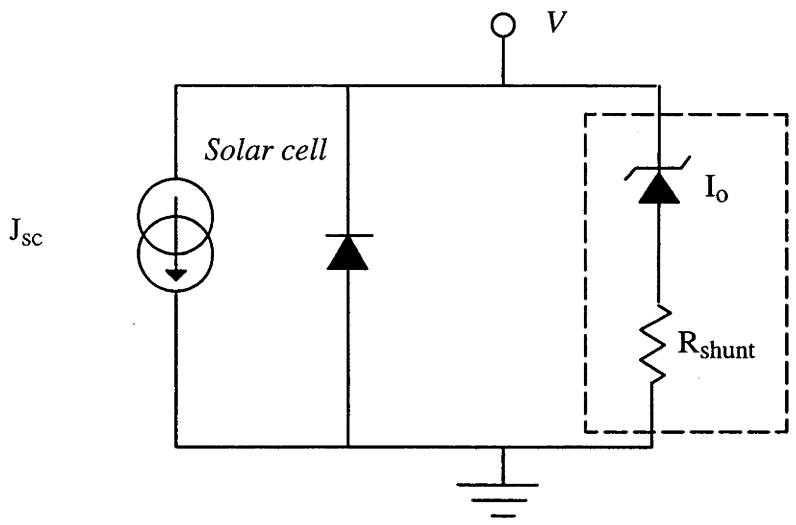

Figure 6.10: *Model of solar cell with shunt in series with a diode.*
The model consisted a solar cell in parallel with a shunt resistance and a diode with low turn on voltage (large I_o). The region in the dashed box was fitted to the low current region of the dark IV curve.

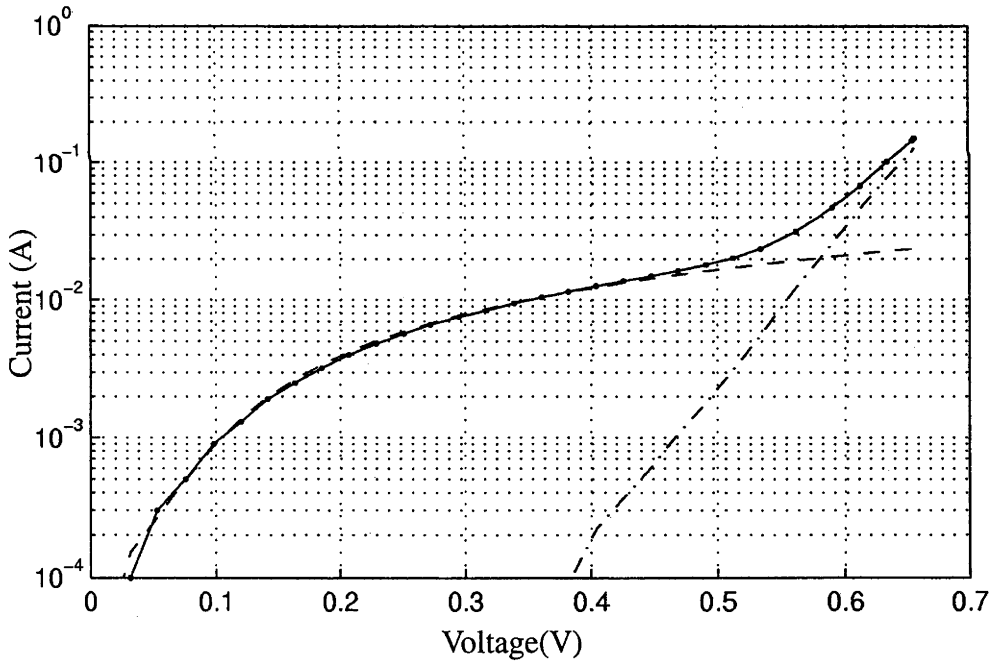

Figure 6.11: *The modelled fit of the shunt in series with a diode for cell s59e.*

—— *dark IV*
– – – *modelled shunt/diode*
– – *dark IV –modelled shunt/diode*
The shunt/diode model explained the cell behaviour at low forward currents. Excellent reverse bias shunt resistance was provided by the shunt diode. The shunt diode has a high J_o ($4x10^{-5}Acm^{-2}$) hence a low turn on voltage while the shunt resistance was 20.6Ω. The behaviour of the cell (figure 6.8) and the model at low currents was independent from illumination level.

effect on the open circuit voltage of s57aa while the 4.5Ω shunt in s57c decreased the open circuit voltage by 75mV.

Cell ID	Rsh(Ω)	Diode I_o (A)	FF	V_{oc}(mV)	V_{oc} (mV) (no shunt)	V_{oc} loss (mV)
s59e	20.6	4.10^{-5}	67%	611	622	11
s57aa	35	10^{-6}	73%	635	639	4
s57c	4.5	10^{-4}	38%	568	643	75

Table 6.1: *Modelled shunt resistance and diode saturation current to fit cell current voltage characteristics.*

The cause of the shunt was difficult to identify. The very low turn on voltages for the diode point towards a Schottky–type metal silicon contact. There is a trend of increasing diode saturation current with decreasing shunt resistance suggesting a relationship between the area of the Schottky diode and the shunt resistance. The prevalence of the shunt/diode on multicrystalline silicon substrates may be due to the roughness of the multicrystalline silicon surface, since the substrates were not polished. This could cause difficulties during photolithographic liftoff or lead to damage to the emitter junction during handling with the consequence that the front contact directly contacts the p–type substrate

Despite the similarity of the shapes of the IV curves, the poor fill factors in some cells (e.g. s58b, figure 6.7(a)) was not due to the diode/shunt behaviour. Fill factors were observed to decrease with increasing illumination, indicating a series resistance problem, rather than a shunt. The dark IV curves for different illumination levels on s58b in figure 6.12 differed greatly at low currents, further evidence supporting large series resistance losses in the cells but the series resistance near open circuit voltage appeared to be low. This was confirmed by comparing the IV curve of s58b at one sun illumination to modelling (figure 6.13) for a range of resistances in series with a two diode model fit of I_{sc} versus V_{oc} (to eliminate series resistance effects). Around open circuit voltage, the one sun IV curve was bounded by the models for 0.25Ω and 0.5Ω series resistance while at lower voltages the current was bounded by 2Ω and 4Ω models.

Such behaviour indicated that the cell had a region of high series resistance and other areas of more typical low series resistance. At low applied voltages, the bad regions were driven further into forward bias by the photogenerated current flowing through the region of high resistance, leading to decreased current. As the photogenerated current increased due to increased illumination, the bad region was forward biased at lower applied voltages leading to lower fill factors. As the applied voltage increased beyond open circuit voltage, both regions of the cell were in forward bias. The majority of the current then flowed through the good region of the cell where the resistance was lower. The resistance approaches the resistance of the good and bad regions in parallel. Consequently the cell would appear to

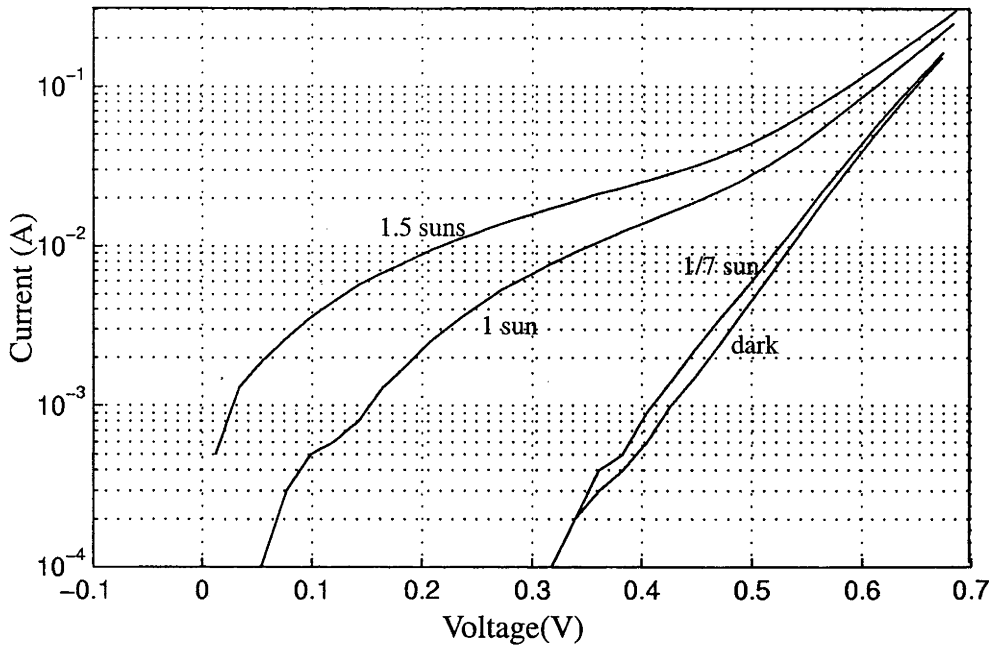

Figure 6.12: *IV curves for s58b for different illumination levels.*
As the illumination intensity and, therefore, the short circuit current increase, the voltage difference between the curves at low currents increases.

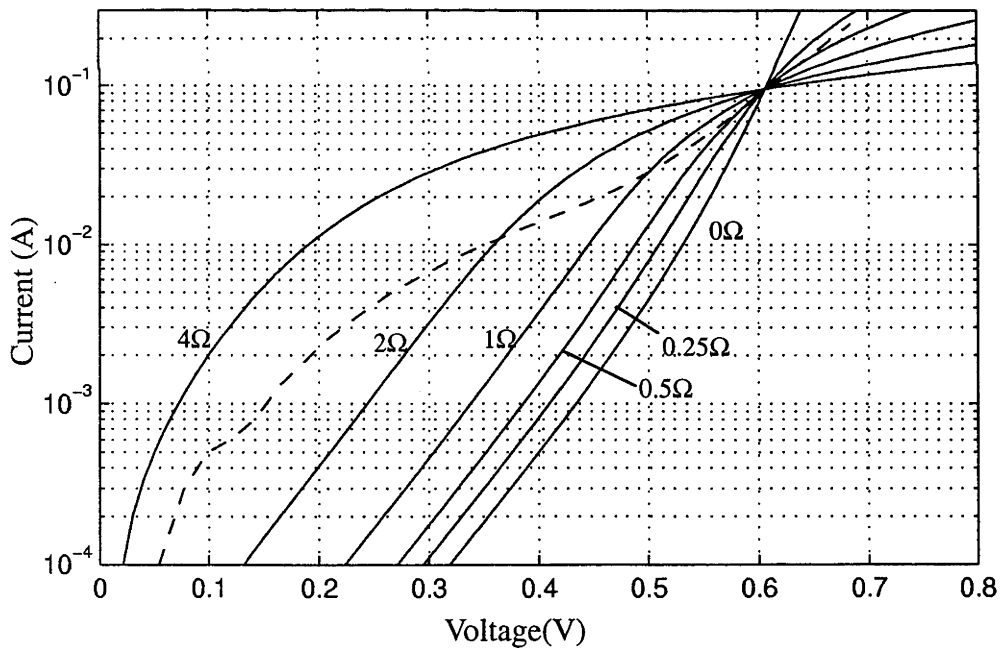

Figure 6.13: *Modelled effect of varying a single global series resistance on cell behaviour at one sun illumination.*
Cell behaviour is not well described by a single series resistance. At higher voltages the cell current is bounded by the models for 0.25Ω and 0.5Ω while at low voltages, the cell current is bounded by the 2Ω and 4Ω models.

have relatively good series resistance at higher voltages while having poor apparent series resistance at lower voltages.

This effect was modelled analytically. The model used can be seen in figure 6.14. A fraction of the cell, f, is connected to a high series resistance in parallel with the remainder of the cell, which is in series with a low series resistance. Diode saturation currents I_{o1} $=4x10^{-12}Acm^{-2}$ and $I_{o2}=2x10^{-7}Acm^{-2}$ were fitted to I_{sc} versus J_{sc} for a range of illumination levels. This fit was not exact since the ideality factor of the cell remained below 1.3 at higher illumination levels. The model resistances and poor fraction, f, of the cell were adjusted to fit the one sun IV curve. The poor fraction, f, was found to be 30% with a series resistance of 3.5Ω while the remainder of the cell was found to have a relatively low resistance of 0.2Ω. Adjusting the short circuit current showed good agreement with the cell behaviour at different light intensities, as shown in figure 6.15.

The cause of the high series resistance in a large region of the cell was a poorly defined front metal grid. The grid was poorly defined during photolithography with breaks visible under the microscope in almost all the metal fingers after electroplating. Measurements of the resistance from the bus bar to other areas of the grid varied from less than 0.1Ω near the bus bar up to 40Ω at points on the grid at the opposite end of the cell. The good region/bad region model was therefore oversimplified, with the cell broken into many more regions with different series resistance, but provided the basis for explaining the observed behaviour.

6.4.5 *Conclusions on long base cells*

The efficiencies of the long base cell were impressive for a simple cell design (>18%). The cells benefited from the high substrate doping which enabled high cell voltages (>650mV) to be achieved. 'Tubs' texturing contributed to the good cell performance, reducing reflection losses and causing increased absorption of light near the front junction, improving cell current.

The long base cell design was limited to low lifetime substrates (<20μs) otherwise substrate thickness needs to be increased to avoid recombination losses at the rear surface. This limits its potential use for higher resistivity substrates with correspondingly higher lifetimes. Further efficiency gains rely on continuing improvements in the lifetimes of heavily doped multicrystalline silicon substrates.

Frequent fill factor problems in the 0.2Ωcm cells were identified to be due to shunts or processing problems related to the front metal contacts, rather than internal recombination in the material.

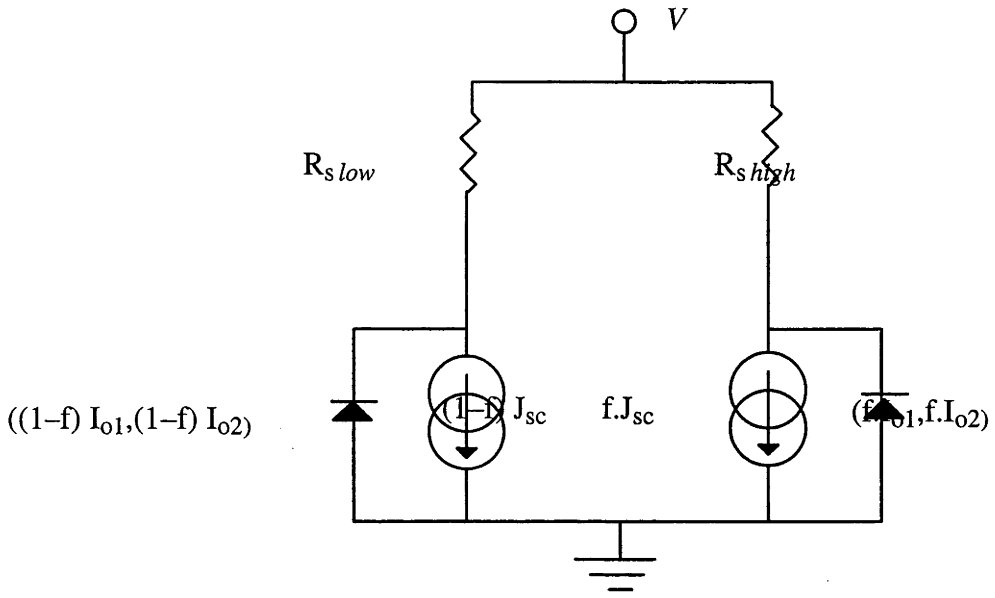

Figure 6.14: *Model for distributed series resistance.*
The model consisted a solar cell in series with a low resistance in parallel with a solar cell in series with a high resistance. A fraction, f, of the total solar cell area is in series with the high resistance, with current and dark saturation currents appropriately scaled.

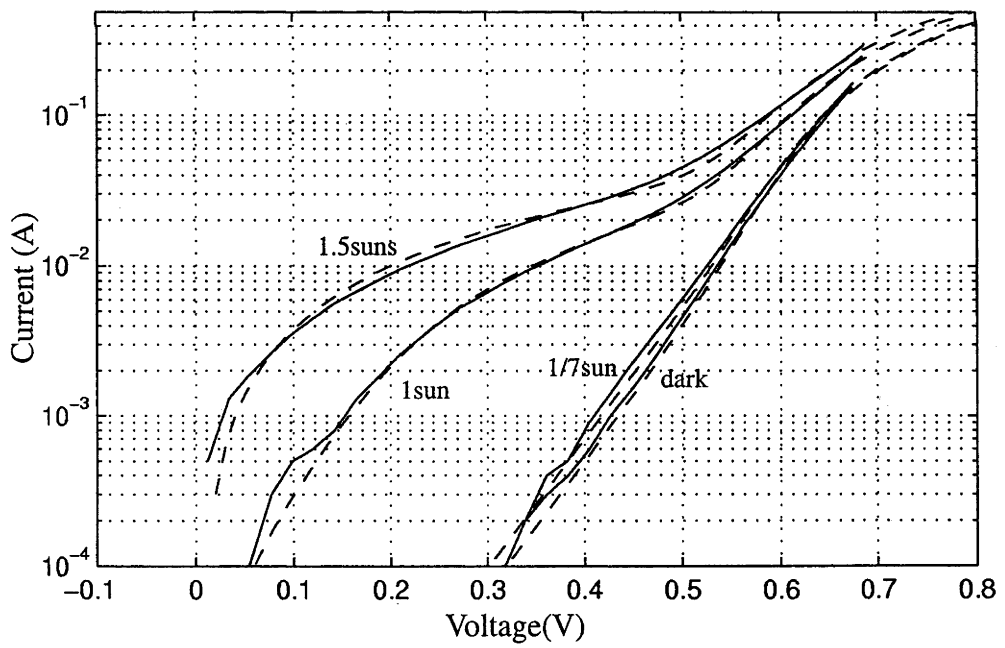

Figure 6.15: *Measured and modelled IV curves for a cell (s58b) with distributed series resistance for a range of illumination intensities.*
——— *measured*
— — — *modelled*
The dark IV curve is not well fitted with an n=1,n=2 two diode model. Despite this the cell behaviour is described by 30% of the cell having a high series resistance (3.5Ω) with the remainder of the cell having a low resistance (0.2Ω).

6.5 Reduced rear contact cells

While the results for the long base 0.2Ωcm cells were excellent, greater potential for further efficiency improvements are apparent in short base cells with good rear surface passivation, as discussed in section 6.3.2.

The next development in high efficiency single crystal silicon solar cells to reduce rear surface recombination after the aluminium alloyed cells were the reduced rear contact cells [135]. The metal contact area to the rear of the cell is reduced with the majority of the rear passivated with a thermally grown, which provides excellent surface passivation. A schematic of the cell design can be seen in figure 6.16.

Modelling of the reduced area contact structure indicates that improvements in voltage and current can be achieved with increased spacing and decreased contact fractions but this needs to be considered in the context of increased resistive losses [139,140]. Surface recombination is reduced by both the reduced metal contact area so that the carriers have less area to recombine and by increasing the spacing of the contacts, so that the minority carriers have further to diffuse to recombine. In the limit of closely spaced contacts (<<diffusion length) the effective rear surface recombination velocity can be determined as the area weighted sum of the surface recombination velocities of the oxide and the metal contacts [139]. Consequently very small metal contact fractions (<<1%) would be needed to reduce surface recombination velocities below 10^4cm/s at the cost of increased contact resistance. Lower effective surface recombination velocities can be obtained by increasing the contact spacing, preferably to greater than a diffusion length.

While requirements of small contact fractions and wide contact spacings are desirable for low surface recombination, the consequence is increased resistive losses. Small contact fractions increase the contact resistance loss, which increases at higher substrate resistivities. Increased contact spacing leads to greater resistance losses in the bulk. This can be alleviated with increased substrate doping, both due to the increased conductivity and reduced spacing required with the decreased diffusion length.

Avoiding resistance losses led to the use of 280μm 0.2Ωcm Fz substrates in record efficiency PERC cells [141]. The lifetime in these substrates was in excess of 160μs, ensuring diffusion lengths greater than the substrate thickness. The heavy doping enabled excellent fill factors to be demonstrated despite small contact fractions (<0.5%) and large contract spacings (2–4mm). The best cell produced a then record efficiency of 22.6% (subsequently adjusted with recalibration of test centres in 1990 [17]) with a voltage 694mV, current of 40.0mA/cm^2 and FF of 81.4%. The metal contacts contributed to 30% of total recombination with 705mV obtained on a cell with rear metal contacts placed outside the active area of the cell.

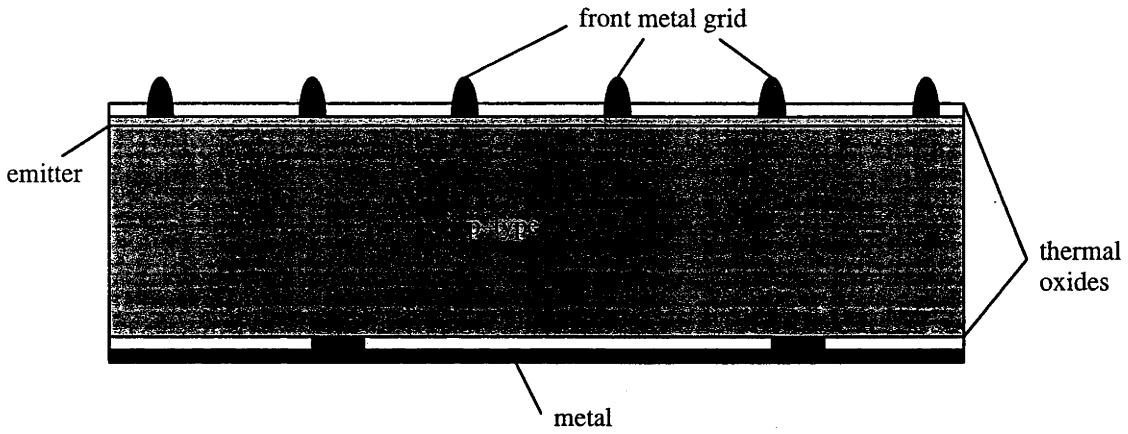

Figure 6.16: *Schematic diagram of the reduced rear contact cell design. The majority of the rear is covered with a passivating thermal oxide. The high surface recombination velocity metal/silicon contacts are restricted to a small fraction of the rear.*

6.5.1 *Multicrystalline silicon reduced rear contact cells*

A choice of multicrystalline silicon substrate resistivity for the investigation was required. In multicrystalline silicon, this appears to be a trade off between sufficiently low resistivity to ensure small resistive losses while maintaining diffusion lengths greater than the substrate thickness. The 1.5Ωcm substrates had excellent diffusion lengths, much greater than the substrate thickness, but the low substrate doping would lead to large resistance losses in the cell both at the rear metal contacts and within the silicon bulk. The 0.2Ωcm substrates alleviate the resistance problems, but the diffusion length was much less than the substrate thickness. An intermediate substrate resistivity (0.5Ωcm) was therefore obtained to examine the efficiency potential of reduced rear contact area cells.

6.5.1.1 *Experimental*

Investigations concentrated on p–type 350μm 0.5Ωcm substrates from Eurosolare. Quasi–steady state photoconductance measurements of minority carrier lifetime were made on phosphorus gettered samples. Lifetime measurement samples were prepared with a heavy $POCl_3$ phosphorus diffusion followed by chemical etching of the heavily diffused layer. The surfaces of the substrate were then passivated with a light $POCl_3$ phosphorus diffusion combined with a brief thermal oxidation, and sintered in forming gas before measurement. Lifetime measurements of the gettered 0.5Ωcm multicrystalline substrates varied from 40 to 90μs which corresponded to diffusion lengths ranging from 350 to 550 microns. Recombination at the rear of the cell was therefore likely to be important, with the potential for benefit from a suitably designed rear.

Cells were phosphorus diffused for four hours at an optimised gettering temperature of 900°C. The resulting diffused layer had a sheet resistivity around 10Ω/□. The heavy phosphorus diffusion was etched from both surfaces with a 10/1 HNO_3/HF solution. An emitter masking oxide was grown in a steam ambient for two hours at 900°C. 2x2cm^2 windows through the masking oxide were defined using photolithography. The n^+ emitter was formed by phosphorus diffusions from solid sources at 850°C for twenty minutes to produce an emitter sheet resistance around 150–180Ω/□. The phosphorus glass was then removed, leaving most of the masking oxide on the rear for surface passivation. A thin oxide for emitter passivation was grown at 900°C for 21 minutes followed by a N_2 anneal for forty to sixty minutes. Front and rear contacts were defined with photolithographic liftoff, followed by the evaporation of aluminium over the rear and silver electroplating of the front grid. A variety of rear contact areas and spacings were investigated. Cells were then annealed at 400°C for twenty minutes in forming gas (4%H_2/Ar).

The best cell had a TiO_2/MgF_2 double layer antireflection coatings added to reduce front surface reflection losses.

6.5.1.2 *Results*

The results for the best cells for a range of different contact geometries are summarised in table 6.2. The cell with 100% rear metal contacts had the lowest current and voltage, but benefited from the highest fill factor to produce a good efficiency of 12.2%. Reducing the rear contact fraction improved the voltage and current on all the cells, but at the expense of decreased fill factors. The largest decrease in fill factor occurred for the smallest contact fraction (1%) despite the closest contact spacing. Better fill factors were achieved with larger contact spacings (3–6mm) but with large contact fractions (10%). 1mm on 3mm (10%) spaced contacts typically had fill factors between 0.78 and 0.80, unless non ideal resistive effects occurred (see section 6.4.4). The best cells had 1mm contacts on 3mm spacing and produced efficiencies of 12.6% and voltages of 644 and 646mV.

cell ID	spacing (mm)	contact percentage	V_{oc} (mV)	J_{sc} (mA/cm$^{2)}$	fill factor (%)	efficiency (%)
S61b	–	100	627	24.0	80.8	12.2
S62c	2	1	637	24.3	77.2	11.9
S61bb	3	10	646	24.9	78.3	12.6
mg4b (with DLAR)	”	”	644 (654.4)	24.5 (34.8)	79.9 (79.7)	12.6 (18.2)
S62cc	6	10	640	24.3	79.3	12.4

Table 6.2: *Performances of the best 0.5Ωcm reduced rear contact cells with different contact geometries.*

The addition of the TiO_2/MgF_2 DLAR coating improved the current of the best cell by 42% and improved the cell voltage by 10mV. Indoor measurement under a tungsten lamp demonstrated a voltage of 655mV, fill factor of 0.803 and current of 34.9mA/cm^2, relative to a Frauhaufer ISE calibrated Fz reference. The cell was then independently measured by NREL. The current and voltage were found to be similar at 34.8mA/cm^2 and 654.4mV, but the fill factor dropped by almost 1% to 0.797, confirmed during remeasurement on the cells return. The fill factor drop reduced cell efficiency from our original in–house measurement of 18.4 to 18.2%.

The measured reflection losses from the cell after the addition of the DLAR coating can be seen in figure 6.18. The reflectivity has a minimum of 3% around 800nm and a weighted reflectance of 6.5% relative to the AM1.5 global spectrum between 400 and 1050nm. The substrate was not textured and the reflectivity above 1000nm was high.

The dark IV and illuminated IV curves for mg4b were measured to provide information on resistive effects. These are plotted in figure 6.19. Some shunt–like behaviour occurs below 550mV, but has little effect on the cell current at maximum power. The cell was fitted with a 2 diode model with $I_{01}=6.5\text{x}10^{-13}\text{Acm}^{-2}$ and $I_{02}=8.3\text{x}10^{-8}\text{Acm}^{-2}$ and series

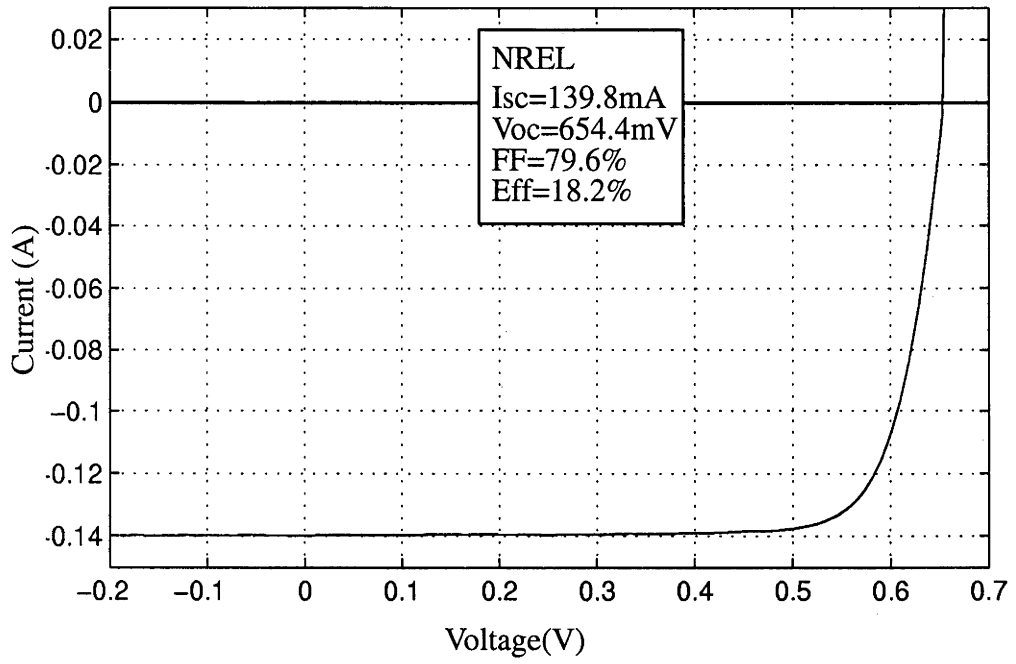

Figure 6.17: *IV curve of mg4b measured by NREL.*
This is the highest independently confirmed voltage for a multicrystalline silicon solar cell. This was due to the low rear surface recombination afforded by the reduced rear contact design. Efficiency was not sacrificed for voltage, with high currents and fill factors.

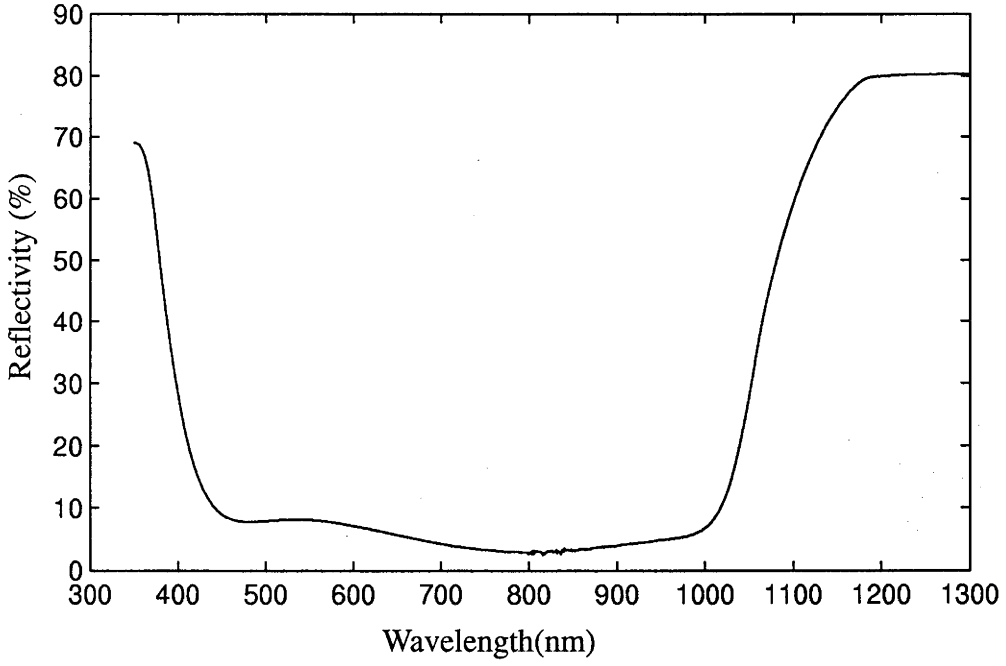

Figure 6.18: *Reflection from mg4b with MgF_2/TiO_2 DLAR coating.*
The cell had a minium reflectance of 3% around 800nm and a weighted reflectance of 6.5% between 400 and 1050nm. In the absence of texturing, the light trapping was poor causing large reflection losses above 1000nm.

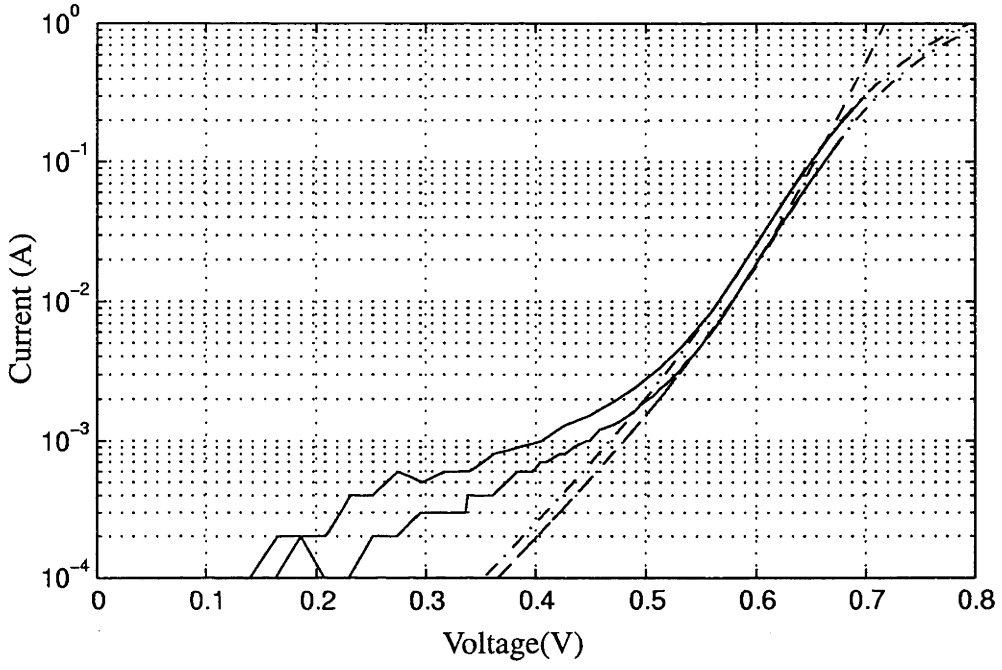

Figure 6.19: *The measured and fitted IV curves for mg4b.*
——— *measured (dark (right) and illuminated (left))*
— — — — *fit for V_{oc} vs J_{sc} (no series resistance)*
— · — *fit with series resistance (dark (right) and illuminated (left))*
The cell demonstrates non–ideal resistive effects at low currents. The cells can be well fitted with a two diode model for currents greater than two milliamps. The ideality factor of the cell increased from n=1.1 at open circuit voltage to n=1.5 at maximum power (550mV). The high ideality factor limits the fill factor of the cell.

resistance of 0.09Ω (4cm^2 cell) in the region where the shunt had little effect, as shown in figure 6.19. The ideality factor of the cell increased from 1.1 at open circuit voltage to 1.5 at maximum power (550mV).

6.5.1.3 *Discussion*

Cell performances varied with the range of different rear surface contact areas and spacings. The electrical parameters of the cells with the best electrical characteristics are listed in Table 6.2 The current and efficiencies were low due to the absence of any antireflection coatings.

The voltage for cells with 100% metal coverage was limited to below 627mV. This is in excellent agreement with the voltages predicted in figure 6.2 for cells with high rear surface recombination velocities and lifetimes of 50 to 100 μs (allowing for a 9mV voltage reduction due to the low current without AR coating). Further improvements in cell lifetime was expected to yield minimal improvement in cell voltage or efficiency, with recombination at the rear surface the dominant source of cell recombination.

The benefit of decreasing the contact area and increasing the contact spacing can be seen from the results for the other cells in Table 6.2 The reduced area contacts led to an increase in cell voltage and current, at the expense of slight decreases in fill factor. Peak voltage on the cells with 3mm spacing is 644mV, which is 17mV greater than the cells with 100% metal coverage, indicating a 50% decrease in the total recombination in the cell. The diffusion length of the 0.5Ωcm substrates after processing is greater than the wafer thickness since the voltage improved significantly with the change in rear contact pattern. The decrease in recombination can be explained by the cell effectively being composed of a good diode (regions covered in oxide) in parallel with a poor diode (regions within one or two diffusion lengths of the metal contacts) with the total recombination the sum of these contributions [141]. The cell with 100% rear contact consists of only the poor diode.

The significance of the reduction in surface recombination caused by replacing 90% of the rear contact with thermally grown oxide is clear by comparing the voltage obtained with the voltages in Figure 6.2. Cells with a back surface field could only achieve 654mV if the effective rear surface recombination velocities are reduced to the range of 100 to 800cm/s for lifetimes in the range of 50 to 100us, respectively. This is substantially better than the surface recombination velocity of 2000cm/s demonstrated with aluminium alloying on the current record efficiency 0.65Ωcm multicrystalline silicon cells [18].

A MgF_2/TiO_2 double layer antireflection coating was added to the best cell (mg4b) and independently tested at NREL. The antireflection coatings increased the cell current by 42%, to 34.8mA/cm^2. The current improvement led to an increase of 10mV in the open circuit voltage to 654.4mV, the highest independently confirmed open circuit voltage for a multicrystalline silicon solar cell. The high voltage is not at the expense of efficiency with

the cell demonstrating an impressive efficiency of 18.2% on 4cm^2 cells (current 18.6% record efficiency cells are 1cm^2).

The primary limit to the fill factor of the best cell was the ideality factor at maximum power. Investigating the illuminated and dark cell behaviour (figure 6.19) showed that the ideality factor, even at open circuit voltage was higher than 1. This was caused by the large n=2 diode saturation current, probably resulting from the grain boundaries or possibly the injection level dependence of the rear oxide [142]. At open circuit voltage, the ideality factor was 1.1, which led to the 10mV improvement in open circuit voltage after the current boost from the DLAR (rather than the expected 9mV). As the cell approaches the maximum power point, the ideality factor increases to 1.5. This reduces the potential upper limit for the fill factor of the cell by 3% to 81.2% compared to 83.8% which could be achieved with an ideality factor one cell with the same open circuit voltage [5]. Series resistive losses account for the remaining 2% of the fill factor loss.

The reflection losses from the cell also restricted the cell efficiency, despite the DLAR coating. Texturing should assist in reducing the reflection losses and boost light absorption. 'Tubs' texturing has the potential to reduce the direct reflection losses from the cell from 6.5% to around 5.2% (figure 6.6). Further benefit could be gained from the light trapping properties of 'tubs' texturing leading to improved red response. 'Tubs' texturing of reduced rear contact cells was therefore investigate in the next section.

An attractiveness of the rear reduced contact cells was the simplicity of the processing sequence. The masking oxide from the phosphorus diffusion was retained to passivate the rear surface and holes were opened through the oxide before metallisation, otherwise the processing sequence was similar to that for the simple cells investigated in Chapter 5. Excellent performance was obtained from cells with coarse 1mm on 3mm spaced contacts opening the possibility for more commercially viable metallisation approaches, such as screen printed contacts driven through the rear passivation.

Further improvements in the efficiency of the reduced contact design will primarily be achieved by further improvements in the bulk lifetime and rear passivation of the multicrystalline substrates. These improvements may result from improvements in the quality of as–manufactured multicrystalline silicon or by improving the process sequence to maximise the minority carrier lifetime of the material after processing. Investigations of low temperature surface passivation techniques has led to the development of plasma enhanced deposition of Si_3N_4, which demonstrate surface recombination velocities lower than good quality thermal oxides [36]. Use of low temperature passivation may avoid the lifetime degradation which can result from high temperature oxidations.

6.5.2 *'Tubs' textured reduced rear contact cells*

Addition of 'tubs' texturing to the reduced rear contact cell design was identified in the previous section as a design change with the potential to improve cell currents and

efficiency. Two different process sequences were developed to incorporate 'tubs' texturing in the cell design. In process one, an additional etch mask oxide for texturing was grown between the gettering and the diffusion oxide mask growth steps. In process two, the masking oxide growth time was lengthened, to ensure that the oxide was sufficiently thick to act as an etch mask and subsequent diffusion mask.

6.5.2.1 *Experiment*

Two process sequences were investigated for 'tubs' texturing, as summarised in figure 6.20. Process 1: 'Tubs' texturing on the 0.5Ωcm substrate followed the same processing sequence as the previous section, except that the sequence had an additional 2 hour masking oxide grown in steam at 900°C for a texture mask. The substrate was textured as per section 6.2.1. The remainder of cell processing followed the same protocol as in 6.5.1.1. for diffusion mask oxide growth, emitter diffusion and thin oxide growth. Rear contact metallisation was 1mm holes on 3mm spacing.

Process 2: The sequence for the second process was similar except a 4 hour steam oxidation at 900°C was used for the texture etch mask, with the oxide retained as an emitter diffusion mask. The remainder of the cell process sequence was the same as for process 1.

6.5.2.2 *Results*

Cell performances with process 1 were disappointing after the excellent efficiencies without 'tubs' texturing. Voltages on all the cells were below 635mV, with the majority between 615mV and 630mV. A plot of current as a function of voltage can be seen in figure 6.21. Cell current demonstrated a strong correlation with voltage improvement. Pairs of cells from the same substrate demonstrate higher or lower currents than the average trend. The fill factors on the cells which were well behaved demonstrated fill factors between 77 and 79%, with fill factors as low as 63% on cells with 'soft' fill factors. The best cell demonstrated an efficiency of 13.9% with 634mV open circuit voltage, 27.9mA/cm^2 current and 78.9% fill factor. Most cells had efficiencies between 12.5% and 13.5%.

The long oxidation process led to an increased spread in cell performances, as shown in figure 6.22. Almost one third of the cells had voltages of between 635mV and 645mV, greater than any of the cells with two oxidations. The efficiency spread of the cells with the long oxidation without AR coatings was correspondingly greater. The fill factors of the cells typically varied from 0.77 to 0.79. Cell efficiencies varied from 12% to 14.5%, with the better efficiencies corresponding to cells with the higher than average currents in figure 6.22.

The currents varied by up to 10% for a given cell voltage. Currents from each of the cells from substrates with a pair of cells tended to be higher or lower than the average performance for a given voltage. Figure 6.23 shows the measured reflection from two substrates, mg5a and mg5f, each with two cells. The reflection from the cells on the same substrate was similar. The weighted reflection losses from mg5a were around 30% while

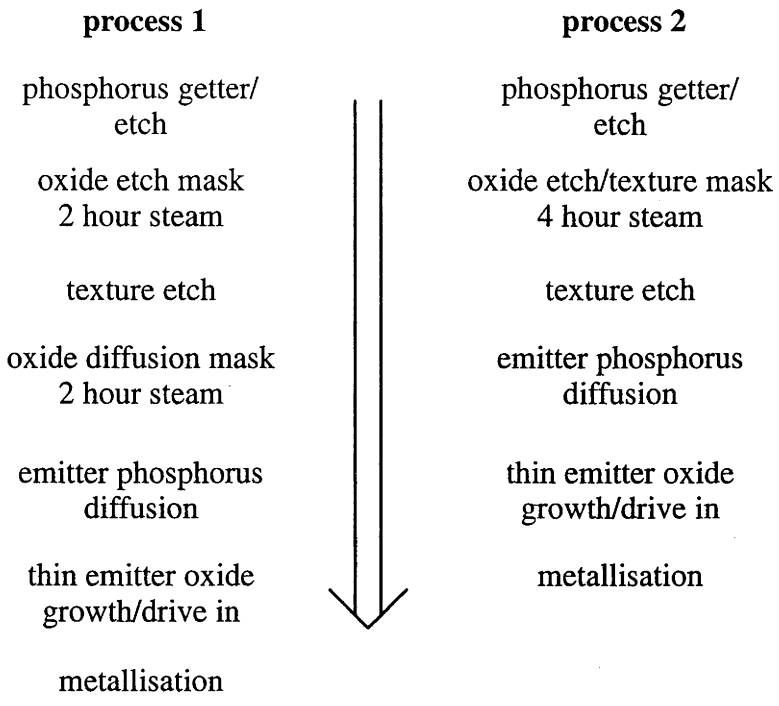

Figure 6.20: *Process sequences investigated for 'tubs' texturing. The processes were similar except process 1 required two short masking oxidations while the second process used one longer oxidation for diffusion and texturing mask. The two oxidation process (1) produced a tighter spread of efficiencies while the long oxidation process (2) produced higher peak cell efficiencies.*

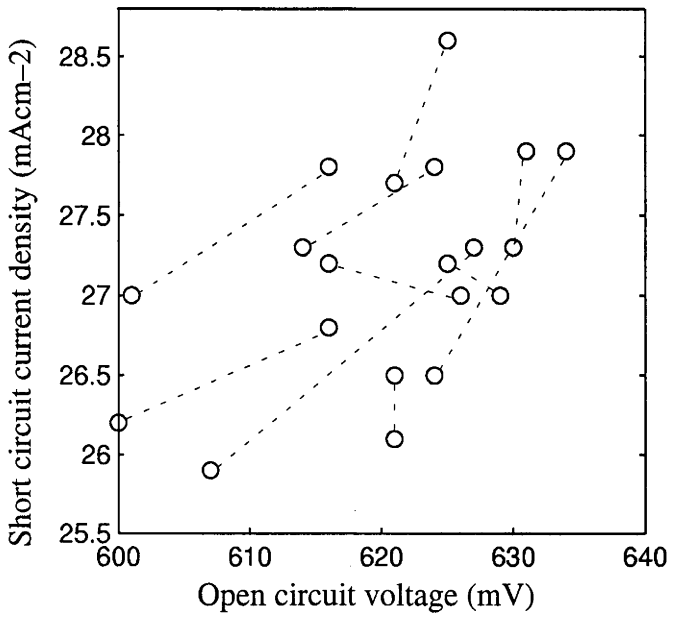

Figure 6.21: *Short circuit current versus open circuit voltage for 'tubs' textured cells with two masking oxidations (process 1).*
The cell currents demonstrated trends of improving with open circuit voltage, indicating a dependence on the substrate effective lifetime. Pairs of cells from the same substrate (joined by dotted line) demonstrated higher or lower currents than the average trend, indicating variations in the 'tubs' texturing reflectivity from substrate to substrate.

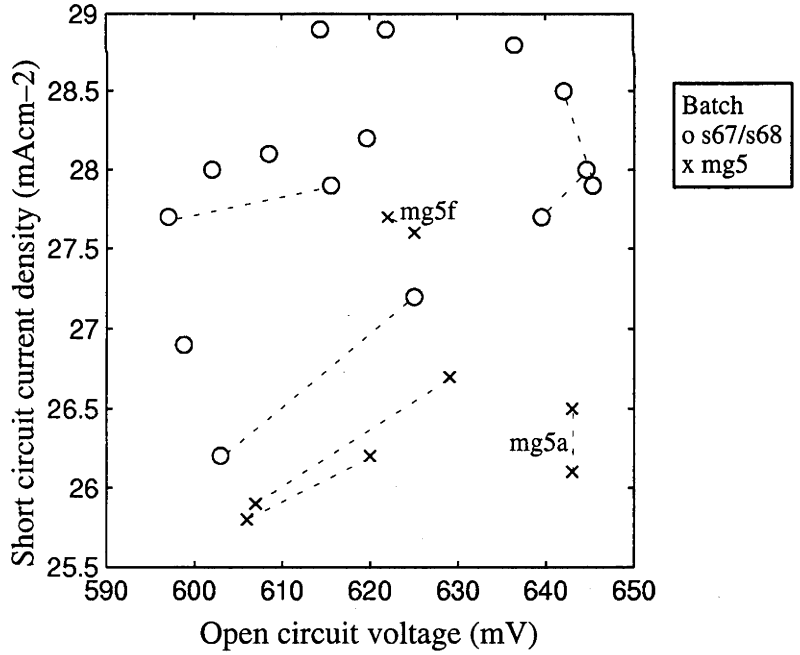

Figure 6.22: *Short circuit current versus open circuit voltage for 'tubs' textured cells with single long masking oxidation (process 2).*
Pairs of cells from the same substrate (joined by dotted line) demonstrated higher or lower currents than the average trend, caused by variations in the 'tubs' texturing reflectivity from substrate to substrate. Batch mg5 tended to have higher reflectivity and therefore lower currents than s67/s68, due to differences in texturing. Some substrates appeared to benefit from the longer oxidation with higher voltages but the majority of cells had lower voltages than the process with two shorter oxidations.

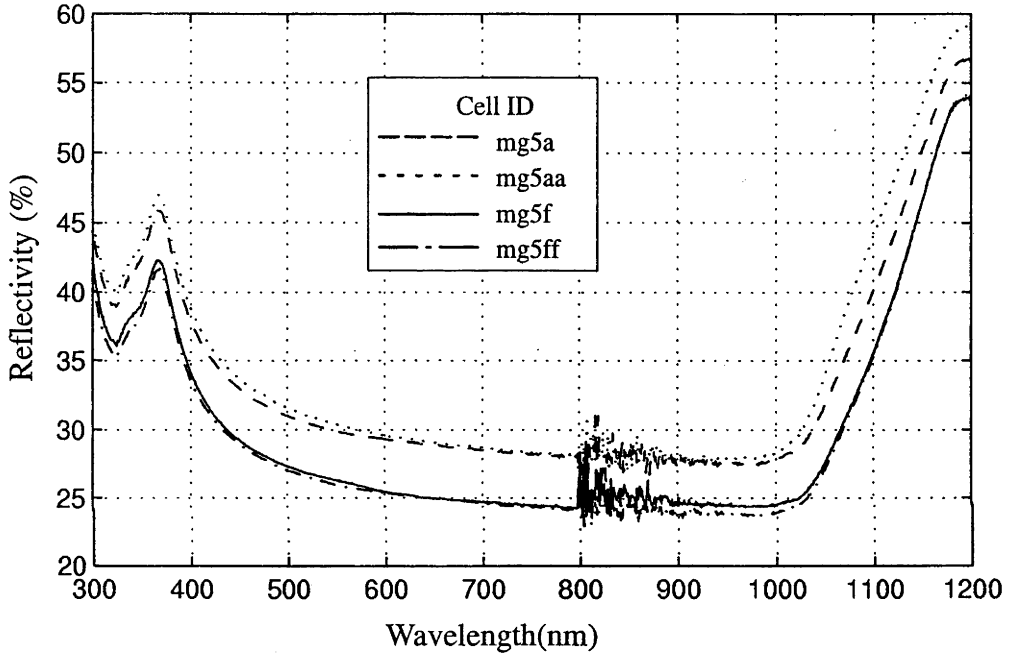

Figure 6.23: *Reflection from 'tubs' textured cells from substrates mg5a and mg5f. The weighted reflectance from substrate mg5f was 26% compared to 30% for mg5a. Adjusting the cell currents accordingly, a tighter relationship between current and voltage was observed in table 6.3.*

the losses from mg5f were around 26%. Adjustments of the currents for the reflection losses can be seen in Table 6.3. This decreases the spread in currents for a given voltage for batch mg5 seen in figure 6.22.

Cell ID	Current density ($mAcm^{-2}$)	Weighted reflectance(%)	Adjusted current 5% weighted ref.	V_{oc} (mV)
a	26.1	29.6	35.2	643
aa	26.5	29.9	35.9	643
b	25.9	26.5	33.4	607
bb	26.7	28.8	35.5	629
d	26.2	28.5	34.8	620
f	27.6	26.1	35.5	625
ff	27.7	25.7	35.4	622

Table 6.3: *Adjustments of current for reflection losses from 'tubs' textured samples from batch mg5*

Reflection losses from unencapsulated 'tubs' textured samples varied from 26% to 30%. Cell current more closely reflected voltage changes after adjusting to equal reflectance of 5%.

6.5.2.3 *Discussion*

Two different spreads of cell voltages occurred with the two processes. In the two oxidation mask process (process 1), the voltages of most of the cells are between 615mV and 630mV, with the best cell voltage only 635mV. In contrast, the distribution was wide for the long oxidation process (process 2) with nearly a third of the cells demonstrating voltages greater than 635mV while another third had voltages less than 615mV. It appears that the long oxidation process produced longer lifetimes on the better substrates, with correspondingly higher voltages. Poorer substrates, in contrast, appeared to suffer less damage from the two step diffusion process. This is interesting, given that the total oxidation time and temperature was the same in each process. Industrial type processing would probably favour the tighter spread of cell performances with the two oxidation process, while higher cell efficiencies were demonstrated with the single long oxidation.

In both processes, the current followed the general trend of improving with voltage (figures 6.21 and 6.22). However, there was a 10% spread in the currents for a given voltage. The current for pairs of cells on a single substrate tended to be be at the same relative level compared to the average trend (high or low) suggesting reflection variations from substrate played a role in determining the current for a given voltage.

Reflection measurements from batch mg5 indicated that reflection differences contributed a significant fraction of the current spread. Cells on the same substrate demonstrated similar reflection losses while quite large variations occurred between substrates, as shown in figure 6.23. This was due to differences in the size of the 'tubs', differences in the size

of the masking oxide holes caused by variations in the quality of photolithography and different grain orientations which all contributed to affect the 'tub' shape and therefore its reflectivity before AR coatings and encapsulation. Weighted reflectance for substrates mg5a and mg5f were 30% and 26% respectively, corresponding to a 6% difference in the quantity of light entering the cell.

Adjusting the cell current for reflectivity differences provided a better comparison of current versus voltage. In table 6.3, the cell current was adjusted for 5% weighted reflectance, as achieved with the long base 'tubs' textured cell with AR coatings. The spread of the cell currents then reduced, and the current voltage relationship became more clear. This indicated the importance of differences in bulk lifetime (given that surface recombination was similar with identical rear contact patterns) on relative cell performance.

Cell fill factors were not improved by 'tubs' texturing, remaining between 77% and 79% on the well behaved cells. Therefore, cell fill efficiency continued to be limited by relatively poor fill factors. The 1mm contacts on 3mm spacing were retained after the good results on the earlier untextured cells, but it may be that a more closely spaced geometry could improve fill factor without sacrificing too much in voltage or current.

Addition of the AR coatings and encapsulation would be expected to improve the efficiencies of the better cells to 18 to 18.4%, assuming a final reflectivity of 5%. Voltages would be expected to improve to 650–652mV on the better cells, slightly lower than the 654mV achieved on the best cell without texturing. Currents would have been slighter better (1%) than the untextured cells. This improvement could be attributed to the decreased reflection loss compared to the DLAR on the untextured cells (6.5%), but there was no apparent gain due to the light trapping and pathlength enhancement properties of 'tubs', though decreases in bulk lifetime due to the extra oxidation required may have offset any of these gains.

6.5.3 *Lifetime monitoring during reduced rear contact cell processing*

Investigations of substrate lifetimes during processing in the previous chapter indicated that substantial lifetime degradation occurred during post phosphorus diffusion oxidations. It was hypothesised that the degradations were related to the release of gettered impurities from the emitter during the phosphorus diffusion.

The introduction of gettering to the cell processing sequence and the importance of thermal oxidations for surface passivation warranted an investigation of lifetimes during processing of reduced rear contact cells.

6.5.3.1 *Experiment*

Cell processing followed a similar protocol to that described for process 2 in section 6.5.2.1. The lifetime of the substrates was measured after each of the furnace steps

(masking oxidation, phosphorus diffusion and passivating oxide growth) and after liftoff of the front and rear metal contacts. The remaining 1μm of aluminium for the rear was then deposited before cell measurement.

6.5.3.2 *Results*

The effective lifetime of the substrates after each processing step can be seen in figure 6.24. The lifetime increased on all the substrates during the phosphorus diffusion for the formation of the emitter from 4–8μs to 15–25μs. Lifetimes then increased during the thin oxide growth and emitter drive in step, with the substrates with the better lifetimes after the phosphorus diffusion improving most. The better substrates improved in lifetime by 60% from 25μs to 41μs while the substrate with lower lifetimes improved only 25% from 15μs to 19μs. During the subsequent metallisation, the measured effective lifetime decreased. The effective lifetime decrease was greatest for the substrates with the largest lifetimes after the thin oxide growth (down to 27μs from 41μs), with very little decrease (down to 17μs from 19μs) in lifetime for the worst substrate.

The 'tubs' texturing on the substrates was poor. Most of the holes were not well defined during photolithography and did not penetrate the masking oxide during oxide etching. Consequently, little reflection reduction occurred on the unencapsulated substrates and reflection losses varied greatly from substrate to substrate. Since current depends directly on reflection losses, cell currents provided little useful information.

Figure 6.25 presents the completed cell characteristics relative to the final measured lifetime. The cells demonstrated trends of increasing voltage with the final measured lifetime. In contrast, the cell current appeared to bear little relationship to the measured lifetime. Cell currents was grouped in pairs from adjacent cells on the same substrate. Visual observation indicated that the texturing quality was similar on each of the cells on the same substrates. Fill factors on all the cells varied from 77 to 78%.

6.5.3.3 *Discussion*

The cell processing sequence was chosen in an attempt to minimise the potential for lifetime degradation during processing and therefore maximise the final minority carrier lifetime of the cells. The samples were gettered with phosphorus to remove mobile impurities from the bulk and the heavily phosphorus diffused surfaces were etched to prevent these impurities from returning to the bulk in subsequent processing steps. The masking oxidation was conducted at low temperatures (900°C) in a steam ambient. The emitter formation was followed by a brief thermal oxidation and anneal to passivate the emitter before reduced rear contact metallisation.

The interesting features of the lifetime measurements were the improvement in lifetime during the thin oxide growth and the subsequent decrease in lifetime during metallisation. This behaviour points towards the substrate effective lifetime during processing being

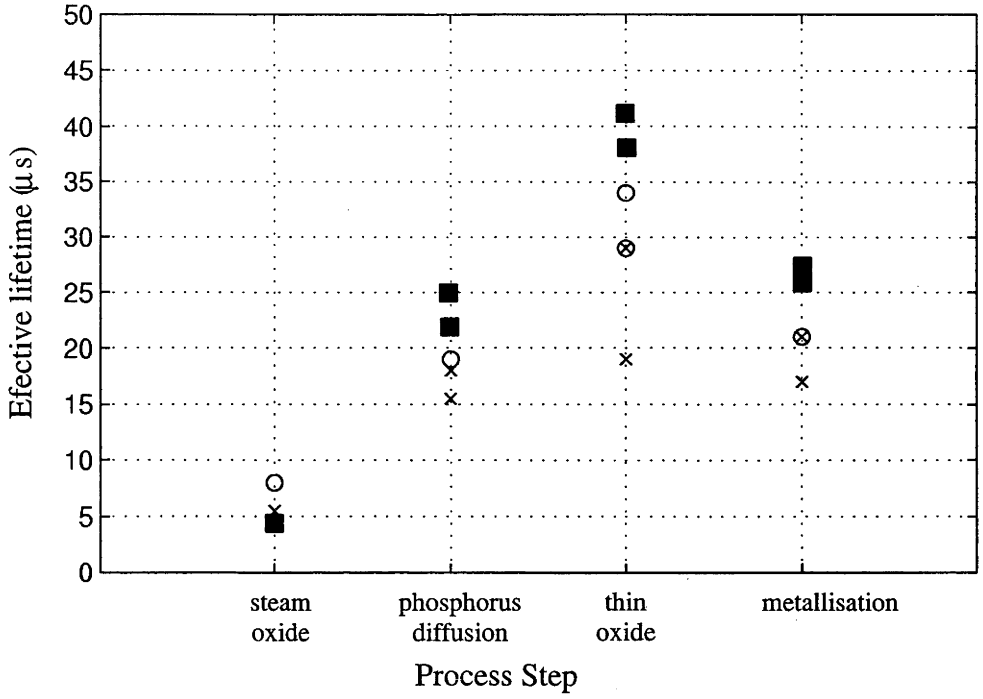

Figure 6.24: *Measured lifetimes of 0.5Ωcm multicrystalline substrates during reduced rear contact cell processing.*
Each symbol represents a different substrate. Substrate lifetimes improved during the phosphorus diffusion and the thin oxide growth due to improvements in the passivation quality of the front surface. Lifetimes decreased during the subsequent metallisation due to increased recombination at the rear surface.

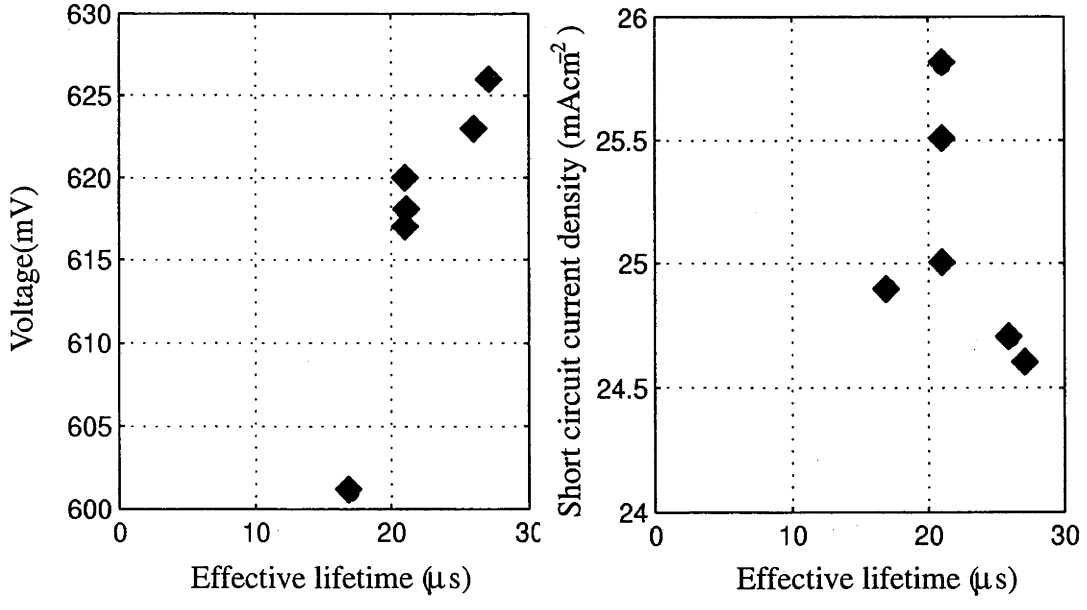

Figure 6.25: *Measured cell characteristics versus final measured lifetime.*
The cell voltage improved as a function of final measured lifetime. The current was dominated by the variations in reflectivity from the poor 'tubs' textured surface, rather than substrate lifetime, with pairs of cells performing similarly.

strongly influenced by the quality of the surfaces, rather than dominated entirely by the bulk lifetime.

The increase in the effective lifetime after the thin oxide growth was particularly interesting, compared to the behaviour observed for the ungettered cells with thin oxides (with and without aluminium alloying) in the previous chapter. Oxidations in the absence of aluminium after the emitter formation led to decreases in the effective lifetime, while aluminium alloying enabled the post phosphorus diffusion effective lifetime to be maintained despite increased rear surface recombination. It was hypothesised that impurities gettered during the emitter formation were released during the subsequent oxidation leading to bulk lifetime degradation in the absence of aluminium. Impurities were released due to the lower peak concentrations of the phosphorus after the oxidation and correspondingly lower solubility of the impurities in the phosphorus diffused regions.

This hypothesis was further supported by the behaviour of these gettered substrates. Mobile impurities gettered during the heavy phosphorus diffusion were removed from the substrate. Consequently, few mobile impurities remained to be gettered during the emitter formation released during the subsequent oxidation, and therefore had little effect on the bulk lifetime. Therefore no degradation in lifetime occurred despite the absence of aluminium gettering.

Gettering has increased the bulk lifetime to the point where the quality of the surfaces had an increased impact on the effective lifetime. The improved passivation of the emitter afforded by the thin oxide decreased emitter recombination, increasing the measured effective lifetime. Substrates with lower effective lifetimes after the emitter formation appear partially limited by the bulk lifetime and improved little with the improved surface passivation. Substrates with better effective lifetimes were limited more by the surfaces and therefore greater increases in effective lifetime resulted from the improvement in the front surface passivation. Substrates with better bulk lifetimes were behaving more like the 0.4Ωcm Fz substrate in figure 5.6, with improvements in lifetime during the emitter formation and subsequent thin oxide passivation.

A consequence of the improved bulk lifetime and corresponding sensitivity to the surface quality was the increased importance of rear surface recombination. The lifetime of all the substrates decreased during the addition of the rear metal contacts. Substrates with the greatest effective lifetimes were affected the most, with the increased recombination at the rear a greater fraction of total recombination. Substrates with poorer lifetimes are less effected, since they are partially limited in effective lifetime by bulk recombination, and fewer carriers can diffuse to the rear. Consequently, the spread in effective lifetimes was reduced by the presence of the rear contacts.

The cell voltages follow the expected trend of increased voltages as the final measured effective lifetime increased. The currents from the substrates were much lower than usual

for 'tubs' textured samples in the previous section due to the poor quality of the texturing due to poor photolithography. Previously, 'tubs' textured cells with voltages greater than 620mV demonstrated currents of 26–29mAcm^{-2} without AR coatings, much greater than the 24.5 to 26mAcm^{-2} from the cells in this batch. The quality of the texturing varied from substrate to substrate, with similar currents from cells from the same substrate (Figure 6.25). It would be possible to adjust the current for the substrate reflection variations with reflection measurements to better determine the relationship between lifetime and current, if desired.

6.5.4 *Conclusions from investigations of reduced rear contact cells*

The minority carrier lifetime of multicrystalline silicon has improved to the point where rear surface recombination can become a significant contributor to total cell recombination. Aluminium alloying has become the established technology in high efficiency multicrystalline cell design due to the gettering benefits of aluminium which help to maintain high minority carrier lifetimes. However, the associated back surface field is not sufficient to significantly reduce the effects of rear surface recombination. Therefore, scope existed for efficiency improvements with multicrystalline silicon cell designs which reduced rear surface recombination.

This investigation has demonstrated that the reduced rear area contact cell was a suitable design for reducing rear surface recombination in multicrystalline silicon cells. The efficacy of the design was clear from the record high open circuit voltage, 654mV and cell efficiencies greater than 18% for 4cm^2 cells. Despite the lack of aluminium alloying, diffusion lengths in gettered substrates remain greater than the wafer thickness, as indicated by the lifetime measurements and the large voltage difference between reduced rear area contact and total rear area contact cells.

Post process lifetimes benefited substantially from the introduction of pre–process phosphorus gettering. Effective lifetime degradation no longer occurred during the oxide growth for passivation of the emitter, important to provide high quality passivation of the emitter while maintaining high device lifetimes.

6.6 Rear Locally Diffused Cells

The problem of further reducing recombination at the rear metal contacts of single crystal silicon solar cells was addressed by the passivated emitter and rear, local–diffused (PERL) cell design [32]. Figure 6.26 is a schematic diagram of a rear locally diffused cell. Boron diffusions are introduced under the rear metal contacts to control recombination. The boron diffusion under the rear metal contacts provides a back surface field for the metal contacts. The increased doping level decreases the minority carrier concentration near the metal contacts, reducing the effective recombination velocity at the rear metal contacts (in

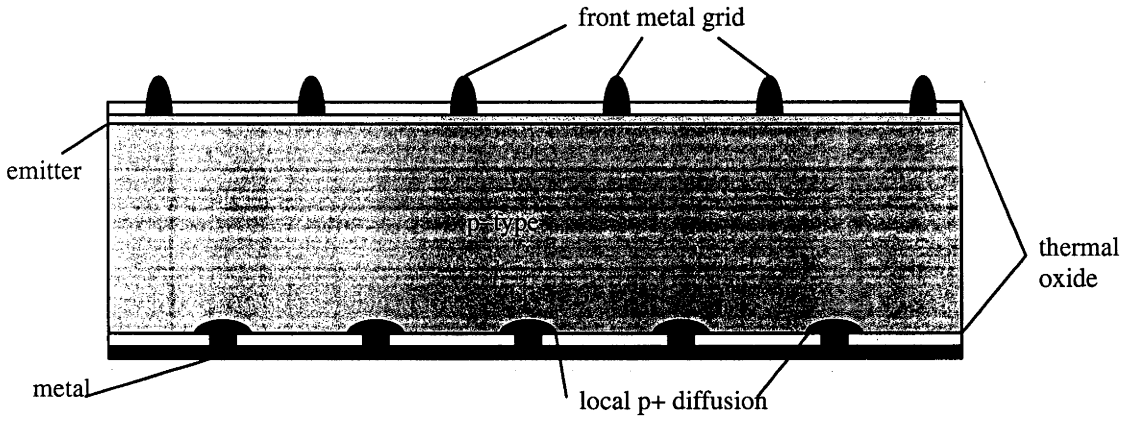

Figure 6.26: *Schematic diagram of the rear locally diffused cell design. The cell design is similar to the reduced rear contact cell except the areas under the rear metal contacts are diffused with boron. This produces a local BSF, reducing the recombination at the contacts and contact resistance. Consequently, contacts can be smaller and closer together, reducing resistive losses.*

the same manner as the full area back surface field). Consequently, recombination at the rear is decreased.

Resistive losses in cells can also be reduced as the rear contacts can be more closely spaced without compromising current and voltage, reducing bulk resistive losses. Higher resistivity substrates can also be used with the reduction in contact resistance losses, with higher cell currents resulting from the improved diffusion lengths. This cell structure holds the current efficiency records for single crystal silicon, improving cell efficiency beyond 24% [11].

6.6.1 *Boron Diffusions*

Boron is an alternative to aluminium alloying to produce heavily doped sheet diffusions for back surface fields. Photolithography can also be used to produce local boron diffusions under rear contacts by using a masking oxidation. Boron is used for locally defined diffusions in the highest efficiency single crystal silicon solar cell designs, such as the PERL cell from UNSW and the point contact cell design from Stanford [143]. The effects of boron diffusions on gettered and ungettered substrates was investigated for 1.5Ωcm and 0.5Ωcm substrates from Eurosolare.

6.6.1.1 *Experiment*

Samples from adjacent wafers were selected, with half the substrates (kept in pairs) receiving a four hour phosphorus getter at 900°C, which was then removed. One of the substrates from each pair then received a typical BBr_3 diffusion at 950°C with a five minute preheat, followed by 30 minute predeposition, 60 minute drive–in and 30 minute oxidation. This produced a sheet resistance of around 40Ω/□. Lifetimes were then measured on these samples with the heavy boron diffusion. The boron diffusions were then removed and all samples received a light phosphorus diffusion and oxidation to passivate the surfaces before lifetimes were again measured.

6.6.1.2 *Results*

The lifetime for the 1.5Ωcm and 0.5Ωcm substrates are displayed in figures 6.27 and 6.28 respectively. The solid symbols represent the substrates which received only the light phosphorus diffusion while the corresponding open symbols represent the adjacent substrate with the same grain structure which received the boron treatment.

In both substrate resistivities, the lifetime of the boron diffused substrates were substantially lower than the corresponding lifetimes without boron diffusions. This was apparent for the phosphorus pre–gettered and as received substrates. There was a slight improvement in effective lifetime on the boron diffused substrates after the boron diffusions were etched and replaced with a light phosphorus diffusion.

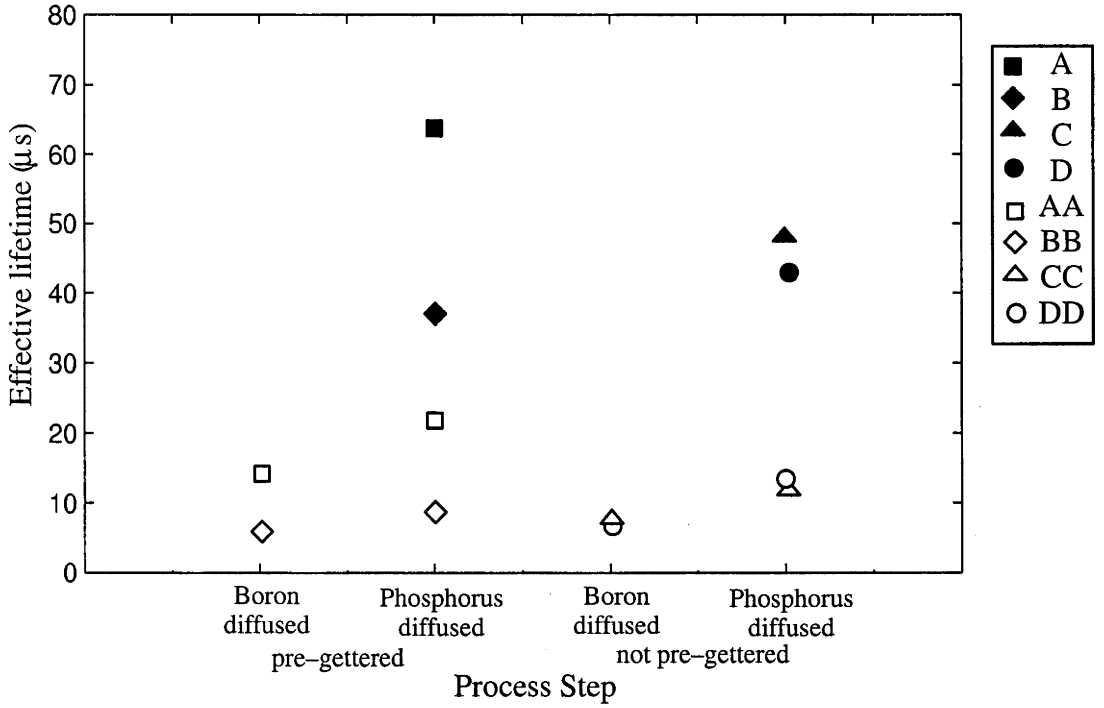

Figure 6.27: *Lifetimes of adjacent 1.5Ωcm substrates with and without boron treatment.*
Substrates with the same lettering (XX and X, open and closed symbols) correspond to adjacent wafers which did and did not receive the boron treatment. Large lifetime degradation resulted from the boron treatment.

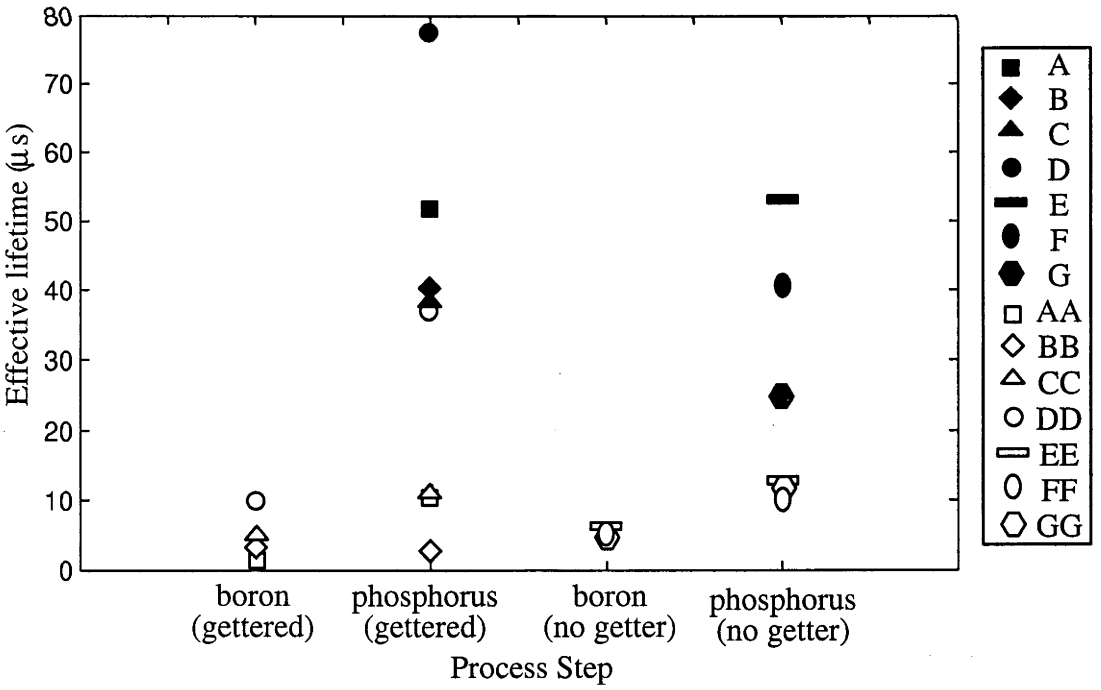

Figure 6.28: *Lifetimes of adjacent 0.5Ωcm substrates with and without boron treatment.*
Substrates with the same lettering (XX and X, open and closed symbols) correspond to adjacent wafers which did and did not receive the boron treatment. Large lifetime degradation resulted from the boron treatment.

6.6.1.3 *Discussion*

A slight improvement in lifetime was observed after the phosphorus diffusion on the boron diffused substrates which can be attributed to the improved surface passivation. The heavy boron diffusions had a relatively poor surface passivation quality, with high dark saturation currents of the order of 10^{-12}A/cm^2. Consequently, the effective lifetimes after the boron diffusion were heavily influenced by the recombination in boron diffused layer. A J_o of 10^{-12}A/cm^2 on each surface limits the lifetime to 8μs on the 0.5Ωcm substrates and 16μs on the 1.5Ωcm substrates. This corresponded to the better effective lifetimes observed after the boron diffusions. Therefore little information on the effect of the boron diffusions on the bulk lifetime could be determined from the lifetime measurements after the boron diffusion.

More useful information was obtained after the boron diffusion had been removed and the surface passivated with the light phosphorus diffusion. The dark saturation current of the oxide passivated phosphorus diffusion was less than 10^{-13}A/cm^2 with the potential for lifetimes greater than 80μs on both substrate resistivities. Since the lifetimes of the substrates which had been boron diffused were substantially lower, the effective lifetime was a good approximation for the bulk lifetime (maximum error of 10%).

From this information, it was clear that the boron diffusions have caused dramatic decreases in bulk lifetime on most substrates. The lifetimes of the gettered and ungettered 1.5Ωcm substrates varied from 37 to 64μs, while identical boron diffused substrates from the adjacent wafer demonstrated lifetimes from 9 to 22μs. This corresponded to 20–35% of the original effective lifetime, or a voltage drop of 27 to 40mV in a completed cell. Similar behaviour was observed with the 0.5Ωcm substrates. The ungettered samples demonstrated lifetimes of 25 to 55μs, dropping to 10 to 13μs after the boron treatment. The gettered samples demonstrated lifetimes from 40 to 78μs, with all but the best sample dropping to 3μs to 12μs after the boron diffusion. The best boron treated sample (DD) demonstrated a lifetime of 39μs, substantially better than the other boron samples, but much lower than the sample without boron treatment (D,78μs). This high value for the lifetime in this substrate indicated that furnace contamination was unlikely to be the cause of the lifetime degradation in the boron treated samples. The lifetime drop was due to interaction between the high temperature boron treatment and the multicrystalline substrates.

The large decrease in lifetime from the boron treatment was of concern for high efficiency devices. As indicated in section 6.3.1, some degradation of bulk lifetime can be tolerated if decreases in rear surface recombination were sufficient. However, bulk lifetimes on most substrates decreased below 20μs, where rear surface recombination becomes unimportant. Degradation on cells with rear local diffusions will need to be substantially lower to achieve high cell efficiencies.

6.6.2 *Rear locally diffused multicrystalline cells*

The rear locally diffused cell structure offers the potential for further reductions in rear surface recombination in multicrystalline silicon solar cells. However, this requires increased high temperature furnace processing with the associated potential for decreases in minority carrier lifetime of the multicrystalline silicon and a net decrease in cell efficiency.

6.6.2.1 *Experiment*

Preliminary investigations of multicrystalline silicon cells with rear local diffusions were undertaken. Cells were constructed on 1.5Ωcm and 0.5Ωcm Eurosil substrates. A 1Ωcm Fz substrate was included with the batch of 1.5Ωcm substrates. Substrates were pre–gettered with phosphorus at 900°C for 4 hours. A steam masking oxide was grown followed by BBr_3 pre–deposition at 950°C and drive–in at 1000°C in 100μm holes through the masking oxide at 800μm spacing. This produced sheet resistivities of around 10Ω/□. The processing sequence was then similar to the reduced rear contact cells, with masking oxide growth, emitter formation and thin oxide growth/drive in. An additional requirement was alignment and liftoff of 50μm on 800μm metal contacts to the rear boron diffusion.

Lifetime measurements were made after each furnace process step and metallisation of the 0.5Ωcm substrates.

6.6.2.2 *Results*

The lifetime of the 0.5Ωcm substrates after each processing step are shown in figure 6.29. The effective lifetime increases during the boron diffusion, then decreased slightly during the second oxidation. The effective lifetime increased during the phosphorus diffusion and the thin oxide growth. Little change in measured lifetime occurred during the final metallisation of the cells.

Voltages on the 0.5Ωcm substrates which were not shunted varied from 622 to 635mV, with cell current improving from 24.0 to 24.7mAcm^{-2} with improvements in cell voltage. Fill factors around 78% were demonstrated on the cells which were not shunted. The current, voltage and fill factor were all lower than the better 0.5Ωcm reduced rear contact cells.

The performance of the 1.5Ωcm substrates was similar, with slightly higher currents and lower voltages. Voltages of most cells varied from 610mV to 622mV with currents improving with voltage from 25.3mAcm^{-2} to 25.5mAcm^{-2}. Some cells had noticeably worse current and voltage, with voltages of 566mV and 575mV on cells with currents of 23.7mAcm–2. Surprisingly, the performance of the Fz substrates was similar to the multicrystalline silicon substrates. The voltage of the best Fz cell was 640mV with a current of 25.3mAcm^{-2}. The fill factors on all of the cells were low. The best fill factor was 77%, with all fill factors falling between 0.74 and 0.77%. The lower fill factors resulted from small shunts in the cells.

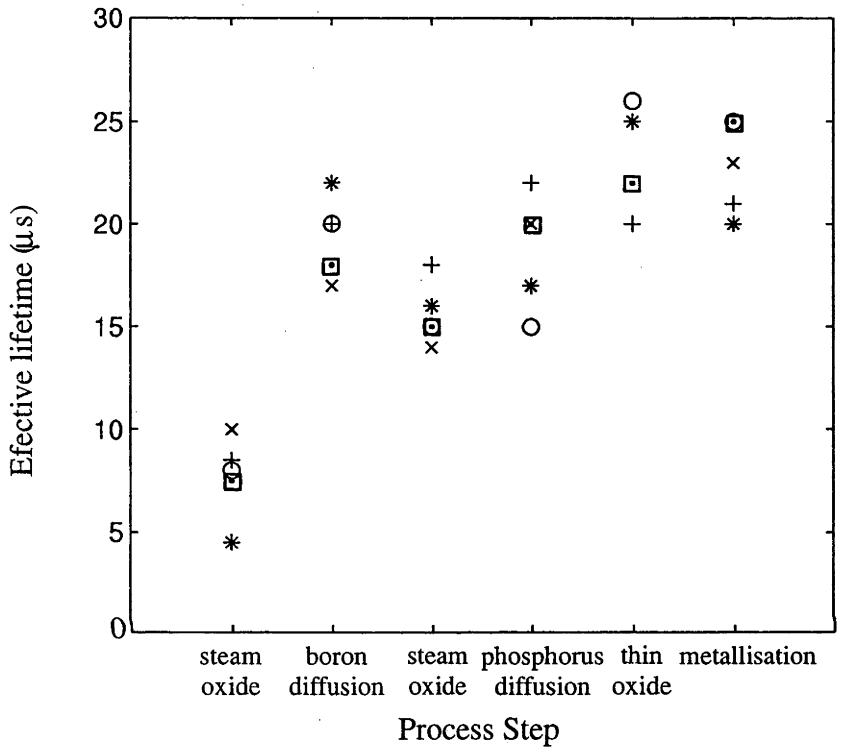

Figure 6.29: *Effective lifetimes of 0.5Ωcm substrates during processing of rear locally diffused cells.*

Each symbol represents a different substrate. The effective lifetime increased during the boron diffusion due to improvements in the oxide passivation properties from the anneal. Lifetimes increased only slightly during the emitter diffusion and the thin oxide growth, indicating that the bulk lifetime rather than the front surface was primarily limiting the effective lifetime. Metallisation had little effect on substrate lifetime, as expected for the rear locally diffused cell design.

The efficiencies of cells produced with this process show the promise of the reduced rear contact design. Efficiencies of 12.3% were demonstrated on both the 1.5 and 0.5Ωcm substrates without AR coatings.

substrate	V_{oc}(mV)	J_{sc}(mA/cm^2)	FF(%)	Eff(%)
1.5Ωcm	622	25.5	77.2	12.3
0.5Ωcm	637	24.7	78.4	12.3
Fz 1Ωcm	640	25.3	76.8	12.4

Table 6.4: *Best rear locally diffused cells*
The characteristics of the cells were very similar. Voltage was slightly higher on the Fz substrate, while current increased with substrate resistivity. The Fz performance was substantially lower than the potential for the reduced rear contact cell.

6.6.2.3 *Discussion*

The results for the 0.5Ωcm substrates were disappointing after the excellent results for the reduced rear contact cells. Despite the potentially lower rear surface recombination velocities, the 0.5Ωcm cells demonstrated (slightly) worse voltage and current. This appears to be attributable to the lower bulk lifetimes after the extra oxidation and boron treatment.

As observed in the previous section, sheet boron diffusions had a detrimental effect on the bulk lifetime of the multicrystalline silicon. This appeared to have been alleviated by reducing the sheet diffusion to a local diffusion since effective lifetimes were higher than those obtained after the sheet boron diffusions.

However, while the magnitude of the degradation was reduced, the lifetimes after the phosphorus diffusion and thin oxide growth were lower than those obtained for the reduced rear contact cells, indicating that some lifetime degradation still occurred. Improving the quality of the emitter passivation with thin oxide growth on the reduced rear contact cells in figure 6.24. improved lifetimes to as high as 40μs, while the better locally rear diffused cells only achieved 25μs.

The addition of the metal contacts had little effect on the effective lifetime of the substrates. This was not unexpected with the boron diffusion designed to minimise recombination at the rear contacts. The effective lifetimes of the substrate were also relatively low, so that the 0.5% contacts would not be expected to significantly affect cell recombination unless the dark saturation current for the diffusions were of the order of 10^{-11}A/cm^{-2}.

Another major difference in cell performance was the low fill factors. The fill factors were poor due to the low contact fraction and the relatively wide (800μm) spacing of the contacts. Zhao *et al.* [144] demonstrated fill factors of 82% for a rear locally diffused multicrystalline silicon cell with 180μm contact spacing. Unfortunately, the only mask set available at the ANU was 50 and 100μm contacts on 800μm spacing (triangular packing), with the larger used for the diffusion and the smaller for the contacts. More compact

arrangements were tested by tripling the contact fraction and halving the spacing with a triple exposure of these masks on 1Ωcm Fz wafers. This led to fill factors over 81%. Improvements in fill factor should result from the use of better contact geometries.

The local rear diffused design has lead to remarkable voltage improvements on the 1.5Ωcm substrates. The voltage for the 1.5Ωcm cell was 20mV greater than results for equivalent aluminium alloyed cells (polished/no AR coating). The dark saturation current indicated that the effective rear surface recombination velocity was less than 900cm/s (upper bound, assuming all recombination occurs at the rear). Assuming no recombination at the rear, the lower bound on the bulk lifetime was 50μs. The 50μs lower bound on the bulk lifetime of the better 1.5Ωcm substrate indicated that the local diffusion caused substantially less degradation than the sheet diffusions, where the bulk lifetime was reduced to less than 25μs on all the 1.5Ωcm substrates. Measurements of the surface recombination velocity of 1.5Ωcm substrates in section 6.7 indicated that annealed steam oxides were capable of producing surface recombination velocities below 150cm/s above $10^{14}cm^{-3}$ injection levels, indicating that lower bulk lifetimes due to the boron diffusion was the main limit on effective lifetime.

The efficiencies of the multicrystalline substrates were similar to that achieved for the Fz substrate. With the addition of AR coatings, these cells would only be expected to achieve 17.8 to 18%. Since PERL cells on Fz silicon have achieved 24% (with texturing), it appears likely that the processing sequence requires improvement to maximise cell efficiency. These multicrystalline silicon cells were amongst the first boron diffused cells to be produced by the solar group at the ANU. Further experience with boron processing is currently being developed with extensive investigations of concentrator cells. Processing has been improved to the point where lifetimes greater than 18ms can be obtained on high resistivity single crystal substrates with local diffusions. Information from these investigations will be useful for developing suitable protocols for processing multicrystalline silicon.

Similar efficiency results have also been achieved with the reduced rear contact cell design on multicrystalline silicon. Zhao *et al.* [144] produced an 18.2% efficient $1cm^2$ rear locally diffused cell on 0.8Ωcm HEM multicrystalline silicon by following a high temperature float zone processing sequence, with process temperatures up to 1100°C. This cell had an open circuit voltage of 643mV, current of $34.5mAcm^{-2}$ and fill factor of 82.0%. $4cm^2$ cells demonstrated lower performance of 17.0%, due to lower voltages from poor response grain boundary regions in the cells. The better performance of the smaller UNSW cells can be attributed to the 5% better fill factor with the reduced rear contact spacing, with V_{oc} and J_{sc} similar (allowing for absence of AR coatings).

Recently, the PERL structure has led to a dramatic jump in multicrystalline silicon cell efficiency, with 19.8% demonstrated on a cell manufactured at the University of New

South Wales [145]. Details are yet to be published but communication [146] indicated that the multicrystalline substrates were sourced from Eurosolare.

6.7 Passivation of multicrystalline silicon with thermal oxides

With the importance of thermal oxides in the passivation of the rear surface of high efficiency solar cells, the recombination properties of thermally grown oxides on (100) single crystal silicon have been extensively studied in recent years [90,142].

The improvements in the lifetime of multicrystalline silicon has increased the importance of rear surface recombination in multicrystalline cells. The performance limit imposed by rear recombination of aluminium alloyed cell designs has led to interest in the high efficiency single crystal silicon cell designs to reduce rear surface recombination. The use of thermally grown oxides on multicrystalline silicon has led to increases in cell voltages in this work and increases in efficiency with the rear locally diffused cell by UNSW [145]. However, no measurements of oxide passivation properties on multicrystalline silicon have been reported.

Concerns exists whether surface recombination with multicrystalline silicon would be worse than that achieved with (100) oriented single crystal silicon. Surface recombination on (111) oriented silicon is higher than (100) due to a higher density of interface states. Consequently, substrates with (111) selective texturing typically demonstrate higher recombination than would be expected from the increase in cell area. The grains in multicrystalline silicon grown by directional solidification tend towards (111) and (110) orientation, rather than (100). This was evident when substrates have been oxidised, with oxide thickness less on the few (100) oriented grains.

The surface recombination velocity obtainable may also influence the choice of substrate resistivity for high efficiency cell designs. Measurements of single crystal silicon indicate that large differences in surface recombination velocity occur with changes in substrate doping [90,142].

Another important issue is whether surface recombination in completed devices will be higher due to the lower injection level typically found in multicrystalline silicon, due to the lower bulk lifetimes than in Fz silicon. Surface recombination velocities for p–type silicon tend to increase with decreasing injection level for higher substrate dopings. This has an impact on the recombination of high efficiency PERL single crystal silicon solar cells at maximum power, leading to lower than expected fill factors [142]. With the multicrystalline silicon cells operating at still lower injection levels, the increase in surface recombination is expected to be even greater, although surface recombination may impose a weaker limit on cell efficiencies already affected by lower bulk lifetimes.

Investigations concentrated on low temperature steam oxidations since steam oxidations were used during the processing of the reduced rear contact and rear locally diffused cells earlier in this work and allow faster, lower temperature processing.

6.7.1 *Experiment*

Three to eight adjacent substrates were selected from the same ingot of 0.5Ωcm and 1.5Ωcm substrates. The 100mm x 100mm substrates were diced into smaller 50mm x 33mm substrates. 1Ωcm Fz substrates were also investigated.

A third of the samples were maintained at the original thickness while the remainder were thinned with multiple cuts of a 1.3mm blade with a dicing saw to two reduced thicknesses, to provide three distinct substrate thicknesses. All the substrates were then etched in HF/HNO_3 to remove saw damage and to clean the substrates. The samples were subjected to phosphorus gettering for three hours at 900°C, and then the heavy phosphorus diffusion was etched in HF/HNO_3, followed by a 10%HF dip.

Furnaces were cleaned with TCA/Oxygen at 1100°C before processing. Samples were loaded at 800°C, oxidised in a steam ambient for 2 hours at 900°C and then annealed for a half hour in argon or nitrogen. The steam was provided by bubbling 100L/hr oxygen through a deionised water bubbler at 85°C. Samples were then annealed in forming gas for 20 minutes at 400°C before quasi–steady state measurements of effective lifetime.

6.7.2 *Results*

The effective surface recombination velocity and bulk lifetime of the substrates were determined by comparing the effective lifetime from adjacent substrates with different thicknesses. If the carrier concentration profile in the sample was flat, the effective lifetime, τ_{eff} can be related to the bulk lifetime, τ_{bulk} and effective surface recombination velocity, S_{eff}, via the modification of equation (4.13)

$$\frac{1}{\tau_{eff}} = \frac{1}{\tau_{bulk}} + \frac{2.S_{eff}}{W} \qquad (6.4)$$

where W is the sample thickness.

Surface recombination velocities and bulk minority carrier lifetimes were determined by fitting equation 6.4 to the measurements of effective lifetime with QSSPC.

The 1Ωcm Fz samples demonstrated trends of increasing effective lifetime as a function of injection level. The effective lifetime of the substrates decreased substantially as the substrate thickness decreased, indicating the importance of the surfaces in total recombination. Figure 6.30 displays the inverse effective lifetimes of the Fz substrates as a function of inverse thickness at an injection level of $10^{15}cm^{-3}$, with the linear relationship between inverse effective lifetime and thickness. From this plot, the surface recombination velocity of the substrate at $10^{15}cm^{-3}$ was 280cm/s and the bulk lifetime was 520μs. The diffusion length of 1.2mm justifies the assumption of a flat carrier profile.

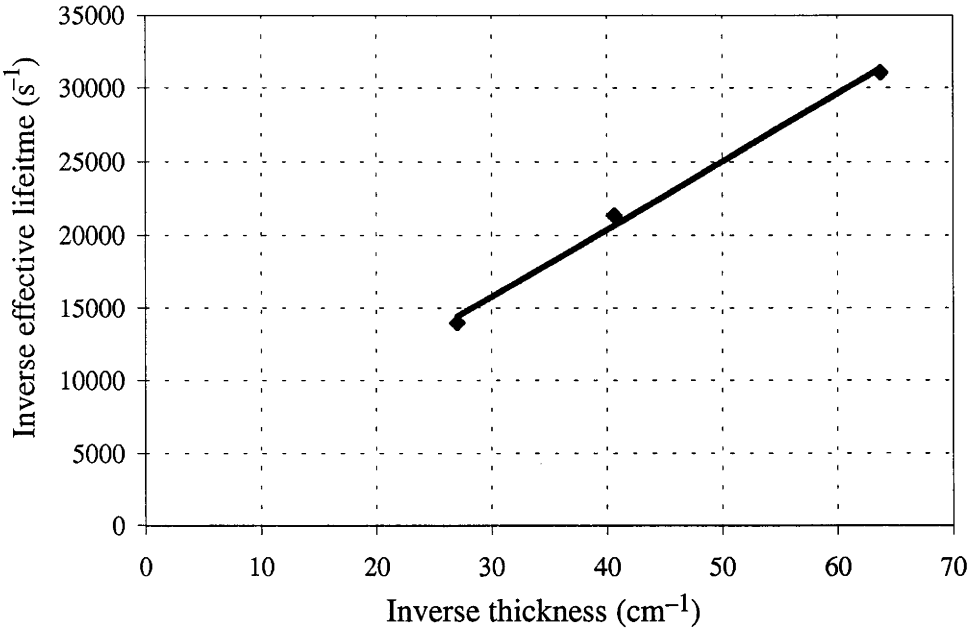

Figure 6.30: *Inverse effective lifetime of steam oxidised 1Ωcm Fz silicon for a range of substrate thicknesses.*
The recombination parameters were determined from the line of best fit of the inverse effective lifetime versus inverse thickness. The injection level was $10^{15}cm^{-3}$. The slope of the line was 560cm/s, corresponding to the sum of the surface recombination velocities of both surfaces. The intercept was $1930s^{-1}$, indicating a bulk lifetime of 520μs.

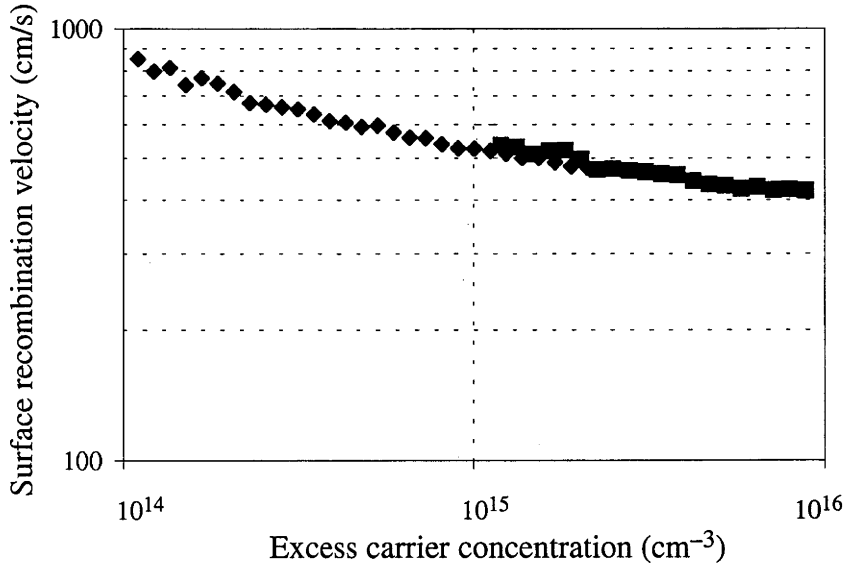

Figure 6.31: *Surface recombination velocity of steam oxide passivated 1Ωcm Fz substrates as a function of injection level.*
The data points correspond to the surface recombination velocity from both surfaces. The surface recombination velocity of the 900°C steam oxide passivated surface increased from 200cm/s at $10^{16}cm^{-3}$ to 400cm/s at $10^{14}cm^{-3}$. This injection level dependence was similar to the behaviour observed by Glunz et al [90] *for an annealed dry oxide, grown at 1050°C, except recombination rates were twice as high on the steam oxide passivated surface.*

The analysis was extended to the range of injection levels measured during the QSSPC measurements, with light intensities varying from from 1/3 to 20 suns. Figure 6.31 displays the changes in surface recombination velocity as a function of excess carrier concentration for the Fz samples. The surface recombination velocity values corresponded to the sum of the contributions from both surfaces. The surface recombination velocity changed from 200cm/s at $10^{16}cm^{-3}$ up to 400cm/s at $10^{14}cm^{-3}$. A lower surface recombination velocity could be expected at maximum power generation, equivalent to injection levels closer to $10^{13}cm^{-3}$.

Similar measurements were made with six 1.5Ωcm multicrystalline silicon substrates from adjacent wafers in the ingot. The inverse effective lifetimes versus inverse thickness at $10^{15}cm^{-3}$ excess carrier concentration can be seen in Figure 6.32. Remarkably, the effective lifetimes were better than the those of the Fz substrates for the range of thicknesses sampled. The surface recombination velocity and bulk lifetime were determined from the line of best fit to these measurements. The surface recombination velocity was 125cm/s and the bulk lifetime 280μs, which corresponds to diffusion lengths of 900μm. The spread in effective lifetimes from the trend line is greater than that observed for the Fz substrates. This spread occurred for the full range of injection levels measured.

Figure 6.33 displays the surface recombination velocity and bulk lifetime of the 1.5Ωcm substrates as a function of injection level. The surface recombination velocity remained fairly constant around 120cm/s between 10^{14} and $4x10^{15}cm^{-3}$, increasing slightly at the lower injection levels. The bulk lifetime was between 200 and 300μs.

Two other groups of three substrates with different grain orientations from the same ingot and another group from a different ingot were measured to compare different crystal orientations. The surface recombination velocities and lifetimes for these substrates can be seen in figure 6.34. The effective lifetimes varied significantly from group to group. After analysis, most of the effective lifetime spread was traced to bulk lifetime variations from 50 to 200μs. The surface recombination velocities, however, were very similar ranging from 75 to 125cm/s. The surface recombination velocity remained fairly constant in the range from 10^{15} to $10^{16}cm^{-3}$ (corresponding to approximately one sun to 10 sun illumination levels).

The effective lifetime measurements of the 0.5Ωcm substrates were dominated by trapping, especially the thinnest substrates (Figure 6.35). Even in the thicker samples, trapping dominated below $10^{15}cm^{-3}$ excess carrier concentration, corresponding to three suns illumination. At illumination levels where trapping was not affecting the measurement, the substrates satisfy the linear relationship between inverse effective lifetime and inverse thickness. Figure 6.36 shows there was little spread in effective lifetimes beyond the linear trend. Surface recombination velocities at $3x10^{15}$ were 180cm/s with the bulk lifetime 48μs. The diffusion length remains larger than the substrate

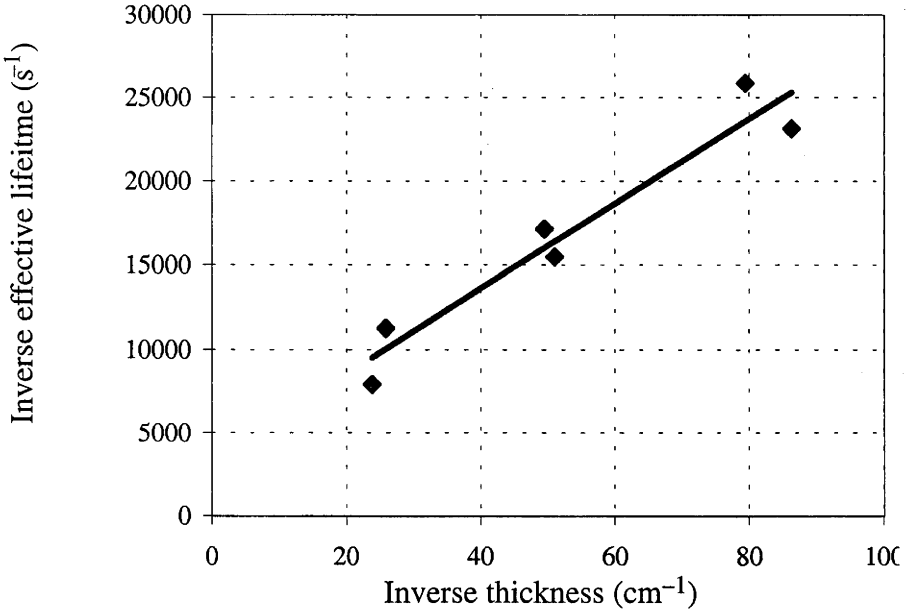

Figure 6.32: *Inverse effective lifetime of steam oxidised 1.5Ωcm multicrystalline silicon for a range of substrate thicknesses.*
The recombination parameters were determined from the line of best fit of inverse lifetime versus inverse thickness. The injection level was $10^{15}cm^{-3}$. The slope corresponded to a surface recombination velocity of 125cm/s, while the intercept corresponded to a bulk lifetime of 280μs.

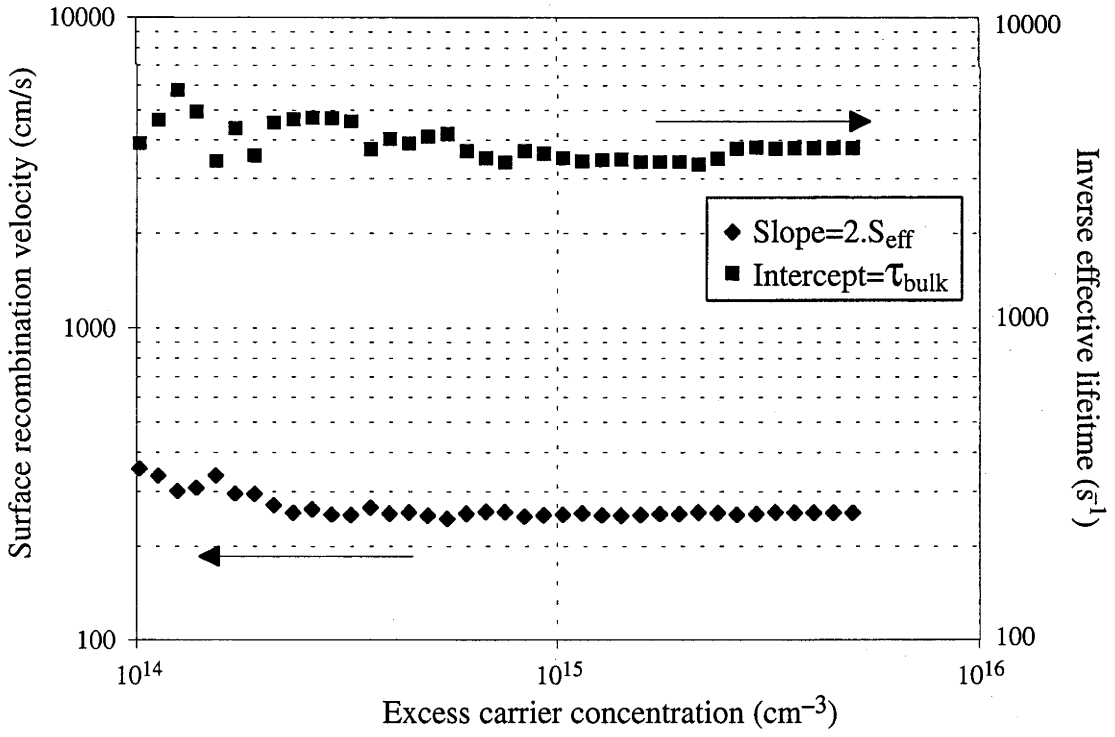

Figure 6.33: *Bulk lifetime and surface recombination velocity as a function of excess carrier concentration for 1.5Ωcm multicrystalline silicon (from above).*

The surface recombination velocity varied little with injection level from 120–150cm/s. The bulk lifetime was approximately 250μs. The 1.5Ωcm multicrystalline silicon substrate had lower surface recombination velocities and less injection level dependence than the 1Ωcm Fz samples.

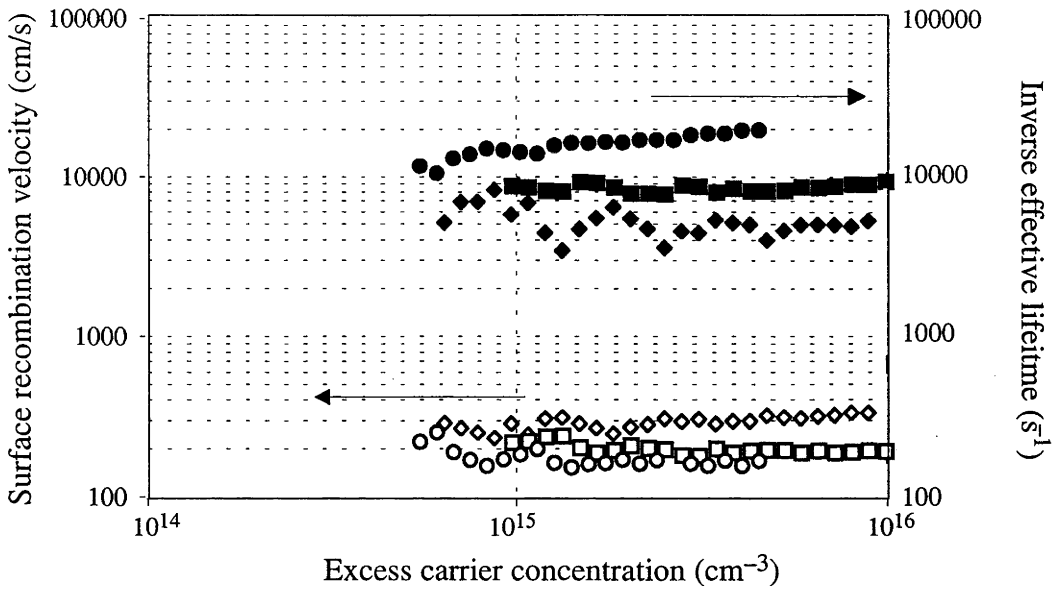

Figure 6.34: *Surface recombination velocities and inverse lifetimes for three sets of steam oxide passivated 1.5Ωcm multicrystalline samples from two different ingots. Each symbol represents a different set of samples. The surface recombination velocity (~100cm/s) of the substrates varied little between substrates. Little injection level dependence of the surface recombination velocity was displayed in this injection level range. The bulk lifetimes of the substrates varied from 50 to 200μs.*

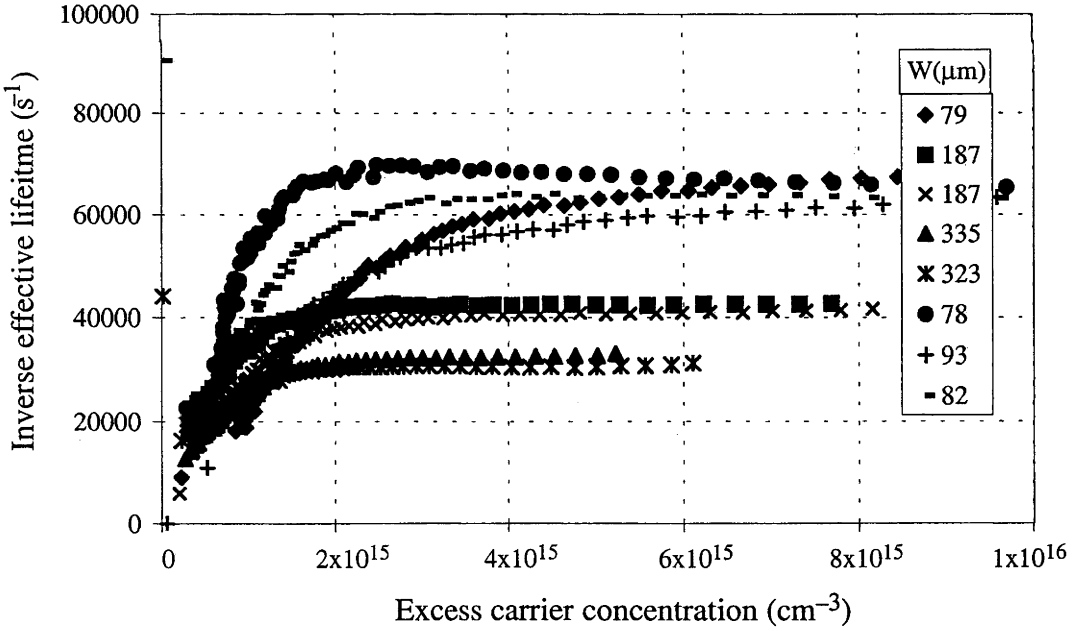

Figure 6.35: *Trapping evident in QSSPC measurements of effective lifetime for steam oxidised 0.5Ωcm multicrystalline silicon substrates.*
Trapping influenced measurements of all substrates at injection levels below $10^{15}cm^{-3}$. This restricted the range of measurements of surface recombination for the 0.5Ωcm substrates. Trapping was sufficiently severe to discard the measurements of the 79μm and 93μm samples.

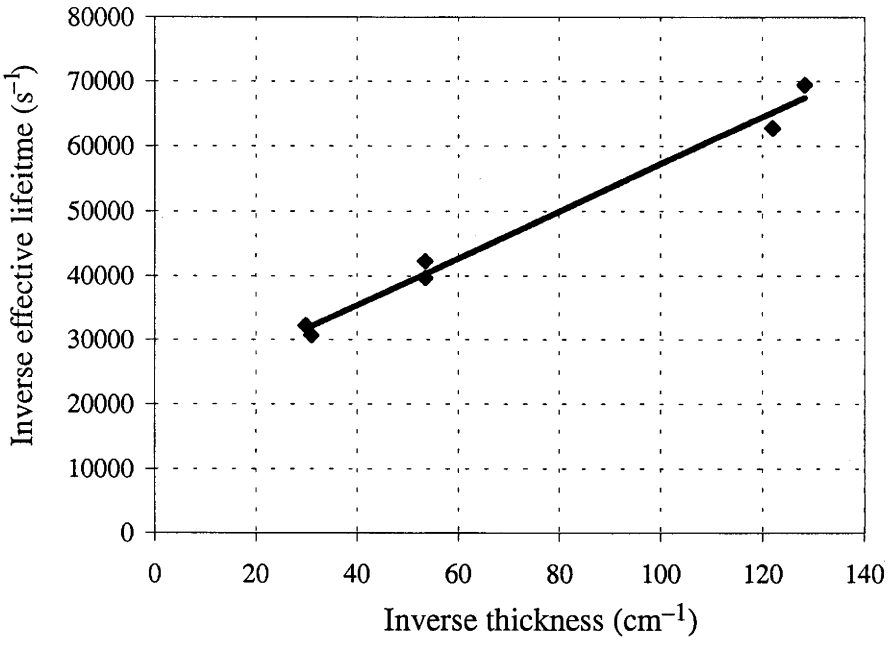

Figure 6.36: *Inverse effective lifetimes of steam oxidise 0.5Ωcm multicrystalline silicon for a range of substrate thicknesses.*
The excess carrier concentration was $3x10^{15}cm^{-3}$. The recombination parameters were determined from the line of best fit of inverse effective lifetime versus inverse thickness. The slope corresponded to a surface recombination velocity of 180cm/s and the intercept to a bulk lifetime of 48μs.

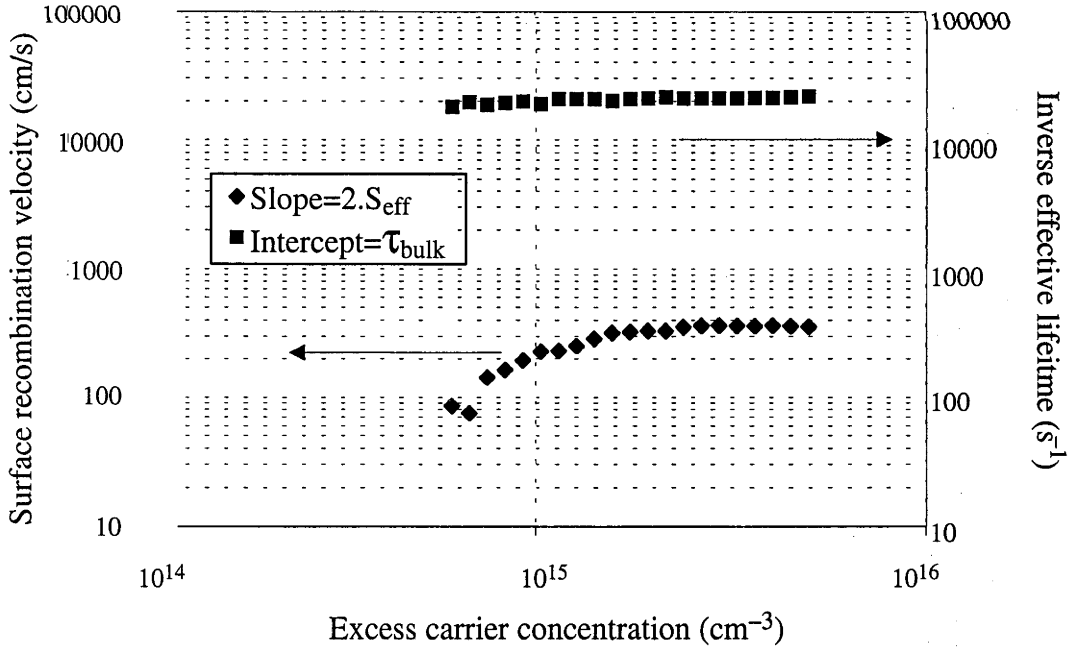

Figure 6.37: *Surface recombination and bulk life versus injection level from QSSPC measurements of 0.5Ωcm substrate.*
Trapping effects limited the useful range of surface recombination measurements to greater than $3x10^{15}cm^{-3}$. This is much greater than the injection levels likely for one sun operating conditions for the material.

thickness but the excess carrier concentration probably deviates slightly from flat in the thickest samples.

Trapping limited the range of useful information on surface recombination as a function of injection level. Between $3x10^{15}$ and $6x10^{15}$ surface recombination velocities were around 180cm/s. Below this injection level, the information was not useful as trapping in the thinner substrates dominated the effective lifetime causing the apparent decrease in surface recombination velocity in figure 6.37.

6.7.3 *Discussion*

The behaviour of the steam oxide passivated 1ΩcmFz substrates was similar to that observed by other investigations of similarly doped silicon passivated with a dry thermal oxide. The surface recombination velocity varied with injection level, doubling as the injection level decreased from $10^{16}cm^{-3}$ to $10^{14}cm^{-3}$. The surface passivation quality of the steam oxide was approximately half as good as that achieved with higher temperature dry thermal oxides. The bulk lifetime of the 1Ωcm Fz sample was 500μs, alleviating concerns of lifetime degradation due to contamination during steam oxidations [144].

The surface recombination velocities of the steam oxide passivated 1.5Ωcm samples were low, and varied little with injection level (Figure 6.33.). The bulk lifetime of the samples was excellent with lifetimes greater than 200μs indicating little contamination or degradation occurred form the steam oxidation process. The lower surface recombination velocity results for the 1.5Ωcm substrates (≈100cm/s) compared to the 1Ωcm Fz substrate (≈200cm/s) can be attributed (at least in part) to the lower substrate doping. The fact that there was little injection level dependence for the surface recombination velocity for the range of injection levels measured ($10^{14}cm^{-3}$ to $5x10^{15}cm^{-3}$) is contrary to what might otherwise have been expected. Thermally oxidised 1.5Ωcm <100> Fz wafers have been reported to demonstrate strong injection level dependence below $5x10^{14}cm^{-3}$ excess carrier concentration [36].

Further experimentation would be useful to attempt to explain the lack of injection level dependence of the 1.5Ωcm substrates. Spatially resolved measurements of the effective lifetimes may demonstrate a relation between surface recombination velocities and the crystallographic structure of the sample, which is influencing the large area measurements.

The low surface recombination velocity and high bulk lifetime provide the potential for excellent open circuit voltages, despite the low substrate doping. Injection levels around $10^{15}cm^{-3}$ corresponds to one sun illumination or open circuit voltage conditions. The base lifetime of 250μs and rear surface recombination velocity of 100cm/s would impose a voltage cap of 662mV on a 300μm substrate. Even better surface passivation would be expected from the oxide in completed devices with the band bending and alneal benefits

of the rear aluminium contacts. The steam oxide was therefore unlikely to be the primary limitation on 1.5Ωcm multicrystalline silicon device performance.

The injection level at maximum power, which is relevant to device efficiency [142], would be of the order of $10^{13}cm^{-3}$. This was lower than could accurately be measured with current QSSPC equipment. Lower injection level measurements would provide information on whether the surface recombination velocity of 1.5Ωcm substrates had stronger injection level dependence at lower excess carrier concentrates which may lead to lower efficiencies than would be expected from the measurements at higher injection.

The available information for the 0.5Ωcm substrates was quite limited due to the trapping effects. The useful measurements were restricted to injection levels above $3x10^{15}cm^{-3}$, which corresponded to illumination levels greater than 10suns. No relevant information on the injection level dependence of the surface recombination could be obtained for the limited injection level range measured. The surface recombination velocity, 180cm/s was less than that found on the 1Ωcm Fz substrates (220cm/s) at equivalent injection levels. This was surprising since the heavier doping would have been expected to cause higher surface recombination velocities. Techniques to determine the effective lifetime of the 0.5Ωcm substrates while avoiding trapping are necessary to evaluate the surface recombination velocity at injection levels corresponding to normal device operation.

If the surface recombination velocities at higher injection levels transfer to open circuit voltage, rear surface recombination at the oxide was playing a small role in limiting cell voltage of the 0.5Ωcm substrates due to the low bulk lifetime of the substrate (50μs). This can be seen for the modelled voltage of 0.5Ωcm substrates in figure 6.2. Changes in voltage were more significant with changes in bulk lifetime than rear surface recombination at these levels. Improvement of bulk lifetimes will lead to greater improvements of cell voltage, with the option of sacrificing surface recombination by a factor of five (up to $10^3cm/s$) if bulk lifetime could be doubled.

This work should be extended by determining the effects of high temperature anneals and dry oxidations on the surface recombination velocity of the multicrystalline samples. This will provide useful information on the best choice of oxide for rear surface passivation while identifying any lifetime degradation which may result from the higher temperature processes in order to further improve the rear reduced contact and rear locally diffused multicrystalline silicon cells.

CHAPTER 7
SUMMARY AND FUTURE DIRECTIONS

In this work, high efficiency approaches to the design and manufacture of multicrystalline silicon solar cells were investigated. The following areas were addressed: reflection control and light trapping, recombination processes in multicrystalline silicon, both in the bulk and at the surface, process monitoring and optimisation, and device design, complemented with theoretical modelling. As a result of this work, multicrystalline silicon solar cell efficiency at the ANU improved from less than 15% to greater than 18%.

7.1 Optical enhancement of multicrystalline silicon

The development of a suitable texture for multicrystalline silicon using isotropic etching provides the opportunity for efficiency improvement in multicrystalline silicon. 'Tubs' texturing has demonstrated excellent control of reflection losses after encapsulation. When combined with TiO_2 and MgF_2 antireflection coatings on the silicon and glass, respectively, weighted reflection losses from a completed cell were reduced to 5.2%, including reflection from the front metal contacts. In addition, the light trapping performance of the texture was particularly good, opening the opportunity for reduced substrate thicknesses while maintaining good light absorption.

The major drawback from 'tubs' texturing is the need for high resolution masked photolithographic processes. This precludes the use of 'tubs' texturing for any low cost cell manufacturing approach at present. The concept, however, remains promising, since it produces the low surface angles required for reflection control and light trapping after encapsulation. The potential for development of a suitable texture with a low cost approach warrants attention. $HF/HNO_3/H_2O$ acid etches can produce various degrees of roughening of silicon surfaces depending upon the etchant concentrations, without the need for oxide masks or photolithography.

7.2 Thin crystalline silicon cell modelling

The efficiency potential of thin conventional and multilayer cells was theoretically evaluated for low lifetime (<50ns) silicon. The cells were optimised for the thickness which provided maximum efficiency. This reduced the gap in performance between the multilayer and conventional cell designs when the cell thickness is not optimised.

Light trapping and surface recombination were identified as important influences on the absolute and relative performance of the thin cell designs. In the absence of light trapping, the multilayer cell design performed 1–2% better in absolute efficiency. With effective light trapping, overall efficiencies improve by more than 3% (absolute) with conventional cells designs slightly outperforming the multilayer approach. The relative merits of the two approaches in practical cells will depend upon the ability to incorporate suitable light trapping and surface passivation in a manner compatible with low cost fabrication.

7.3 Process monitoring and material quality enhancement

Systematic use of quasi–steady state photoconductance was made throughout this investigation. The quasi–steady state technique was shown to provide a more realistic area averaged effective lifetime of multicrystalline silicon than transient photoconductance decay, which was dominated by the effective lifetime in the better grains. Higher resistivity multicrystalline silicon substrates behaved similarly to single crystal silicon during measurement, but lower resistivity substrates displayed trapping behaviour, where measured lifetimes rapidly increased below a threshold carrier injection level.

The trapping phenomena requires further investigation to identify its cause and to enable development of a suitable measurement technique for these substrates at lower injection levels. The use of pulsed steady state measurements may provide further insight into the cause of the phenomena.

Process monitoring of the effective lifetime was established as an important tool for developing suitable protocols for manufacturing multicrystalline silicon cells. Process monitoring allowed the effect of each process step on the effective lifetime of the substrates to be observed. Mobile impurities were found to dominate the effective lifetime of Eurosil substrates during processing. Phosphorus diffusions and aluminium alloying gettered impurities from the bulk, improving the effective lifetime after these process steps typically used for solar cell fabrication. Oxidations to passivate emitters after phosphorus diffusions led to decreased effective lifetimes (despite improved surface passivation) due to the release of the previously gettered impurities as the peak phosphorus concentration decreased.

The multicrystalline silicon substrates demonstrated considerable benefit from phosphorus pre–gettering of the substrates. The more lightly doped substrates showed remarkable gain, with record effective lifetimes greater than 250μs on the 1.5Ωcm substrates and diffusion lengths greater than the typical substrate thicknesses on 0.5Ωcm substrates. This is further proof of the importance of mobile impurities in the original wafers. An important beneficial consequence of the removal of the mobile impurities from the substrate was that high effective lifetimes were then maintained during oxidations after phosphorus diffusions, eliminating the need for aluminium alloying during the final passivating oxide growth. This opened up the opportunity for increased device design flexibility. The use of process monitoring enabled rapid improvement of processing sequences to obtain higher effective lifetimes and cell efficiencies.

7.4 Rear surface recombination and high efficiency cell designs

Minority carrier diffusion lengths greater than the substrate thickness increased the importance of rear recombination. Modelling indicated that device designs with low rear surface recombination were required to further improve multicrystalline silicon cell

efficiencies. Aluminium alloying restricts cell efficiency due to relatively high rear surface recombination velocities, partly counteracting aluminium's gettering benefits on the bulk lifetimes.

The low lifetime of the 0.2Ωcm material (<15μs) ensured that diffusion lengths were significantly less than the substrate thickness. Cell efficiency was independent of rear surface recombination and contacts were applied to the entire rear of the cell. Cells benefited from the high substrate doping to demonstrate excellent open circuit voltages (>650mV) and fill factors. The inclusion of 'tubs' texturing produced low reflection losses and good light absorption with 18.6% (not independently confirmed) demonstrated on an encapsulated cell. The excellent cell performance obtained with a low lifetime, simple cell design should encourage commercial manufactures to increase substrate doping to improve cell voltages, especially if combined with the development of selective emitters to improve the blue response of the cells.

High efficiency designs typically used for single crystal silicon were modified to process sequences suitable for multicrystalline silicon, including steam oxidations and phosphorus pre–gettering. Reduced rear contact cell designs produced record open circuit voltages of 654mV on 0.5Ωcm multicrystalline silicon substrates and independently confirmed efficiencies of 18.2%. Despite the small fractional area, the addition of the rear metal contacts significantly increased the total recombination in the best cells, as shown by cell performance with different rear geometries and effective lifetime measurements.

Further improvement in cell performance required still lower surface recombination at the rear. This was attempted by introducing diffusions under the rear metal contacts. With the boron diffusions, no decrease in effective lifetime was detected during rear contact metallisation. Rear locally diffused cells demonstrated the highest voltages (622mV before AR coating) on 1.5Ωcm substrates, 20mV higher than voltages on aluminium alloyed cells of the same resistivity. However this falls substantially below the performance potential demonstrated after gettering, with 250μs effective lifetimes promising voltages close to 675mV.

The 0.5Ωcm material performed worse with the rear local diffusions than with reduced rear contacts. This poor performance can be attributed to lifetime degradation due to the boron treatment. Boron sheet diffusions degraded the lifetime of the 0.5Ωcm and 1.5Ωcm multicrystalline silicon substrates by 50–80%. Masked local diffusions produced less lifetime degradation, but the degradation was still sufficient to decrease the efficiency potential of the cells. Boron diffusion protocols need to be developed which avoid degrading the substrate lifetime if the benefit of the low surface recombination velocities of rear locally diffused cells is to be obtained.

Designs to reduce recombination at the rear of single crystal cells relied on the passivation properties of thermal oxides. Measurements of steam oxidised 1.5Ωcm silicon substrates

indicated that surface recombination velocities can be low (<150cm/s) at injection levels near open circuit voltage. This low surface recombination velocity provides the potential for voltages greater than 660mV, much higher than demonstrated with the 1.5Ωcm substrates to date. Surface recombination velocities are expected to be even lower if an aluminium capping layer is present. Measurements over a wider range of injection levels and substrate resistivities are necessary to determine the efficiency potential of multicrystalline silicon cells with rear oxides. Investigations in the future may indicate that PECVD silicon nitrides are a better candidate for rear surface passivation on multicrystalline silicon with the associated benefits of low temperature processing and hydrogen passivation.

7.5 Thinner multicrystalline silicon solar cells

The cost of multicrystalline silicon substrates can be reduced by reducing the substrate thickness, thus increasing the number of wafers cut from a single ingot. Other technologies, such as ribbon growth, can produce thin multicrystalline layers directly. The importance of optimising thickness for cell efficiency was highlighted in the thin silicon cell modelling. Reducing the substrate thickness reduces the material quality required for high cell efficiencies, provided suitable light trapping and surface passivation can be achieved.

For many of the lower resistivity substrates (<0.5Ωcm) with diffusion lengths of the order of typical substrate thicknesses (300μm) or less, the efficiency of the cells could be considerably enhanced by reducing the substrate thickness, with the potential for higher currents and voltages. 'Tubs' texturing can provide the light trapping required, with thermally oxidised rear surfaces combined with reduced rear contacts or rear local diffusions suppressing rear surface recombination. Thin multicrystalline silicon solar cells warrant research efforts for their potential for improved cell efficiencies and reduced substrate costs.

REFERENCES

[1] H.W. Schock and A. Shah "Status and prospects of photovoltaic thin film technologies," *Proc 14th Euro. PVSEC.,* Barcelona, Spain, 1997, pp2000–2005

[2] P. Meyers and R. Birkmire "The future of CdTe photovoltaics," *Prog in PV,* **3,** pp393–402 (1995)

[3] V. Nadenau, D. Braunger, D. Hariskos, M. Kaiser, C.H. Koble, A. Oberacker, M. Ruckh, U. Ruhle, R. Schaffer, D. Schmid, T. Walter, S. Zweigart and H.W. Schock "Solar cells based on $CuInSe_2$ and related compounds:material and device properties and processing," *Prog in PV,* **3,** pp363–382 (1995)

[4] F. Ferrazza and D. Margadonna "New developments and industrial perspective of crystalline silicon technologies for PV," *Proc 13th Euro. PVSEC,* Nice, France, 1995, pp3–8

[5] M.A. Green *Solar cells: operating principles, technology and system applications,* University of New South Wales, Australia (1986)

[6] M.A. Green *High efficiency silicon solar cells,* Trans Tech Publications, Switzerland (1987)

[7] M.A. Green *Silicon solar cells: advanced principles and practice,* Centre for Photovoltaic Devices and Systems, University of New South Wales, 1995

[8] A.G. Aberle, S.R. Wenham and M.A. Green "Decreased emitter sheet resistivity loss in high–efficiency silicon solar cells," *Prog in PV,* **2,** pp3–17 (1994)

[9] E. Yablonovitch and G.D. Cody "Intensity enhancement in textured optical sheets for solar cells," *IEEE Trans. El. Dev.,* **29,** pp300–305 (1982)

[10] J. Schmidt, A. Aberle and R. Hezel "Investigation of carrier lifetime instabilities in Cz–grown silicon," *Proc 26th IEEE PVSC,* Annaheim, Ca., USA, Oct., 1997. *In press.*

[11] J. Zhao, A. Wang, P. Altermatt and M.A. Green, "Twenty–four percent efficient silicon solar cells with double layer antireflection coatings and reduced reflection losses," *Appl. Phys. Lett.,* **66,** p3636 (1995)

[12] J. Zhao, A. Wang and M.A. Green "Emitter design for high efficiency silicon solar cells. part I: terrestrial cells," *Prog. in PV,* **1,** pp193–202 (1993)

[13] F. Ferrazza,. "Growth and post growth processes of multicrystalline silicon for photovoltaic use," *Proc. of Polycrystalline Semiconductors '95,* Gargnano, Italy, Sept., 1995

[14] C.P. Khattak and F. Schmid "High–efficiency solar cells using HEM silicon," *Proc. 1st World Conf. on PV Energy Conversion,* Hawaii, 1994, p1351–1355

[15] A. Rohatgi and S. Narashima "High–efficiency cell fabrication on low–defect density materials," *Proc. 6th Workshop Role Impurities and Defects in Silicon Device Processing,* ed B. Soppori, NREL Golden, Colorado, 1996, pp127–138

[16] S. Narayanan, S.R. Wenham and M.A. Green, "17.8% Efficient polycrystalline silicon solar cells," *IEEE Trans. Electron Dev.,* **37,** p. 383 (1990)

[17] M.A. Green, "Recent Advances in Silicon Solar Cell Performance", *Conf Record 10th Euro. PVSEC,* Lisbon, April 1991, pp250–253

[18] A. Rohatgi, S. Narashima, S. Kamra, P. Doshi, C.P. Khattak, K. Emery and H. Field, "Record high 18.6% efficient solar cell on HEM multicrystalline material," *Proc. 25th IEEE PVSEC,* Washington, May, 1996, p1554.

[19] R. Monna, D. Angermeier, A. Slaoui and J.C. Muller "Poly–Si thin films on graphite substrates by rapid thermal chemical vapour deposition for photovoltaic application," *Proc 14th Euro. PVSEC.* Barcelona, Spain, 1997, pp1456–1459

[20] A.M. Barnett, S.R. Collins, J.E. Cotter, D.H. Ford, R.B. Hall and J.A. Rand "Polycrystalline silicon–film™ solar cells: present and future" *Prog in PV,* **2**, pp163–170 (1994)

[21] M.A. Green, A. Wang, J. Zhao, G.F. Zheng, W. Zhang, Z. Shi, C.B. Honsberg and S.R. Wenham, "23.5% efficiency and other recent improvements in silicon solar cell and module performance," *Proc. 12th Euro. PVSEC*, Amsterdam, Netherlands, April, 1994, pp776–779

[22] C.B. Honsberg, F. Yun, M.A. Green and S.R. Wenham, "Mechanically grooved, multi–junction, interdigitated rear contact silicon solar cells for low lifetime substrates," *Proc. 12th Euro. PVSEC*, Amsterdam, Netherlands, April, 1995, pp63–66

[23] G. Ballhorn, K.J. Weber, S. Armand, M.J. Stocks and A.W. Blakers "High efficiency thin multicrystalline silicon solar cells by liquid phase epitaxy," *Proc. 14th Euro. PVSEC.* Barcelona, Spain, 1997, pp1011–1014

[24] R. Brendel "A novel process for ultrathin monocrystalline silicon solar cells on glass," *Proc 14th Euro. PVSEC.* Barcelona, Spain, 1997, pp1354–1357

[25] K. Weber, K. Catchpole, M.J. Stocks and A.W. Blakers "Lift–off of silicon epitaxial layers for solar cell applications," *Proc 26th IEEE PVSC,* Annaheim, Ca., USA, Oct, 1997. *In press.*

[26] S. Hamamoto, H. Morikawa, H. Naomoto, Y. Kawama, A. Takami, S. Arimoto, T. Ishihara and K. Namba "Development of the VEST cell process for low cost substrates," *Proc 14th Euro. PVSEC,* Barcelona, Spain, 1997, pp2328–2332

[27] J. Zhao, A. Wang, S.R. Wenham and M.A. Green "21.5% efficient 47μm thin–layer silicon cell," *Proc 13th Euro PVSEC,* Nice, France, 1995, pp1566–1569

[28] M.A. Green "Silicon solar cell: the ultimate photovoltaic solution," *Prog in PV,* **2**, p87–94 (1994)

[29] K.A. Emery and D.L. King "Photovoltaic measruements — science and engineering" *Conf. Tutorial 19th IEEE PVSC,* New Orleans, Louisana, May 1987

[30] M.A. Green and M.J. Keevers "Optical Properties of Intrinsic Silicon at 300K," *Prog. in PV,* **3** p189–192 (1995)

[31] D. Redfield "Method for evaluation of antireflection coatings" *Solar Cells,* **3**, pp27–33 (1981)

[32] J. Zhao, A. Wang, P.P. Altermatt., S.R. Wenham and M.A. Green "24% efficient silicon solar cells," *Proc. 1st World Conf. on PV Energy Conversion,* Hawaii, 1994 p1477–1480

[33] Hecht and Zajac *Optics,* Addison–Wesley, Philippines (1974)

[34] O.S. Heavens *Optical Properties of Thin Solid Films,* Butterworths, London (1955)

[35] P.E. Gruenbaum, J.Y. Gan, R.R. King and R.M. Swanson "Stable passivations for high–efficiency solar cells" *Proc. 21st IEEE PVSC*, Kissimimee, 1990, pp317–322

[36] J. Schmidt, T. Lauinger, A. Aberle and R. Hezel, "Record low surface recombination velocities on low–resistivity silicon solar cell substrates," *Proc. 25th IEEE PVSEC*, Washington, May, 1996, p413

[37] A. Cuevas, G Giroult–Matlakowski, P. Basore and R. King. "Extraction of the surface recombination velocity of passivated phosphorous–doped silicon emitters," *Proc. 1st World Con.f on PV Energy Conversion*, Hawaii, 1994, pp1446–1449

[38] G. Hass "Thin films of titanium dioxide," *Vacuum,* **11,** pp331–345 (1952)

[39] A. P. Bradford and G. Hass "Anodically produced multiple oxide films for increasing the reflectance of evaporated aluminium" *J. Opt. Soc. Amer.,* **36**, p701 (1946)

[40] H.K. Pulker, G. Paesold and E. Ritter "Refractive indices of TiO_2 films produced by reactive evaporation of various titanium–oxygen phases," *Appl. Optics,* **15,** pp2986–2991 (1976)

[41] E.T. Fitzgibbons, K.J. Sladek and W.H. Hartwig "TiO_2 film properties as a function of processing temperature," *J Electrochem. Soc.,* **119,** pp734–739 (1972)

[42] H.J. Hovel. "TiO_2 antireflection coatings by a low temperature spray process," *J. Electrochem. Soc.* **125** pp983–985 (1978)

[43] K.L. Hardee and A.J. Bard "Semiconductor Electrodes I. The chemical vapour deposition and application of polycrystalline n–type titanium dioxide electrodes to the photosensitised electrolysis of water," *J Electrochem. Soc.,* **122,** p738–742 (1975)

[44] A.W. Blakers, "Shading losses of solar cell metal grids," *J. Appl. Phys.*, **71,** pp5237–5241 (1992)

[45] A.M. Barnett, D.H. Ford, R.B. Hall, C.L. Kendall and J.A. Rand, "Silicon–film solar cell development on ceramic substrates," *Proc. 9th Euro. PVSEC*, Freiburg, 1989, pp697–700

[46] A.W. Blakers, J.H. Werner, E. Bauser and H.J. Queisser, "Silicon epitaxial solar cell with 663mV open circuit voltage," *Appl. Phys. Lett.,* **60**, p2752 (1992)

[47] F. Restrepo and C.E. Backus, "On black solar cells or the tetrahedral texturing of a silicon surface," *IEEE Trans. on Elec. Dev.*, **23**, pp1195–1197 (1976)

[48] M.A. Green, A. Wang, J. Zhao, S.R. Wenham and Campbell P. "Enhanced light–trapping in 21.5% efficient thin–layer silicon solar cells," *Proc 13th Euro. PVSEC,* Nice, France, 1995, pp13–16

[49] S Narayanan "High efficiency polycrystalline silicon solar cells" *Ph. D. Thesis, UNSW* (1989)

[50] J.C. Zolper, S. Narayanan, S.R. Wenham and M.A. Green "16.7% efficient, laser textured, buried contact polycrystalline silicon solar cell" *Appl. Phys. Lett.,* **55,** pp2363–2365 (1989)

[51] M. Gross, private communication to Andrew Blakers, 1990

[52] U. Kaiser, M. Kaiser and R. Schindler, "Texture etching of multicrystalline silicon," *Proc. 10th Euro. PVSEC,* Kluwer Academic Publishers, Lisbon, April, 1991 pp293–294

[53] G. Willeke, H. Nussbaumer, H. Bender and E. Bucher, "A simple and effective light trapping scheme for polycrystalline silicon solar cells", *Sol. En. Mat. Sol. Cells,* **26,** pp345–356 (1992)

[54] J.M. Gee, W.K. Schubert, H.L. Tardy and T.D. Hund. "The effect of encapsulation on the reflectance of photovoltaic modules using textured multicrystalline–silicon solar cells," *Proc. 1st World Conf. on PV Energy Conversion*, Hawaii, 1994, pp1555–1558

[55] G. Willeke, P. Fath and E. Bucher "Progress on the Power Silicon Solar Cell Concept," *Proc. 1st World Conf. on PV Energy Conversion,* Hawaii, 1994, pp1283–1286

[56] A.W Blakers, "High efficiency silicon solar cells," *Festkörperprobleme, Advances in Solid State Physics* **30**, ed. U. Rössler, Vieweg, p403–423 (1990)

[57] C.T. Sah, R.N. Noyce and W. Shockley, "Carrier generation and recombination in p–n junctions and p–n junction characteristics," *Proc. IRE,* **45**, p1228 (1957)

[58] S.C. Choo, "Carrier generation–recombination in the space charge region of an asymmetrical p–n junction," *Solid State Elec.* **11**, p1069 (1968)

[59] H.J. Hovel, "The Effect of Depletion Region Recombination Currents on the Efficiencies of Si and GaAs Solar Cells," *Proc. 10th IEEE PVSC*, 1974 p34

[60] G.A.M. Hurkx, D.B.M. Klaassen and M.P.G Knuvers. "A new recombination model for device simulation including tunnelling," *IEEE Trans. Electron Dev,*. **39**, p331–338 (1992)

[61] R. Häcker and A. Hangleiter, "Intrinsic upper limits to the lifetime in silicon," *J. Appl Phys.* **75**, p7570 (1994)

[62] J. Dziewior and W. Schmid, "Auger coefficients for highly doped and highly excited silicon," *Appl. Phys. Lett.,* **31**, p346 (1977)

[63] J.G. Fossum and D.S. Lee, "A physical model for the dependence of carrier lifetime on doping density in non–degenerate silicon," *Solid State Electronics* **25**, p741 (1982)

[64] H.S. Bennett, "Comparison of theoretical and empirical lifetimes for minority carriers in heavily doped silicon," *Solid State Electronics* **30**, p893–897 (1984)

[65] D. Margadonna, F. Ferrazza and R. Peruzzi., "Donor and acceptor neutralisation in multicrystalline silicon," *10th Euro PVSEC*, Lisbon, Portugal, 1991, p678

[66] A. Rohatgi, W.A. Doolittle, A.W. Smith, F.V. Wald, R.O. Bell and C.E. Dube, "Doping and oxygen dependence of efficiency EFG silicon solar cells," *Proc. 21st IEEE PVSC*, Kissimimee, p581 (1990)

[67] T. Markvart "Review: Radiation damage in solar cells", *J. Mat. Sci: Materials in Electronics,* **1,** p1 (1990)

[68] D.J. Roulston, N.D. Arora and S.V. Chamberlain, "Modelling and measurement of minority–carrier lifetime versus doping in diffused layers of n^+–p silicon diodes," *IEEE Trans. Electron Dev.* **29**, p284 (1982)

[69] W.M. Bullis, "Properties of gold in silicon," *Solid State Electronics*, **9**, p143 (1966)

[70] W. Schmid and J. Reiner, "Minority–carrier lifetime in gold–diffused silicon at high carrier concentration," *J. Appl. Phys.,* **53,** p6250 (1982)

[71] M.A. Green and S.R Wenham. "Novel parallel multijunction solar cell," *Appl. Phys. Lett.* **65** pp2907–2909 (1994)

[72] A.B. Sproul, S. Edmiston, S.R. Wenham and M.A. Green, "Innovative Structures for thin film crystalline silicon solar cells to give high efficiencies from low quality silicon," *1st World Conf. on PV Energy Conversion*, Hawaii, 1994, pp1563–1566

[73] A.B. Sproul, Z. Shi, J. Zhao, Y.H. Tang, F. Yun, T. Young, Y. Huang, S. Edmiston, S.R. Wenham and M.A. Green, "Characterisation and analysis of multilayer solar cells," *1st World Conf. on PV Energy Conversion,* Hawaii, 1994, pp1410–1412

[74] S.R. Wenham, M.A. Green, S. Edmiston, P. Campbell, L. Koschier, C.B. Honsberg, A.B. Sproul, D. Thorpe, Z. Shi and G. Heizer, "Limits to the efficiency of silicon multilayer thin film solar cells," *1st World Conf. on PV Energy Conversion*, Hawaii, 1994, pp1234–123

[75] U. Rau and M. Goldbach, "Modelling of the electronic transport in multijunction solar cells," *Proc. 1st World Conf. on PV Energy Conversion,* Hawaii, 1994, p1421–1424

[76] P. Basore "PC–1D status and plans," *1st World Conf on PV Energy Conversion,* Hawaii, 1994

[77] A.K. Ghosh, C. Fishman and T. Feng, "Theory of the electrical and photovoltaic properties of polycrystalline silicon," *J. Appl. Phys.* **51**, p446 (1980)

[78] A. Sproul and M.A. Green "Experimental measurement of the intrinsic carrier concentration of silicon," *Proc 21st IEEE PVSC*, Kissimmee, 1990, pp380–385

[79] S.A. Edmiston, A.B. Sproul, M.A. Green and S.R. Wenham. "Modelling of Thin–film Crystalline Silicon Parallel Multi–junction Solar Cells," *Prog. in PV.* **3**, pp333–350 (1995)

[80] A. Cuevas, G Giroult–Matlakowski and P. Basore. "Surface recombination velocity and bandgap narrowing of highly doped n–type silicon," *12th Euro. PVSEC*, Nice, France, 1995, pp337–342

[81] R.R King and R.M. Swanson "Studies of diffused boron emitters: saturation current, surface recombination velocity and quantum efficiency," *IEEE Trans. Elec. Dev.,* **38**, pp1399–1409 (1991)

[82] R.R. King, R.A. Sinton and R.M. Swanson "Studies of diffused phosphorous emitters: saturation current, surface recombination velocity and quantum efficiency," *IEEE Trans. Elec. Dev.,* **37**, pp365–371 (1990)

[83] Z. Chen and A. Rohatgi, "Silicon surface and bulk defect passivation by low temperature PECVD oxides and nitrides," *1st World Conf. on PV Energy Conversion, Hawaii*, 1994, pp1331–1334

[84] M. Schöfthaler, R. Brendel, G. Langguth and J.H. Werner "High quality surface passivation by corona–charged oxides for semiconductor surface characterisation," *1st World Conf. on PV Energy Conversion*, Hawaii, 1994, pp1509–1512

[85] A. Neugroschel, F.A. Lindholm, S.C Pao and J.G. Fossum, "Emitter current suppression in a high–low emitter solar cell using an oxide–charge–induced electron accumulation layer" *Appl. Phys. Lett.*, **33**, pp168–170 (1978)

[86] R. Corkish and M.A. Green "Junction recombination current in abrupt junction diodes under forward bias" *J. Appl. Phys.,* **80**, 3083–3090 (1996)

[87] M.A. Green "Depletion region recombination in silicon thin–film multilayer solar cells," *Prog in PV.* **4** pp375–380 (1996)

[88] D.K. Schroder *Semiconductor material and device characterisation* John Wiley & Sons, New York, USA (1990)

[89] D.T. Stevenson and R.J. Keyes "Measurement of carrier lifetimes in germanium and silicon," *J. Appl. Phys.* **26** pp190–195 (1955)

[90] S. Glunz, Sproul A.B., Warta W. and Wettling W. "Injection–level–dependent recombination velocities at the Si–SiO_2 interface for various dopant concentrations," *J. Appl. Phys.* **75** pp1611–1615 (1994)

[91] J. Schmidt and A.G. Aberle "Accurate method for the determination of bulk minority carrier lifetime of mono and multicrystalline silicon wafers," *J. Appl. Phys.*, **81**, pp6186–619 (1997)

[92] R.A. Sinton, A. Cuevas and M. Stuckings "Quasi–steady state photoconductance, a new method for solar cell material and device characterisation," *Proc 25th IEEE PVSC*, Washington, USA, May 1996, pp457–460

[93] A. Cuevas and R.A. Sinton "Prediction of open circuit voltage of solar cells from the steady photoconductance," *Prog. in PV* **5** pp79–90 (1997)

[94] Sinton Consulting, 1132 Green Circle Boulder, CO 80303. Phone: 303–554–7580. FAX: 303–554–7582. Email Ronsinton@aol.com

[95] R.A. Sinton and R.M. Swanson "Simplified backside–contact solar cells" *IEEE Trans. El. Dev.*, **37**, pp348–352 (1990)

[96] D.E. Kane and R.M. Swanson "Measurement of the emitter saturation current by a contactless photoconductivity decay method" *Proc. 18th IEEE PVSC,* 1985, pp578–583

[97] A. Cuevas, M. Stocks and R. Sinton "Overview of the quasi–steady state photoconductance technique," *2nd World Conf. PV Energy Conversion,* Vienna, Austria, July, 1998 (to be presented)

[98] H. Nagel, J. Schmidt, A. Aberle and R. Hezel "Exceptionally high bulk minority–carrier lifetimes in block–cast multicrystalline silicon," *Proc 14th Euro. PVSEC.* Barcelona, Spain, 1997, pp762–765

[99] R. Brendel "Note on the interpretation of the injection–level–dependent surface recombination velocities," *Appl. Phys. A.*, **60**, p523 (1995)

[100] A. Aberle, J. Schmidt and R. Brendel "On the data analysis of light biased photoconductance decay measurements," *J. Appl. Phys.*, **79**, pp1491–1496 (1996)

[101] J. Gee "Phosphorus diffusions for gettering–induced improvement of lifetime in various silicon materials," *Proc. 22nd IEEE PVSC,* 1991, pp118–123

[102] H. Lautenschlager, F. Lutz, C. Schetter, U. Schubert and R. Schindler "Unpassivated and passivated multicrystalline silicon solar cells with >17% efficiency," *Proc 14th Euro. PVSEC.* Barcelona, Spain, 1997 pp1358–1360

[103] S. Martinuzzi, F. Ferrazza, F. Floret, I. Perichaud and M. Bacon "Influence of oxygen and subgrain boundaries in Eurosil multicrystalline silicon wafers and cells" *Proc. 13th Euro. PVSEC*, Nice, France, October 1995, pp1382–1385

[104] Z. Chen and A. Rohatgi "Silicons surface and bulk defect passivation by low temperature PECVD oxides and nitrides," *Proc. 1st World Conf. on PV Energy Conversion*, Hawaii, 1994, pp1555–1558

[105] P. Lölgen, A. Rohatgi, P. Sana, W.C. Sinke, A.W. Weeber, C. Leguijt, R.A. Steeman and J.A. Eikelboom, "Al treatment–induced improvement in bulk carrier lifetime measured independently from surface effects," *Proc. 12th Euro. PVSEC,* Amsterdam, Netherlands ,April, 1994, p1778.

[106] H.E. Elgamel, S. Sivoththaman, M.Y. Ghannan, J. Nijs, R. Mertens, M. Rodot, D. Sarti and Le Quang Nam, "640mV open–circuit voltage multicrystalline silicon solar cells: role of base doping on device parameters," *Solar En. Mat. and Solar Cells,* **36**, pp99–105 (1994)

[107] H.E. Elgamel, A.M. Barnett, A. Rohatgi, Z. Chen, C. Vinckier, J. Nijs and R. Mertens, "Efficient combination of surface and bulk passivation schemes of high–efficiency multicrystalline silicon solar cells," *J. Appl. Phys.,* **78**, p3457 (1995)

[108] W.K. Schubert "Multicrystalline silicon solar cells: gettering optimisation and characterisation," *Proc 23rd IEEE PVSC,* Louisville, Kentucky, USA, May, 1993, pp230–235

[109] Runyan W.R. and Bean K.E. *Semiconductor integrated circuit processing technology,* Addison–Wesley, Reading, Mass. USA 1990

[110] J. Gee, R.R. King, J.H. Reiss, K.W. Mitchell and S. Narayanan "Effect of oxidation on phosphorus–diffused crystalline silicon substrates," *Proc. 6th Workshop Role Impurities and Defects in Silicon Device Processing* ed B. Soppori, NREL Golden, Colorado 1996 pp264–267

[111] J.H. Werner, J.K. Arch, R. Brendel, G. Langguth, M. Konuma, E. Bauser, G. Wagner, B. Steiner and W. Appel, "Crystalline thin film silicon solar cells," *Proc. 12th Euro. PVSEC,* Amsterdam, Netherlands, April, 1994.

[112] R.D. Thompson and K.N. Tu "Low temperature gettering of Cu, Ag and Au across a wafer of Si by Al," *Appl Phys Lett,* **41,** p440 (1992)

[113] A.W. Blakers and M.A. Green "20–percent efficient silicon solar cell,"*Appl Phys Lett.,* **48**, pp215–217 (1986)

[114] A. Luque, A. Moehlecke, R. Lagos and C. del Canizo "Segregation model for Si gettering by Al," *Phys. Sta. Sol.(a),* **155**, pp43–49 (1996)

[115] A. Rohatgi, S. Narashima, S. Kamra, and C.P. Khattak "Fabrication and analysis of record high 18.2% efficient solar cells on multicrystalline silicon material," *IEEE Elec. Dev. Lett.* **17** p401–403 (1996)

[116] P. Lölgen, C Leguijt, J.A. Eikelboom, R.A. Steeman, W.C. Sinke, L.A. Verhoef, P.F.A. Alkemade and E. Algra, "Aluminium back–surface field doping profiles with surface recombination velocities below 200cm/s," *Proc 23rd IEEE PVSC* Louisville, Kentucky, USA, May, 1993, p236.

[117] P.A. Basore "Extended spectral analysis of internal quantum efficiency," *Proc. 23rd IEEE PVSC,* Louisville, Kentucky, USA, May, 1993 pp147–152

[118] R.R. King, E.W. Thomas, W.B. Carter and A. Rohatgi "The effect of aluminium and boron solid–source doping on the recombination in silicon solar cells," *Proc. 22nd IEEE PVSC* 1991 pp229–234

[119] P. Hahne, W. Wettling and R. Schindler "Aluminium back surface field doping profiles by conventional" *12th Euro PVSEC,* Amsterdam, Netherlands, April, 1994, pp1011–1013

[120] J.S. Kang and D.K. Schroder "Gettering in silicon," *J. Appl. Phys.,* **65**, pp2974–2984 (1989)

[121] S. Narasimha and A. Rohatgi "The effects of rapid pre–getter anneal treatments on the performance of cast mc–Si solar cells," *Proc. 7th Workshop Role Imp. and Def. in Si Device. Processing* ed B. Soppori, NREL, Vail, Colorado Aug 1997 pp191–194

[122] R.L. Meek, T.E. Seidal and A.G. Cullis "Diffusion gettering of Au and Cu in silicon," *J. Electrochem. Soc.* **70** pp786–796 (1975)

[123] E.J. Mets "Poisoning and gettering effects in silicon junctions," *J. Electrochem. Soc.,* **112**, pp420–425 (1965)

[124] Y. Hayaufji, T. Yanuda and Y. Aoki "Laser damage gettering and its application to lifetime improvement in silicon," *J. Electrochem. Soc.,* **128**, pp1975–1980 (1981)

[125] M.C. Chen and V.J. Silvestgri "Post–epitaxial polysilicon and Si_3N_4 gettering in silicon," *J. Electrochem. Soc.,* **129**, pp1294–1299 (1982)

[126] T.E. Seidal, R.L. Meek and A.G. Cullis "Direct comparison of ion–damaged gettering and phosphorus–diffusion gettering of Au in Si," *J. Appl. Phys.,* **46**, pp600–609 (1975)

[127] A. Kinomura, J. Wong–Leung, J.S. William and M. Petravic "Gettering of metals to nanocavities in silicon," *Proc. IEEE COMMAD* Canberra, Australia Dec 1996, pp474–478

[128] S. Narasimha, S. Kamra and A. Rohatgi "The optimisation and fabrication of high–efficiency HEM multicrystalline silicon solar cells," *Proc. 25th IEEE PVSC* Washington, May 1996 pp449–452

[129] A.W. Stephens and M.A. Green "Effectiveness of 0.08 molar iodine in ethanol solution as a means of chemical surface passivation for photoconductance decay measurements," *Sol. En. Mat. Sol. Cells,* **45**, pp255–265 (1997)

[130] E. Yablonovitch, D.L. Allara, C.C. Chang, T. Gmitter and T.B. Bright "Unusually low surface recombination velocity on silicon and germanium surfaces," *Phys. Rev. Lett.,* **57**, p249–252 (1986)

[131] A. Aberle, personal communication, 1997

[132] S.A. McHugo, H. Heislmair and E.R. Weber "Gettering of metallic impurities in photovoltaic silicon," *Appl. Phys. A.,* **64**, pp127–137 (1997)

[133] A. Rohatgi and S. Narashima "High–efficiency cell fabrication on low–defect density materials," *Proc. 6th Workshop Role Impurities and Defects in Silicon Device Processing,* ed B. Soppori, NREL Golden, Colorado, 1996, pp127–138

[134] R.R. King and R.M. Swanson, "Studies of diffused boron emitters: saturation current, bandgap narrowing and surface recombination velocity," *IEEE Tran.s Electron Dev.,* **38**, p1399 (1991)

[135] A.W. Blakers, J. Zhao, A. Wang, A.M. Milne, X. Dai and M.A. Green, "23% efficient silicon solar cell," *Proc. 9th Euro. PVSEC*, Freiburg, Germany, 1989, p32.

[136] R. Einhaus, E. Van Kerschaver, F. Deurinckx, A. Zeibakowski, J. Szlufcik, J. Nijs and R. Mertens "Optimisation of a selective emitter process for multicrystalline silicon solar cells to meet industrial requirements," *Proc 14th Euro. PVSEC.* Barcelona, Spain, 1997 pp187–190

[137] S. Noel, R. Schindler, S.W. Glunz, W. Warta and W.Wettling "Single step rapid thermal diffusion for selective emitter formation" *Proc 13th Euro PVSEC,* Nice, France, 1995, pp1406–1408

[138] C.M. Chong ,S.R. Wenham and M.A. Green " High–effficiency, laser grooved, buried contact silicon solar cells" *Appl. Phys. Lett.* **52**, p407 (1988)

[139] M. Schöfthaler, U. Rau, W. Füssel and J.H. Werner, "Optimisation of the back contact geometry for high efficiency solar cells," *Proc. 23rd IEEE PVSEC,* Louisville, Kentucky, USA May, 1993, p1490.

[140] S. Sterk, J. Knobloch and W. Wettling, "Optimisation of the rear contact pattern of high–efficiency silicon solar cells with and without back surface field," *Prog. in PV.* **2**, p19 (1994)

[141] A.W. Blakers, A. Wang, A.M. Milne, J. Zhao, X. Dai and M.A. Green "22.6% efficient silicon solar cells," *Proc 4th Photovoltaic Solar Energy Conf.* Sydney, Jan 1989 p111

[142] A.G. Aberle, S.J. Robinson, A. Wang, J. Zhao, S.R. Wenham and M.A. Green "High efficiency silicon solar cells: fill factor limitations and non–ideal diode behaviour due to voltage–dependent rear surface recombination velocity" *Prog in PV.*, **1**, pp133–143 (1993)

[143] R.A. Sinton, Y. Kwark, J.Y. Gan and R.M. Swanson "27.5% Si concentrator Solar Cells," *Elect. Dev. Lett.* **7** p567 (1986)

[144] J. Zhao, A. Wang and M.A. Green, "High efficiency multicrystalline silicon solar cells using standard float–zoned processing," *Prog. in PV.*, **5**, p169–174 (1997)

[145] Photovoltaics Special Research Centre, UNSW Web Page "*Achievements*," (http://www.pv.unsw.edu.au/achiev.html) March 1998

[146] M.A. Green, personal communication. E–mail to Andres Cuevas, March 1998

Appendix A. Publications

Publications arising from the research in this thesis:

Refereed journal papers as joint author

1. M.J. Stocks, A.J. Carr and A.W. Blakers "Texturing of polycrystalline silicon" *Solar Energy Materials and Solar Cells,* **40** pp33–42 (1996)
2. M.J.Stocks, A. Cuevas and A.W. Blakers "Theoretical Comparison of Multilayer and Conventional Thin Silicon Solar Cells" *Progress in Photovoltaics* **4** pp35–54 (1996)
3. A. Cuevas, M.J. Stocks, S. Armand, M. Stuckings, A.W. Blakers and F. Ferrazza "High minority carrier lifetime in multicrystalline silicon" *Applied Physics Letters* **70** pp1017–1019 (1997)
4. K.J. Weber, G. Ballhorn, M.F. Stuckings, S. Armand, M.J. Stocks and A.W. Blakers "High efficiency multicrystalline silicon solar cells by liquid phase epitaxy" *Solar Energy Material and Solar Cells* **52** pp61–68 (1998)
5. M.J. Stocks, A.W. Blakers and A. Cuevas "Record open circuit voltage multicrystalline silicon solar cells" *IEEE Transactions on Electron Devices* (accepted for publication)

Conference Publications

6. M.J. Stocks, A.J. Carr and A.W. Blakers "Reflection losses from silicon solar cells" *32nd Annual Australian and New Zealand Solar Energy Society Conference.* Sydney, New South Wales. Dec 1994. pp155–160
7. M.J. Stocks, A.J. Carr and A.W. Blakers "Texturing of polycrystalline silicon" *First World Conference on Photovoltaic Energy Conversion*, Waikoloa, Hawaii Dec 1994 pp1551–1554
8. M.J. Stocks and A.W. Blakers "Junction recombination in multilayer silicon solar cells" *13th EC Photovoltaics Specialists Conference,* Nice, France. Oct 1995. pp1219–1222
9. M.J. Stocks and A.W. Blakers "Thin multilayer versus conventional silicon solar cell designs" *33rd Annual Australian and New Zealand Solar Energy Society Conference.* Hobart, Tasmania. Nov/Dec 1995. pp169–174
10. Matthew Stocks, Andrew Blakers and Andres Cuevas "Process monitoring of multicrystalline silicon solar cells using quasi–steady state photoconductance measurements" *34th Annual Australian and New Zealand Solar Energy Society Conference.* Darwin, Australia Oct, 1996. pp31–38
11. K.J. Weber, G. Ballhorn, M.F. Stuckings, S. Armand, M.J. Stocks and A.W. Blakers "Efficient thin multicrystalline silicon solar cells" *34th Annual Australian and New Zealand Solar Energy Society Conference.* Darwin, Australia Oct, 1996. pp150–157
12. Matthew Stocks, Andrew Blakers and Andres Cuevas "Process dependence of minority carrier lifetimes in multicrystalline silicon solar cells" *IEEE Conference on Optoelectronic and Microelectronic Materials and Devices*, Canberra, Australia, Dec 1996 pp8–11
13. G. Ballhorn, A.W. Blakers, M.F. Stuckings, M.J. Stocks, S. Armand and K.J. Weber "Efficient thin multicrystalline silicon solar cells" *IEEE Conference on Optoelectronic and Microelectronic Materials and Devices*, Canberra, Australia, Dec 1996 pp24–28
14. M.J. Stocks, A.W. Blakers and A. Cuevas "High efficiency, reduced rear contact area multicrystalline silicon solar cells" *14th European Photovoltaic Solar Energy Conference*, Barcelona, Spain, June/July 1997 pp766–769

15. M.J. Stocks, A. Cuevas and A.W. Blakers "Minority carrier lifetimes of multicrystalline silicon during solar cell processing" *14th European Photovoltaic Solar Energy Conference*, Barcelona, Spain, June/July 1997 pp770–773
16. G. Ballhorn, K.J. Weber, S. Armand, M.J. Stocks and A.W. Blakers "High efficiency thin multicrystalline silicon solar cells by liquid phase epitaxy" *14th European Photovoltaic Solar Energy Conference*, Barcelona, Spain, June/July 1997 pp1011–1013
17. M.J. Stocks, A.W. Blakers and A. Cuevas "Multicrystalline silicon solar cells with low rear surface recombination" *26th IEEE Photovoltaics Specialist Conference*, Annaheim, California, 1997 *In press*
18. M.J. Stocks, A. Cuevas and A.W. Blakers "Process monitoring of multicrystalline silicon solar cells with quasi–steady state photoconductance" *26th IEEE Photovoltaics Specialist Conference*, Annaheim, California, 1997 *In press*

Publications related to the work in this thesis:

Refereed journal papers as joint author

19. A.W. Blakers, K.J. Weber, M.F. Stuckings, S. Armand, G. Matlakowski, A.J. Carr, M.J. Stocks, A. Cuevas and T. Brammer "17% Efficient thin film silicon solar cell by liquid phase epitaxy" *Progress in Photovoltaics* **3** pp193–195 (1995)

Conference Publications

20. K.J. Weber, A.W. Blakers, M.J. Stocks, M.F. Stuckings, A. Cuevas, A.J. Carr and T. Brammer "17% Efficient thin film silicon solar cell by liquid phase epitaxy" *First World Conference on Photovoltaic Energy Conversion*, Waikoloa, Hawaii Dec, 1994 pp1391–1393
21. A.W. Blakers, K.J. Weber, M.F. Stuckings, S. Armand, G. Matlakowski, M.J. Stocks and A. Cuevas "18% Efficient thin film silicon solar cell by liquid phase epitaxy" *13th EC Photovoltaics Specialists Conference*, Nice, France. Oct 1995. pp33–36
22. A.W. Blakers, K.J. Weber, M.F. Stuckings, S. Armand, G. Matlakowski, M.J. Stocks and A. Cuevas "18% Efficient thin film silicon solar cell by liquid phase epitaxy" *33rd Annual Australian and New Zealand Solar Energy Society Conference.* Hobart, Tasmania. Nov/Dec 1995. pp81–86
23. A.W. Blakers and M.J. Stocks "Modelling the measurement of silicon solar cells under natural sunlight" *14th European Photovoltaic Solar Energy Conference*, Barcelona, Spain, June/July 1997 pp305–308
24. K.J. Weber, K. Catchpole, M. Stocks and A.W. Blakers "Lift–off of epitaxial layers for solar cell applications" *26th IEEE Photovoltaics Specialist Conference*, Annaheim, California, 1997 *In press*